PB84-199793

In situ Field Portable Fine Particle Measuring Device

Particle Measuring Systems, Inc., Boulder, CO

Prepared for

Industrial Environmental Research Lab.
Research Triangle Park, NC

May 84

U.S. Department of Commerce
National Technical Information Service
NTIS

PB84-199793

EPA-600/2-84-096
May 1984

IN SITU FIELD PORTABLE FINE PARTICLE MEASURING DEVICE

by

Robert G. Knollenberg
Particle Measuring Systems Inc.
1855 South 57th Court
Boulder, Colorado 80301

EPA Contract No. 68-02-2668

EPA Project Officer: D.Bruce Harris
Industrial Environmental Research Laboratory
Research Triangle Park, N.C. 27711

INDUSTRIAL ENVIRONMENTAL RESEARCH LABORATORY
OFFICE OF RESEARCH AND DEVELOPMENT
U.S. ENVIRONMENTAL PROTECTION AGENCY
RESEARCH TRIANGLE PARK, NC 27711

REPRODUCED BY
NATIONAL TECHNICAL
INFORMATION SERVICE
U.S. DEPARTMENT OF COMMERCE
SPRINGFIELD, VA. 22161

TECHNICAL REPORT DATA

(Please read Instructions on the reverse before completing)

1. REPORT NO. EPA-600/2-84-096	2.	3. RECIPIENT'S ACCESSION NO. PB84 199793
4. TITLE AND SUBTITLE In Situ Field Portable Fine Particle Measuring Device		5. REPORT DATE May 1984
		6. PERFORMING ORGANIZATION CODE
7. AUTHOR(S) Robert G. Knollenberg		8. PERFORMING ORGANIZATION REPORT NO.
9. PERFORMING ORGANIZATION NAME AND ADDRESS Particle Measuring Systems, Inc. 1855 South 57th Court Boulder, Colorado 80301		10. PROGRAM ELEMENT NO.
		11. CONTRACT/GRANT NO. 68-02-2668
12. SPONSORING AGENCY NAME AND ADDRESS EPA, Office of Research and Development Industrial Environmental Research Laboratory Research Triangle Park, NC 27711		13. TYPE OF REPORT AND PERIOD COVERED Final; 9/77 - 8/79
		14. SPONSORING AGENCY CODE EPA/600/13

15. SUPPLEMENTARY NOTES IERL-RTP project officer is D. Bruce Harris, Mail Drop 62, 919/541-7807.

16. ABSTRACT The report describes the design, development, and testing of an in situ fine particle measuring device--the Fine Particle Stack Spectrometer System (FPSSS). It is a laser-fed optical system with detection by near-forward light scattering. Sample volume is established by a high-resolution optical system that views particle images in a dark field through a masked beam splitter. The FPSSS covers an 0.5 to 11.0 micrometer size range with 60-channel resolution. Absolute theoretical accuracy is + or - 20% of size for completely unknown refractive index. The FPSSS is designed to operate continuously at in-stack temperatures up to 250 C at flow velocities up to 30 m/sec. It has been laboratory characterized and field tested on coal-fired power plants at both the inlets and outlets of control devices. Its performance indicates good agreement with impactors and excellent agreement with opacity meters in computed mass loading and optical opacity. Its size resolution is greater than other currently known techniques. Its eventual use will be directed at characterizing particulate emissions of stacks or other stationary sources and qualitatively evaluating the performance and collection efficiencies of particulate control devices now in operation.

17. KEY WORDS AND DOCUMENT ANALYSIS

a. DESCRIPTORS		b. IDENTIFIERS/OPEN ENDED TERMS	c. COSATI Field/Group	
Pollution	Light Scattering	Pollution Control	13B	20N
Spectrometers		Stationary Sources	14B	
Particles		Fine Particulate	14G	
Dust			11G	
Lasers			20E	
Optics			20F	

18. DISTRIBUTION STATEMENT Release to Public	19. SECURITY CLASS *(This Report)* Unclassified	21. NO. OF PAGES 228
	20. SECURITY CLASS *(This page)* Unclassified	22. PRICE

NOTICE

THIS DOCUMENT HAS BEEN REPRODUCED FROM THE BEST COPY FURNISHED US BY THE SPONSORING AGENCY. ALTHOUGH IT IS RECOGNIZED THAT CERTAIN PORTIONS ARE ILLEGIBLE, IT IS BEING RELEASED IN THE INTEREST OF MAKING AVAILABLE AS MUCH INFORMATION AS POSSIBLE.

NOTICE

This document has been reviewed in accordance with U.S. Environmental Protection Agency policy and approved for publication. Mention of trade names or commercial products does not constitute endorsement or recommendation for use.

ABSTRACT

During the past two years an *in situ* fine particle measuring device has been developed by Particle Measuring Systems for the Environmental Protection Agency. The resulting instrument is designated a Fine Particle Stack Spectrometer System. The instrument utilizes a laser fed optical system with detection by near-forward light scattering. Sample volume is established through the use of a high resolution optical system viewing particle images in a dark field through a masked beam splitter. The instrument covers an 0.5 to 11.0 μm size range with 60 channels resolution. Absolute theoretical accuracy is ±20% of size for completely unknown refractive index. The instrument is designed to operate continuously at in-stack temperatures up to 250°C at flow velocities up to 30 m/sec. Flow velocities are determined from measured particle transit times through the laser beam. Internal probe components are cooled by a water jacket and external heat exchanger. The heat exchanger, probe pulse processing electronics, data acquisition system and operating controls are housed in a central electronics console. The data acquisition system utilizes a microprocessor, EROM firmware, and a matrix printer/plotter to provide a variety of processed data reports. It has been laboratory characterized and field tested on coal-fired power plants at both the inlets and outlets of control devices. Its performance indicates good agreement with impactors and excellent agreement with opacity meters in computed mass loading and optical opacity. Its size resolution is greater than other current known techniques. Its eventual use will be directed at the characterization of particulate emissions of stacks or other stationary sources and to qualitatively evaluate the performance and collection efficiences of particulate control devices in operation.

CONTENTS

Abstract ii
Figures iv
Tables viii
1. Introduction 1
2. Discussion of the Stack Environment and FPSSS Design Criteria 5
3. Overview of the FPSSS 10
3.1 FPSSS Optical System 15
3.2 FPSSS Head 15
3.3 FPSSS Support Beam and Port Bearing 19
3.4 Thermal Control System 20
3.5 FPSSS Electronics Console 20
3.6 Operation and Use 22
4. Examination of the Optical Properties of Particles and their Implication for Stack Measurements 29
5. Results of Aerodynamic Tests and Thermal Modeling . . . 54
6. Expanded Description of FPSSS Systems 82
6.1 The FPSSS Electro-Optical System 82
6.2 Electronic Subsystems 88
6.3 Basic Data Processing Equations 97
7. Calibration and Laboratory Test and Simulation of Fly Ash Environments 102
7.1 Calibration and Evaluation of the FPSSS at PMS 102
7.2 IERL Test Summary 111
8. Field Testing 148
8.1 Initial Testing at Valmont Power Plant 148
8.2 Field Tests in Charlotte, North Carolina 158
8.3 Final Tests at Valmont 166
9. Conclusions 204
References 209
Appendix I 210
Addendum 216

FIGURES

Number		Page
1	FPSSS block diagram	12
2	Photograph of FPSSS components	13
3	Photograph of FPSSS electronics console	14
4	Optical system diagram	16
5	Assembly diagram of the FPSSS probe head	17
6	FPSSS installation at IERL	18
7	Close-up of FPSSS head and split lateral bearing	18
8	FPR FPSSS heat exchanger assembly	21
9	FPSSS numerical testing output samples	25
10	FPSSS size distribution graphics samples	26
11	FPSSS mass distribution samples	27
12	Sample of FPSSS time series plot	28
13	Wavegroups contributing to light scattering	31
14	Collecting angle required to collect 89% of diffracted light	32
15	Collecting angle required to collect 80% of diffracted light	34
16a	Average intensity vs. scattering angle for D = 0.6 μm	35
16b	Average intensity vs. scattering angle for D = 2 μm	36
16c	Average intensity vs. scattering angle for D = 5 μm	37
17	MIE response of the Royco 218 particle counter for particles with refractive indices 1.33, 1.70, 1.90 and 2.20	39
18	Response of the Royco 245 particle counter	40
19	MIE response for PMS CSAS-100 spectrometer model	41
20	MIE response of the Climet particle counter for particles with refractive indices 1.33, 1.45, 1.70 and 1.90	42
21	MIE response for PMS LAS-200 spectrometer	43
22	MIE response of the Royco 218 particle counter for particles with refractive indices 1.54, 1.54 - 0.05i, and 1.54 - 1.0i	45
23	MIE response of the Climet particle counter for particles with refractive indices 1.54, 1.54 - 0.05i, 1.54 - 0.5i and 1.54 - 1.0i	46
24	Sensitivity of 4° - 22° collecting angles to real index dispersion	48
25	Sensitivity of 4° - 22° collecting angles to complex index dispersion	49
26	Sensitivity of 2° - 11° collecting angles to real index dispersion	50
27	Sensitivity of 2° - 11° collecting angles to complex index dispersion	51
28	Sensitivity of 2° - 11° collecting angles to 1° errors	53
29	Conceptual FPSSS probe optical-mechanical packaging	55

Figures (Cont.)

Number Page

30 Test with 4 inch annular ring probe mock-up 56
31 Test with 6 inch annular ring probe mock-up 57
32 FPSSS probe head configurations during wind tunnel tests 59
33 Test with breadboard FPSSS probe head scan along optical axis from window to mirror 60
34 Test with breadboard FPSSS probe head transverse scan across sample plane 61
35 Test with breadboard FPSSS probe head transverse scan across sample plane behind standoffs 62
36 Head cross section for thermal model 65
37a FPSSS sensor head nodal layout 70
37b Nodal diagram of FPSSS coolant loop 71
38 Brassboard 80
39 Relative size and position of sample volume cross section 86
40 Image sizes and positions on masked aperture detector . . 87
41 Image size as a function of sample volume position for the case of 4X gain ratio of masked-to-signal aperture 89
42 FPSSS electronics console block diagram 90
43a FPSSS probe electronics block diagram 92
43b FPSSS data acquisition system block diagram 95
44 Relative scattering response 104
45 FPSSS sample volume map 105
46 FPSSS interrange comparison 107
47 FPSSS/CSAS comparison (submicron particles) 108
48 FPSSS/CSAS comparison (medium sized particles) 109
49 FPSSS/CSAS comparison (large particles) 110
50 Schematic of IERL wind tunnel showing dust handling equipment 112
51 IERL screw feeder and IERL fluidized bed aerosol generator 114
52 SEM photomicrographs display the primarily spherical Duke Power Plant fly ash (upper) and the clumped aggregates of iron oxide (lower) 116
53 FPSSS/Coulter Duke power fly ash size distribution comparisons 117
54 FPSSS/Coulter counter iron oxide size distribution comparisons 118
55 FPSSS accumulative mass distribution for the iron oxide for run number 14 122
56 Size distribution for IERL run number 1 125
57a Mass distribution for IERL run number 1 126
57b Accumulative mass distribution for IERL run number 1 . . 127
58 FPSSS size distribution for IERL run number 5 128
59a FPSSS mass distribution for IERL run number 5 129
59b FPSSS accumulative mass distribution for IERL run number 5 130

Figures (Cont.)

Number		Page
60	FPSSS accumulative mass distribution for IERL run number 7	131
61	IERL impactor/FPSSS mass distributions comparison . . .	133
62	Impactor/FPSSS mass distribution comparison for iron oxide	134
63	FPSSS time series and number density plot in IERL tunnel	135
64	Time series for rotation of probe head in IERL tunnel .	136
65	Effects of rotation in windstream on mass loading . . .	138
66	Spatial Variations of number density and mass loading in IERL tunnel	139
67	FPSSS size distribution for IERL heated tunnel using Duke fly ash, for run ending at 11:05 on February 8 .	141
68	FPSSS mass distribution for IERL heated tunnel using Duke fly ash, for run ending at 11:05 on February 8 .	142
69	FPSSS time series plot of number density and mass loading for 6 minute run ending at 43:00 on February 8	143
70	FPSSS size distribution for IERL test in fuel oil boiler flue, ending at 13:00 on February 14	145
71	FPSSS mass distribution for IERL test in fuel oil boiler flue, ending at 13:00 on February 14	146
72	Schematic drawing of a steam electric generating station	149
73	Average in-stack size distribution	152
74	Average in-stack extinction cross section distribution .	153
75	Lear Siegler RM41 opacity record for April 24, 1978 between 14:00 and 15:00, during which the FPSSS performed measurements in the stack	154
76a	Average in-stack volume (mass) distribution	155
76b	Average in-stack volume (mass) distribution from 0.4 to 0.85 μm	157
77	Valmont control device removal efficiency	159
78	Charlotte total mass comparisons	160
79	FPSSS number density for sample run ending at 14:55 on April 17	162
80	FPSSS mass loading for sample run ending at 14:55 on April 17	163
81	Charlotte outlet mass distribution	164
82	Charlotte cumulative mass distribution	165
83	Valmont outlet velocity profiles	168
84	Average FPSSS size distribution observed using ranges 3 and 4 during first impactor run (Valmont outlet) . .	171
85	Average FPSSS mass distribution observed using ranges 3 and 4 during first impactor run (Valmont outlet) . .	172
86	FPSSS size distribution for run ending at 14:11 on September 13 (Valmont outlet)	173
87	FPSSS mass distribution for run ending at 14:11 on September 13 (Valmont outlet).	174

Figures (Cont.)

Number — Page

88 FPSSS size distribution covering third impactor run, ending at 10:14 on September 14 (Valmont outlet) 176
89 FPSSS mass distribution covering third impactor run, ending at 10:14 on September 14 (Valmont outlet) 177
90 FPSSS size distribution for time period ending at 10:23 on September 14 (Valmont outlet) 178
91 FPSSS mass distribution for time period ending at 10:23 on September 14 (Valmont outlet) 179
92 FPSSS size distribution at 14:00 on September 14 (Valmont outlet) 181
93 FPSSS mass distribution at 14:00 on September 14 (Valmont outlet) 182
94 FPSSS size distribution for run ending at 16:49 on September 14 (Valmont inlet) 183
95 FPSSS mass distribution for run ending at 16:49 on September 14 (Valmont inlet) 184
96 FPSSS size distribution for run ending at 10:13:24 on September 15 (Valmont inlet) 186
97 FPSSS mass distribution for run ending at 10:13:24 on September 15 (Valmont inlet) 187
98 Valmont rapping sequence as observed in opacity and mass median diameter. 188
99a Rapping sequence for September 15th at approximate mean mass size 190
99b Rapping sequence for September 15th at submicron sizes (CSAS-HTS). 191
100 Lear Siegler RM41 opacity record for September 14 . . . 192
101 Valmont - % opacity scattergram 193
102 Valmont rapping sequence as observed in mass loading and number density 194
103 Valmont inlet mass distribution 196
104 Valmont inlet impactor run number 6 cumulative mass loading 197
105 Valmont outlet mass distribution 198
106 Valmont outlet cumulative mass loading FPSSS/impactor comparison 199
107 SEM photomicrographs at equal magnifications display Valmont impactor samples 201

A1 Photograph of PMS calibration wind tunnel facility . . 212
A2 Diagram of PMS calibration wind tunnel facility 213
A3 Wind tunnel monodispersed aerosol source subsystem . . 214
A4 Sample inlet tube installed in tunnel test section with FSSP's 215

TABLES

Number		Page
I	FPSSS Component Power Dissipations	64
II	FPSSS Nodal Descriptions	72
III	FPSSS Radiation Conductances	74
IV	FPSSS Temperatures for Balanced 1 GPM Flow	75
IV	FPSSS Temperatures for Balanced 2 GPM Flow	76
IV	FPSSS Temperatures for Unbalanced 1 and 2 GPM Flow	77
V	FPSSS Thermal Analysis Results	78
VI	IERL Wind Tunnel Mass Loading Comparisons	120
VII	Mass Loading Increases	144
VIII	Summary of Valmont FPSSS, Impactor and Opacity Data	169

1. INTRODUCTION

In September, 1977, Particle Measuring Systems, Inc. (hereafter PMS) was contracted by the Environmental Protection Agency (hereafter EPA) to design, fabricate, and evaluate an *in situ* Fine Particle Stack Spectrometer System (FPSSS). The development of the FPSSS was intended for application to characterize the particulate emissions of stacks and other stationary sources and to qualitatively evaluate the performance and collection efficiences of particulate control devices now in use or under development. The primary EPA design criteria that the FPSSS had to satisfy were to provide *in situ* high-resolution particle sizing over a size range from 0.5 to 5.0 μm diameter, with number densities in this range above $10^4 cm^{-3}$ and integrated particulate loading from 0.3 to 3.0 g m^{-3}. The FPSSS was also required to operate at temperatures from 20 to 250°C and at flow velocities from 1 to 30 m sec^{-1}. An operational prototype instrument has been designed, fabricated, and performance-tested. This report describes the design, development, and testing of this new high-resolution in-stack particle size spectrometer system.

The basic design approach utilized existing technology. Three major areas of previous work provided the underpinnings of the FPSSS design. These were:

a) The well-developed PMS technique of utilizing high-resolution imaging systems with light scattering to perform *in situ* single particle size measurements.

b) The experience by PMS in stack measurements using plumbed instruments.

c) The Pioneer Venus Large Probe Cloud Particle Size Spectrometer (LCPS) development work, involving cooperative efforts between PMS and the Ball Brothers Research Corporation (BBRC).

Probably the greatest desire of the research performing particle size measurements is to do so without disturbing the particles and thereby making the measurements *in situ*. In some respects the concept of *in situ* sampling is an unattainable goal; what one desires is to minimize sample perturbation. As far as single particle sizing devices are concerned, this ability to size particles *in situ* generally requires additional imaging technology to dimension sample volume. In PMS *in situ* light scattering spectrometers, sizing is through pulse height analysis of scattered light and the sample cross section is defined through imaging. The sample volume is defined as the product of the sample cross section and the particle velocity. The particle velocity can be determined through independent airspeed measurement or directly from image trajectory measurements. Particle number densities in stacks are extremely high, particularly at submicron sizes. Such high number densities require the use of reasonably high magnification imaging systems to localize a much smaller region than is common practice with commercial aerosol counters employing similar light scattering approaches.

Prior to the current efforts, PMS began to apply existing light scattering instrument technology to stack measurements (Knollenberg, 1977). Our efforts with in-stack measurements largely dealt with the development of an extractive stack sampling duct and a high sample test section which allowed existing PMS instruments to view the hot particle flow through protective windows and make quasi *in situ* measurements in the hot flow. Because of similarities in the aspiration of PMS spectrometers this provided a method of direct application of several instruments covering different particle size ranges. It also allowed for the probing of other hot particle sources requiring sample removal--particularly chemical process ovens.

Another area of work that provided a developed technology base was the Pioneer Venus Large Probe Cloud Particle Size Spectrometer (LCPS) involving both PMS and BBRC. Results from this successful experiment are given in Knollenberg and Hunten, 1979a, 1979b, and 1980, and a full instrument description is given in Knollenberg and Gilland, 1980. From the beginning, we realized the design of an instrument to measure the particle size and number density in the Venusian atmosphere and continuous cloud canopy would face difficult environmental requirements. Operating temperatures ranged from -50°C to 450°C, pressures up to 100 atmospheres, sample velocities to 50 m sec^{-1}, and the reentry G-load was on the order of 400 G's. The instrument had to cover a size range of from 0.5 to 5.0 μm by *in situ* optical single particle methods. Such requirements are similar to, although more rigid than, those being sought by the EPA for an in-stack instrument. The FPSSS was intended for operations to only 250°C. The in-stack pressures are also much closer to ambient. The size range of 0.5 to 5 μm was equivalent to the scattering subrange of the LCPS, which was one of four separate size ranges. The LCPS maximum sample velocities were nearly twice as high as those expected in-stack. The important point is that the LCPS instrument had to stay in alignment through the mission profile (two hour descent) and remain relatively contamination-free. These problems were also paramount in the FPSSS design. The Venusian environment has another similarity to that found in stacks. The clouds of Venus are composed largely of sulfuric acid and thus the atmosphere is hot and highly corrosive. Heaters had to be installed on the LCPS windows to prevent condensation. Aerodynamic shields had to be developed to provide additional protection from wetting.

The FPSSS design draws heavily from these areas of previous work. In essence, the FPSSS is the result of using existing technology rather than the result of basic research and development. An early prototype operational device was constructed and tested within the first 9 months of the contract. The final prototype FPSSS instrument would appear to meet the original EPA design objectives. It has a near-forward light scattering optical system with an expanded 60 channel 0.4 to 11.0 μm size range divided into four subranges of 15 size channels each. The instrument is capable of relatively accurate measurements at number densities up to 5×10^4 cm^{-3}, without significant sensitivity to refractive index. An optical velocimeter has been designed and incorporated in the FPSSS. The instrument can operate continuously at 250°C temperatures utilizing a water-cooled head design and external heat exchanger.

Extensive theoretical modeling of thermal as well as optical performance has been utilized in configuring the FSPSS probe head. Wind tunnel facilities at PMS have played an extremely important role in measuring aerodynamic impacts of the FPSSS sampling section. Calibration has included laboratory and wind tunnel tests (at both PMS and the IERL facilities at the EPA) on particulates having known or independently verifiable size distributions. Field tests on three operating coal-fired power plants were conducted during the course of this work and are discussed in detail.

The next section provides a discussion of the design criteria established by the EPA for the FPSSS. Section 3 introduces the FPSSS. The fourth section gives an in-depth description of the tradeoffs imposed by various optical collecting geometries to sizing performance. Section 5 describes the results of aerodynamic testing and thermal modeling. Section 6 details the prototype FPSSS system, followed by its initial calibration and laboratory test results discussed in Section 7. The field test results are discussed in Section 8, followed by our general conclusions.

2. DISCUSSION OF THE STACK ENVIRONMENT AND FPSSS DESIGN CRITERIA

Optical instruments for sizing aerosol particles have been around for 20 years or more. However, they have difficulty performing measurements in stack environments. The following is a list of problem areas that can generally be attributed to stack environments:

1) High particle number densities
2) High temperatures
3) Corrosive environment
4) Contamination problems, generally from condensable vapors
5) Poor accessibility
6) Relatively high and variable particle velocities
7) Irregular shaped particles
8) Mixed particle composition and refractive index
9) Electrical charging

The above listing is, in general, in order of importance and difficulty. Obviously, one is not worried about effects of irregular shape or refractive index if his instrument is being consumed by hot sulfuric acid. We will expand on some of these problems.

Particle number densities in stacks are extremely high, particularly at submicron sizes. Such high number densities require the use of imaging systems to localize a much smaller region of optical uniformity than is common practice with commercial aerosol counters, where particles can be plumbed through an illuminated volume of one mm^3 or so.

The high temperatures encountered in stacks generally restrict one's ability to actually place an instrument, with its electronics, optical systems, etc., inside the stack. A partial solution is to remote the passive portions of the optical system in the stack environment and couple the input and output of the optical system through fiber optics or other light communication devices to the electronics. However, a cooling jacket is required if electronics are placed within the environment, and the risk of damage to an usually expensive piece of apparatus must be recognized.

The hot corrosive environment requires the use of heated or purged windows and relatively inert adaptive hardware. Contamination problems always exist in a stack environment, and it is generally best to recess optics and flood their surfaces with clean purge gases. Because the stack velocity is quite high and variable, the instrument design cannot be sensitive to particle velocities. An accompanying problem is turbulence-induced vibrations.

Stacks and control devices are generally fitted only with small access ports--typically 3 to 5" I.D. The poor accessibility to the particulate environment is often compounded by placement at locations requiring traverses along catwalks, staircases, and exposure to outside environments.

The fact that the particle species within the stack environment are often of irregular shape, have mixed particle composition, and unknown refractive index (with considerable absorption) suggests imaging methods might be applied. They are, in general, much less subject to error than light scattering methods. Some imaging systems can provide particle morphology information as well. However, imaging techniques are unsatisfactory below a few microns due to lack of resolution. Light scattering systems are thus the only easy alternative. In order for light scattering systems to perform at all well, they must collect a large portion of diffracted light as compared to refracted light (strong forward scattering). This generally limits their application to sizes less than 5 μm diameter in which it is possible to collect nearly all of the diffracted light while minimizing the amount of refracted light collected. This generally means collecting the light scattered down to angles of a few degrees.

On stacks using electrostatic precipitator control devices, the particles exhausted in the stack are highly charged and represent a potential Electromagnetic Interference (EMI) problem. Static discharge from conductive apparatus is sufficient in frequency and magnitude to pose a threat to integrated circuits--particularly MOS and CMOS devices.

The EPA delineated eight objectives that the FPSSS should be designed to meet. These are listed below, followed by a discussion of our interpretation, areas of concern, and other considerations that our design was based upon. The objectives specified by the EPA were:

1. *In situ* operation.
2. Particle size range: 0.5 to 5.0 μm.
3. Particulate loading: 0.03 to 3.0 g m^{-3}.
4. Number density: 10^6-10^8 particles cm^{-3}.

5. Temperature range: 20°-250°C.

6. Free stream gas velocity: 1-30 m $\sec^{-1}$.

7. Flow duct area: 0.1-40 m^2.

8. Real-time operation: maximum allowed integration time is 3 min.

9. Portability: The device shall be designed such that a two-man sampling team could easily move and operate the apparatus.

1) We have already touched upon the elusive aspect of truly *in situ* measurements. In the context used here it is interpreted as measurement in the stack without extraction and with minimal disturbance such that the size distribution measured in the presence of the FPSSS is not altered by more than 10% from that existing at the same point of measurement in its absence. The primary disturbing effect is aerodynamic and the problem is addressed in Section 5.

Because of the environment encountered in stack measurements, one's ability to pipe particles around in small bore tubing and force particles to interact with a small uniformly illuminated light region required by more standard single particle light scattering methods is almost nil. Only *in situ* methods are really applicable. The only way we have found that measurements can be truly *in situ* using light scattering is to employ a good imaging system in combination with the light scattering optics or to use multiple-beam or other signature-producing illumination sources. We thus reemphasize the definite tie between imaging instruments and light scattering instruments through the necessity for a well corrected high performing imaging optical system in both cases. In the light scattering techniques the imaging system is used to define the sample volume, although sizing is through measurements of the amount of light scattered. In imaging techniques, sizing as well as sample volume definition is inherently by imaging.

2) The particle size range of 0.5-5.0 μm is close to standard size ranges on several PMS particle size spectrometers as well as being the exact range of the LCPS scattering subrange. We anticipated and found no problems in meeting the detectivity required and provided an extended range capability of 0.4-11 μm. We did find, however, that a tradeoff existed between minimum detectable size and maximum number density. Questions of best optical design for high accuracy are addressed in Section 4.

3) Examination of the particle mass loading and number densities showed the two to be incompatible. An inquiry to the EPA revealed that the 10^7 cm^{-3} to 10^8 cm^{-3} number densities were meant to apply to all particles down to sizes as small as 0.01 μm. They suggested much lower number density values for the restricted 0.5 to 5.0 μm range. From our own work in stack environments and from worst-case considerations for the mass peaking out at sizes in the 0.5 to 5.0 μm range (nearer 5 μm than 0.5 μm) a suggested range of 10^4 cm^{-3} to 10^5 cm^{-3} is a more appropriate upper limit. It is this upper limit that is important to single particle methods as it establishes related coincidence error. The high number densities were recognized as a "design driver"--particularly since even slightly increased sensitivity to below 0.5 μm would be accompanied by much higher number densities.

4) The 250°C upper temperature limit was also an important design driver. It was sufficiently high to necessitate thermal-modeling work and played an important part in the FPSSS design. This subject is treated in detail in Section 5.

5) The range of velocities encountered in stacks is for the most part in between those encountered by airborne spectrometers and aspirated laboratory instruments. Our primary area of concern here was the low end of 1 m sec^{-1} and the maintenance of satisfactory airflow characteristics to satisfy the *in situ* sampling requirements. We also found turbulence to be significant in actual field testing.

6) Assuming the ducts or stacks are round, the duct areas specified translated to diameters ranging from about 0.4 to 7 meters. In our design, this determined the overall distance the probe head would be maneuvered. It also established cable and cooling line lengths. We did not judge it to be an influential design driver, although we did find that in our design, which involved a boom-supported probe head, oscillations were induced at supporting lengths greater than 12 feet. However, on most stacks opposing ports precluded the need for maximum boom extension.

7) The high number densities encountered invariably lead to particle count rates approaching several KHz. Samples of 10,000 particles or more have statistical sampling uncertainties of less than 1% (∿1/N). Thus, sampling runs of much less than 3 minutes would be sufficient to characterize the number

distribution. Quantifying the mass would ordinarily require greater sampling times, since the larger more infrequent particles have much greater weight, but it would in any case be stable for sample sizes accumulated in much less than 3 minutes.

Data acquisition was an area where we already had good experience. Existing PMS system capabilities appeared to be more than adequate to meet design goals. An existing production data acquisition system specifically designed for such intended usage was utilized in initial work. We found no reason to modify it until actual stack experience dictated specific desired changes and specialized outputs. The final FPSSS design incorporated a computer-directed data acquisition system that embodied an on-site data analysis capability; it is described in detail in Section 6.

8) The question of portability means portability from stack to stack and also maneuverability within the stack. Since EPA compliance methods for stack sampling currently require as many as 48 sample points (U.S. EPA Method 5), the eventual similar use of the FPSSS dictated a multipoint sampling or stack-scanning capability. We recognized the difficulty in handling unwielding apparatus in the design and restricted the total weight to 150 lbs., with no single subsystem weighing more than 60 pounds.

Reproduced from
best available copy.

3. OVERVIEW OF THE FPSSS

The FPSSS is described in this section as it was finally delivered to the EPA. Since it is a one-of-a-kind device we still must regard it as a prototype. In the following sections we will refer (chronologically) to certain initial configurations; however, it will benefit the reader to have a basic familiarity with the final instrument during these presentations and analyses. A more in-depth treatment of primary FPSSS hardware and its performance is given in Section 6.

The development of the FPSSS was not considered a high risk task, although it did require the application of diverse and demanding technology. The performance requirements were within the range of standard PMS instruments (with the exception of the high temperatures involved). Prior successes in developing technology to perform measurements in even more severe environments were used to good advantage in the development of the FPSSS--for instance, the LCPS developed for NASA and the Pioneer Venus payload withstood 450°C. This technology base was applied to the FPSSS design. An 80-node thermal model for the probe head was developed by BBRC. It provided predictions of cooling requirements, thermal gradients, and mechanically induced changes in optical alignments. The FPSSS design reflects efforts to minimize the alignment error predicted by the model.

Our early analysis of the design requirements for the FPSSS suggested that an approach be followed utilizing as much existing technology as practical. We had previously designed an extractive sampling train to adapt another PMS instrument to take stack measurements. The instrument used was a classical scattering aerosol spectrometer (Model CSAS-100) unit; it makes measurements while viewing particles a few inches away from its collecting optics. Those results showed that existing optical system designs were capable of handling the projected high particle number densities associated with stack flue gas at sizes larger than 0.5 μm diameter. However, those measurements also revealed size distribution spectra where the number density was rapidly increasing with decreasing particle size. Obviously, with such a size distribution, at some smaller size any instrument finds a limitation due to coincidence error. Sampling ahead of control devices might further limit use--even at 0.5 μm--

but this PMS basic detection system appeared to be the most adaptive of existing technology and the least problematic.

The real problem was performing the measurements in the hot environment. Stacks are often well above boiling temperature, and, if continuous measurements are desired, an instrument of this type must be cooled to survive. Our approach was to provide a reasonable thermal environment for a modified PMS Model CSAS-100 electro-optical system using an active cooling system. The resulting FPSSS design utilizes a He-Ne laser-fed high-resolution imaging optical system with particle detection and sizing by strong forward light scattering. The imaging system provides accurate sample volume definition and enables particle transit time measurements to extract flow velocity.

The FPSSS has four size ranges covering 0.4-1.15, 0.5-2.0, 1.15-5.65, and 2.0-11.0 µm. Each size range has 15 size classes. In normal operation, two size ranges are sampled concurrently (e.g., 0.5-2.0 µm and 2.0-11.0 µm), producing 30 classes from 0.5 to 11.0 µm. The maximum number density that can be measured is 5×10^4 cm^{-3}. A block diagram of the various FPSSS subsystems is given in Figure 1.

Figure 2 is a photograph of the instrument head, heat exchanger, and two lateral support bearings (mounted to port flanges). The bearings allow the operator to extend the head on a segmented boom up to 6 meters into the particulate environment. The water-cooled head can operate continuously at temperatures above 250°C. The head contains the laser, condensing and imaging optics, photodetectors, and programmable preamplifiers.

Figure 3 shows the FPSSS electronics console, housing the signal processing electronics and the data acquisition and display system. Data acquisition is accomplished using a microcomputer with firmware programs and random access memory. Both CRT and hard copy displays are generated. Sufficient memory capacity exists to generate size, area, mass and accumulative mass distributions for up to 7 individual samples. In addition, numerical listings and time series plots of selected parameters (e.g., mass loading and number density) may be generated. Calibration parameters can be entered manually; for instance, the particle density is invariably entered to compute mass and aerodynamic diameter. The latter can be chosen as the relevant size parameter for various outputs.

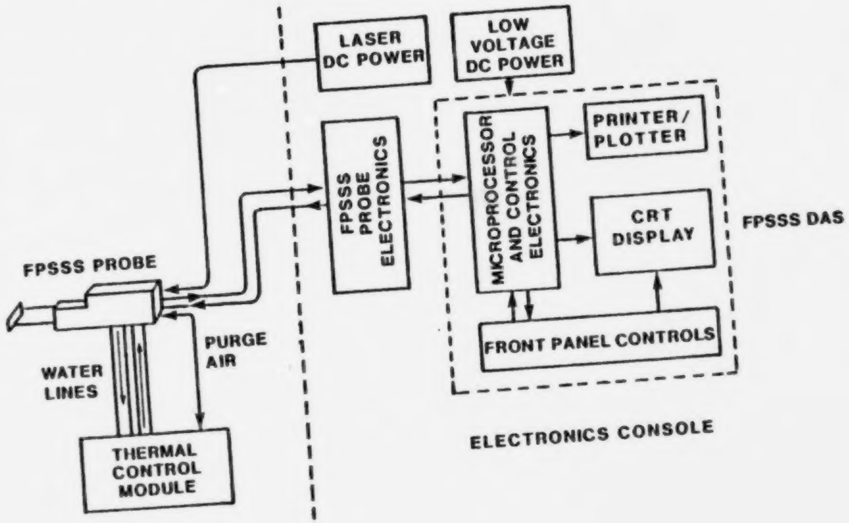

Figure 1. FPSSS block diagram.

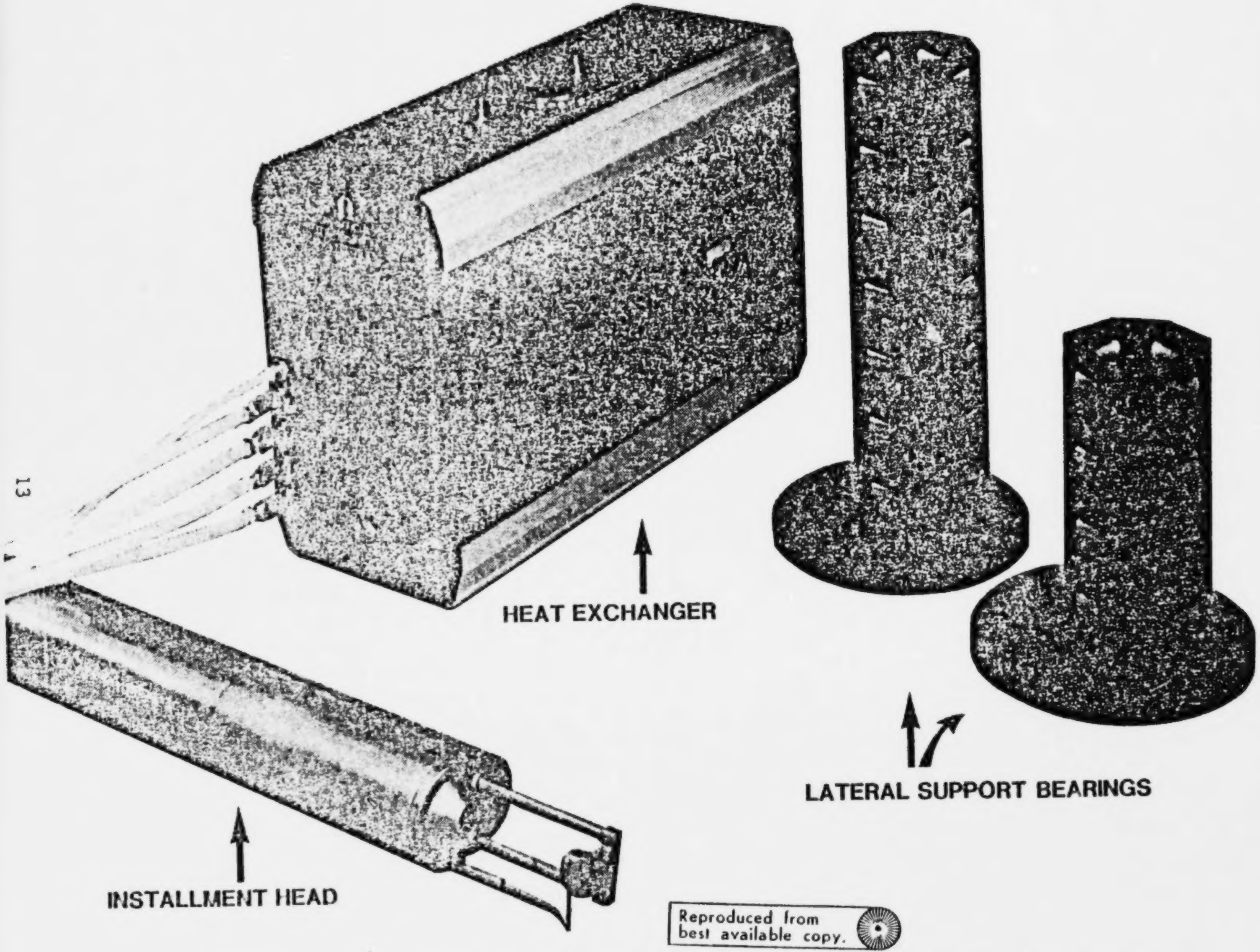

Reproduced from best available copy.

Figure 2. Photograph of FPSSS components. Two sizes of lateral support bearings are shown for maximum boom extensions of 4 and 6 meters respectively. The heat exchanger also contains the purge air pump. Boom sections are not shown.

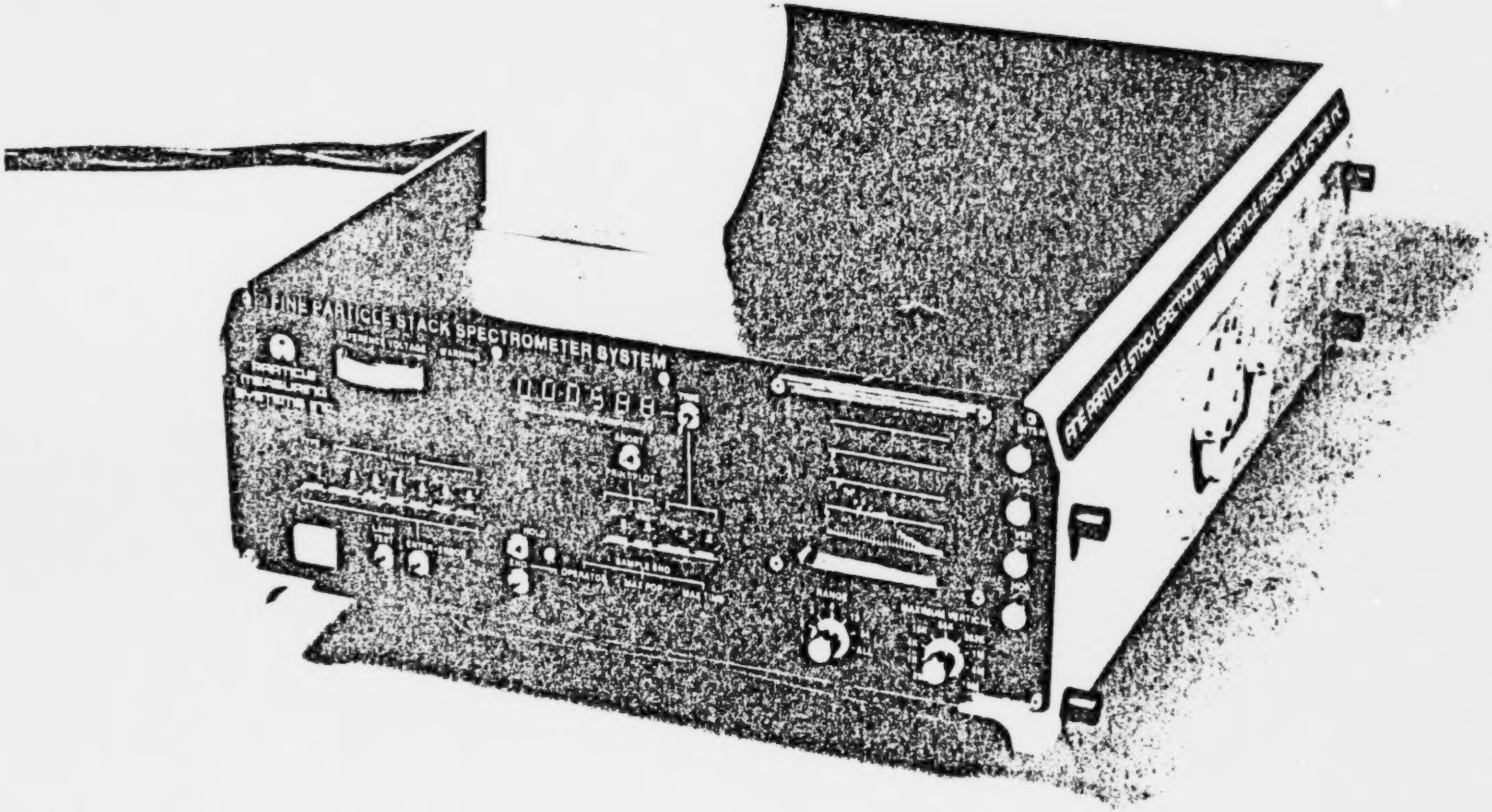

Figure 3. Photograph of FPSSS electronics console.

3.1 FPSSS Optical System

The optical system became the primary design driver of the FPSSS. Its alignment is the single most important optical parameter requiring control. The FPSSS optical system shown in Figure 4 is quite similar to that originally proposed to the EPA. The output of a 5 mW high-order multimode laser is directed towards a 75 mm radius condensing mirror by a pair of plane mirrors. The condensing mirror focuses the laser beam down to approximately 125 μm diameter at the object plane of the light collecting/imaging system. The laser beam then expands to approximately 3 mm diameter before being absorbed by a "dump" spot (or central field stop) on the FPSSS window. Particles in the vicinity of the object plane scatter energy through the window which is collected by the prime objective and relayed at 2:1 magnification to the secondary objective, which is a microscope objective operating at 10X. The total magnification is thus 20X. The particles are imaged onto a pair of exit faces of a beam splitter. The reflected image face is overlaid with a narrow opaque mask aligned in the direction of particle flow. The second transmission prism face is unmasked. A pair of photodiodes and their associated preamps view the particle images through each prism face.

The capabilities of this optical system are of a fundamental nature in that they provide a means for defining a desired sample volume, thus effecting the *in situ* measurement capability (Knollenberg, 1975 and 1976a). The masked beam splitter derives two signals, providing (in conjunction with double pulse height analysis) a means of determining if a particle's position is in the desired sample volume. The relative size of the sample volume cross section varies inversely with the magnification used in the collecting optics. The light transmitted on axis through the beam splitter is the signal used to size the particles.

3.2 FPSSS Head

The head of the prototype FPSSS shown in the photograph in Figure 2 is further illustrated in Figure 5. The head is approximately 20" long, has a 2.25" x 3.5" elliptical cross section, and weighs 7 pounds. The head body is fed by two water lines which form a pair of circuitous paths through the head body, making several internal bends before running back to the rear and exiting. Thus, four water lines are fed through the boom. Two high voltage laser leads,

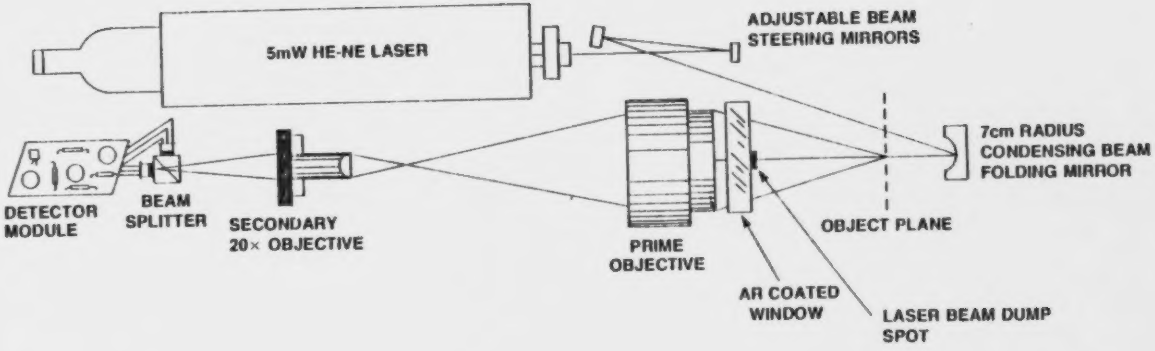

Figure 4. The above optical system is housed entirely within the FPSSS head, except for the 7 cm radius mirror. Only this mirror and the outside face of the window are exposed to the particle media and these surfaces are flooded with purge air.

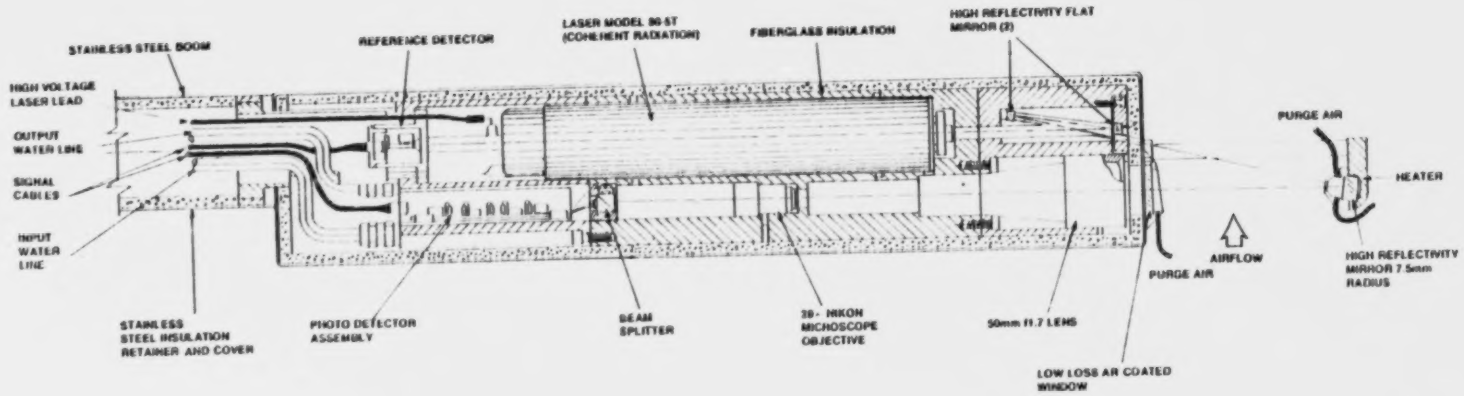

Figure 5. Assembly diagram of the FPSSS probe head.

Reproduced from
best available copy.

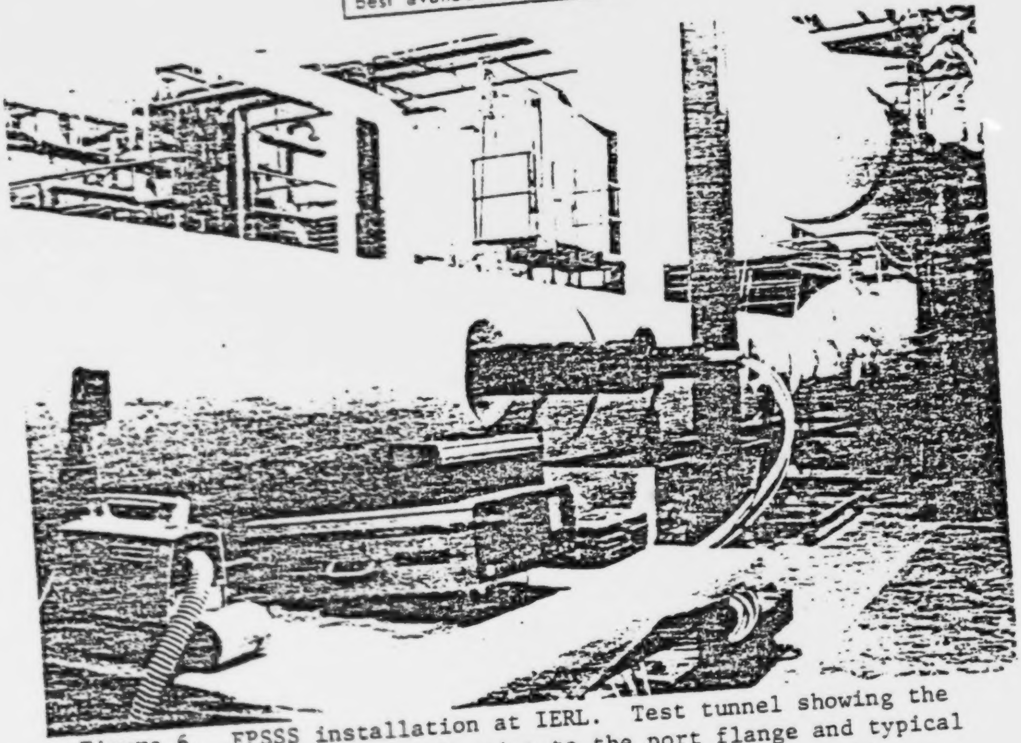

Figure 6. FPSSS installation at IERL. Test tunnel showing the attachment of the lateral bearing to the port flange and typical proximity of thermal control system and electronics console.

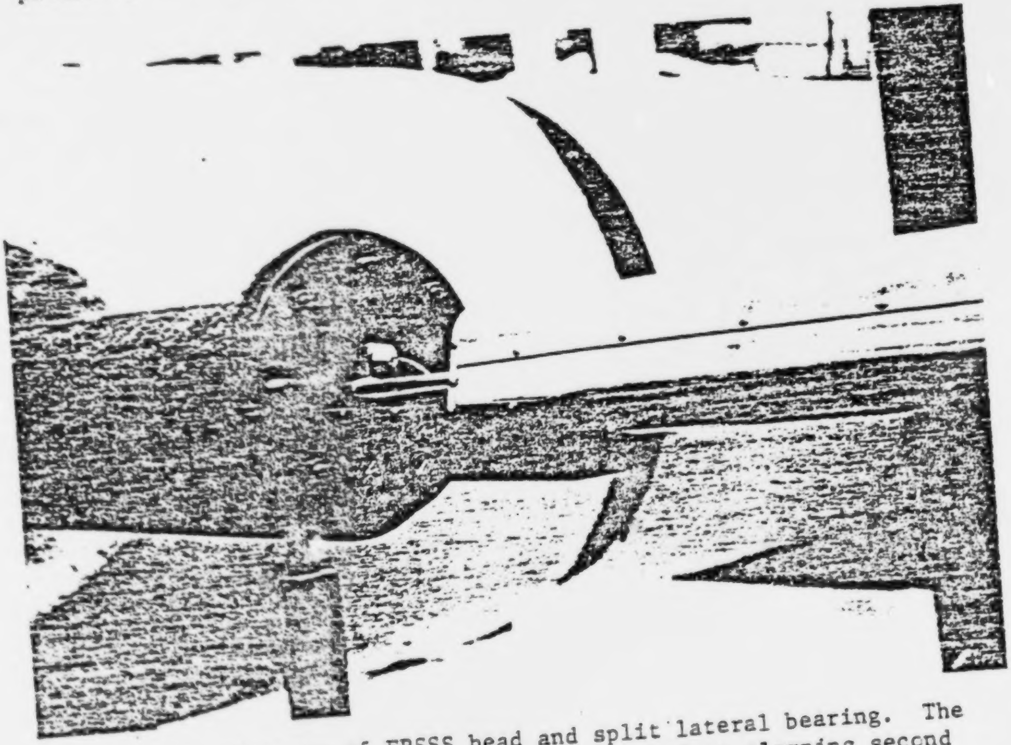

Figure 7. Close-up of FPSSS head and split lateral bearing. The probe head must pass clear of the bearing before clamping second bearing half.

a multiconductor signal cable, and an air line also feed through the boom to the FPSSS head.

The optical system just described demanded careful mounting. The laser is mounted on 'O' rings without adjustments. The only adjustments are x-y adjustments on the first beam-folding mirror and the 75 mm mirror. The adjustment on the 75 mm mirror was not planned initially; however, it was found necessary when we discovered that adjustment using the beam-folding mirror had near zero effect at the object plane because the object plane is centered at the focus of the 75 mm mirror.

The head body was constructed in three sections to give access to the various optical element cells and for machinability. 'O' ring seals are used for the water paths, and sealing is positive up through 100 p.s.i. The head body is covered by 1 cm of fiberglass insulation and by a protective stainless steel jacket with openings only for optical viewing and connections. The photodetector assembly loads from the rear and can be removed without splitting the head body.

Initially, purge air was provided only for the 75 mm mirror. This element has a small aperture and is easily purged. Contamination on its surface, however, is more critical than on the window. We eventually purged the window, but did not do so initially in order to determine its potential exposure and rate of contamination. The probe head was also purged to prevent contamination of the folding mirror surfaces.

3.3 FPSSS Support Beam and Port Bearing

The FPSSS is designed to permit installation on a stack port flange and can penetrate into the stack to considerable length, sampling anywhere across the inside diameter of the stack. This was accomplished by using a section tubular support beam fed through a lateral bearing mounted to a stack port flange. A typical installation is shown in Figure 6 and 7. All water lines and electrical cables are continuous through all boom sections. To add a section one simply screws it into the preceding one. All boom sections are 4 feet in length. The boom sections are constructed of thin-walled stainless steel tubing, 2.5" O.D. and 0.09" thickness. Approximately 0.5" of fiberglass insulation and an inner 1.125" I.D. PVC sleeve allow sufficient room to slide the lines and cables when joining and separating sections. A thin, nylon-braided abrasion jacket bundles all of the water, air, and electrical lines together to allow the boom sections to slide freely. Each boom section adds about 6 pounds of suspended weight, although the final section is slightly heavier due to the larger wall thickness required to support the increasing side loads.

The port bearing design is of a clamshell nature and is split to allow passage of the larger probe head (see Figures 2 and 7). Once the head is by the bearing, it is closed, forming a snug fit to the 2.5" O.D. stainless steel walls of the boom sections. Two lateral bearings having four and six sets of concave stainless steel rollers were constructed. The larger bearing is used for configurations where the boom is extended beyond 12 feet (3 sections).

3.4 Thermal Control System

The thermal control system (TCS) shown in Figure 2 and diagrammatically in Figure 8 was rather simply constructed using a small centrifugal pump, an automotive-type heater radiator, an instrument blower, and a storage reservoir all packaged in a single housing. The purge air pump is also housed in the thermal control system. The water pump has a throughput of 1 gpm with 30 feet of line and a corresponding pressure drop of 7 p.s.i. Quick disconnects are used on all water and air lines.

3.5 FPSSS Electronics Console

The FPSSS electronics console shown in Figure 3 contains all electronics with the exception of the laser, photodetectors, and preamplifiers in the probe head. The mechanical envelope was constructed from aluminum extrusions for ruggedness. The packaging is very compact yet dense, resembling a heavy suitcase in handling. Various scope carts adapt to the unit easily.

The probe head generates three photo signals (two scattering and one reference) while accepting two control signals for switching size range gains. (Programmable preamplifiers are used to switch gains and thus size ranges). The scattering signals are ac-coupled, requiring baseline restoration by signal conditioning circuitry. The scattering signal pulse train is pulse height analyzed and processed to establish sample volume validity. The widths of the scattering pulses are related to the velocity of the particles traveling through the laser beam; a selected range of pulse amplitudes is processed to determine flow velocity.

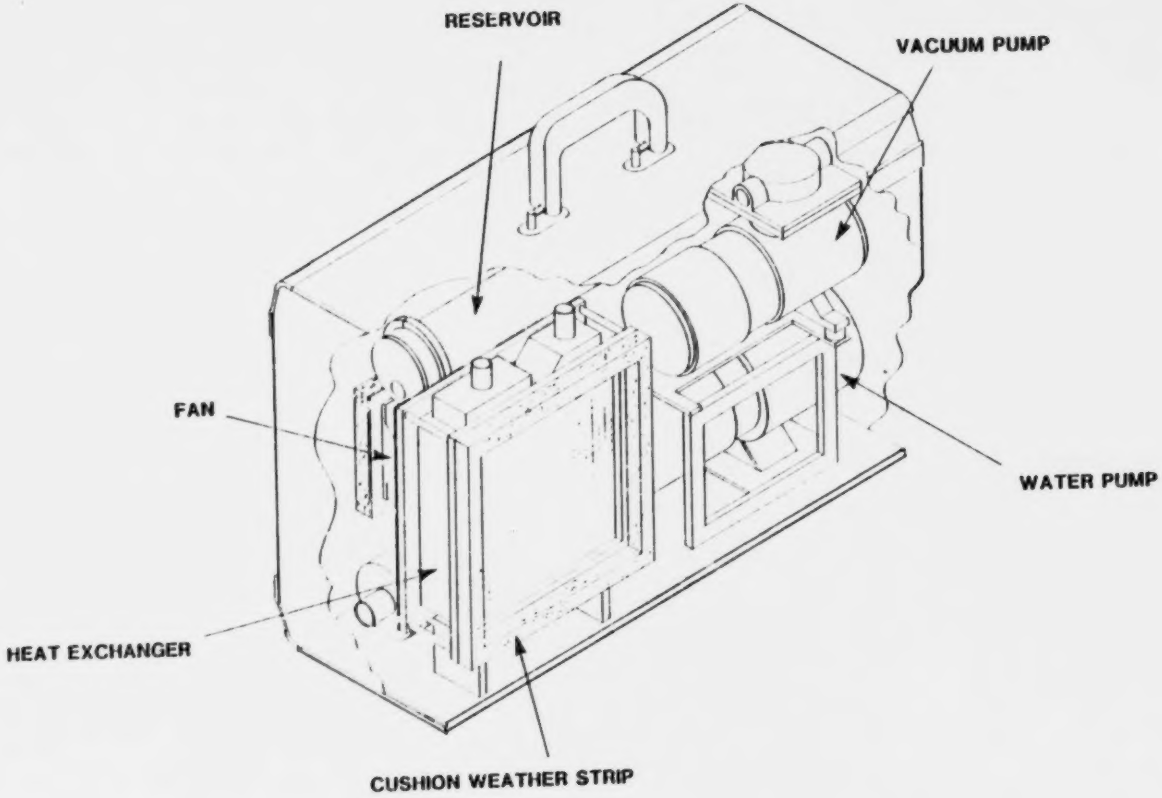

EPA FPR FPSSS heat exchanger assembly.

The above probe-related information is input to memory through direct memory access (DMA) without computer control. Data entry from front panel switches and the time-of-day clock also is input to memory via DMA. Information as to sample duration is entered automatically through a data port under program control; size range information is passed to the probe head and pulse height analyzer via a complementary type of port. Program storage resides in a 16 K ROM while data storage consists of 4 K of RAM. The RAM data storage also serves to provide CRT refresh memory. The CRT gives a 4" display of all size range data simultaneously, individually, or in any paired grouping. A six digit numeric display provides close inspection of specific data. The printer-plotter accesses information for hard copy generation as called for in the program plotting sequence selected. An important feature of the system is the ability to present time-line (strip-chart) data such as mass loading and number density for a selected time period and plot out size and mass distributions from up to 8 sequential time segments within the selected period. A statistical analysis package also lists important analysis summaries.

The Z-80 CPU is, of course, responsible for the exercising of all instructions and controls all operations intended to be under program control. Power supplies for all probe electronics, data acquisition, displays, and the laser are also contained in the electronics console. The printer-plotter is an Axiom unit which has self-contained power supplies. Also residing in the electronics console are a temperature sensor and thermal limit sensing circuit with an audio alarm.

Maintenance consists primarily of cleaning and periodically checking probe calibration with monodispersed spheres. Most problems arise from optical contamination when the probe is operated with "sticky" particulates, or less frequently, from mirror misalignment after physical abuse or accident. The laser has the lowest MTBF (mean time between failure), with about a two year expected lifetime.

3.6 Operation and Use

The FPSSS is rather easy to install and operate; results of experiments can be interpreted readily too. The power requirements at the measurement site are only 7 A of 115 VAC, 60 Hz. The operator screws together as many boom sections as required by probe insertion depth. He then makes electrical power and signal interconnections between the probe and DAS and connects the air and water lines between the probe and the TCS. The lateral bearing is mounted at the stack port of interest and the probe is inserted through the bearing into the stack, observing the orientation of the probe with respect to the airstream. The DAS is powered, and associated data are entered to reflect current conditions such as time of day, stack airstream velocity (although the velocity may be measured by the probe if so required), particulate density, and stack diameter (used only to compute opacity). Finally, the type of output desired such as time plots or spectral plots is selected for output data logging.

The probe reports only properly sized particles to the data processing circuitry, but it also transmits an activity signal which reflects the percentage of time any particle is detected by the probe, valid or not. Activity is useful when correcting for coincidence error and is consequently monitored for use by the operator. Automatic correction for coincidence loss is performed by the FPSSS DAS.

Built into the probe head photodetector module are gain switchable preamplifiers for the masked and unmasked detectors which are under program control. Four sets of gains are provided, enabling the probe to operate over all four particle size ranges, one range at a time. The FPSSS ordinarily uses one pair of ranges to cover 0.4 to 5.65 μm and the other pair of ranges to cover 0.5 to 11 μm. The operator chooses the pair of ranges to be used at the DAS.

In each range, each properly sized, or valid, particle is assigned to one of fifteen size classes, depending on the amount of light scattered. Under ideal conditions with monodispersed spheres the resolution attainable approaches the resolution provided by the system. Under the actual stack conditions, with high temperatures and nonspherical and inhomogeneous particles, resolution of this instrument is surely degraded but overall accuracy is sufficient for most analyses required.

Data processing can employ any or all of the devices, whether the microcomputer, printer-plotter, six digit numeric display, or the cathode ray tube to display real-time data. Number density and mass spectra may be printed or plotted, and parameters such as mass median diameter and opacity may be printed or plotted versus time. For easy intercomparison against aerodynamic devices such as impactors, optical diameters may be automatically transformed to aerodynamic diameters.

The printer-plotter is the primary data output mechanism; the variety of processed output options are discussed in detail in Section 6. The remainder of this section will be devoted to a discussion of samples of data outputs.

During a data accumulation cycle the operator normally observes the raw size spectra on the CRT. At the end of the cycle a header is printed out of various housekeeping data, followed by program-selected processed data.

Figure 9 is a sample of numerically listed data consisting of the header data, summary of size counts, and processed statistical information. Figure 10 is a sample of normalized size distributions from the two groups of paired size ranges. Figure 11 gives the mass distributions for the data given in Figure 10. Figure 12 is a plot of number density and mass loading versus time. It is a sample of the time series (strip-chart) capabilities of the FPSSS. Mass loading, number density (concentration), opacity, or any pair of these parameters may be followed at selected plotting speeds down to 1 second per sample.

These data samples are obviously photostats of the actual FPSSS printer-plotter output which is an electroconductive metalized paper. Because of difficulties in reproduction, we have selected to redraft all other data samples in this report. However, the presentations resemble those of the actual output in nearly every detail.

Reproduced from
best available copy.

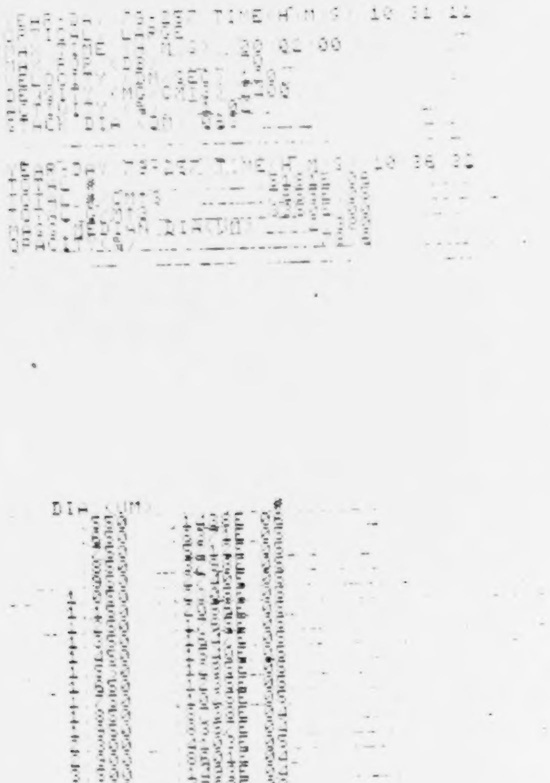

Figure 9. FPSSS numerical testing output samples. Above, at the start of a data sample, a listing of housekeeping data is printed with the time. The second listing includes the run end time and the total number of particles measured, average number density, mass loading, mass median diameter, and opacity. Below, a listing of the total number of particles counted in each of 30 size classes prior to graphics presentation. (Data from Valmont power plant, Boulder, Colorado.)

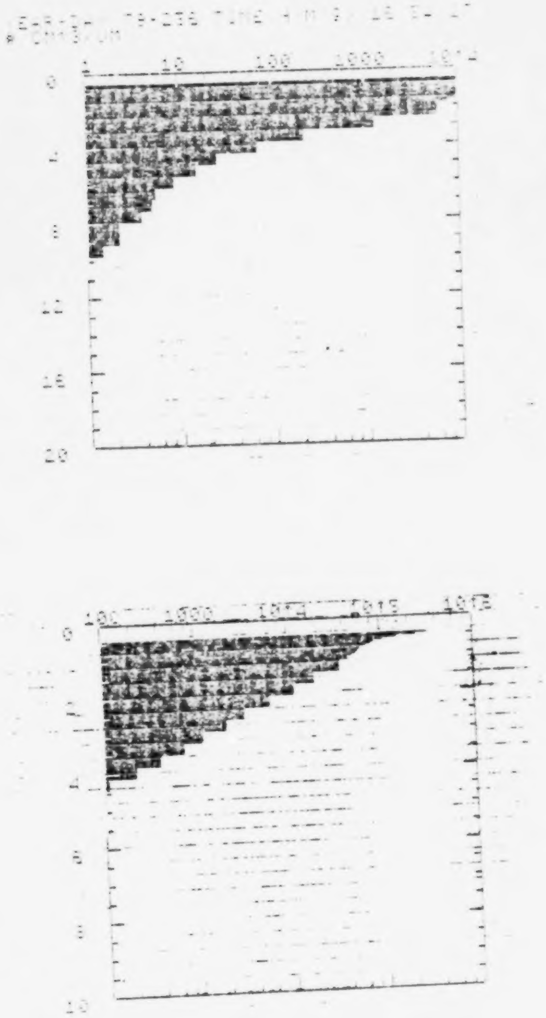

Figure 10. FPSSS size distribution graphics samples. Left, size distribution generated using ranges 3 and 4. Right, size distribution generated using ranges 1 and 2. (Data from Valmont power plant, Boulder, Colorado.)

Reproduced from
best available copy.

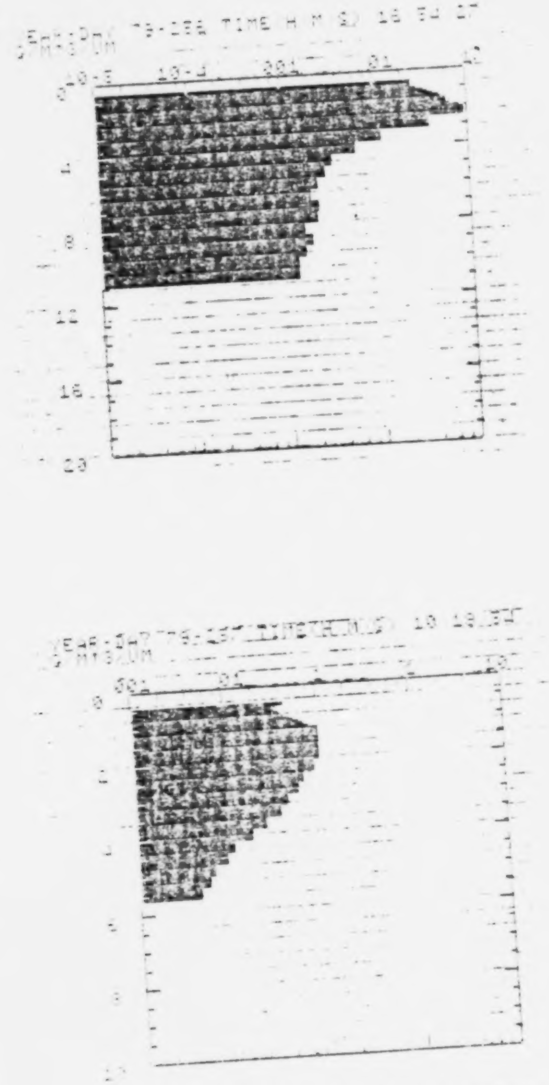

Figure 11. FPSSS mass distribution samples corresponding to data in Figure 10. (Data from Valmont power plant, Boulder, Colorado.)

Reproduced from
best available copy.

Figure 12. Sample of FPSSS time series plot. Time is in hours and minutes. (Data from Valmont power plant, Boulder, Colorado.)

4. EXAMINATION OF THE OPTICAL PROPERTIES OF PARTICLES AND THEIR IMPLICATION FOR STACK MEASUREMENTS

In this section we review the light scattering (Mie) theory of particles. The FPSSS design range of 0.5 to 5 μm covers a difficult region of particle size ($\sim \lambda$ and slightly above) for light scattering sizing techniques. Our intent is to present those important underlying aspects that bear upon the design of all light scattering optical particle size spectrometers. The results can easily be extended to instruments using the extinction effect as well. We will begin by trying to bridge the gaps in our common knowledge of scalar theory (ray trace), physical optical theory, and wave theory (Mie results). We will provide examples of the importance of such results in the design of optical particle size spectrometers and discuss the necessary tradeoffs that must be made in such designs. The final result is the optimum FPSSS optical system design.

The response of optical counters is invariably calculated utilizing Mie theory. Even though one seldom deals with the ideal boundary conditions required for the exact solution to Maxwell's equations (infinite plane wave, coherent illumination, spherical particles, etc.), the theory gives a good representation of what to expect. The response for nonspherical particles is only approximate in most cases. For instance, for finite cylinders the solutions are only tractable for low aspect ratios (less than three) and sizes near the wavelength. Furthermore, advanced numerical methods deal with particles of random morphology with only approximate results.

In general, Mie theory can give us a theoretical calibration curve that later invariably must be tailored by empirical results using physical particle standards. This is not simply due to the deviations from proper boundary conditions cited above. It also comes from the difficulty in modeling optical transmission and detector response as a function of collecting angle, wavelength, and state of polarization.* In actual practice, although one might use ideal laser sources and measured optical parameters, it is difficult to directly use Mie-derived calibrations without some adjustments from empirical results using monodispersed spheres.

---

*To our knowledge, the optical transmission characteristics are always neglected in computed Mie results. Probably the best analysis yet provided is that of Cook and Kerker (1975). It adequately accounted for source, spectral, and detector responses, but still neglected optical transmission functions.

In trying to gain insight into the optical behavior of particles, we have found it helpful to break down the total scattering into reflected, defracted, diffracted, and absorbed wave group components. This method can be qualitatively used regardless of particle morphology and size; it provides a physical interpretation of Mie computational results. The primary scattering wave group components are shown in Figure 13 for a particle of a few mircons' size. As illustrated, most of the light is scattered in the forward direction, and instruments designed to optimize collection in the forward direction obviously provide the greatest sensitivity. This simple fact is a fundamental premise in most optical system designs for light scattering particle counters.

The shape of the diffracted wave group is the only one that is size-dependent, although the amplitude of all wave groups varies as $\sim \pi r^2$, or cross section. The total amount of reflected light is nearly isotropic and very small (< 10% of total) but proportionately greater for backscattering angles. In general, light scattering problems are dominated by refracted and diffracted light components. Diffracted light is always present in an amount dependent upon intercepted cross section and equals 50% of all the light scattered. The central diffraction peak, or lobe, is called the Airy disk and contains 85% of the total diffracted light. The angular distribution of refracted light is a function of the real index of refraction, n_{re}; its overall contribution is diminished by absorption, accounted for by an imaginary index value, n_{im}. The presence of absorption thus generates a complex refractive index, $n = n_{re} - in_{im}$. The scattering collecting solid angle requirements for selected emphasis on refracted or diffracted light are thus different and certain instruments are intentionally designed to maximize the collection of one as opposed to the other. The solid angle is generally limited by a pair of inner and outer collecting angles which define a conic. In principle, strong forward scattering optical system designs can reduce the inner collecting angle to essentially 0° and the collecting geometry can be simply expressed in terms of the outer collecting angle. The collecting angles required to collect 89% of the light diffracted (90% of Airy disk) are shown in Figure 14. It is readily apparent that coverage

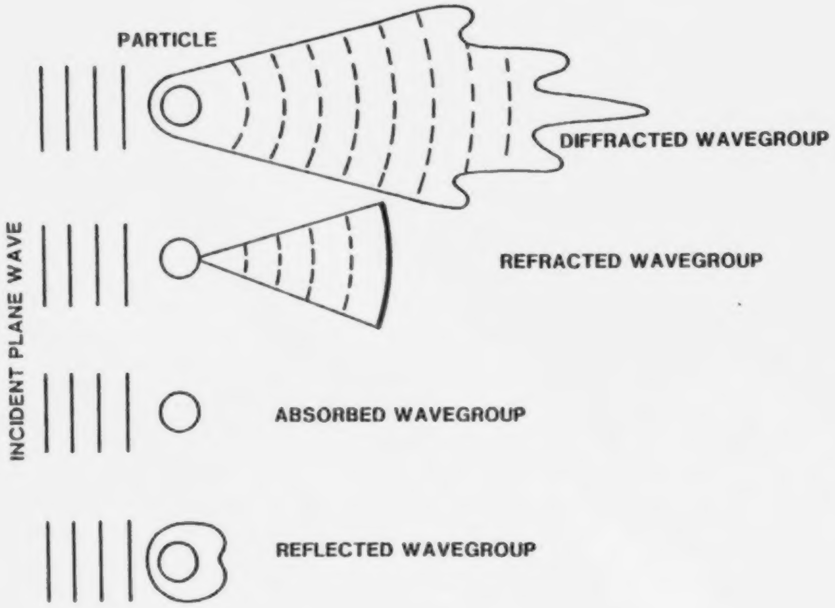

Figure 13. Wavegroups contributing to light scattering.

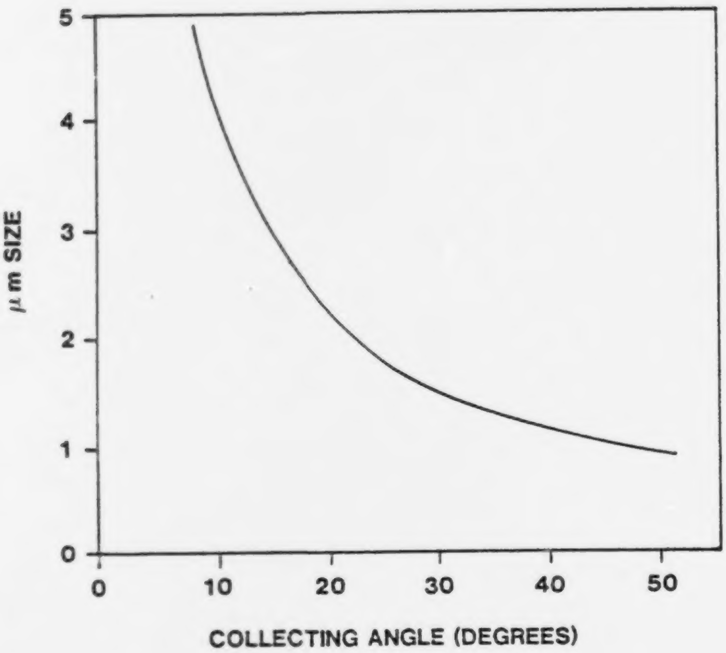

Figure 14. Required light collecting angles to collect 89% of the light refracted by particles in the 0.5 to 5 micron range.

(by diffracted light) of a 0.5 to 5 μm size range requires a reasonably large outer collecting angle for small particles and a small inner collecting angle for larger particles. For most refractive indices, refracted light accounts for up to 45% of the remaining scattered light, its exact amount determined by the complex index. Figure 15 shows the relationship between collecting angles and refractive index in order to collect all refracted light excluding that involving internal reflections. It is important to bear in mind that absorption occurs from the attenuation of refracted light and that size affects only its magnitude and not angular distribution.

Note that the refracted and diffracted wave groups are strongly forward scattered. They dominate the scattering characteristics of most particles. Since they normally contribute greater than 90% of the scattered light, the highest detectively of particles is obtained by optical systems oriented to collect them.

Figures 16a, b, and c illustrate the total scattering phase functions for particles of 0.6, 2, and 5 μm diameter computed from Mie theory. The pronounced forward scattering is obvious in all cases and for the index and size used contains refracted and diffracted components in similar quantities. If one introduces varying amounts of absorption, the amplitude of the refracted wave is reduced, with an at first expected reduction in the total amount of forward scattering. However, at this point one must be careful not to oversimplify the Mie results. For coherent radiation the phases as well as the amplitudes of the scattered waves must be considered. Since the refracted wave suffers a phase lag proportional to the optical path length it traverses, while the diffracted wave's phase relationship is defined as a function of scattering angle and size, they may interfere to produce a resonant combined amplitude greater than less than the sums of their independent intensities--i.e., coherence-induced resonance or destruction interference. The effect is most pronounced when the particle size is chosen so that the central maximum of the diffraction pattern (Airy disk) is of comparable size to the refracted wave cone and collecting solid angle is sized to just collect both scattered contributions. The phase change from the center to the edge of the Airy disk is $\pi/4$ (see Borne and Wolfe, 1972). Because there is just such a size for any fixed collecting solid angle, it is impossible

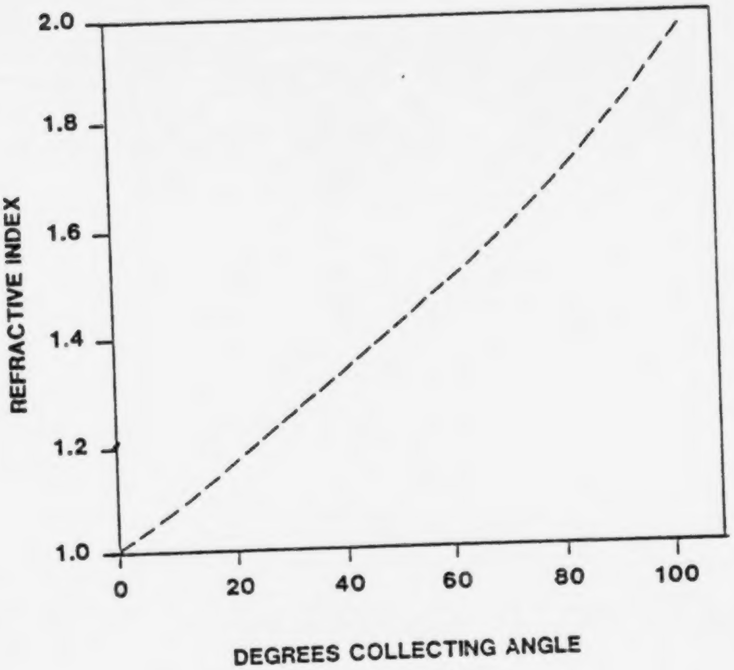

Figure 15. Required collecting angles in order to collect 80% of all refracted light involving single pass transmission through the particles. The complex index is assumed to be zero.

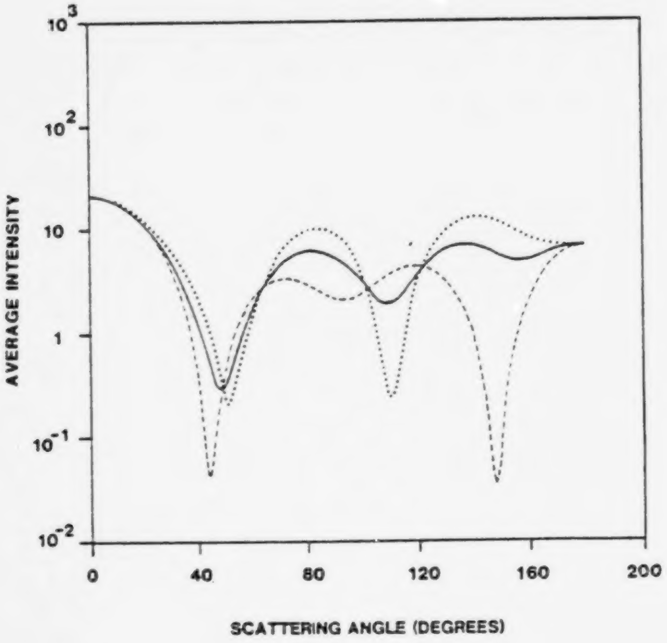

Figure 16a. In the above diagram, the S_1 and S_2 polarization states and average intensities are shown for monochromatic light of λ = 632.8 nm. (D = 0.6 μm)

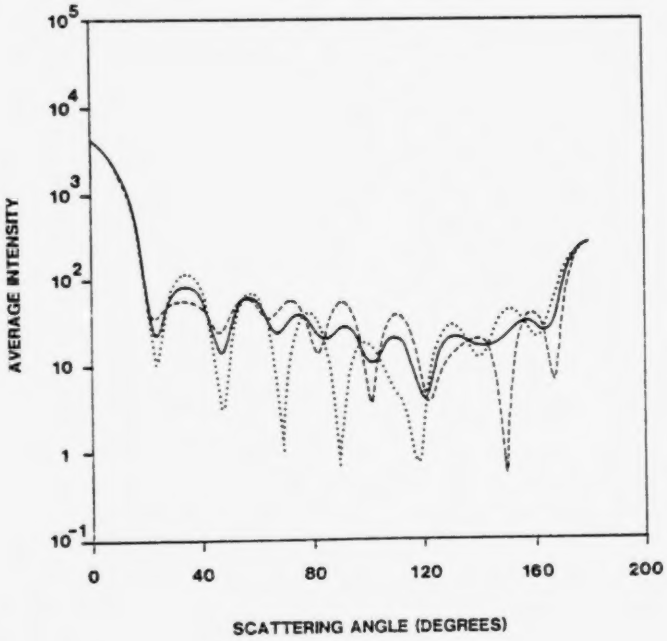

Figure 16b. In the above diagram, the S_1 and S_2 polarization states and average intensities are shown for monochromatic light of λ = 632.8 nm. (D = 2 μm)

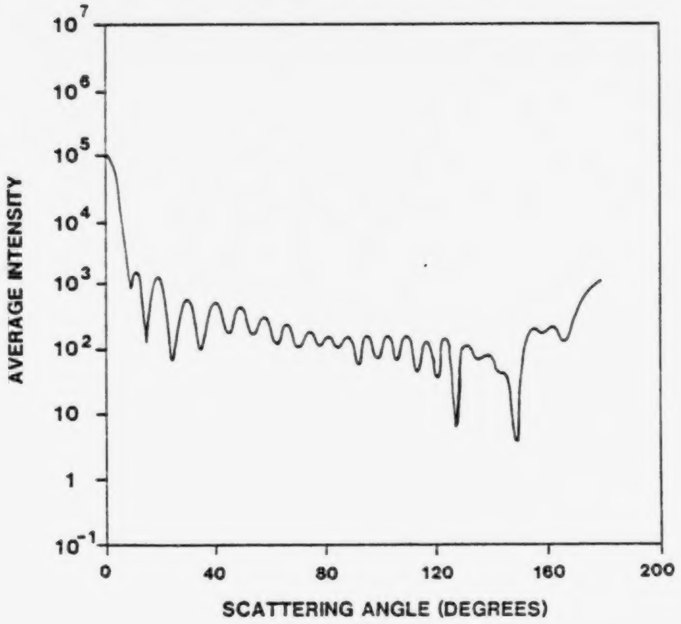

Figure 16c. In the above diagram, only the average intensity is shown for monochromatic light of $\lambda = 632.8$ nm. ($D = 5$ μm)

to avoid the effects. The general result is a smaller or greater scattering response than expected; if pronounced it can lead to ambiguous scattering-size relationships (i.e., a larger particle producing a smaller signal).*

Regardless of whether the refracted and diffracted waves overlap and interfere, a similar result occurs if the inner scattering angle cannot be maintained close to 0°, which, while easy to do with lasers, is nearly impossible to approach (within 10°) without them. This limitation results from the fact that as particles increase in size (e.g., from 1 to 5 μm) the diffracted light is suppressed to smaller and smaller angles and eventually cannot be separated from the transmitted light of the source. As previously stated, the refracted light is maintained in an angular cone that does not change with size but is generally smaller in contribution than the diffracted light. Under such conditions there is the probability that a smaller particle, whose strong forward scattering contribution (dominated by diffraction) is well matched to the collecting optics solid angle, may produce a larger collected response than a larger one whose diffracted light is lost inside the apodimized region of the collecting optics. It occurs whether coherent or incoherent light is used. Thus, ambiguities in sizing are the expected rule in certain size ranges. In order to select the most appropriate collecting geometry for the FPSSS, various existing designs were reviewed and a series of Mie computations performed.

In Figures 17 and 18 two responses from Cooke and Kerker (1975) show the optical oscillating response in two optical counters using white light. Figure 19 shows the similar results for the laser-fed PMS CSASP-100. If one chooses to avoid the forward region, a smoothed response is obtained, as illustrated in Figure 20 for a white light counter and in Figure 21 for a laser-fed PMS LAS-200. These are both essentially refracted light instruments in the 0.5 to 5 μm range.**

---

*Coherence-induced resonance effects are generally observed to be damped because of lack of fulfillment of plane wave conditions. Multimode lasers are sufficiently lacking in spatial coherence to reduce some of the effects (Knollenberg, 1976b). It is a primary reason for the use of high-order multimode lasers in CSASP instruments.

**The above result may appear surprising to some since it is often claimed that lasers are not as desirable as white light sources for particle sizing purposes because of the coherence-induced resonant interference. However, the overall problem is obviously dominated by collecting optics consideration.

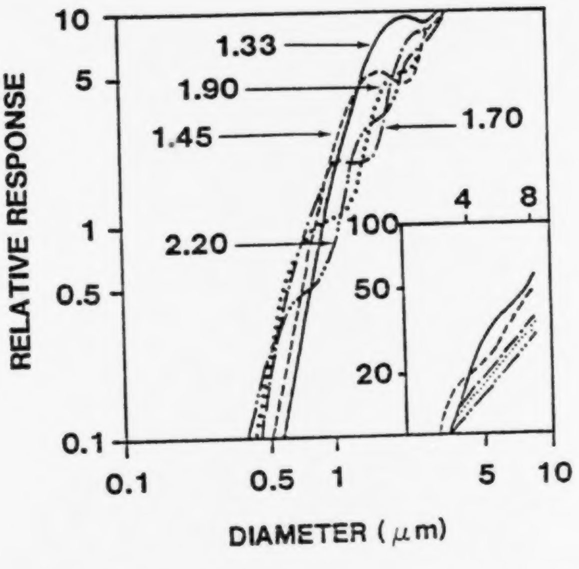

Figure 17. Response of the Royco 218 particle counter for particles with refractive indices 1.33, 1.70, 1.90, and 2.20. The curve for 2.50 is very close to that for 2.20 (from Cooke and Kerker 1975).

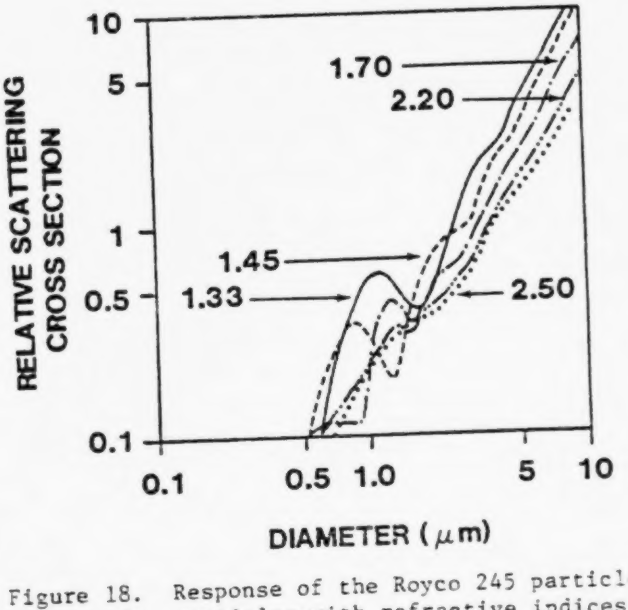

Figure 18. Response of the Royco 245 particle counter for particles with refractive indices 1.33, 1.45, 1.70, 2.20 and 2.50. The curve for 1.90 is very close to that for 2.20 (from Cooke and Kerker 1975).

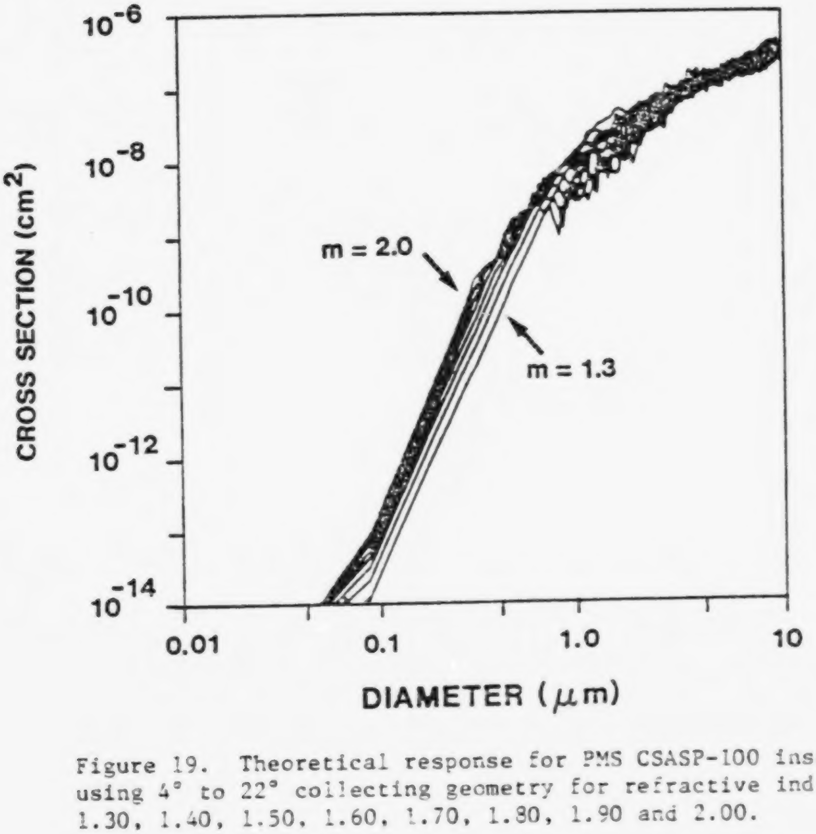

Figure 19. Theoretical response for PMS CSASP-100 instrument using 4° to 22° collecting geometry for refractive indices 1.30, 1.40, 1.50, 1.60, 1.70, 1.80, 1.90 and 2.00.

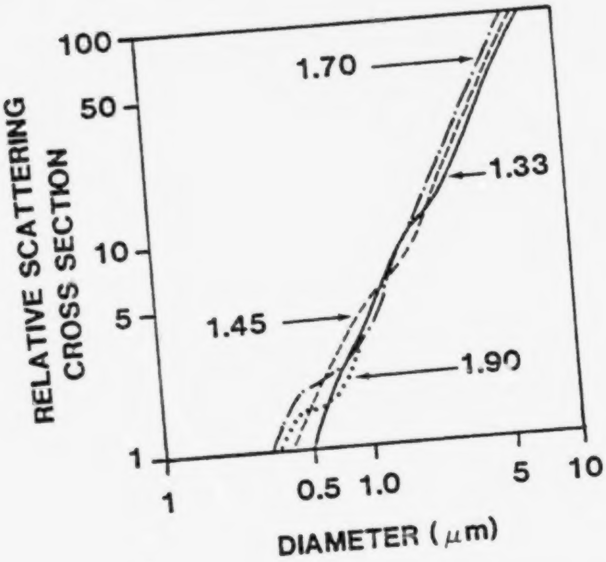

Figure 20. Response of the Climet particle sensor for particles with refractive indices 1.33, 1.45, 1.70 and 1.90. The curves for 1.90, 2.20, and 2.50 are very close to each other and above radius 0.45 μm are very close to 1.70.

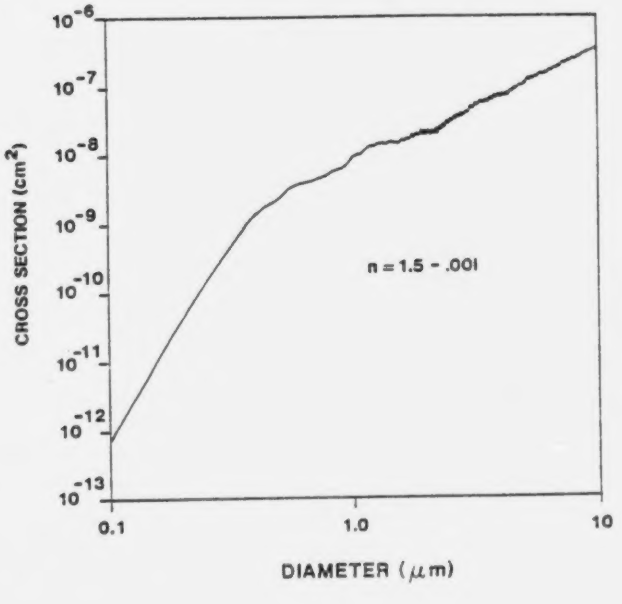

Figure 21. Response for PMS Model LAS-200 aerosol spectrometer using 35° to 120° collecting solid angles. Negligible change for other real indices between 1.30 to 2.30.

One might invoke that the large collecting angle (nonforward) is most desirable because of the monotonic calibration curve. However, if one considers the effects of absorption this is not the case. Again from Cooke and Kerker we can compare the instruments in Figures 22 and 23 with absorbing particles shown in Figures 17 and 20. Clearly, unless one knows he is dealing with transparent spheres, the Royco instrument has less total uncertainty. The Climet, like the LAS-200 (being a refracted light instrument) loses signal when the refracted light is attenuated by absorption. Furthermore, if one considers unknown shape, the larger collecting angles of the Climet or the PMS LAS-200 are subject to scintillations (direct reflections from crystal planes) and without the morphology independent diffracted light contribution may give quite spurious results.

In our experience and from this current analysis, it is clear that a strong forward scattering system would generate the least uncertainty in sizing, with the exception of particles that are nearly spherical and rather transparent. A laser-fed optical system provides the opportunity to collect the strongest forward scattered light. The particles in a stack are often spherical but seldom transparent. Ordinarily, they are translucent, made up of possibly several chemical species of differing refractive index. Most are at least slightly absorbing at visible wavelengths. Considering these facts, we selected a strong forward scattering laser-fed optical system. Finally, we can also note that the phase integrity of the refracted light is randomized in translucent particles, reducing potential interference and coherence-induced resonance.

Also, it may not be apparent, but a range of collecting angles from 35 to 120° cannot easily be used for *in situ* measurements unless another means is used simultaneously to define particle position. Reflecting optics are required for the large collecting angles of the Climet and the LAS-200 instruments, and they cannot be easily manufactured with the tolerance demanded by the imaging required for sample volume definition, nor is a particle *in situ* if totally enwrapped in optics.

If we truly desire *in situ* measurements we should also point out that background light is nearly impossible to deal with unless monochromatic sources are used to enable filtering. If a monochromatic situation is desired, then a laser is even more desirable. As it turns out, filtering is required less often when using laser sources because of their higher energy density permitting the use of photodiodes rather than the more sensitive, but also quite temperature-

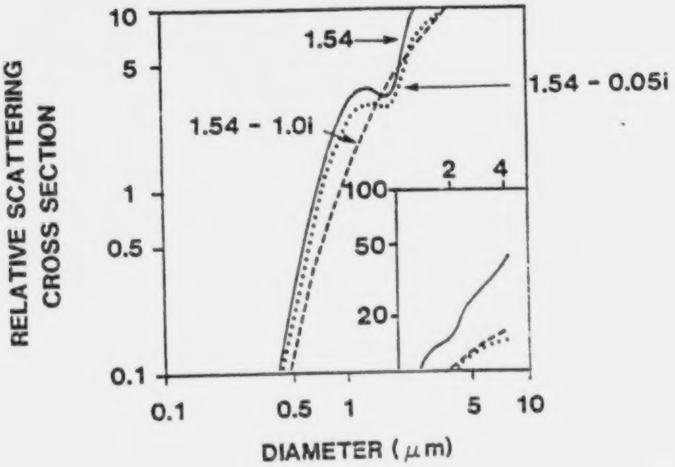

Figure 22. Response of the Royco 218 particle counter for particles with refractive indices 1.54, 1.54-0.05i, and 1.54-1.0i. The curve for 1.54-0.5i is very close to that for 1.54-1.0i.

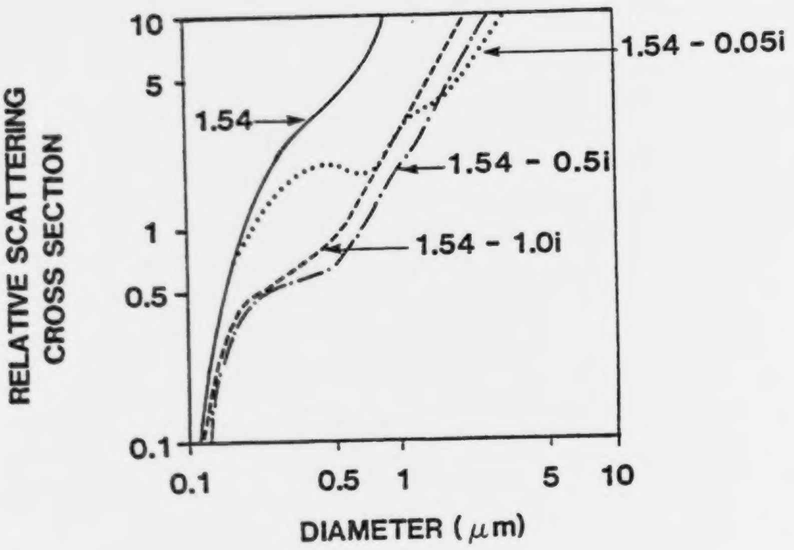

Figure 23. Response of the Climet particle sensor for particles with refractive indices 1.54, 1.54-0.05i, 1.54-0.5i, and 1.54-1.0i.

sensitive, photomultiplier tubes. The reader is referred to Knollenberg (1975, 1976b) for detailed discussions on the advantages of laser light sources over white light sources and comparative signal-to-noise analysis of solid state photodiodes and photomultiplier tubes.

Thus far we have discussed many aspects of particle optics, possible effects of differing light sources, and factors affecting design. What can we conclude with regard to the possible FPSSS optical design? First, that we want a laser light source. Second, that we need a collecting optical design that permits the collection of light as close as possible to the optical axis. If the particles are not nonabsorbing spheres and are to be measured *in situ*, a forward scattering imaging optical system is required and the best light source is a laser. The task remaining is thus one of optimizing a forward scattering optical system for the FPSSS.

There are two standard instruments manufactured by PMS that use strong forward scattering: the Model ASAS-100 and the Model CSAS-100. Both happen to have 4-22° collecting angle geometries. The computed response for 4-22° collecting angles is given in Figures 24 and 25. Figure 24 shows the range of responses for real indices from 1.33 to 2.5 in the absence of absorption. Considerable uncertainty exists at sizes from 1 to 2 microns and indices between 1.33 and 1.7 due to strong resonance. Furthermore, above 6 microns there is a systematic difference in sizing; the signal is greater the lower the real refractive index. Figure 25 exhibits the sensitivity to dispersion of imaginary index with a real index of 1.5. The primary effect of strong absorption is in the smoothing of the oscillations--the effect being more noticeable the larger the size or the greater the amount of absorption. For strong absorbers a systematic oversizing begins to show up at diameters greater than 4 microns.

These results have been known for some time. In many cases we have found a reduction in the sensitivity to changes in both real and imaginary index components by reducing the inner collecting angle. By selectively manipulating the inner and outer collecting angles, we determined that the least sensitivity to changes in complex refractive index is achieved with a range of collecting angles of approximately 2-11°. Figures 26 and 27 show the computed sensitivity to dispersions in real and imaginary components, respectively, for 2-11°. Comparison

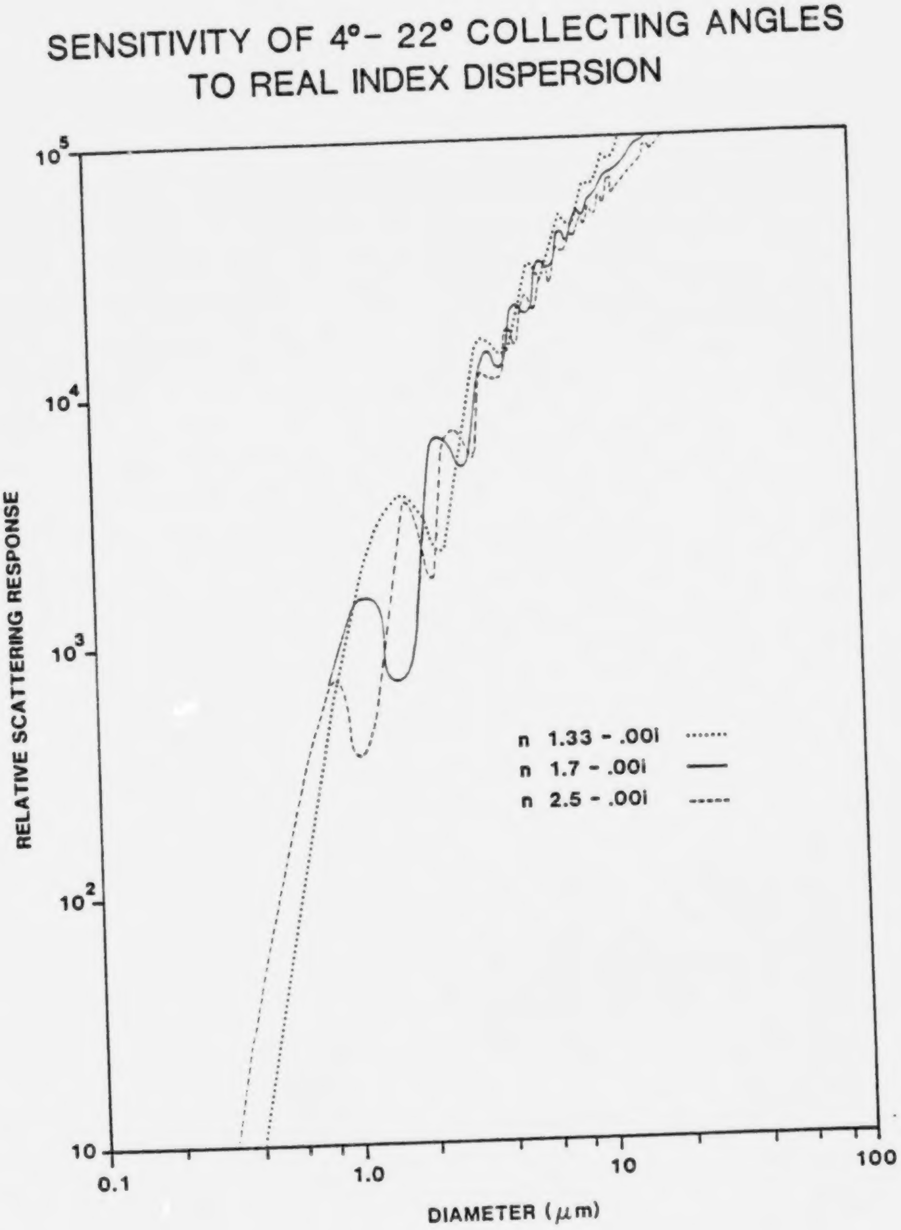

Figure 24. Computations above for λ = 632.8 nm.

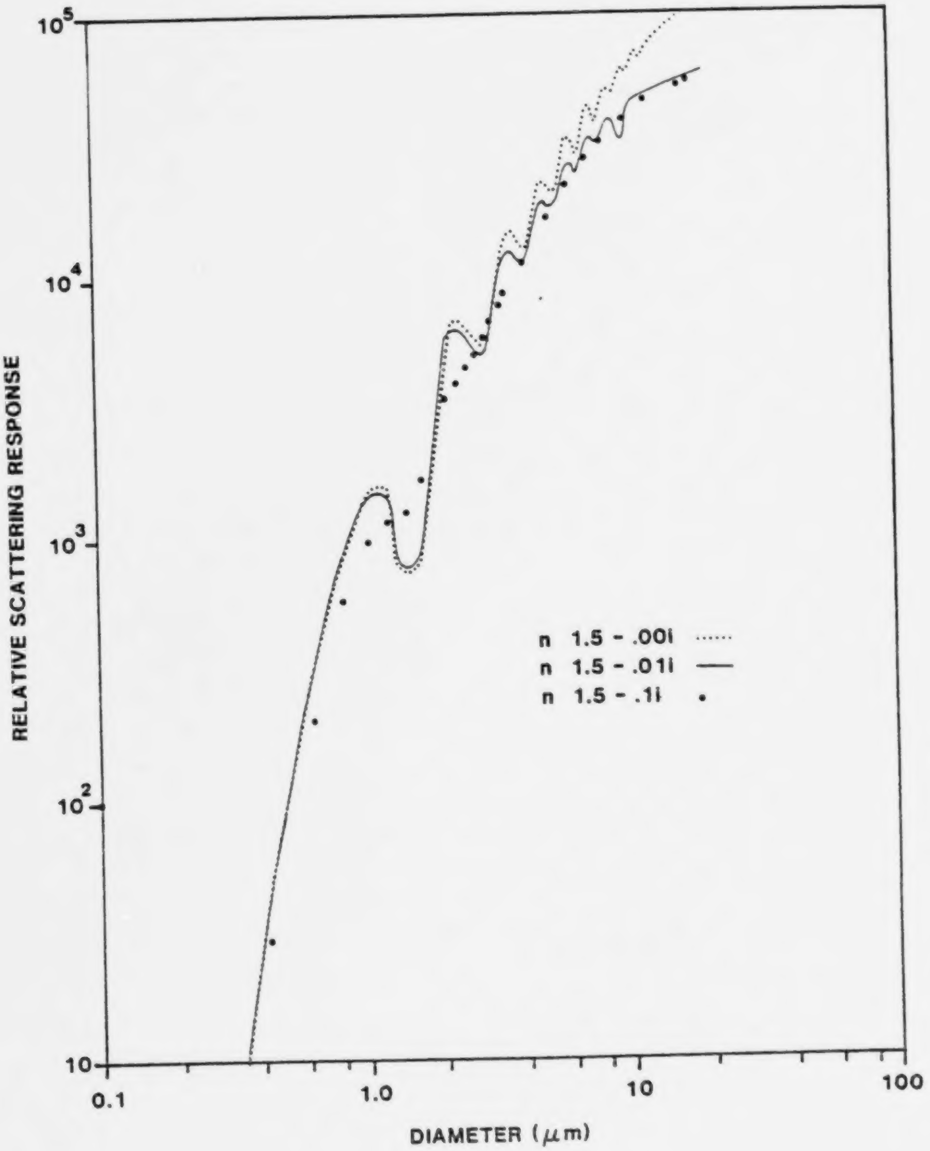

SENSITIVITY OF 4°- 22° COLLECTING ANGLES TO COMPLEX INDEX DISPERSION

Figure 25. Computations above for λ = 632.8 nm.

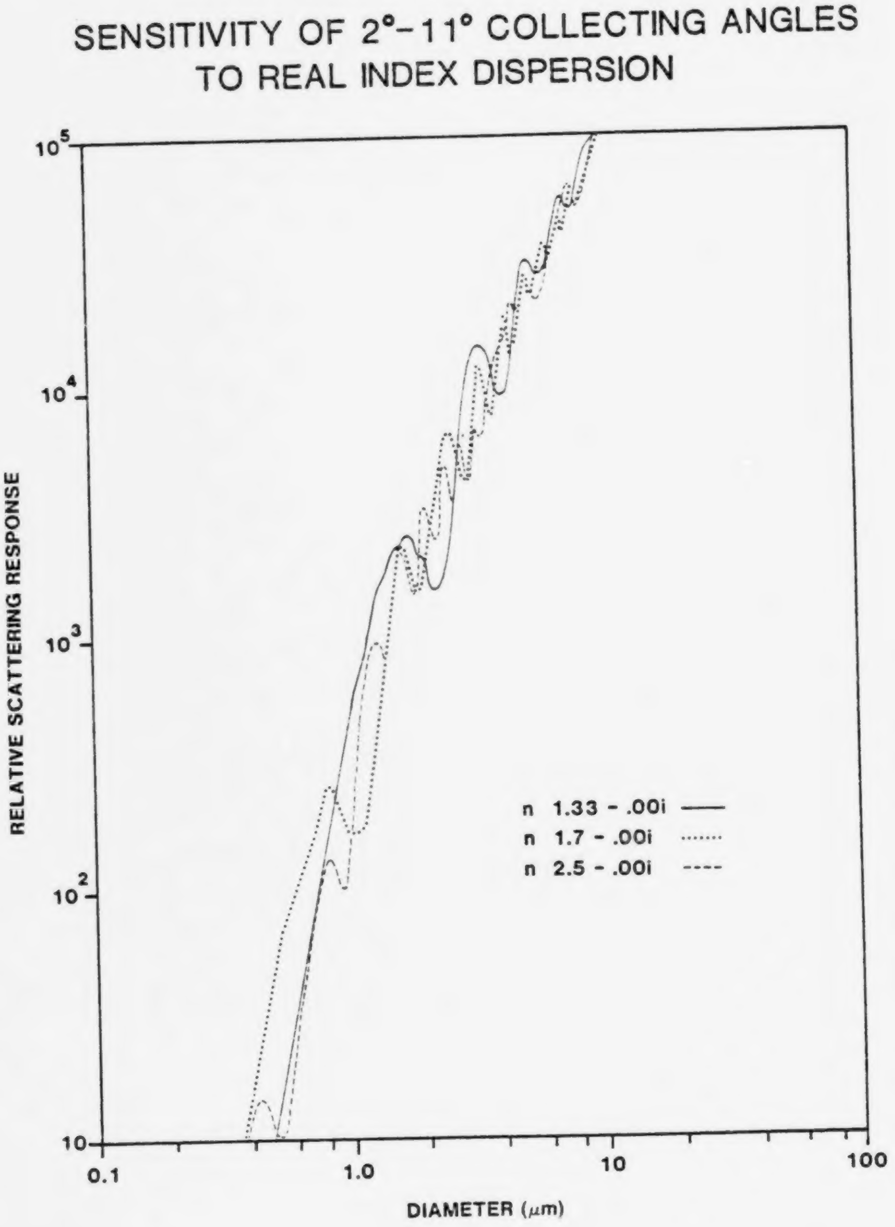

Figure 26. Computations above for λ = 632.8 nm.

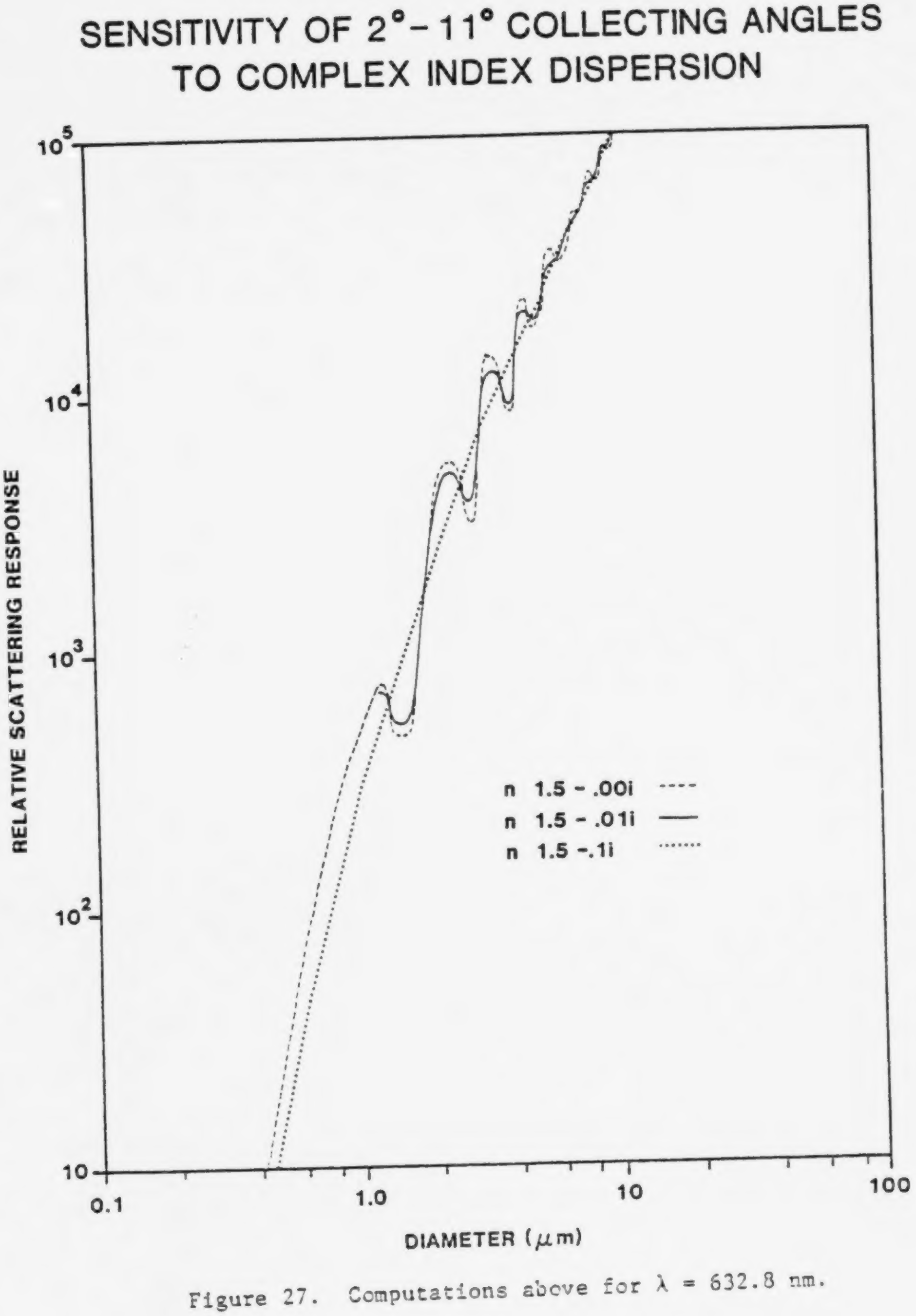

Figure 27. Computations above for λ = 632.8 nm.

with Figures 24 and 25 shows improvement in terms of the dampening of the oscillatory behavior of the response functions and the elimination of systematic errors in the responses attributable to variations in real or imaginary components. A further advantage of the 2-11° collecting angle range for particle sizes from 0.5 to 10 microns is that small errors in either inner or outer collecting angle have negligible effect on the scattering response. Figure 28 shows the effect of varying either collecting angle by 1°. It is clear that changes on the order of 1° should result in nearly negligible difference from the 2 to 11° collecting angles selected.

Of course, we are trying to optimize for a range of 0.5 to 10 microns. Were one to concentrate on the submicron region, one might opt for an outer collecting angle of 22°. Likewise, if the emphasis were on sizes as large as 50 microns, the optimal and the outer collecting angles would be smaller still. In any case, utilizing a best fit calibration curve through the center of the envelope of nested curves in Figure 26 results in a tolerance of 0.3 microns at 1 micron diameter, 0.4 microns at 2 microns diameter, reducing to less than 10% at sizes greater than 6 microns diameter. The average error is, of course, much smaller. Verifications of these theoretical results are deferred to Section 7.

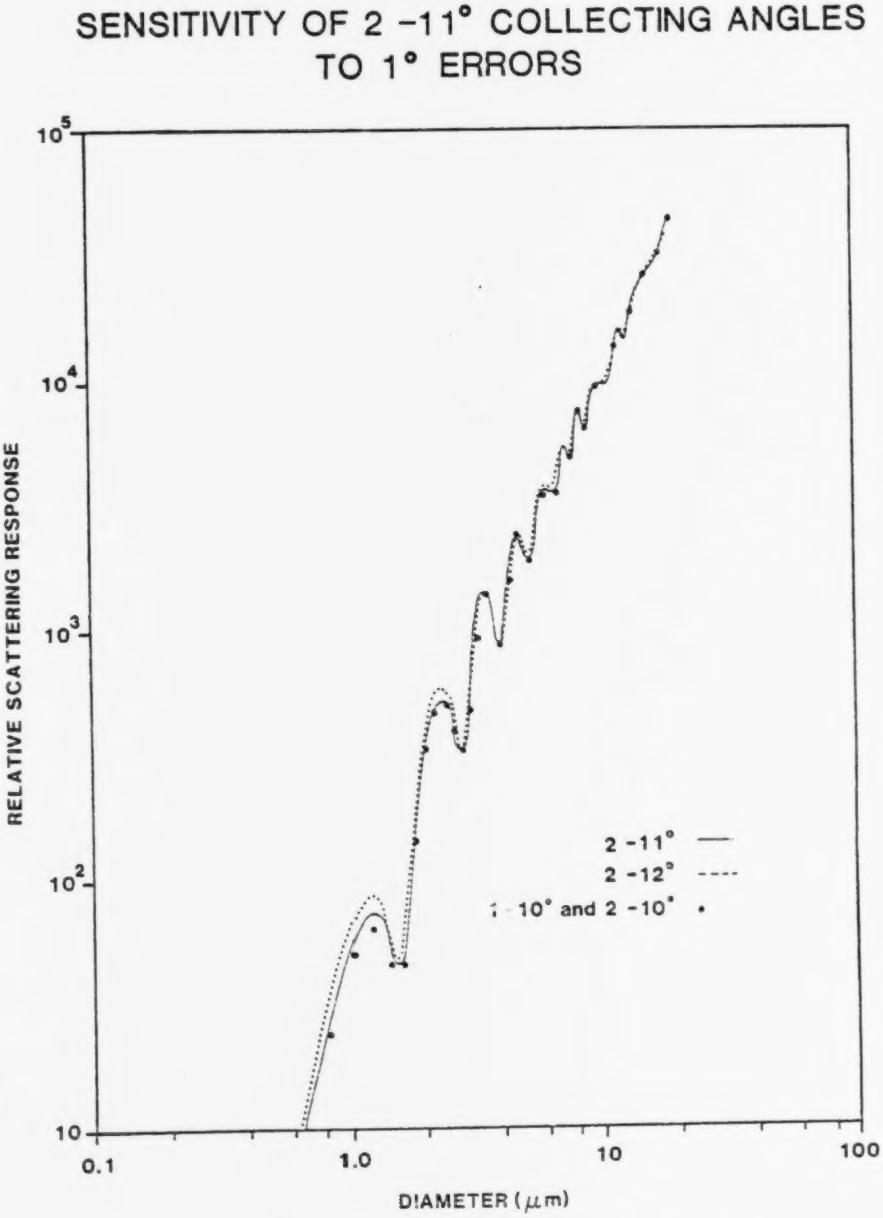

Figure 28. Computations above for λ = 632.8 nm.

5. RESULTS OF AERODYNAMIC TESTS AND THERMAL MODELING

Aerodynamic Tests

As mentioned previously, aerodynamics play an important role in the *in situ* measurement of particle size. To provide the least disturbance to a field of particles their trajectories must not be strongly influenced by the presence of the measuring device. Since a particle's trajectory is basically controlled by the surrounding pressure, which controls the streamlines of the carrier of gas, modeling or measurement of the pressure field at the desired point of measurement is quite useful. From experience in measurements at high number densities we anticipated that our greatest success would come from pursuing the basic CSAS design. This instrument concept requires near proximity to the particle field to be viable. The primary collecting optics must be only a few inches away from the particles being sampled. More importantly, the collecting angles required are fairly well fixed. Since the diameter of the collecting optics would increase in proportion to the distance removed from the particle, any advantage of maximizing the working distance is cancelled by the increasing size of the collecting optics because the aerodynamic disturbances scale in an identical manner, i.e., the degree of disturbance is directly proportional to the size of the intruding object and inversely proportional to the distance from it.

We realized that some disturbance to the particles would probably exist and looked at this problem in the early design stages. In fact, our pre-proposal experimentation included wind tunnel testing of a mock-up probe model to define the magnitude of the problem. That and early tests during the contract period centered around a probe construction utilizing an annular sample ring construction to force a balanced flow around the sample point. This early FPSSS probe configuration is shown in Figure 29; it could accommodate the optical design suggested in the previous section.

Wind tunnel tests were conducted on the configuration using test models employing 4" by 6" diameter sample rings. The resulting pitot pressure profiles are given in Figure 30 and 31 as measured in our wind tunnel (see Appendix I for a description of the PMS wind tunnel test facility). These figures indicate essentially identical flow (pressure) fields for the two tests. The tests also showed that there is nothing to be gained by the larger structure. We were

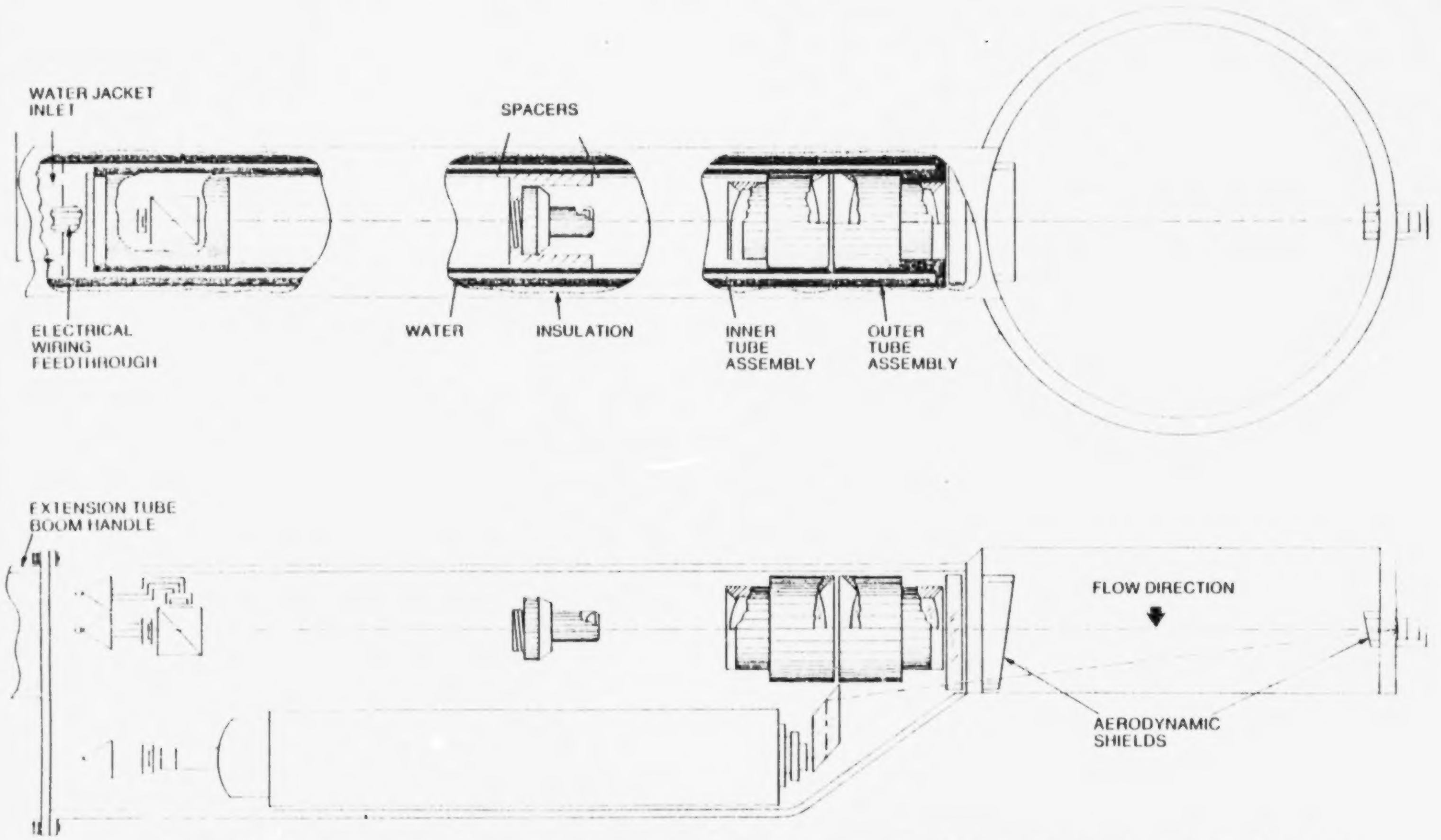

Figure 29. The above diagram depicts the first conceptual FPSSS probe head, models of which underwent initial wind tunnel testing. Both 4" and 6" diameter rings were tested.

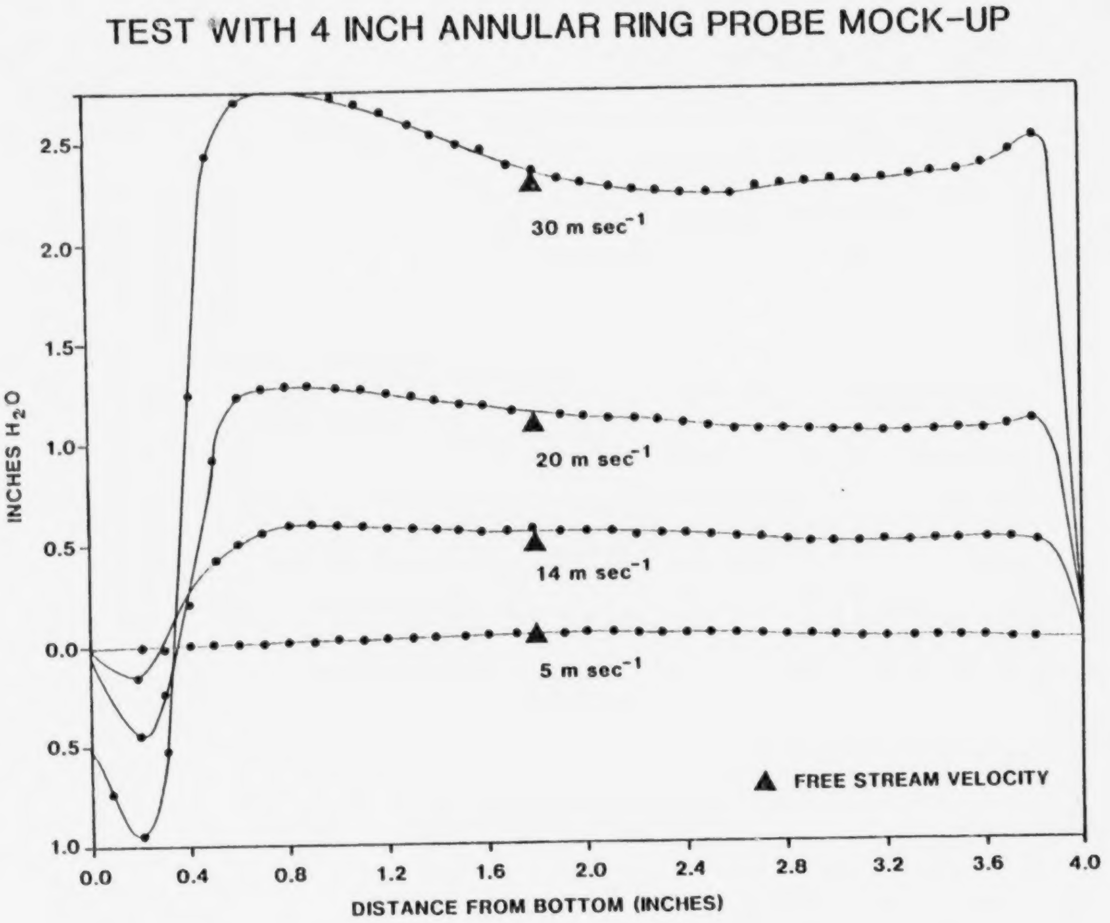

Figure 30. Probe mock-up mounted in vertical orientation.

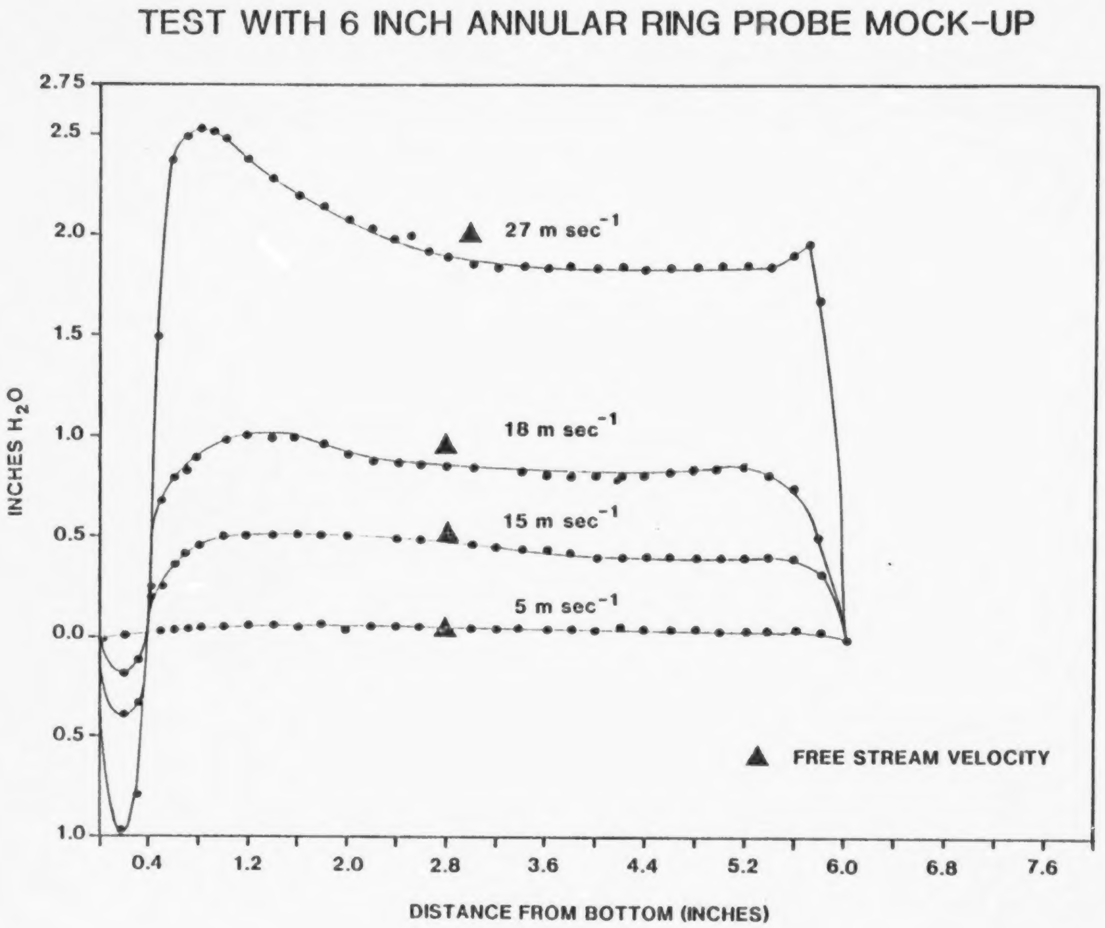

Figure 31. Probe mock-up mounted in vertical orientation.

somewhat surprised by the magnitude of the reverse eddy as one approached the probe body--roughly one half that of the free stream flow. The best region for sampling was found to be closer to the external mirror than the objective. One notable difference between the two envelopes was the observation that the measured velocity at the sample ring center was less than free stream for the 6" ring but greater than free stream for the 4" ring. We attributed this effect to the fact that the ring thicknesses were the same (3/8"), forcing a larger relative volume through the smaller ring's I.D. Other than the thickness of the ring, exact similitude was followed.

The above aerodynamic results were satisfactory as the basis for a prototype design. However, other factors required the consideration of alternatives. Most important was the observation that nearly all stack installations had standardized 4" series pipe ports. The maximum diameter circular ring that could be inserted along the lines of our conceptual model was 3". A rough scaling of our tunnel results indicated that it might be risky, and iterations with our thermal model (described below) indicated added areas of uncertainty. We thus considered an alternative model which became our adopted configuration.

The final FPSSS probe head configuration is shown in Figure 32. It strongly resembles the LCPS design--particularly with regard to the pair of standoffs to support the external beam folding mirror. The cantilever mirror support design allows particles to be sampled before encountering the disturbance created by the standoff support rods. Pressure field mapping was conducted axially along the optical axis, transversely across the object plane, and transversely behind the pair of standoffs as indicated in Figure 32. The results shown in Figures 33-35 were better than expected. In particular, the axial scan of Figure 34 showed the surprising loss of the reverse eddy near the window. In fact, we were not able to sample within 1/4" of the window; a reverse eddy likely still exists within the boundary layer. However, only evidence for greatly reduced flow was found behind the shield. A slight positive excess is noted ahead of the shield. We concluded that the improved results were largely due to the loss of the sample ring and the addition of the aerodynamic shields. Further work was not justified in attempting to investigate further alterations of the design. Additional tunnel testing was conducted to tailor the aerodynamic

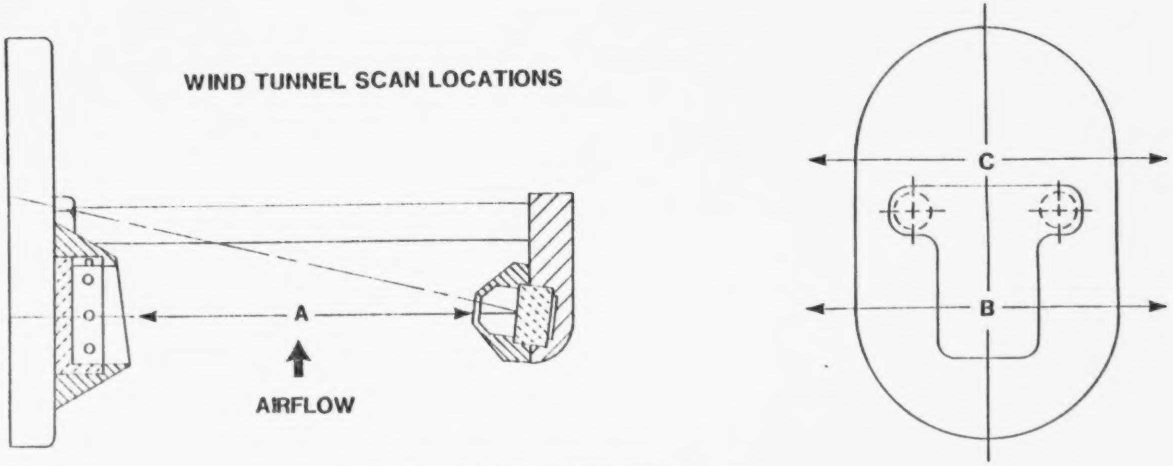

A AXIAL SCAN ALONG OPTICAL AXIS

B TRANSVERSE SCAN ACROSS OBJECT PLANE

C TRANSVERSE SCAN BEHIND STANDOFFS BEHIND OBJECT PLANE

Figure 32. FPSSS probe head configurations during wind tunnel tests. Initial mapping of the pressure field used a miniature pitot-static system on this head configuration, results of which are presented in the following figures. More recently, they have been verified with a hot-wire anamometer.

TEST WITH BREADBOARD FPSSS PROBE HEAD
SCAN ALONG OPTICAL AXIS FROM WINDOW TO MIRROR

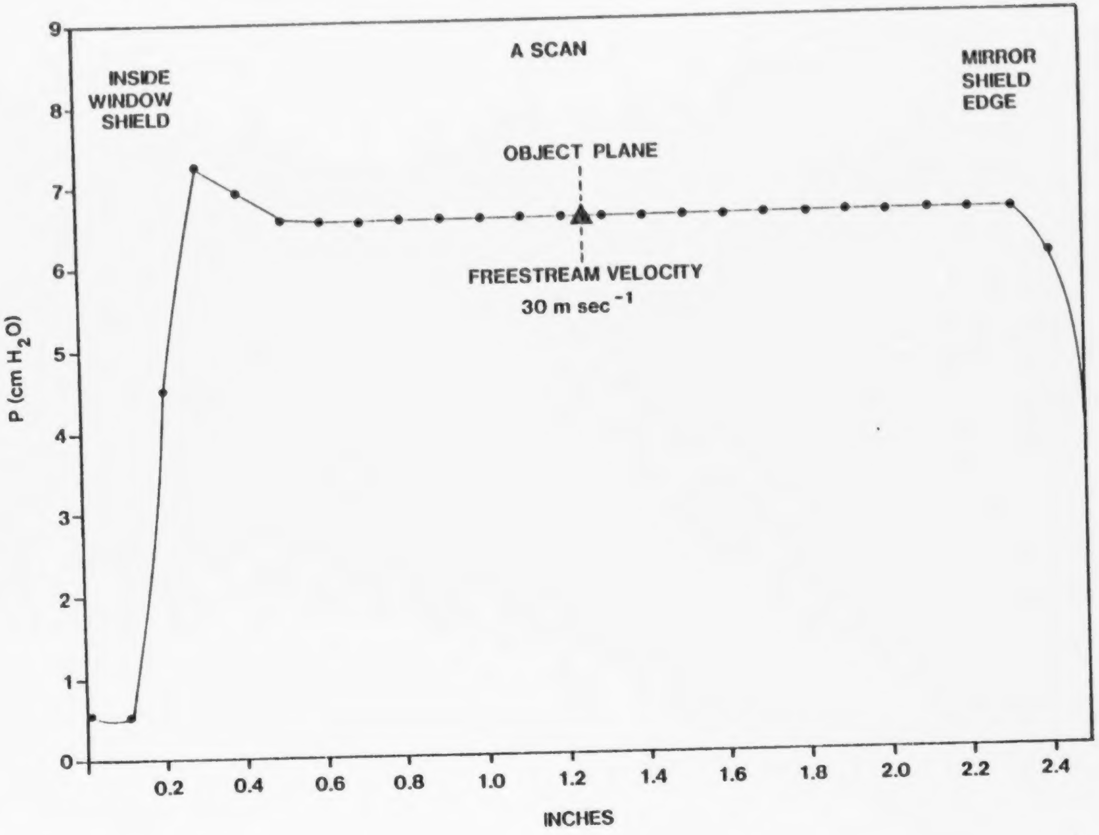

Figure 33

TEST WITH BREADBOARD FPSSS PROBE HEAD
TRANSVERSE SCAN ACROSS SAMPLE PLANE

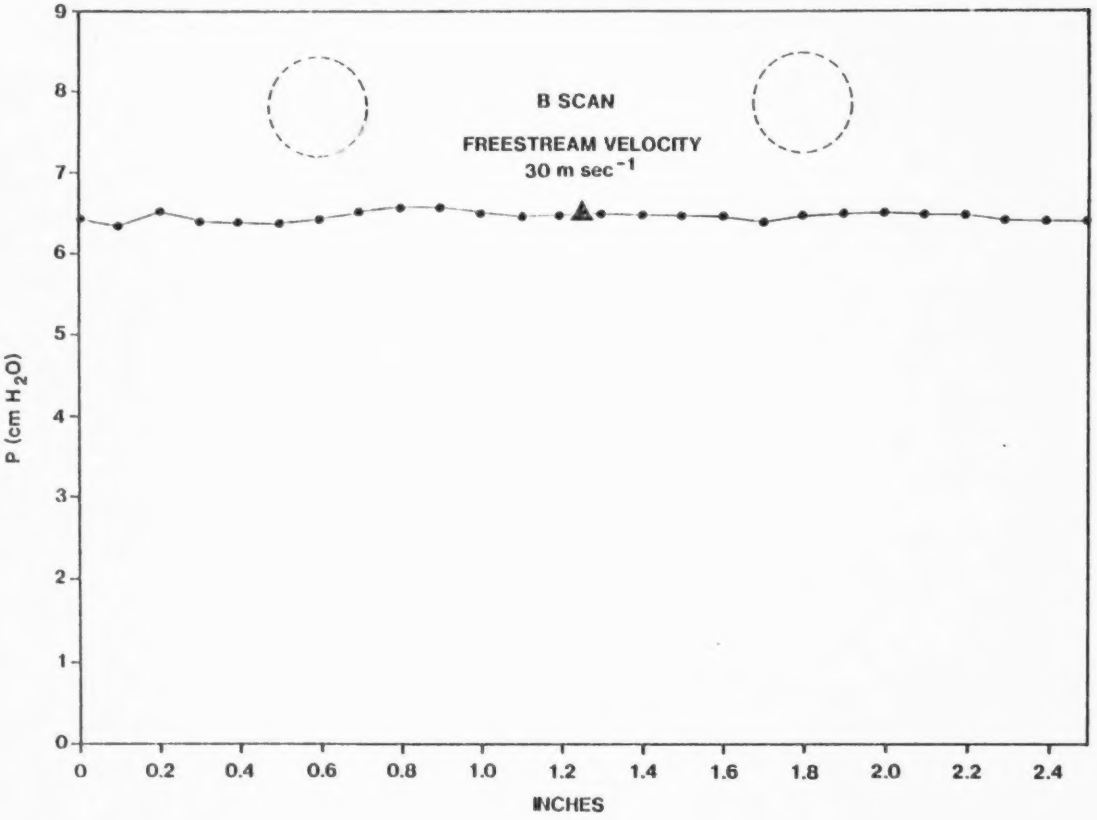

Figure 34

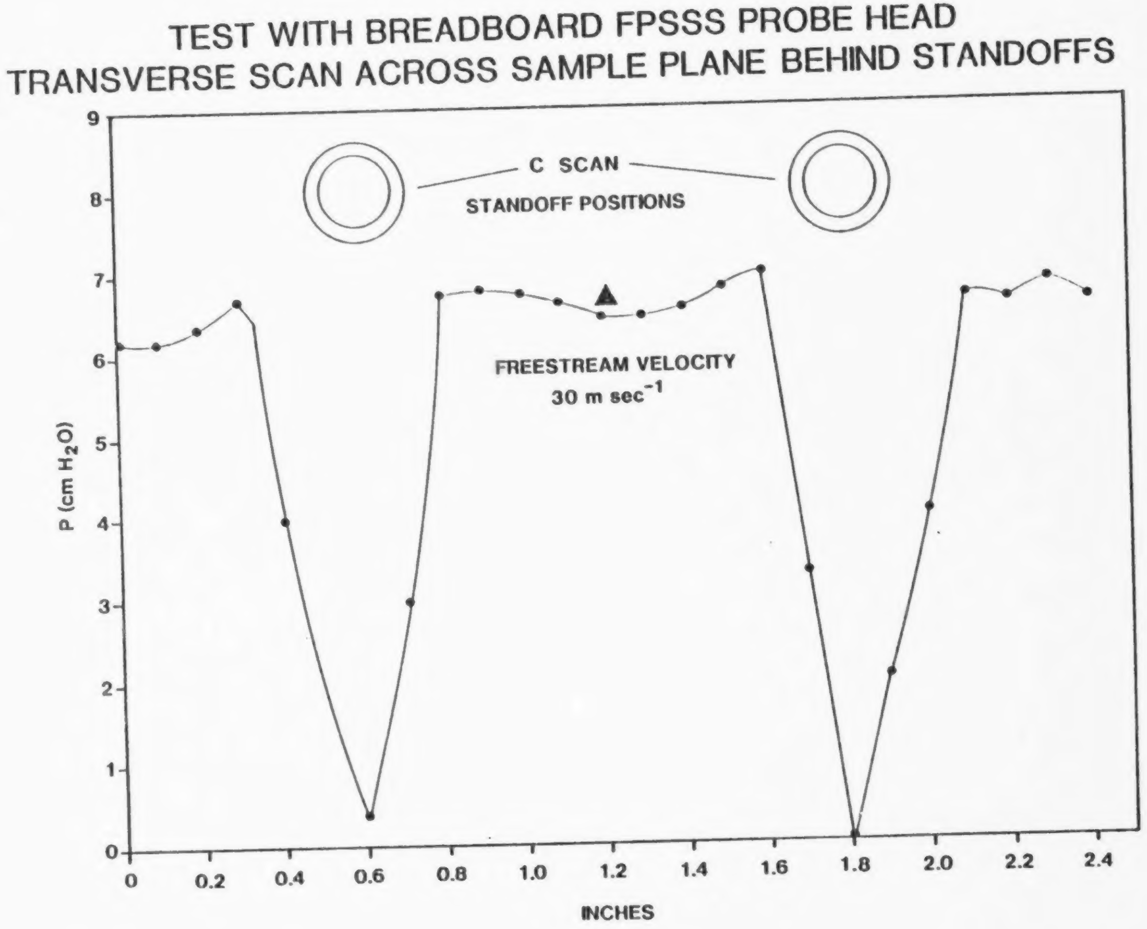
TEST WITH BREADBOARD FPSSS PROBE HEAD
TRANSVERSE SCAN ACROSS SAMPLE PLANE BEHIND STANDOFFS
C SCAN
STANDOFF POSITIONS
FREESTREAM VELOCITY
30 m sec^{-1}
P (cm H_2O)
0
1
2
3
4
5
6
7
8
9
0
0.2
0.4
0.6
0.8
1.0
1.2
1.4
1.6
1.8
2.0
2.2
2.4
INCHES

Figure 35

mirror and window shields as well as to investigate the effects due to misalignment of the probe to the flow. Water injection was used to study the shield designs. (Their primary purpose is to prevent the soiling of optical components.) No noticeable deleterious effects were discernible in the flow field at misaligned test angles up to 20° (axially).

Thermal Modeling

All of the FPSSS probe designs required an active cooling system. This is necessitated by the proximity of the laser and photodetector circuitry to the high temperature environment. Computations showed that although insulating materials were capable of maintaining operable temperatures in an unpowered probe for a couple of hours with a kilogram of phase change material the head load from the laser itself was sufficient to demand active cooling. These internal heat sources are given in Table I.

Obviously, if we are to have electronics and optics (aligned) operate continuously in a 250°C environment we definitely need to cool them. Thus, as a first step Ball Brothers Research Corporation (BBRC) provided a first-order analysis of the potential thermal load. For computational purposes the FPSSS head body envelope considered was essentially that of Figure 36 which is a water cooled, flat walled, insulated cylindrical section of 30 cm length. Our goal was to calculate the thermal resistance (R) of this envelope, then compute from this calculation a temperature rise for the water for an estimated reasonable water flow.

We used the following input values:

Water flow:	2 gpm
$\overline{h}_o$ = heat transfer coefficient for stack gas:	284 Watts (W) $\text{m}^{-2}\,{}^{\circ}\text{C}^{-1}$
K - thermal conductivity of fiberglass insulation:	0.052 W $\text{m}^{-1}\,{}^{\circ}\text{C}^{-1}$

The Thermal insulation resistance, $R_i = \frac{1}{C_i}$, must be calculated as a parallel network of conductance terms for the flat side walls and cylindrical top and bottom sections:

TABLE I

FPSSS COMPONENT POWER DISSIPATIONS

NODE NO.	DESCRIPTION	POWER (WATTS)
11	PC Board	1.5 to 2.0
23	Laser	12 to 15
50	Window Heater	1 to 5

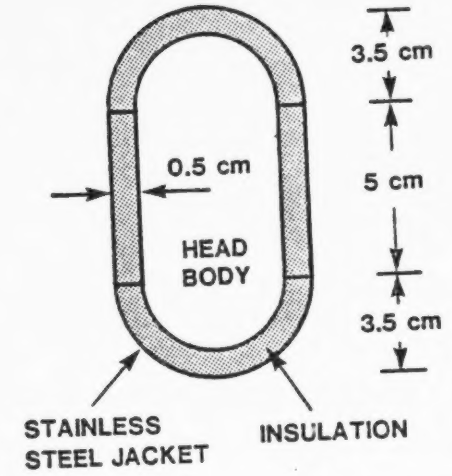

Figure 36. Simplified model of the FPSSS head cross section used for thermal analysis.

$$C_i = \frac{2\Pi kL}{L_n D_o/D_i} + \frac{k\ 2\ HL}{X}$$

$$= \frac{2\ \Pi(0.052)\ (0.40)}{\text{Ln } 7/6} + \frac{(0.052)\ (0.04)}{0.005} = 1.264\ \text{W °C}^{-1}$$

Then,

$$R_i = \frac{1}{C_i} = 0.7912\ \text{°C W}^{-1}$$

The thermal resistance between the outside wall and the stack gas can be calculated by

$$R_{sg} = \frac{1}{h_o\ (\Pi DL + 2\ HL)} = \frac{1}{(284)\ (0.1281)} = 0.02751\ \text{°C W}^{-1}.$$

The total thermal resistance is the series sum of the insulation resistance and that between the outside probe wall and the stack gas:

$$\Sigma R = R_i + R_{sg}$$

$$= 0.08187\ \text{°C W}^{-1}$$

$$C = \frac{1}{\Sigma R} = 1.2214\ \text{W °C}^{-1}$$

We assumed a temperature difference between water and stack gas

$= 250 - 45 = 205°C$

And thus our thermal load is

$q = C\Delta T$

$= (1.2214)\ (205°C) = 250.4\ W$

The temperature rise of the water is

$$\Delta T_w = \frac{q}{C_p \times 1\ \text{gpm}} = \frac{250.4}{(1)\ (126.2\ \text{grams/sec})\ (4.18)} = 0.47°C$$

Since the temperature rise computed is small, additional iterations change the resultant only slightly. A low temperature rise is important in that it lowers the thermal gradient in the envelope and reduces the "hot dog" type bending that could introduce optical misalignment. The small amount of water required is an advantage in minimizing total system packaging complexity. In fact, actual tests revealed that halving the water supply and doubling the temperature were tradeoffs. In any case, the ability to cool an instrument assembly of the type we envisioned in the stack environment was found to be a straightforward process.

The thermal numerical model of the FPSSS was designed to be flexible and allowed an iterative approach to the final design. Essentially what was modeled here is a thermal control system (TCS). The TCS is designed to protect the sensor head from thermal distortions that could degrade optical performance, to cool the electronics, laser, and internal optics, and to prevent condensation from forming on the external optics and window. It consists primarily of fiberglass insulation, coolant loop, and a window heater. (The window heater was later deleted when purge air was added.) The following description gives the important thermal properties of the TCS.

Both the sensor head and the boom are thermally protected from the stack gas environment by a one-half inch thick layer of fiberglass insulation. The insulation on the head is sandwiched between the head itself and a thin metal jacket that protects it from being damaged by impact and/or abrasion. The boom insulation is located inside the 2¼-inch diameter tube that forms the jacket for the boom. The coolant loop consists of two parallel flow passages (¼-inch in diameter) through which one to two gpm of water are circulated. Water is pumped through two ¼-inch I.D. tubes in the boom to the sensor head where it flows first along the bottom of the head (from the rear optics housing to the front) and then back out through the top. On leaving the head it flows back through the boom to a heat exchanger where it mixes and rejects (to the ambient air) the heat that it has picked up in the boom and sensor head. Included in the model was a 2-watt heater mounted on the periphery of the window on the front of the sensor head used to prevent condensation from forming on the window. It was envisioned that the heater would keep the window temperature above that of the stack gas but it was later replaced with a purge air system. The external optics, which are connected to the sensor head by low conductance standoffs, were not modeled with heating elements, because their temperature was expected to be above the dew point of the stack gas.

The thermal performance requirements on which the FPSSS thermal control system (TCS) is based are as follows:

a. The sensor head (optics housing) shall not exceed 70°C (158°F).

b. None of the electronics shall exceed 85°C (185°F).

c. Temperature gradients in the sensor head (either side-to-side or top-to-bottom) shall be no greater than 1°C (1.8°F).

d. The window heater shall maintain the outer surface of the window approximately 10°C (18°F) above the environment.

It was assumed that the FPSSS would not be subject to stack gas temperatures in excess of 250°C (482°F) and the ambient air temperature would not exceed 35°C (95°F).

The FPSSS thermal analyses were performed with the SSFLD computer program, a version of BBRC's steady-state thermal analyzer program known as SS1 that has the capability of modeling a fluid loop. The input data describe the thermal network of conductive, radiative, and directive conductive couplings between nodes that represent the parts of the hardware for which temperatures are calculated. Boundary nodes are defined with specified temperatures and become sources or sinks. Thermal heat dissipation is applied to each node that has joule or other internal heat generation. The directed conductive couplings permit heat conduction in one direction only and are used to mathematically establish the direction of the fluid flow in the stationary solid nodes.

The program forms energy balance equations for each floating node (not specified temperature), and the resulting nonlinear equations in T and T^4 are solved by iteration for the temperatures (T). After convergence, the energy balance is computed and tabulated for each node. The heat flow through each coupling to every other node and the nodal dissipation are tabulated along with the residual unbalance at convergence.

The FPSSS thermal mathematical model consists of 103 nodes, of which 100 are mass nodes, 1 (the window heater) is a massless node, and 2 (the ambient air and stack gas) are specified nodes. The three types of nodes are defined as follows:

a. Mass - a node that has a finite thermal capacitance; its temperature is calculated in the network solution.

b. Massless - a node that has no thermal capacitance; its temperature is calculated in the network solution.

c. Specified - a node, sometimes referred to as a boundary node, that has an infinite thermal capacitance; its temperature is specified in the network solution.

Figure 37a and 37b show the nodal breakdown and Table II lists the nodes in numerical order and gives a complete description (identification number, material, and thermal capacitance) of each. See Table II for the thermo-physical properties of the various materials used in the construction of the FPSSS and Table III for the computed radiation conductances.

The steady-state thermal analyses discussed here were performed to determine the equilibrium temperatures that the FPSSS would attain if it were exposed to a 250°C stack gas and rejecting heat to 35°C ambient air. Three different coolant flow conditions were considered. They were:

balanced flow of 1 gpm in each loop;
balanced flow of 0.5 gpm in each loop;
unbalanced flow with 1 gpm in one loop and 0.5 gpm in the other.

These flow rates bracket the range of flow that can be easily obtained using available circulating pumps. The unbalanced flow condition was analyzed to determine if the sensor head would "hot dog" as a result of side-to-side and top-to-bottom temperature gradients.

The steady-state temperatures associated with each of the above flow conditions are presented in Table IV. Table V presents a few of the most significant findings from the analyses including the coolant temperature rise through the FPSSS, the amount of heat rejected, and certain component temperatures. For a description of the nodes listed in these tables, refer to Table II.

The results indicate that the FPSSS TCS would do the job for which it was designed, i.e., cool the internal optics and laser, minimize thermal distortion in the sensor head, and prevent condensation from forming on the window. In actual practice, we found that the heater was not required to prevent condensation from forming on the window. However, the purge air was necessary to preclude ash deposition. We reran computations without the heater source, resulting in slight changes in the temperatures associated with the flow conditions shown in

FPSSS SENSOR HEAD NODAL LAYOUT

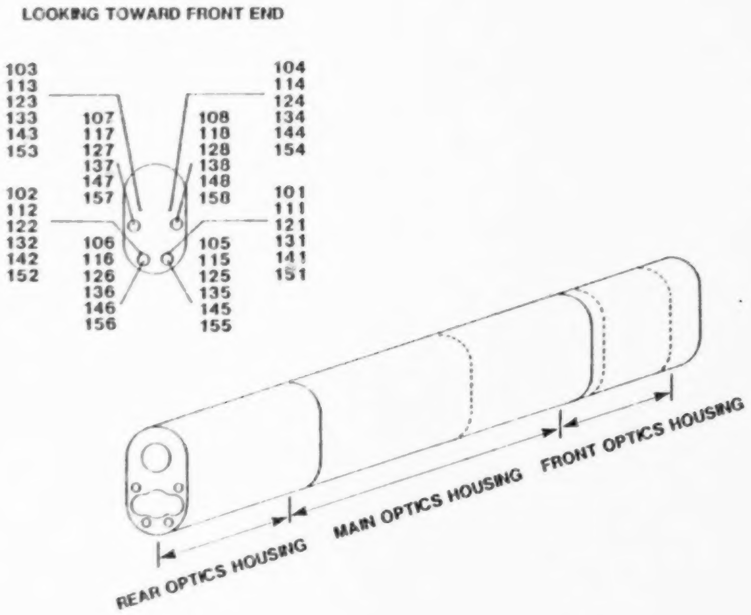

Figure 37a

NODAL DIAGRAM OF FPSSS COOLANT LOOP

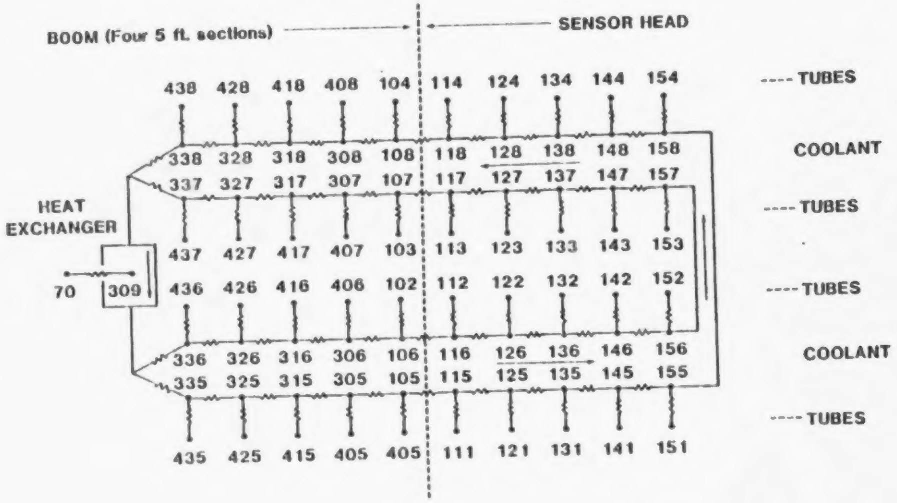

Figure 37b

TABLE II

FPSSS NODAL DESCRIPTIONS

NODE NO.	DESCRIPTION	MATERIAL	CAPACITANCE (BTU/°F)
11	PC Board	Composite	0.05
12	Reference Detector	Composite	0.001
21	Beamsplitter & Photo Detectors	Composite	0.001
22	Nikon Microscope Objective	Composite	0.016
23	Laser	Composite	0.375
31	Lens	Composite	0.038
32	Mirror Mount Insert	Al 6061	0.017
33	Mirror Mount	Al 6061	0.007
41	Window	Glass	0.01
42	Window Frame	Al 6061	0.01
43-44	Outer Mirror Standoffs		0.015 (ea)
45	Outer Mirror Mount	SS 304	0.017
46	Outer Mirror	SS 303	
50	Window Heater	---	---
70	Ambient Air	---	---
99	Stack Gas	---	---
101-104	Rear Optics Housing	Al 6061	0.027(ea) lower/ 0.045(ea) upper
105-108	Coolant in Rear Optics Hsg.	Water	0.007 (ea)
111-114	Main Optics Housing, Rear Half	Al 6061	0.046(ea) lower/ 0.063(ea) upper
115-118	Coolant in Rear Half of Main Optic Hsg.	Water	0.008 (ea)
121-124	Main Optics Housing, Front Half	Al 6061	0.035(ea) lower/ 0.059(ea) upper
125-128	Coolant in Front Half of Main Optics Hsg.	Water	0.006 (ea)
131-134	Front Optics Housing, Rear Section	Al 6061	0.003(ea) lower/ 0.010(ea) upper
135-138	Coolant in Rear Section of Front Optics Hsg.	Water	0.003 (ea)

TABLE II (continued)

NODE NO.	DESCRIPTION	MATERIAL	CAPACITANCE (BTU/°F)
141-144	Front Optics Housing, Center Section	Al 6061	0.010(ea) lower/ 0.045(ea) upper
145-148	Coolant in Center Section of Front Optics Hsg.	Water	0.003 (ea)
151-154	Front Optics Housing, Front Section	Al 6061	0.003(ea) lower/ 0.017(ea) upper
155-158	Coolant in Front Section of Front Optics Hsg.	Water	0.001 (ea)
201	Optics Housing Cover, Rear End	SS 304	0.009
202	Optics Housing Cover, Cylindrical Section	SS 304	0.02
203	Optics Housing Cover, Front End	SS 304	0.009
301	Extension Adapter & Coupling	SS 303	0.02
302	Boom Jacket	SS 321	0.02
305-308	Coolant in Boom Section Nearest Optics Hsg.	Water	0.235 (ea)
309	Heat Exchanger in 5/8 Coolant Loop	Water	1.080*
310	Heat Exchanger in 6/7 Coolant Loop	Water	1.080*
315-318	Coolant in Boom (Midsection)	Water	0.235 (ea)
325-328	Coolant in Boom (Midsection)	Water	0.235 (ea)
335-338	Coolant in Boom Section Nearest Heat Exchanger	Water	0.235 (ea)
405-408	Boom Tube Section Nearest Optics Hsg.	SS 321	1.065 (ea)
415-418	Boom Tube (Midsection)	SS 321	1.065 (ea)
425-428	Boom Tube (Midsection)	SS 321	1.065 (ea)
435-438	Boom Tube Section Nearest Heat Exchanger	SS 321	1.065 (ea)

*Combined into a single heat exchanger (Node No. 309) in final analyses

TABLE III

FPSSS RADIATION CONDUCTANCES

NODE		B(N.M)	NODE		B(N.M)	NODE		B(N.M)	NODE		B(N.M)
N	M	FT**2	N	M	FT**2	N	M	FT**2	N	M	FT**2
11	101	0.130E-01	11	102	0.130E-01	11	103	0.130E-01	11	104	0.130E-01
23	12	0.300E-02	23	103	0.800E-02	23	104	0.800E-02	0	0	0.000E-00
23	113	0.210E-01	23	114	0.210E-01	23	123	0.120E-01	23	124	0.120E-01
41	50	0.850E-02	42	50	0.660E-00						

TABLE IV

FPSSS TEMPERATURES FOR BALANCED 1 GPM FLOW

NODE NO.	TEMP (°F)	NODE NO.	TEMP (°F)	NODE NO.	TEMP (°F)	NODE NO.	TEMP (°F)	NODE NO.	TEMP (°F)
11	175.867	12	131.568	21	130.047	22	130.047	23	148.201
31	129.810	32	130.601	33	161.052	41	529.505	42	540.253
43	460.971	44	460.971	45	479.584	46	479.804	50	543.823
101	129.624	102	129.624	103	131.200	104	131.200	105	128.322
106	128.322	107	129.168	108	129.168	111	129.553	112	129.553
113	130.541	114	130.541	116	128.481	116	128.441	117	128.992
118	128.992	121	129.501	122	129.501	123	130.278	124	130.278
125	128.541	126	128.541	127	128.850	128	128.850	131	128.922
132	128.922	133	129.606	134	129.605	135	128.589	136	128.589
137	128.771	138	128.771	141	129.469	142	129.469	143	130.151
144	130.151	145	128.616	146	128.615	147	128.722	148	128.722
151	130.010	152	130.010	153	131.052	154	131.052	155	128.644
156	128.644	157	128.673	158	128.673	201	459.438	202	449.726
203	475.986	301	248.644	302	463.298	305	127.986	306	127.986
307	129.537	308	129.537	309	128.751	315	127.434	316	127.434
317	130.085	318	130.085	325	126.882	326	126.882	327	130.632
328	130.632	335	126.328	336	126.328	337	131.179	338	131.179
405	128.368	406	128.367	407	129.917	408	129.917	415	127.817
416	127.817	417	130.468	418	130.485	425	127.265	426	127.265
427	131.011	428	131.000	435	126.712	436	126.712	437	131.557
438	131.557								

TABLE IV (continued)

FPSSS TEMPERATURES FOR BALANCED 2 GPM FLOW

NODE NO.	TEMP (^{0}F)	NODE NO.	TEMP (^{0}F)	NODE NO.	TEMP (^{0}F)	NODE NO.	TEMP (^{0}F)	NODE NO.	TEMP (^{0}F)
11	160.905	12	104.325	21	113.275	22	113.275	23	131.300
31	113.154	32	113.696	33	114.038	41	529.215	42	539.893
43	459.952	44	459.952	45	479.467	46	479.697	50	543.468
101	112.983	102	112.987	103	113.981	104	113.981	105	112.388
106	112.388	107	112.828	108	112.828	111	112.953	112	112.953
113	113.597	114	113.597	115	112.483	116	112.443	117	112.729
118	112.729	121	112.988	122	112.986	123	113.450	124	113.450
125	112.489	126	112.489	127	112.689	128	112.649	131	112.639
132	112.639	133	112.959	134	112.855	135	112.512	136	112.512
137	112.608	138	112.608	141	112.954	142	112.954	143	113.355
144	113.355	145	112.528	146	112.524	147	112.583	148	112.583
151	113.271	152	113.278	153	114.039	154	114.039	155	112.539
156	112.539	157	112.556	158	112.556	201	458.351	202	448.182
203	474.970	301	237.198	302	462.433	305	112.217	306	112.217
307	113.025	308	113.025	309	112.618	315	111.929	316	111.929
317	113.312	318	113.312	325	111.641	326	111.641	327	113.598
328	113.598	333	111.353	336	111.353	337	113.885	338	113.885
405	112.417	406	112.417	407	113.224	408	113.224	415	112.129
416	112.129	417	113.511	418	113.511	425	111.841	426	111.841
427	113.797	428	113.797	435	111.553	436	111.553	437	114.083
438	114.083								

TABLE IV (continued)

FPSSS TEMPERATURES FOR UNBALANCED 1 & 2 GPM FLOW

NODE NO.	TEMP (⁰F)	NODE NO.	TEMP (⁰F)	NODE NO.	TEMP (⁰F)	NODE NO.	TEMP (⁰F)	NODE NO.	TEMP (⁰F)
11	166.206	12	120.460	21	119.176	22	119.176	23	137.271
31	119.000	32	119.637	33	120.033	41	529.317	42	540.020
43	460.283	44	460.338	45	479.508	46	479.735	50	543.594
101	119.455	102	118.278	103	119.450	104	120.765	105	118.603
106	117.467	107	118.079	108	119.124	111	119.163	112	118.374
113	119.032	114	120.136	116	118.669	116	117.548	117	117.954
118	118.987	121	119.113	122	118.364	123	118.925	124	119.805
125	118.712	126	117.623	127	117.851	128	118.888	131	118.909
132	117.845	133	118.349	134	119.289	135	118.733	136	117.659
137	117.794	138	118.841	141	119.217	142	118.303	143	118.898
144	119.583	145	118.747	146	117.677	147	117.757	148	118.816
151	119.815	152	118.586	153	119.572	154	120.495	155	118.765
156	117.697	157	117.718	158	118.786	201	458.737	202	448.726
203	475.329	301	241.265	302	462.741	305	118.280	306	117.287
307	118.279	308	119.482	309	118.144	315	117.714	316	117.004
317	118.562	318	120.046	325	117.146	326	116.719	327	118.845
328	120.609	335	116.577	336	116.435	337	119.127	338	121.171
405	118.673	406	117.484	407	118.476	408	119.873	415	118.107
416	117.201	417	118.759	418	120.463	425	117.540	426	116.917
427	119.041	428	120.999	435	116.972	436	116.633	437	119.323
438	121.560								

TABLE V

FPSSS THERMAL ANALYSIS RESULTS
(250°C Stack Gas/35°C Ambient Air)

Flow Condition	Heat Rejected (BTU/HR)	Coolant Loop Temperature Rise(°F)		Component Temperatures (°F)				
				PC Board	Laser	Window	Sensor Head	
		5/8 Loop	6/7 Loop	w/2 Watts	2/15 Watts	2/15-Watt HTR	Side/Side ΔT_{MAX}	TOP/BTM ΔT_{MAX}
Balanced 2 GPM Flow	2718	2.8	2.8	161	131	529	0	1.0
Balanced 1 GPM Flow	2603	5.4	5.4	176	148	530	0	1.6
Unbalanced 1 & 2 GPM Flow	2678	5.2	3.0	166	137	529	1.3	1.3

Table IV but no noticeable change in the parameters of Table V. Also, the model was run for an elevated 500°C temperature. The result was predictable: near doubling of the thermal loading and temperature elevations for the nodes listed.

The above information can be used to adequately specify the TCS requirements, but it does not solve the problem of alignment. Rather, it simply provides the inputs necessary to compute thermally induced alignment error. To test these results an instrument "brassboard" was constructed from which computed distortions (using temperature data) could be set and the misalignment measured.

The brassboard optical system (shown in Figure 38) used an F/1.8 55 mm objective lens operating at approximately 3X magnification. The secondary objective operates at 6.7X, providing total magnification of 20X. The probe optical system was laid out on a flat aluminum plate with adjustable mounts provided on critical optical elements. These adjustments were not used in the final design; they were provided in order to verify our calculations of alignment sensitivity to certain distortions or displacements due to thermal changes in the structure supporting the optical elements. For instance, axial displacement of the condensing mirror will laterally displace the condensed laser beam at the object plane. Obviously, the laser beam must be of sufficient width to allow for such displacements. By theoretical considerations one finds that the error is:

$$\text{Beam Displacement} = R_m \left[\text{Sin}\left(1/2\ \theta - \theta_r\right) - \text{Sin}\ 1/2 . \theta\right]$$

where R_m = mirror radius and $\theta_r = \text{Sin}^{-1} \dfrac{[\text{Sin}\ 1/2\ \theta \times (\text{Axial Displacement}]}{R_m}$

For an axial displacement of 1 mm and $\theta = 30°$, the error is 0.19 mm or 190 microns. The brassboard actually revealed a much lower sensitivity of 22 microns of lateral displacement for each millimeter of axial mirror displacement. Of course, the angle (θ) on the brassboard is less than 10°. An axial displacement of 1 mm would only occur if the head were constructed of aluminum and heated to 500°C. At 250°C the error is only 11 microns which is quite small but for which our design must account.

The displacements and distortions at all other optical mount points were also measured. The x-y adjustments of the laser produce lateral displacement errors of approximately 2.36 and 2.71 mm/mm, respectively. Although this is a more sensitive region to misalignment it is not affected by thermal changes, and, in any case, the laser was intended to be in the thermostated probe region.

Reproduced from
best available copy.

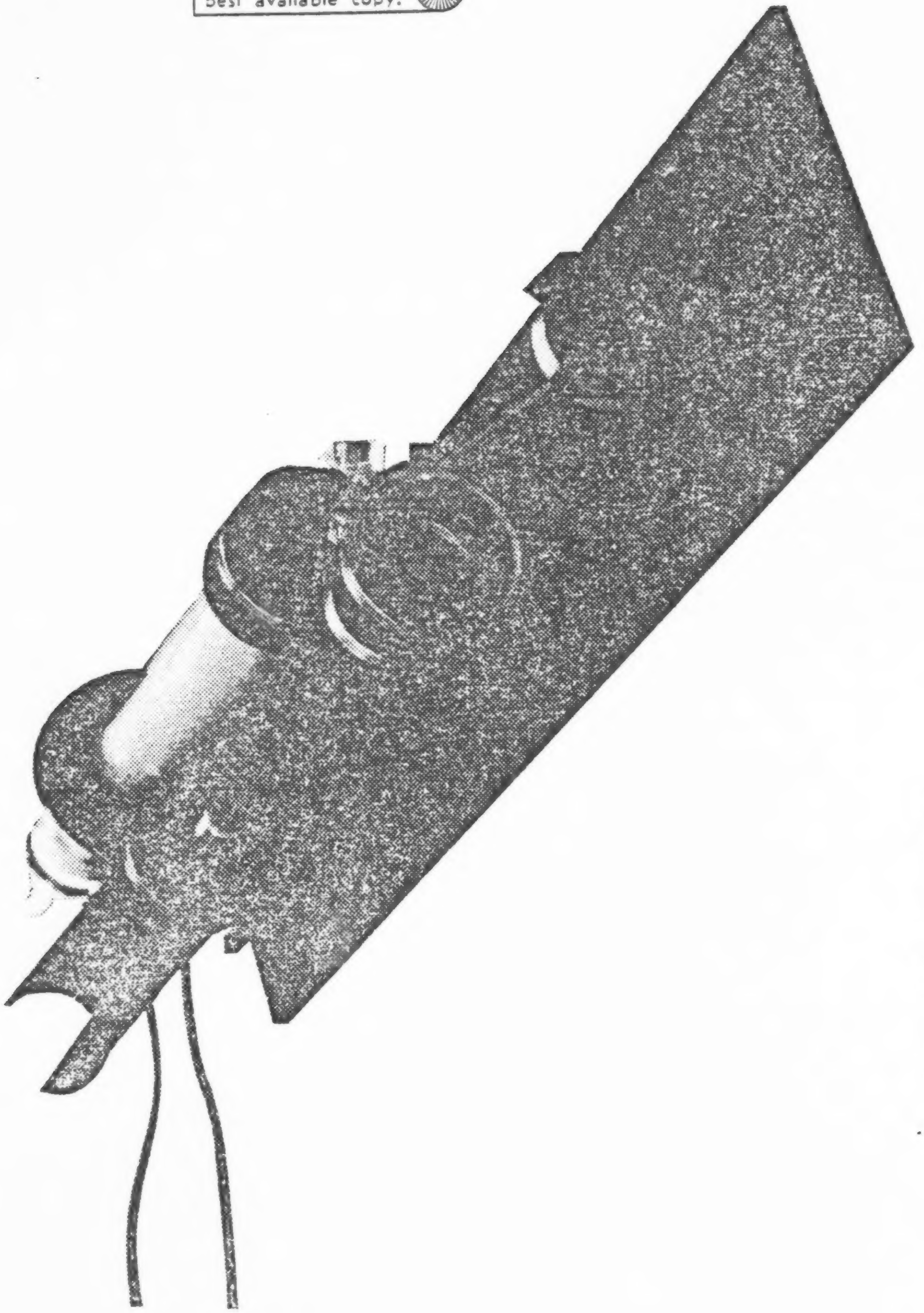

Figure 38. Brassboard

The external mirror is the critical optical element since it is exposed to full thermal extremes.

6. EXPANDED DESCRIPTION OF FPSSS SYSTEMS

Our primary purpose in giving an overview of the FPSSS at the outset of this report (see Section 3) was to offer the reader an early understanding of the instrument to prepare him for the sections dealing with theoretical optical and thermal modeling. These sections are more readily understood with the FPSSS firmly in mind. In this section we discuss certain systems within the FPSSS in detail, emphasizing the theory and functioning of the probe optics and electronics as well as the DAS architecture and computational software. First, a detailed description of the electro-optical operation of the FPSSS probe optics.

6.1 The FPSSS Electro-Optical System

In a device with the anticipated performance of the FPSSS, a laser is a required light source. It provides the greatest amount of diffraction-limited, usable light energy expressed in both focusing capability and effective collimation of all output energy. A He-Ne laser was the most practical, but the questions of size and model configuration hinged on other requirements besides practicality.

As a result of theoretical scattering arguments (given in Section 3), we desired to collect as close to the axis as possible in order to develop scattering responses which would not be sensitive to refractive index changes. The results of Section 4 showed that an inner collecting angle of 2° was adequate. This inner collecting angle automatically specifies the permissible divergence of the laser beam. The sample volume itself requires that the laser beam be about 100 μm in dimension, a size requiring focusing since no laser produces a beam that small on exit. For a TEM_{oo} mode laser the focused spot size is given approximately as $f\lambda/D$, where f is the focal distance of the element used, λ the wavelength, and D the beam diameter at the focusing element. With a typical laser beam of 1 mm dia. and $\lambda = 0.6328$ μm, a focal distance of 150 mm is required to generate a beam of 100 μm dimension. This, of course, is an impractically large distance over which to maintain alignment. To reduce the focal distance one generally must first expand the beam diameter with condensing optics before focusing with a shorter focal length element. The TEM_{oo} mode would allow for collection down to a few tenths of a degree in the FPSSS with an illuminated sample volume 100 μm wide. However, we previously showed that there was no need for such a small inner collecting angle. This fundamentally allows one to consider multimode lasers that have higher rates of convergence or divergence. Multimode lasers also have much higher powers, and, if of high order, a fairly flat energy density profile. The governing equation for the focused spot size for multimode lasers is $Cf\lambda/D$, where C is a constant which is closely approximated by the degree of mode degeneracy ±1. For a fourth-order degeneracy and a beam width of 1.5 mm (multimode lasers intrinsically have larger beams), a focused beam of less than 100 µm requires a focal distance of one third that for the TEM_{00} case. This type of multimode laser typically generates 2.5 times the power of its TEM_{00} counterpart. It has the same input power for the same length of discharge.

Thus, we selected a high-order multimode laser for the FPSSS. It gives a greater amount of power than others over the same sample volume without condensing optics. The optical system briefly described in Section 3.1 indicated an output power of 5 mW. The device selected was a Coherent Radiation Model 5 T. This tube has an aluminum jacket extrusion (which also serves as its cathode), affording good thermal contact for heat dissipation. The laser output is steered to a 75 mm focusing (condensing) mirror by the use of a pair of plane mirrors (see Figure 4). Because the plane mirrors are buried in the probe head thermostat, their alignment is not subject to thermal effects. The condensing mirror focuses the directed laser beam down to approximately 100 µm at its 37.5 mm focal point; it is the only element with power that is exposed to the ambient high temperatures. The window is also exposed to high temperatures but it is a plano-plano element. It is fitted with a beam dump spot or inner optical stop on the optical axis which dissipates the laser beam.

The light collecting optics include a primary objective of 50 mm f.l., operating at a magnification of 2X, and a secondary microscope objective operating at 10X. The F/1.8 lens operating at these conjugates provides a maximum aperture to permit an outer collecting scattering angle of 11°. Its performance is quite good on axis although it has noticeable distortion in wide field applications. Because our interest was in objects ±50 µm from the optical axis it proved more than adequate. The secondary objective is a standard 20X Nikon microscope objective. Reducing its magnification by a factor of 2 results in almost no change in its important primary conjugate (front object distance) and thus near optimum performance. Its back focal distance includes a 50 mm air path and a 7 mm glass path through a beam splitter. The beam splitter has a 2:1 split of reflected and transmitted light.

The optical signals from particle images are simultaneously produced on the two exit faces of the beam splitter and are analyzed and compared in magnitude by the probe electronics after they are detected by photodiodes and amplified by pre-amps housed in the probe head. The method by which these signals can be processed to extract both size and positional information is a subject of considerable interest and requires detailed explanation. Before elaborating on this technique we should mention that all optical surfaces have coatings to enhance optical performance. The mirrors have dielectric coatings delivering better than 99% reflectivity. The window and beam splitter faces have dielectric anti-reflection (AR) coatings with less than 1% loss. The photodiodes have a dielectric AR coating on their windows as well as their substrates, effecting less than 3% total loss. The objectives have broadband AR coatings and lose 15% each. Therefore, they account for nearly all of the approximately 35% loss in the entire optical system.

The collecting optics essentially comprise a high resolution (although low magnification) imaging system. It is a dark field situation; the particle images resemble a moving star field. The beam splitter is aligned such that all observed particle trajectories cross the photodiodes. Each photodiodes' active area is 2500 μm in diameter so all particles at the object plane and in the laser beem are observable (100 μm at 20X = 2000 μm). However, the photodiode observing the reflected image from the beam splitter is obscured along its diameter by a mask 0.78 mm wide. Thus, a particle passing through the center of the laser beam (and thus its image behind the mask) is only observed by the photodetector with the clear aperture. This photodetector is used to provide particle size information. The masked photodetector only receives signals for particles off axis laterally but in focus when displaced axially, or from large unfocused images that spill out behind the narrow mask. A sample volume of prescribed dimension can be established by comparing the signals from the pair of photodetectors and defining accept/reject criteria. Typically, we have required unmasked to masked signal ratios of 4:1 for acceptance. The sample volume is a direct function of this acceptance signal ratio. To derive the acceptance signal ratio we actually provide a higher optical (through beam splitter reflectance) or electronic gain to the masked detector and then compare for equality of amplitude and refer to a gain ratio rather than signal ratio. The following discussion further details the actual situation in the FPSSS.

The relative size of the FPSSS sample volume cross section with respect to the laser beam is depicted in Figure 39. The sample volume includes only the region near the center of the laser beam. The sample volume cross section is noticeably diamond shaped. The diamond shaped sample cross section results from the accept/reject criteria used in comparing signals at the masked and unmasked detectors. The center of this diamond cross section concides with the object plane of the collecting optics. The points of this diamond cross section define the limiting depth-of-field of the FPSSS. Both the width of the cross section and the depth-of-field vary inversely with the magnification used in the collecting optics.

Shown in Figure 40 are the size and positions of images formed by particles at various positions in the illuminated volume. It is important to understand that for small particles (essentially point objects) the image size is only a function of its axial displacement from the object plane.* The image size is linearly related to the numerical aperture of the collecting optics and is given approximately by:

Image size = N.A. x displacement from object plane.

It is apparent that only images that are near the object plane and the center of the sample volume form images with light concentrated on the opaque mask, as illustrated in Figure 40. Thus, such images transmit little signals through the masked aperture. Particles whose pulse amplitudes, as seen by the masked aperture detector, are greater than those seen by the signal aperture detector are rejected. This defines the diamond shaped sample cross section and image re-

---

*Larger particles will generate image sizes that are size-dependent. At a 2X gain ratio there is never any sample volume size dependency. At higher gain ratios there is a real effect but it is not as large as what one might first suppose because of the localization of the light scattering energy in the center of the images of large particles.

RELATIVE SIZE AND POSITION OF SAMPLE VOLUME CROSS SECTION

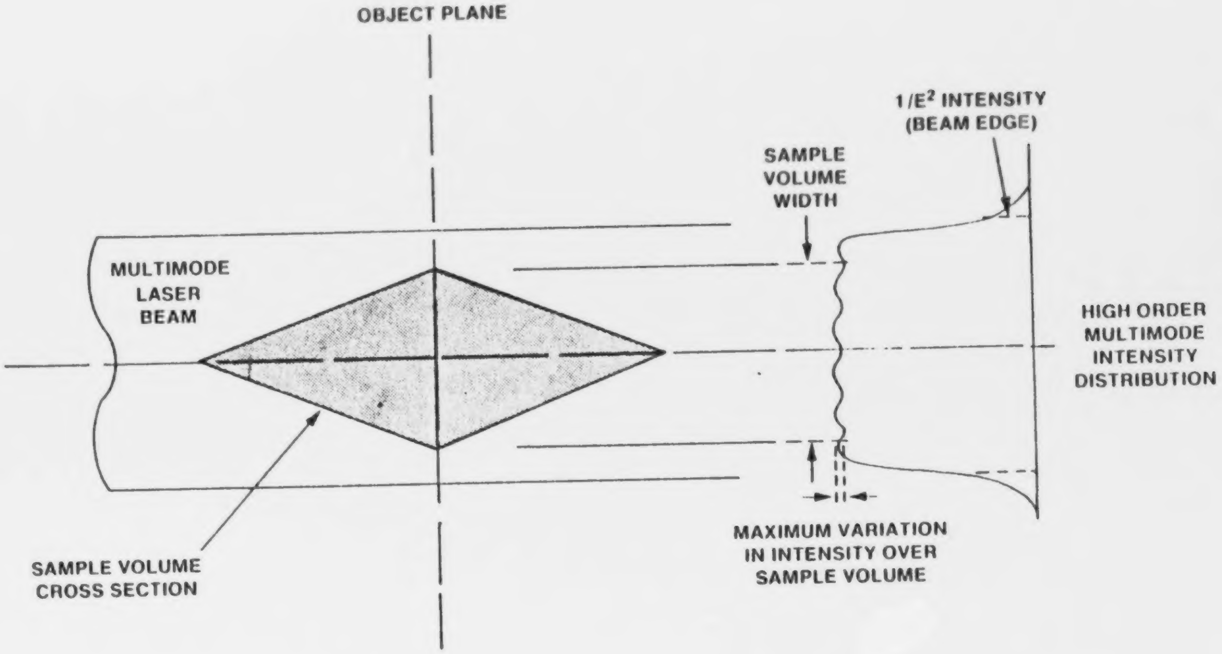
OBJECT PLANE
1/E^2 INTENSITY (BEAM EDGE)
SAMPLE VOLUME WIDTH
MULTIMODE LASER BEAM
HIGH ORDER MULTIMODE INTENSITY DISTRIBUTION
SAMPLE VOLUME CROSS SECTION
MAXIMUM VARIATION IN INTENSITY OVER SAMPLE VOLUME

Figure 39. In the FPSSS, the beam width at the object plane is approximately 100 microns wide.

IMAGE SIZES AND POSITIONS ON MASKED APERTURE DETECTOR

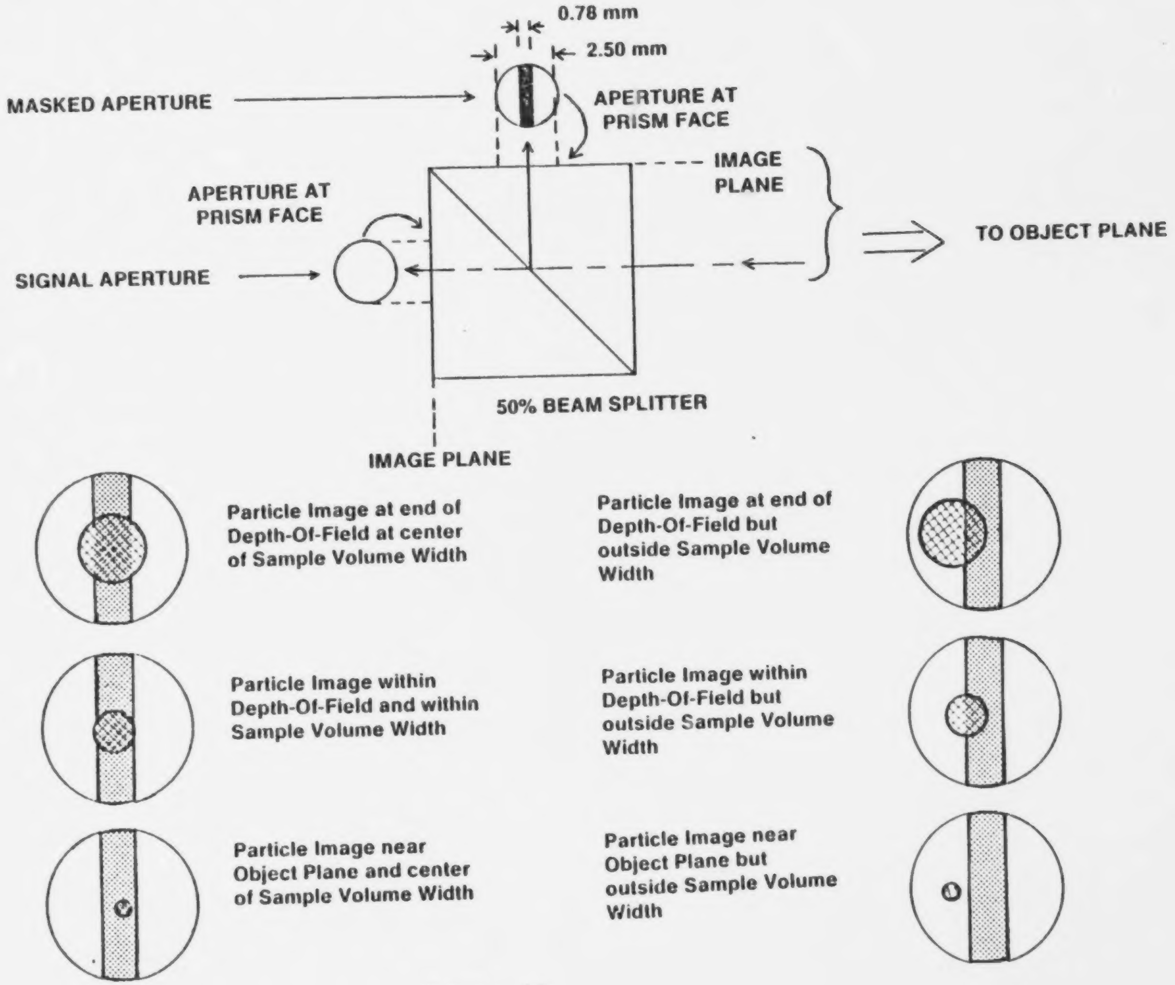

Particle Image at end of Depth-Of-Field at center of Sample Volume Width

Particle Image at end of Depth-Of-Field but outside Sample Volume Width

Particle Image within Depth-Of-Field and within Sample Volume Width

Particle Image within Depth-Of-Field but outside Sample Volume Width

Particle Image near Object Plane and center of Sample Volume Width

Particle Image near Object Plane but outside Sample Volume Width

Figure 40

lationship shown in Figure 41. We use a gain ratio of masked aperture detector to signal aperture detector of 4X for the best noise immunity. The sample cross section area is the product of the sample volume width and one-half the depth-of-field.

One final aspect of the sample volume needs explanation. As we have defined it, the sample volume is only the region of accepted measurements. The total view volume includes a much larger volume where both accepted and rejected particles are viewed. This view volume is as much as ten times larger than the sample volume and must be used for coincidence error estimates. The ratio of sample volume to view volume is a function of the inner numerical aperture (N.A.) of the collecting solid angle (2°, N.A. - 0.03). This presents an obvious trade-off between a design to collect very strong forward scattering and one that optimizes measurements at the highest number densities.

Because of the near proximity of the laser beam and the inner collecting angle, we had to map the total view volume experimentally. In general, the view volume is $\sim 5 \times 10^{-6}$ cm^3. It is this volume that establishes coincidence probability but not coincidence error. Coincidence errors in such a system are dominated by particles within the view volume but not the sample volume. Because of the large 4X gain ratio, any time one of the particles of a coincident pair is outside the sample volume the pair is most likely rejected. The only time it would not be rejected is when the particle in the sample volume is large enough to generate more than four times as much signal; in such a case it would be better to accept the measurement since the error would be negligible in size (typically less than 10% since scattering signal is proportional to N^2 to N^3). In this type of system coincidence generally results in a loss in counted particles but negligible sizing error. The coincidence loss is corrected for by monitoring the total activity of the probe electronics (activity is the percentage of time pulses that are present and reflects and effective duty cycle).

6.2 Electronic Subsystems

With the exception of the photodetector module, all of the FPSSS electronics are contained within the electronics console. A block diagram of the electronics console is shown in Figure 42. For a detailed description of actual circuit operation the reader is referred to the FPSSS manual. For descriptive purposes

IMAGE SIZE AS A FUNCTION OF SAMPLE VOLUME POSITION FOR THE CASE OF 4X GAIN RATIO OF MASKED-TO-SIGNAL APERTURE

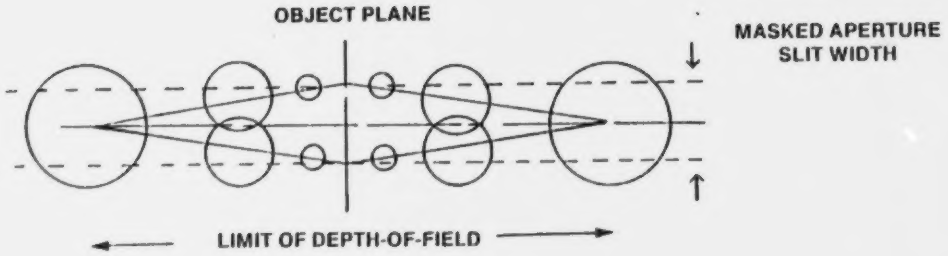

Figure 41

FPSSS ELECTRONICS CONSOLE BLOCK DIAGRAM

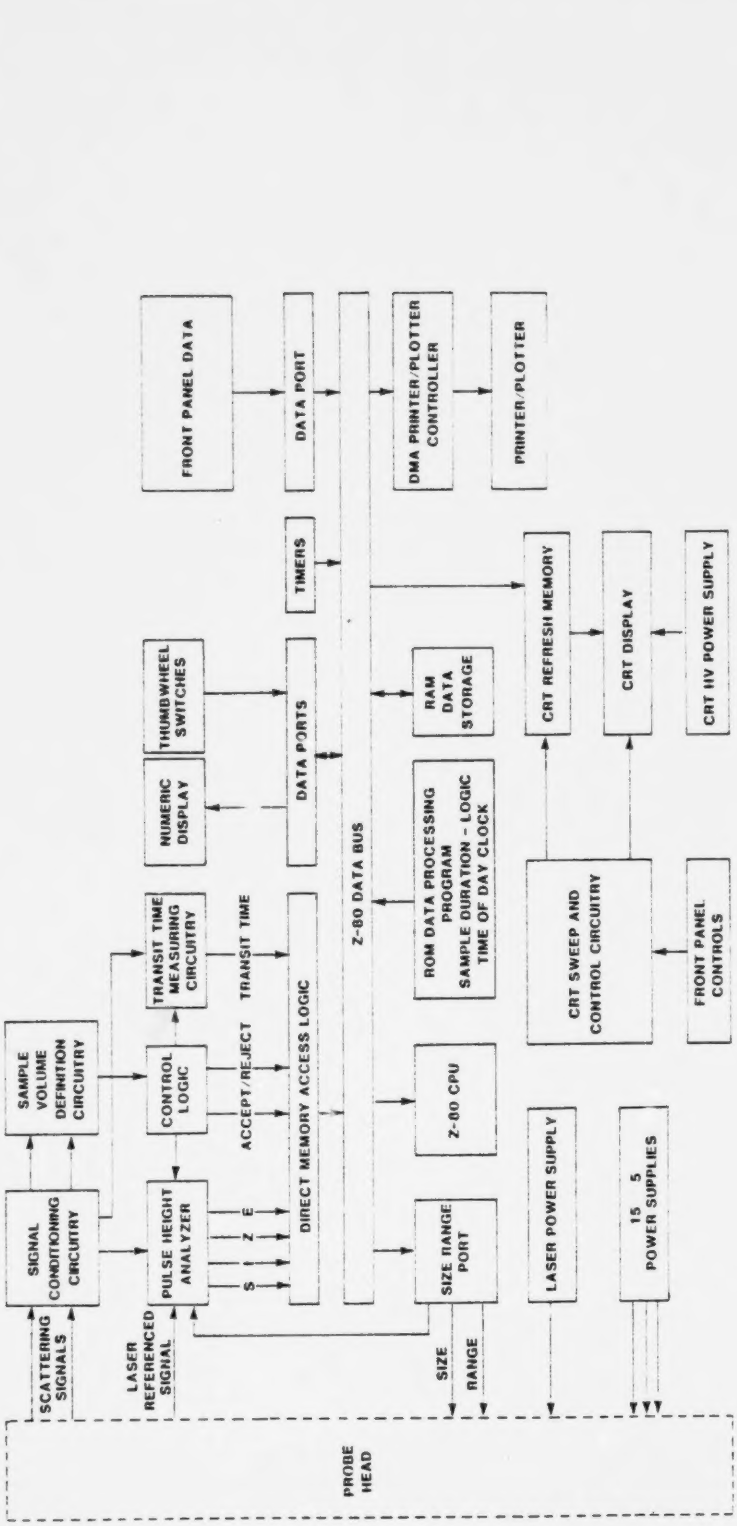

Figure 42

here, we can only give a walk-through of signal processing and systems architecture.

The scattering photodetectors and pre-amplifiers are housed on a single photodetector module circuit board inside the FPSSS probe head. A separate photodiode with pre-amplifier attaches to the rear of the laser as a reference. A block diagram of the "probe" electronics is shown in Figure 43a. The photodetector module is identified by the dashed section.

The three-stage amplifier sections have a minimum bandwidth of 300 KHz. The second stage is a programmable amplifier used to gain-switch between size ranges. The two diodes with their pre-amps provide the signals that make the FPSSS capable of distinguishing whether a particle is within the proper sample volume and rejecting particles that are not. The reference detector provides a reference signal proportional to the power output of the laser. Changes in laser output are thus cancelled when the signal is applied as the reference input to the pulse height analyzer.

The remainder of the FPSSS electronics is contained in the electronics console. The two signal pulse streams are first properly leveled with baseline restoration and DC offset circuitry. Dual peak readers then momentarily store the pulse heights from both the signal and the masked aperture detectors. The peak readers are used to provide inputs to a comparator (sample volume validation comparator) to determine which of the two pulse heights from the pre-amps is the greatest. This measurement determines when particles are in the accepted sample volume.

A pulse height analyzer sizes the signal pulses of all particles passing through the beam. The pulse height analyzer has a set of 16 voltage comparators and latches. The reference voltage to the comparators provided by the reference detector is divided by resistive dividers. A separate group of resistive dividers is associated with each size range. Because its reference voltage is derived from the source of illumination, the entire system has an effective automatic gain control (AGC). The output of the pulse height analyzer is encoded in 4 binary weighted address lines that access memory via DMA (see Figure 43a).

A separate set of voltage windows selects pulses of a narrow range of amplitudes within the transit time analyzer. These same pulses are also delayed

FPSSS PROBE ELECTRONICS BLOCK DIAGRAM

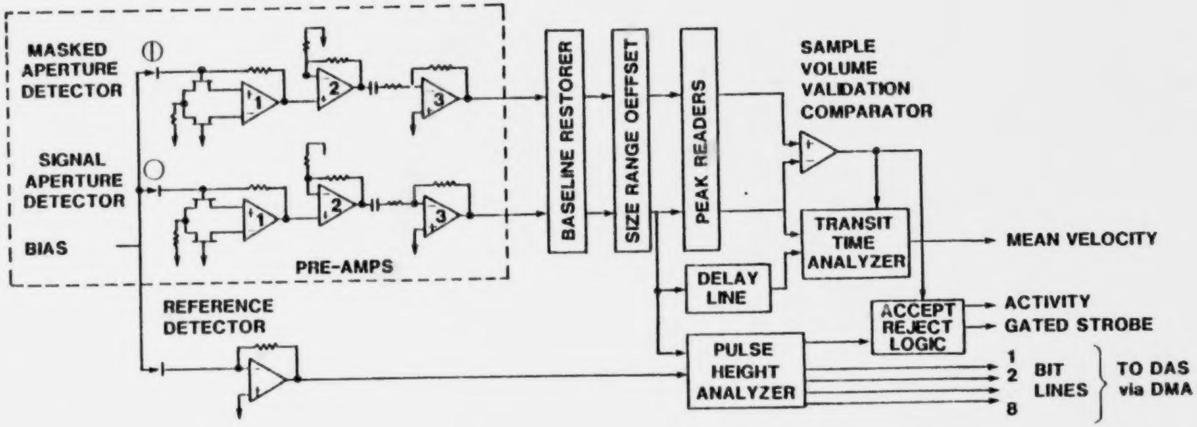

Figure 43a

through a delay line. The transit time analyzer measures the half-width of the delayed pulses that are found to be in the sample volume. The transit times are averaged over a great number of particles to provide a true statistical velocity average. (Note that velocity is actually the reciprocal of transit time.)

The control (accept/reject) logic provides the proper delay between an event and the strobe and reset pulses. This logic also provides gating for valid and invalid strobes. Circuitry within this section also computes the percentage of time that the pulse processing electronics are busy. This activity signal (A) is directly related to the coincidence loss correction as follows:

$$N_T = N_{meas.} \cdot \frac{1}{1-.006A} ,$$

where N_T is total number and $N_{meas.}$ is the measured number. Activity, in percent, is in the form of a 0-100 Hz frequency.

The pulse height analyzer is configured to provide four size ranges of 15 channels each, as follows:

Range 1	0.4 - 1.15 µm (0.05 µm intervals)
Range 2	1.15 - 5.65 µm (0.3 µm intervals)
Range 3	0.5 - 2.0 µm (0.1 µm intervals)
Range 4	2.0 - 11.0 µm (0.6 µm intervals)

All size intervals are linear; the maximum resolution in range 3 is 0.03 µm. As mentioned in Section 3, ordinarily ranges 1 and 2 or 3 and 4 are paired for routine data gathering. The ability to switch ranges has been found to be particularly important in field measurements. As previously noted, if you had unlimited size sensitivity and a wide dynamic range (e.g., that produced by logarithmic amplifiers) you would inevitably find a small enough size to saturate the instrument through coincidence error. The ability to range-switch with desired levels of minimum size sensitivity provides a method of approaching conditions limited by coincidence error without jeopardizing measurements at larger sizes which in themselves would present no coincidence error problems. Logarithmic amplifiers also pose other difficulties compared to range-switching linear amplifiers. The primary difficulty in the FPSSS arises from the necessity for excellent matching of the two signal trains. Due to lack of control over the necessary amplifier parameters as well as variable baselines (caused by changes in background light levels at each photodetector), logarithmic amplification suffers further.

The maximum particle number density that can be measured by the probe electronics depends to a certain degree on the size distribution and the particular size range in question. Although the electronics do not process particle sizes smaller than the lower limit of the size range in use, they do process particles that are larger than the upper limit. Thus, it is possible to have a fairly low apparent number density on a certain size range yet very high activity. Correction through the relationship given allows retrieval of the proper number density. For the typical measurement environment presented by stack work, the FPSSS can perform at number densities above 2×10^4 cm^{-3}. We observed measured number densities as high as 5×10^4 cm^{-3} in field testing at precipitator inlets (see Section 8).

The electronic circuits involved in the FPSSS size measurements are conservatively designed. Components within the probe head are MIL STD parts and the remainder are largely commercial grade. Circuit stability involving such parameters as amplifier offsets, voltage dividers, and bias levels generally exceeds requirements. The limitations on sizing performance are essentially determined by the optics and laser light source. The mode stability of the laser probably limits overall sizing accuracy and sample volume definition to 90-95% (5-10% error).

The FPSSS data processor is a Z-80 based microcomputer. Up to 16K bytes of ROM and 4K bytes of RAM are available. All I/O except for DMA activity (probe and printer) is implemented with Z-80 PIO circuits. The time-of-day clock and other timing functions are implemented with a Z-80 counter-timer chip, or CTC. Particle accumulations and plotting-printing raster drive are implemented with a single DMA circuit. Activity is started by generating an interrupt with each positive transition of the activity line and driving internal counters. The CRT is refreshed from a separate 256 X 8 bit dual port memory; this memory appears as write-only memory in parallel with a 256 byte segment of RAM. The DAS is shown expanded in Figure 43B.

Figures 43a and 43b show the logical interface between "probe" circuitry and "data processing" circuity. Two lines from the processor define the

FPSSS DATA ACQUISITION SYSTEM BLOCK DIAGRAM

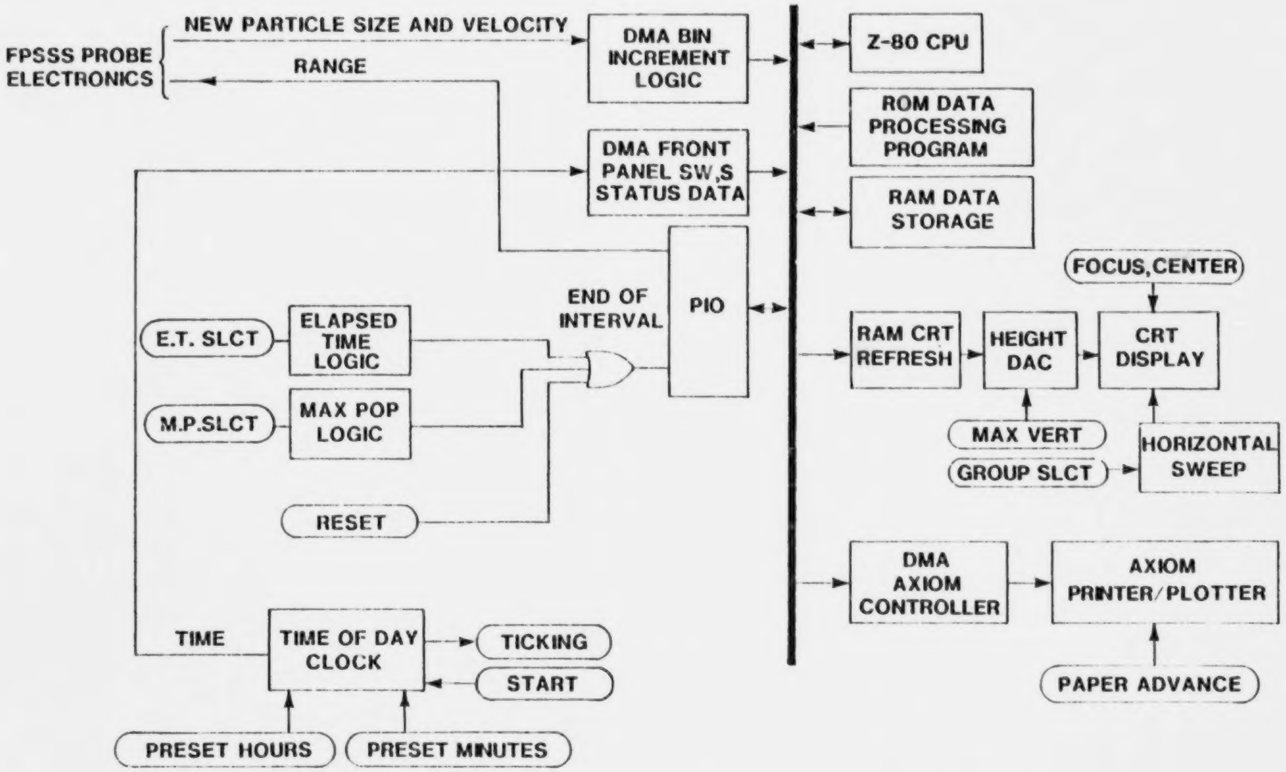

Figure 43b

range in use. Four lines and a strobe mark the detection of a valid particle and the bin into which its size falls. The 0-100 Hz activity line encodes 0-100% activity. A single status signal, WARNING, is asserted whenever the laser power output goes below a certain level. Finally, 9 lines encode the average particle velocity; the processor asserts an inhibit signal to prevent the probe from changing the velocity lines while they are being read.

The firmware resides in 8 integrated circuits which are 2K X 8 bit UV erasable field-programmable, read-only memories.* (Consecutive memory chips represent consecutive ascending segments of address space.) RAM is implemented with 4K X 1 bit dynamic devices. The Z-80's built-in refresh feature is used to refresh the RAM.

Z-80 code is written entirely in Z-80 assembly language. The program is currently written in 14 relocatable segments and linked with a relocatable loader to form a contiguous memory image. A MOSTEK SDB-80 with extended memory is required to assemble and link the program. In addition, the program makes heavy use of a floating point package that resides in a fixed area of memory.

When the FPSSS is powered up, an RC circuit on the CPU reset line causes it to be asserted for about 0.2 second. When it terminates, the CPU begins executing instructions at memory location 0. The reset also causes initialization of various other latches in the hardware. The program executes an initialization of various other latches in the hardware. The program executes an initialization phase. Memory is cleared, PIO operating modes established, and the default parameter set (a set of operating conditions and output programs initiated if not set before sampling is begun) is installed in RAM. The main loop consists of two phases: acquiring data and printing data just acquired. There is a "repeat" mode that is a variation of this basic cycle. When repeating, the data just acquired are moved into one of seven auxiliary buffers. When all samples have been acquired, each data set is moved back into the primary data buffer to be printed.

When acquiring data, first in the odd range and then in the even, the program continually tests the elapsed time counters (interrupt driven), total population (DMA driven), and the operator pushbutton (interrupt driven) to see if the end of the range interval has expired. If so, the program moves to the print phase. The diagnostic modes are another variation on the basic cycle in which only one specified range is sampled (rather than a pair) and the print phase is skipped.

---

*The term "firmware" (as opposed to "software") is often used herein to illustrate memory involatility.

A switch allows one to temporarily suspend data accumulation. It is sampled in the clock interrupt service routine, which in turn sets a bit in a PIO that disables/enables DMA-driven particle accumulations. The same status bit also controls accumulation of elapsed time and activity counting.

The print phase begins by examining the most significant output program switch, which specifies one of sixteen output programs. The ABORT switch allows one to bypass or suspend printer-plotter operation. It is checked each time a print line is to be transferred to paper, and the transfer is skipped if the switch is set. If the ABORT switch is clear, the HOLD switch is checked; if set, the program waits until it clears, suspending printout. The output program switches are checked again when the print is complete; if they have changed, the print is repeated under the new switch setting. In addition, the ABORT switch is checked at the beginning and end of the print; if set at the beginning and clear at the end, the program is repeated.

The possible data sampling and output modes are too numerous to mention and are rather flexible. Some output programs take several minutes to print out. You can also process and print the same data set with more than one output program. Scale sensitivity can also be changed if initially inadequate. Most of these capabilities will be evident in the data samples presented in Sections 7 and 8.

6.3 Basic Data Processing Equations

This section provides an overview of the basic mathematical manipulations performed by the DAS electronics in the FPSSS. The FPSSS can size particles in four sets of size ranges numbered 1, 2, 3, and 4. Only one range can be in use at any one time. In a normal sampling operation, ranges 1 and 2 or 3 and 4 are automatically paired together giving "small" and "large" size ranges of 0.4-5.65 and 0.5-11.0 μm, respectively. The operator selects either "small" or "large" size range mode from the front panel, which evenly time shares the sampling time between the respective range pairs. Each range has 15 size classes or channels. Since two ranges are used alternatively, it is convenient to consider the probe as having 30 "bins". In the small mode, bins 1-15 correspond to range 1, channels 1-15; bins 17-31 correspond to range 2, channels 1-15.* In the large mode, bins 1-15 correspond to range 3, channels 1-15; bins 17-31 to range 4, channels 1-15. The bin is represented by the index "i".

Associated with each channel of each range, or each bin, is a minimum, mean, and maximum (optical) diameter of particles sized into that bin. Every channel of a given range has the same bin width or size interval. The maximum diameter of bin i is the same as the minimum diameter of bin i + 1. The mean diameter is the arithmetic average of the minimum and maximum diameters.

If DL_i represents the minimum, or lower, diameter of bin i, D_i represents the mean diameter of bin i, DU_i represents the maximum, or upper, diameter of bin i, and BW_i represents the bin width of bin i, then

$BW_{1-15} = 0.05$ µm
$BW_{17-31} = 0.3$ µm
$DL_1 = 0.4$ µm
$DU_{15} = 1.15$ µm
$DL_{17} = 1.15$ µm
$DU_{31} = 5.65$ µm

if in the small mode

and

$BW_{1-15} = 0.1$ µm
$BW_{17-31} = 0.6$ µm
$DL_1 = 0.5$ µm
$DU_{15} = 2.0$ µm
$DL_{17} = 2.0$ µm
$DU_{31} = 11.0$ µm

if in the large mode.

Particles are accumulated first in range 1 (or 3 if in the large mode) for a length of time, then in range 2 (or 4) for another (usually equal, possibly different) length of time.

---

*Bins 0 and 16 are reserved for time and housekeeping.

ET_{1-15} corresponds to the range 1 time interval
ET_{17-31} corresponds to the range 2 time interval } if in the small mode;

ET_{1-15} corresponds to the range 3 time interval
ET_{17-31} corresponds to the range 4 time interval } if in the large mode.

N_i = number of particles accumulated in bin i during the interval of elapsed time ET_i.

The probe has a fixed sample area, SA, which is normal to the direction of particle flow. The particles have a velocity, V, with respect to the probe. Therefore, each range accumulation interval has an associated sample volume.

$$SV_i = ET_i \cdot SA \cdot V$$

The number density, or concentration, of particles in bin i is

$$C_i = \frac{N_i}{SV_i}$$

Similarly, the mass density, M_i, particles in bin i is

$$M_i = \frac{N_i \cdot \pi/6 \cdot D_i^3 \cdot \rho}{SV_i}$$

where ρ is the density of the particles.

It is convenient to normalize number and mass densities by their bin widths, to arrive at number density per unit diameter, C_i/BW_i, and mass density per unit diameter, M_i/BW_i.

The total number of particles observed during the accumulation interval is

$$N = \sum_{i=1}^{15} N_i + \sum_{i=17}^{31} N_i$$

Similarly, we have total concentration,

$$C = \sum_{i=1}^{15} C_i + \sum_{i=17}^{31} C_i$$

and total mass,

$$M = \sum_{i=1}^{15} M_i + \sum_{i=17}^{31} M_i.$$

To simplify the nomenclature, introduce an index j, and a bin-to-index assignment b_j, such that,

$$b_{1-15} = 1\text{-}15$$

$$b_{16-30} = 17\text{-}31$$

Having made this definition, we could restate the definition for total mass, for example, as

$$M = \sum_{j=1}^{30} M_{b_j} .$$

The mass median diameter MMD is that diameter at which half the mass resides at smaller sizes and half at larger sizes. Let:

$$M_k^1 = \sum_{j=1}^{k} M_{b_j}$$

$$M_{k-1}^1 = \sum_{j=1}^{k-1} M_{b_j}$$

where k is selected so $M_{k-1}^1 < 0.5 \cdot M$, $M_k^1 \geq 0.5 \cdot M$. Then the median is computed from a linear interpolation over the interval k-1 to k. That is:

$$MMD = DU_{b_{k-1}} + \frac{(DU_{b_k} - DU_{b_{k-1}}) \cdot (0.5 \cdot M - M_{k-1}^1)}{(M_k^1 - M_{k-1}^1)}$$

Note that the upper limit of diameter is used here rather than the mean diameter since it reflects all the mass in the bin rather than only a portion of it.

The opacity (OPA) is a measure of the percent loss of incident collimated light by particles distributed uniformly throughout a volume of specified thickness (T) which in our case is the diameter of the stack at the point where the measurement is made. The light source should ideally be taken as the integral over a source spectrum typical of opacity meters, but for the purpose of simplifying computations, it is taken here to be monochromatic at $\lambda = 0.55$ µm, near the center of the visible spectrum. The extinction loss occurs due to scattering.

Thus,

$$OAP = 100 \times [1 - I/I_o]$$

where I/I_o = transmission ratio.

From Beer's law $I/I_o = e^{-\delta T}$, where δ = total extinction coefficient given by:

$$\delta = \sum_{i=1}^{15} \delta_i + \sum_{o=17}^{31} \delta_i \text{ , where}$$

$$\delta_i = C_i \cdot [\pi \cdot (D_i/2)^2] \cdot Q_i^{ext} \cdot$$

The extinction efficiency Q_i^{ext} may be approximated as

$$Q_i^{ext} = 2 - 4/\rho_i \sin \rho_i + 4/\rho_i (1 - \cos \rho_i),$$

where $i = \frac{2 D_i(m-n_{re})}{\lambda}$ and n_{re} = the real index of refraction of the particles taken to be the value for glass (1.51). The absorption component is ignored here for simplicity.

Finally, the FPSSS can display spectral data against either optical (physical) diameters or aerodynamic diameters. Ignoring the slip correction factor, the aerodynamic diameter D_a of a particle of optical diameter D is a function of the density (mass per unit volume) of the particle:

$$D_a = D \sqrt{\rho_a/\rho_{water}}.$$

7. CALIBRATION AND LABORATORY TEST AND SIMULATION OF FLY ASH ENVIRONMENTS

As we noted in Section 4 it is extremely difficult to adequately model an instrument's response characteristics from theory alone. In particular, the behavior of photodetectors and electronics in the signal train can modify an anticipated optical signal in an unexpected way. Thus, the FPSSS was thoroughly calibrated empirically with an assortment of monodispersed spheres of known size and refractive index. This provides a primary calibration curve for the instrument through primary particle standards. A second form of laboratory evaluation was the intercomparison of the FPSSS with other PMS particle size spectrometers serving as secondary standards. These intercomparisons are with particles of random morphology and shape (often ambient aerosol) and provide broad size spectra. The FPSSS velocimeter calibration involved wind tunnel tests at uniform flow velocities to establish a relationship between particle transit time and tunnel velocity.

All of the above calibrations and tests were conducted at PMS. However, a series of tests was also conducted at the EPA test facilities at IERL. These included a substantial number of tests in the wind tunnel test facility using known dispersal rates of collected fly ash and intercomparison with impactors. Tests of the velocimeter were also performed along with sensitivity checks of the FPSSS to flow alignment. A second set of measurements was made in a separate hot flow facility incorporating a precipitator. A final set of measurements was performed in the flue of an oil-fired combustion unit.

7.1 Calibration and Evaluation of the FPSSS at PMS

The primary calibration curve for the FPSSS was established using monidispersed latex and glass spheres. Through prior experience we have found that only a few points are generally required, although it is a fairly simple test and many different sizes can be run quickly. Most of the sizes used are in the submicron region since the signal becomes a stronger function of size the smaller the particle. Polystyrene latex (PSL) or polyvinyl toluene (PVT) spheres are available from 0.01 to several microns and have similar optical properties (nearly identical refractive indices); they are generally referred to simply as latex spheres. For the FPSSS, latex spheres were used to cover sizes from 0.312-2.02 μm. Glass beads having modal diameters of 5.5 and 11.5 μm established the upper end. The glass bead distributions are fairly broad, with standard deviations of several microns as compared to the few hundredths of a micron generally quoted for latex, but their modal size is sharply defined.

The results of FPSSS sizing with these standard spheres are given in Figure 44. Theoretical response curves for latex (n = 1.58-.01i) and crown glass (n - 1.51-.01i) are also shown for reference. Inspection clearly shows relatively good agreement up to several microns, but a reduction in scattering signals at larger size. This is an expected result caused by the fact that large particles scatter more strongly at directions closer to the optical axis while optical transmission is greater at larger angles. The overall calibration must thus be adjusted systematically, giving the modified error envelope and centerline (adopted) calibration shown. This adopted calibration curve is then normalized to the measured reference signal and the individual gains for each range established to provide best overall signal-to-noise ratio and coverage of the size range selected. Each size range is divided into 15 equal width size classes with their normalized signal windows determined directly from the primary calibration curve.

The calibration just described is generally only necessary for each type of instrument, and identical copies of an instrument will calibrate without modification of the primary curve. However, sizing calibration is only one aspect of total calibration. It is also useful to determine whether an instrument counts the correct number of particles of each size which in effect is a check on how well the sample volume is defined. For this purpose one can choose to map the sample volume with a precisely controlled particle source stream or make comparisons with other secondary standard instruments. Both kinds of tests were performed for the FPSSS. Figure 45 shows the relative counting rate of the FPSSS observed by moving a hypodermic needle through which a microstream of latex particles is injected along the depth-of-field of the FPSSS sample volume. It clearly defines the diamond shaped sample volume with maximum counting rate at the object plane and minimum at the ends of the depth-of-field. This type of experiment is not sufficiently controllable to afford an accurate calibration, but it is a particularly nice demonstration of the technique's mode of operation and answers questions of size dependency of the rejection processes used to define sample volume.

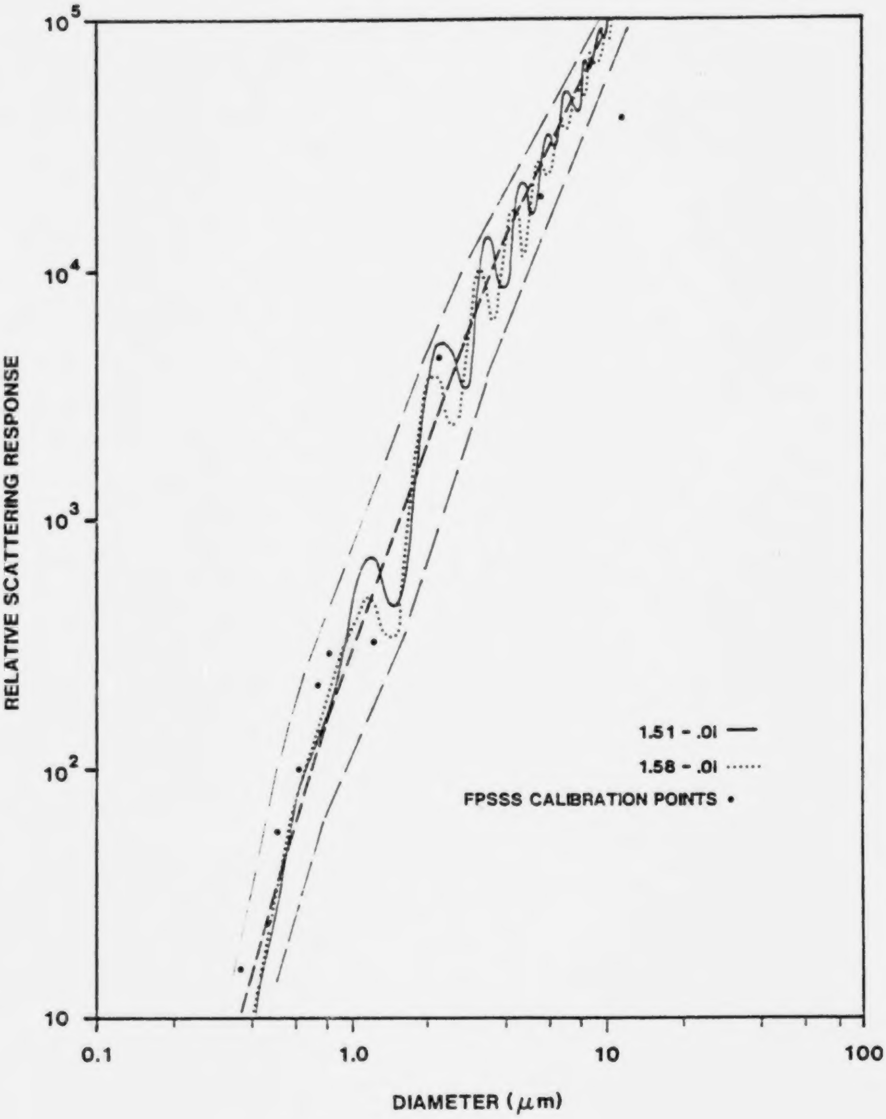

Figure 44. In addition to the use of latex and crown glass spheres, particles of other refractive indices were generated with a vibrating orifice generator; however, these are difficult to use as primary calibration points.

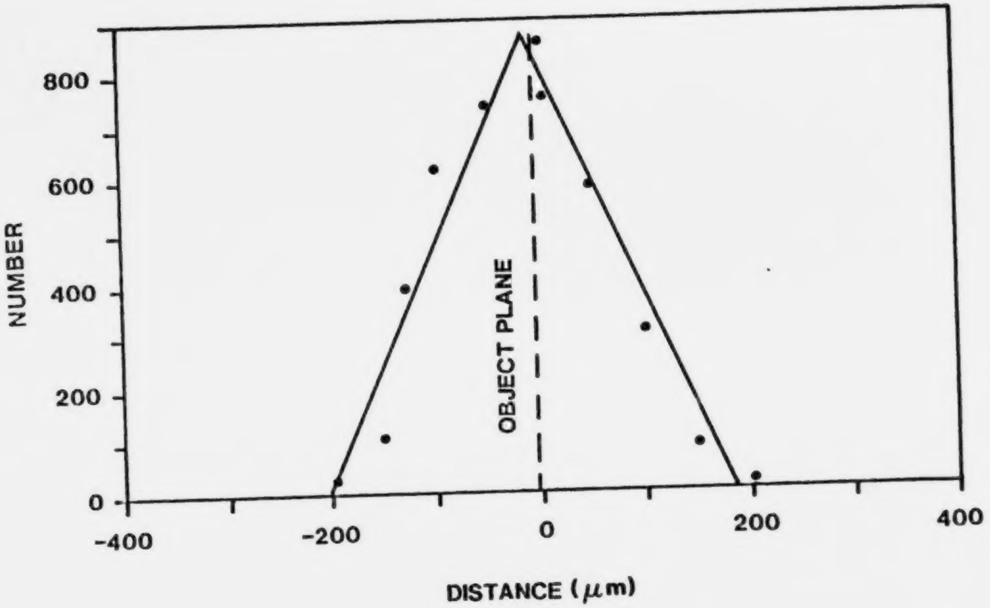

Figure 45. The above sample volume map was constructed using a 28 gauge hypodermic needle, which generates an aerosol stream approximately 75 microns wide. The needle was moved at 25 μm distance intervals starting outside the depth-of-field and continuing until beyond the depth-of-field.

In any multirange device such as the FPSSS, a certain amount of overlap exists between size ranges. In the FPSSS this overlap is nearly 50% and allows a check to be made on its internal consistency. Figure 46 is a plot of size distribution data obtained during a sample run using glycol aerosol at high number density (worst case condition). Two spectral peaks are sharply defined using both the small and the large size modes. The effect of lower resolution in the 0.5-11 μm range is evident in the smoothing of spectral features at submicron sizes.

Probably the simplest means of evaluating an instrument's performance is through intercomparison with other instruments that have been sufficiently calibrated and characterized to serve as laboratory standard instruments. At PMS one instrument in each of the standard product lines is maintained as a relative standard. For comparison with the FPSSS the PMS Model CSAS-100 was selected. The particle sources used included natural ambient aerosol and atomized glycerin. The instruments were configured in such a way that the aerosol flowed through the sample sections of both instruments in series. This dismisses any questions about differing flow rates. A uniform velocity of about 6 $msec^{-1}$ was used. The results are shown in Figures 47, 48, and 49. The first two figures are in ambient aerosol with fairly low number densities revealing a rather steep distribution. Such a distribution is a good test of systematic sizing error which is typically observed as a lateral shift. Figure 47 covers entirely the smallest submicron particles of interest (FPSSS range 1), while Figure 48 includes sizes up to 2 microns (FPSSS range 2). Figure 49 was obtained using atomized glycerin, providing coverage of sizes from 2-11 μm, which corresponds to FPSSS range 4. Range 3 of the FPSSS is entirely overlapped by ranges 2 and 4 and its consistency was checked relative to measurements in them.

These results are probably as good as can be expected from a pair of different instruments. In fact, the FPSSS and the CSAS-100 differ considerably in some respects--the most apparent being the 2-11° versus 4-22° collecting angles. The magnification in the FPSSS is double that of the CSAS-100, resulting in a much smaller sample volume, yet the comparisons stand on their own merit.

Finally, the FPSSS was wind tunnel tested to calibrate the velocimeter. These tests were repeated at several different periods in the contract to try

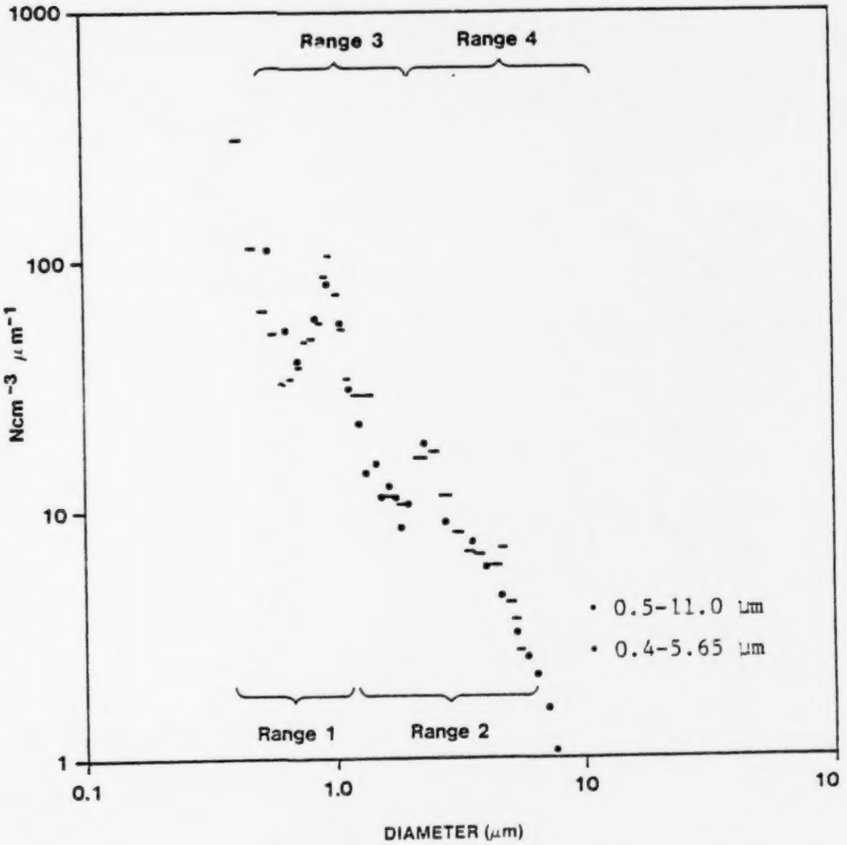

FPSSS INTERRANGE COMPARISON

Figure 46

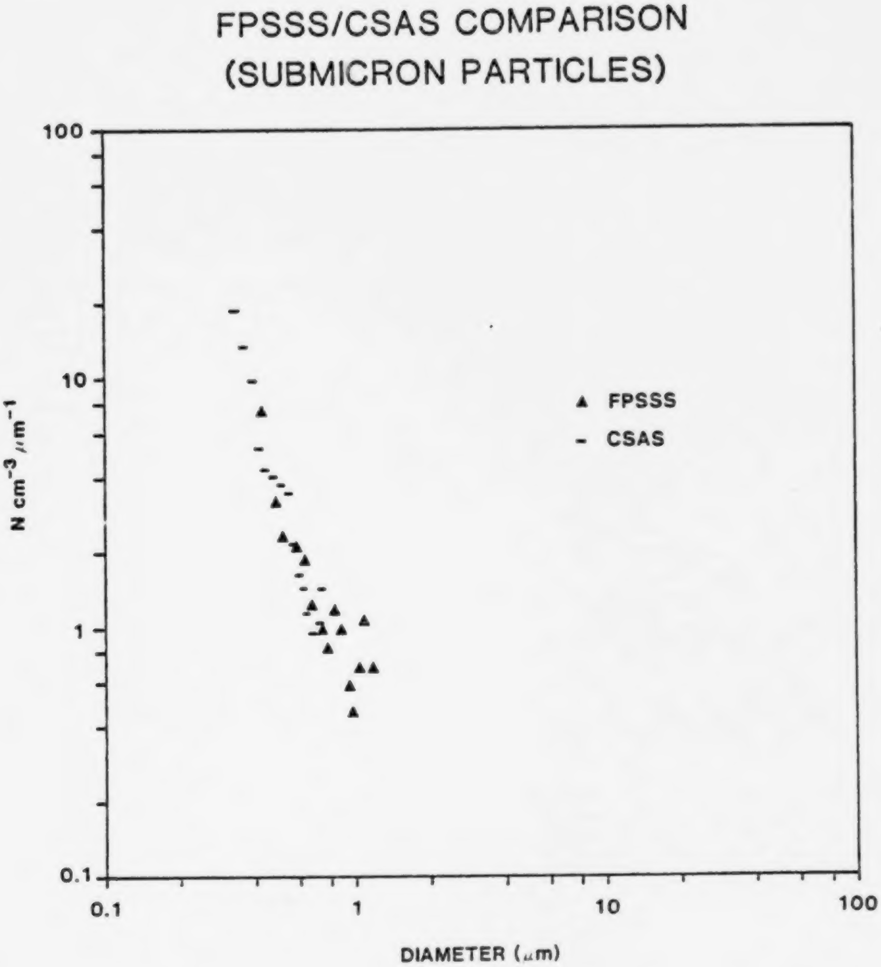
FPSSS/CSAS COMPARISON
(SUBMICRON PARTICLES)
100
10
1
0.1
N cm^{-3} μm^{-1}
0.1
1
10
100
DIAMETER (μm)
▲ FPSSS
- CSAS

Figure 47

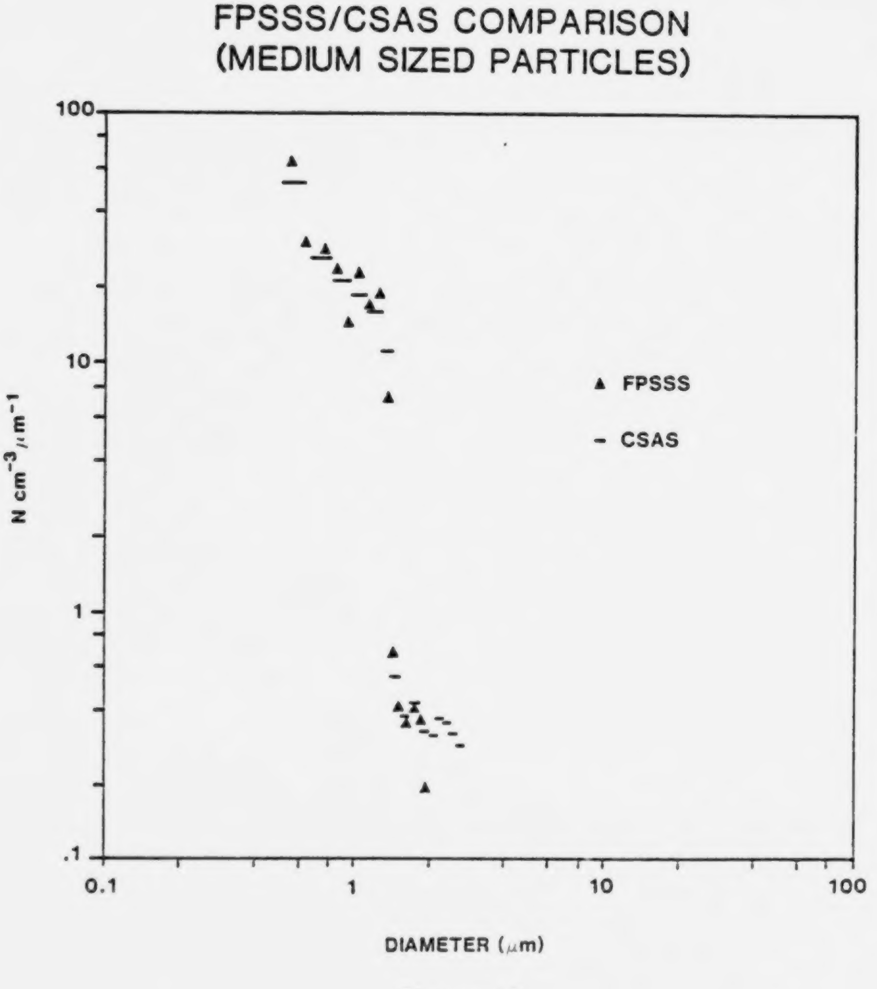
FPSSS/CSAS COMPARISON
(MEDIUM SIZED PARTICLES)
100
10
1
.1
N cm^{-3}/μm^{-1}
0.1
1
10
100
DIAMETER (μm)
▲ FPSSS
- CSAS

Figure 48

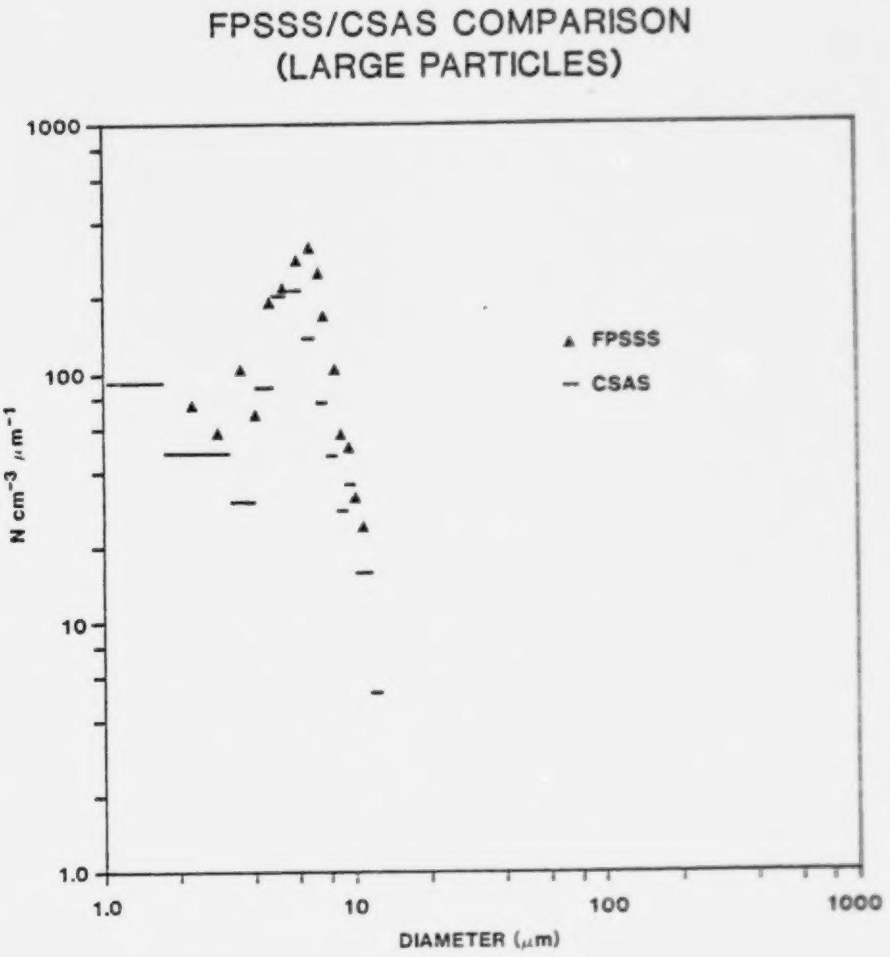

FPSSS/CSAS COMPARISON
(LARGE PARTICLES)

Figure 49

to refine the measurement. In early tests the calibration was found to be size-dependent and we found it necessary to select a fairly narrow range of sizes for pulse width measurements to avoid amplitude (and thus size spectral) dependency. During early field studies the velocimeter always read about 50% high, and independent velocity measurements were utilized. The velocimeter, of course, is not as accurate as standard pitot measurement techniques but because the measurement is made at exactly the point of interest it can be extremely useful even if of reduced intrinsic accuracy. For this reason a considerable effort was made to refine this measurement as the FPSSS developed. In its final delivered form, the velocimeter calibration appeared to be within ± 10-15% over a range of 3-30 $msec^{-1}$. Below 3 $msec^{-1}$ it is not reliable due to triggering of multiple particle transit pulses for each particle vent. Possible improvements to the velocimeter are suggested in Section 9.*

7.2 IERL Test Summary

During the two week period from February 6 to February 16, eight days of intercomparisons were performed with the FPSSS and various EPA samplers at IERL. Facilities exist at IERL to test various particle sizing and sampling instruments under simulated in-stack conditions. Of primary importance to this program was the IERL wind tunnel, which, while operating at room temperature, was useful in characterizing the FPSSS using a variety of fly ash collections. In addition to measurements of the size distribution and the ability to correlate with other measurement systems, the tunnel was useful to study effects of orientation and rates of contamination and to observe its internal velocimeter under a wide range of velocities and mass loadings. A diagram of this facility is given in Figure 50.

The second IERL facility in which tests were made was a heated wind tunnel that had an operating electrostatic precipitator. Although this particular test facility was not capable of generating the range of velocities or the variety of test conditions possible in the primary facility, it did offer the added dimension of elevated temperature.

---

*Since completion of the prototype three additional FPSSS instruments have been delivered with improved velocimeters (see Section 9).

SCHEMATIC OF IERL WIND TUNNEL
SHOWING DUST HANDLING EQUIPMENT

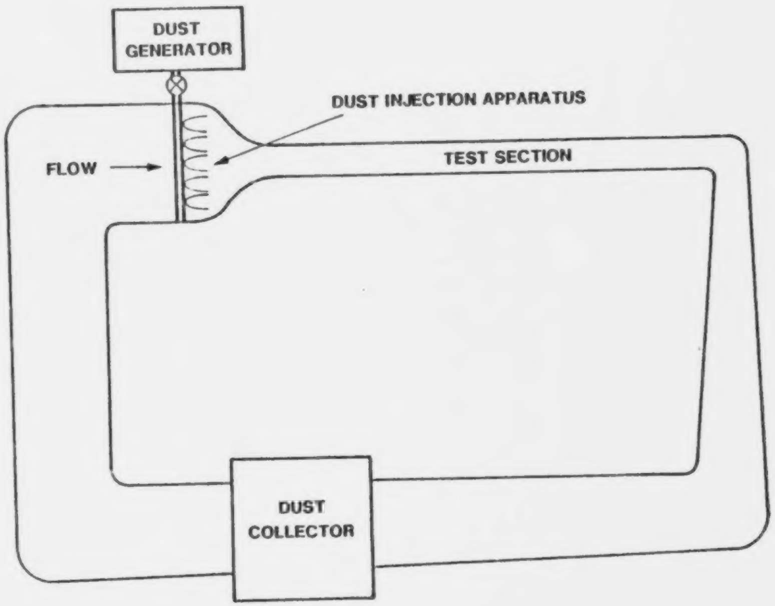

Figure 50

The third and final IERL test facility used was a fuel oil boiler. Measurements were performed in the flue of the boiler while varying the fuel load, excess air, and the amount of water injection.

Four types of particle environments were sampled using the three above test facilities:

1. In the first series of tests, the IERL wind tunnel operated at velocities from 2 to 30 $msec^{-1}$ and fly ash loadings from 0.06 to 3 gm^{-3}. The tunnel was operated at room temperature and with room air. The ash had been collected from a coal burning utility and redispersed into the tunnel air flow using a feedscrew, blower, and vibrating lead shot fluidizing bed (see Figure 51). Water was added to the feed system to minimize loss or agglomeration of ash due to static attraction. A few Climet Particle Counter observations, 13 impactor runs, 12 Coulter Counter analyses, and on the order of 100 FPSSS observations (resulting in 200 computed number density and mass spectra and 100 numerical summaries) were made. These tests included characterization of the velocimeter and tests of the FPSSS sensitivity to flow alignment.

2. The same wind tunnel was also tested with dust collected from a steel mill whose primary constituent was iron oxide. A limited range of mass loadings (0.06 to 0.12 gm^{-3}) was used due to difficulties in feeding the material at higher rates and uncertainties in the tunnel airspeed at low airspeeds. Three impactor runs, 8 Coulter analyses, and about 15 FPSSS observations were made.

3. The third kind of test involved the heated wind tunnel with rectangular cross section and incorporated an electrostatic precipitator (ESP). Three hours of FPSSS observations at the inlet to the precipitator were made. The tunnel was loaded with 1 gm^{-3} of ash at a velocity of 1 $msec^{-1}$ airspeed. Feed system characteristics were largely unknown to us, but appeared to be considerably more rudimentary than the tunnel used above, and indications of uneven mass loading in the tunnel's cross section were noted.

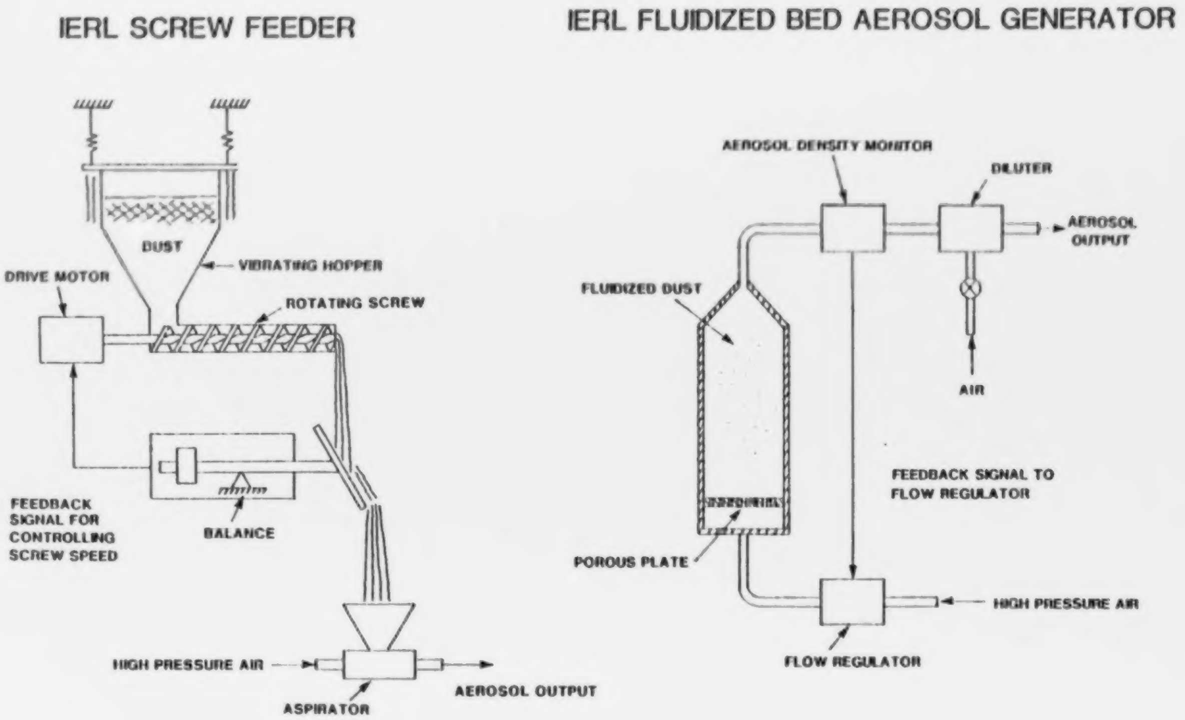
IERL SCREW FEEDER

IERL FLUIDIZED BED AEROSOL GENERATOR

Figure 51. The two aerosol feed systems depicted above can be used independently or jointly to achieve the desired aerosol dispersal characteristics.

4. In the final test series, an attempt was made to characterize a 38 cm diameter #6 fuel oil boiler flue at 230°C. Particulate loading versus water injection and percent excess air relationships was examined. About 5 hours of FPSSS observations were made; no other reference information or other instruments were available for simultaneous intercomparison. Impactor runs at presumably similar boiler conditions made prior to this experiment were available for comparison.

A series of 15 specific test runs were performed in the IERL wind tunnel. Twelve of these tests were performed using fly ash from a coal-fired power plant. The last three tests used an ash that was very high in iron oxide. The normal fly ash was collected from the Duke Power Station electrostatic precipitator plants. The collection procedure for the iron oxide rich ash was not known. Figure 52 shows SEM photomicrographs of material from these two sources. An obvious problem with the iron oxide is the tendency for the material to clump into aggregates, which the results show remain after fluidizing procedures. Difficulties with the friability of both materials require humidity control to reduce static attraction. Coulter Counter analysis of both of these materials is given in Figures 53 and 54 along with relative comparisons of measurements using the FPSSS. In Figure 53 the Coulter analysis of the fly ash appears to be in excellent agreement with the FPSSS, especially when the 100 μm orifice was used; however, the results with the iron oxide (shown in Figure 54) showed disagreements we have attributed to clumping.

For the Duke Power Plant fly ash, the initial run with the Coulter Counter was made with a 200 micron orifice to make certain that all particles up to approximately 128 microns were measured. Since the FPSSS has a limited range extending only up to 11 microns, a sub-sample was taken and sieved to remove all particles larger than 44 microns and that sample analyzed with the Coulter Counter using a 100 micron orifice. These results are all presented in Figure 53. The set of distributions is obviously quite different for the Coulter analysis using the different orifices. The median volume diameter computer using the 200 micron orifice and the Duke fly ash was 14.5 microns, while that for the 100 micron orifice is approximately 8 microns. In the relative comparison shown, we truncated the Counter analyses at 11 microns to coincide with the FPSSS. In this region of overlap a median volume diameter of 3.8

Reproduced from
best available copy.

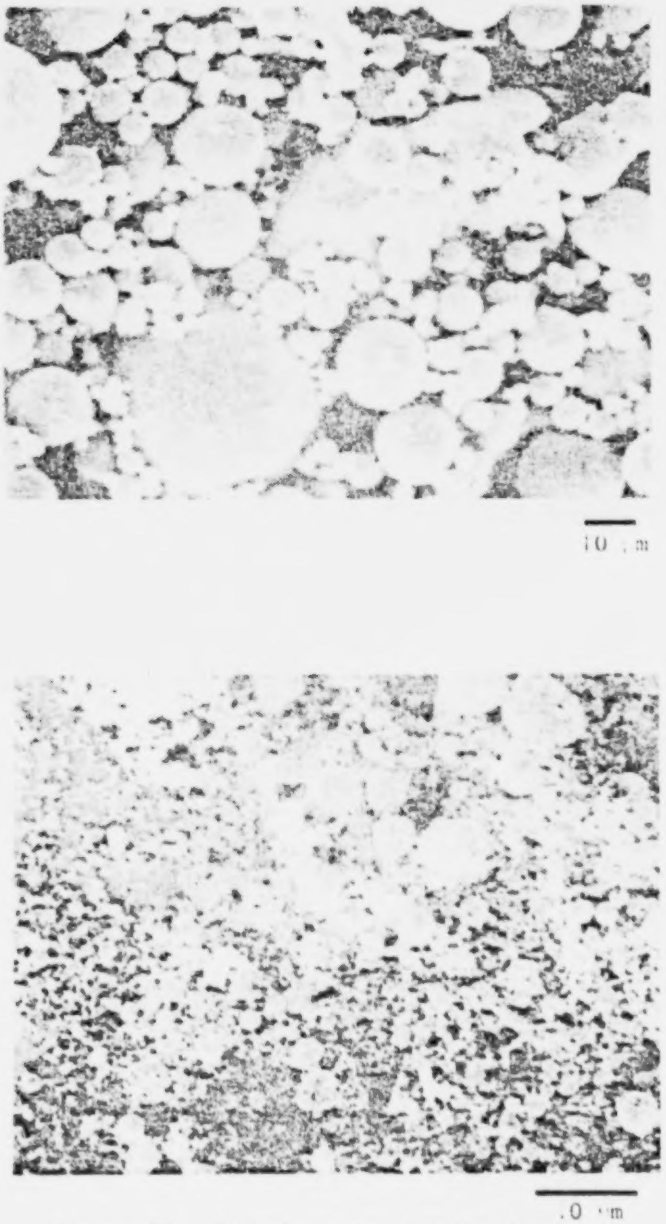

Figure 52. SEM photomicrographs display the primarily spherical Duke Power Plant fly ash (upper) and the clumped aggregates of iron oxide (lower).

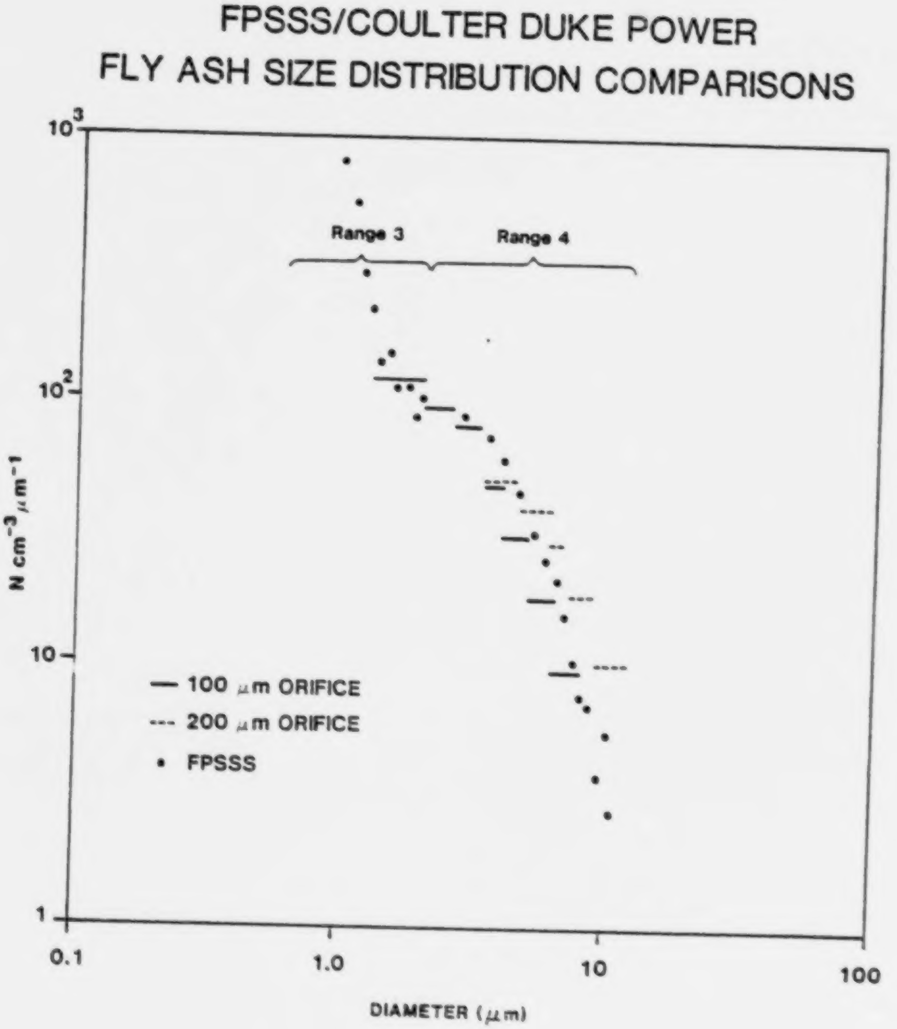

FPSSS/COULTER DUKE POWER
FLY ASH SIZE DISTRIBUTION COMPARISONS

Figure 53

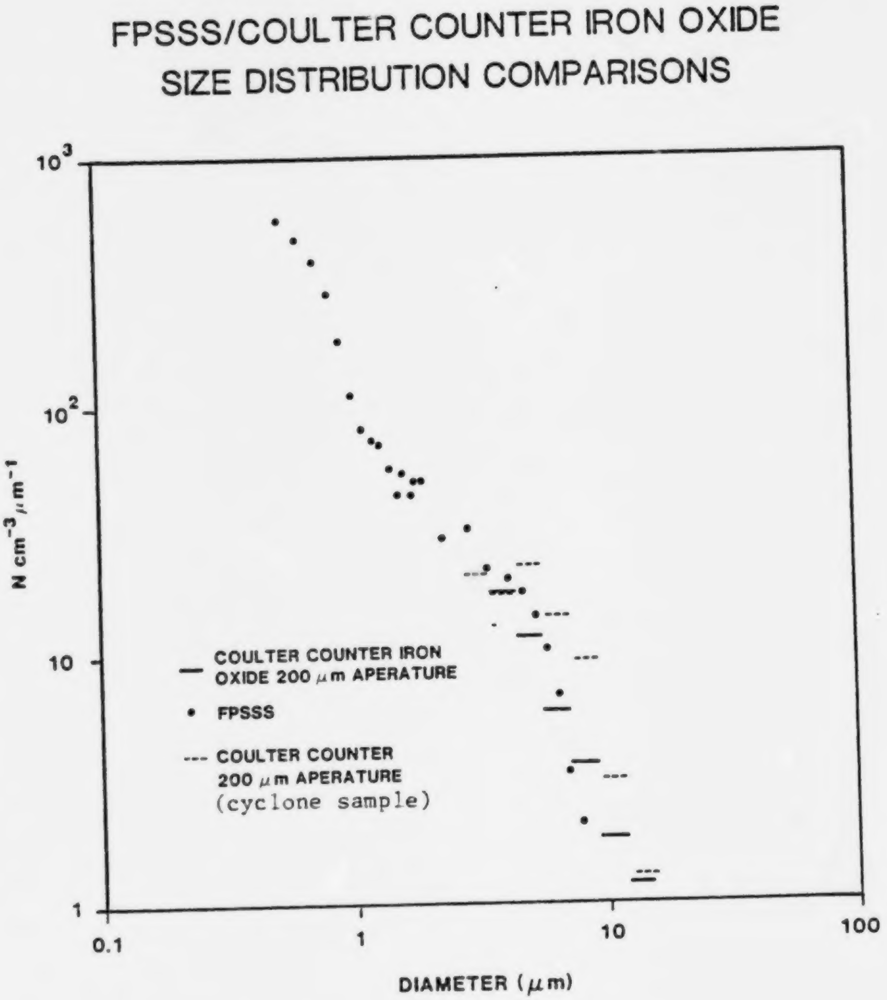
FPSSS/COULTER COUNTER IRON OXIDE SIZE DISTRIBUTION COMPARISONS
10^3
10^2
10
1
0.1
1
10
100
N $cm^{-3} \mu m^{-1}$
DIAMETER (μm)
— COULTER COUNTER IRON OXIDE 200 μm APERATURE
• FPSSS
--- COULTER COUNTER 200 μm APERATURE (cyclone sample)

Figure 54

microns is computed.

The iron oxide measured with the Coulter Counter using a 200 μm orifice revealed a higher median volume diameter of 25 microns. No measurements with the 100 μm orifice were made due to sieving difficulties. Inspection of the material as revealed in Figure 52 shows that the most numerous particles are invariably submicron. Only through clumping are particles of large size generated. This problem will be discussed in more detail later.

Beginning now for the 15 test runs we should first state that the primary means of comparison was through gravimetric analysis of a 9 stage Anderson Impactor. Because of certain unknown factors in the impactor analysis, primary cut points, and the lower resolution as compared to the FPSSS, the fairest comparison is in terms of total mass loading. A summary of the mass loading comparison is given in Table VI. During these test runs the tunnel speed ranged from 2 to 30 $msec^{-1}$. The sampling intervals for the impactor runs varied from 10 minutes to 2 hours depending on the mass loading and velocity produced. In general, the impactor was run sub-isokinetic with the exception of the final pair of runs. Sub-isokinetic conditions tend to over-sample large particles while super-isokinetic conditions under-sample the larger particles. However, with the mass distributions measured the average error would probably be less than 15%.

The first run was performed at a set mass loading of 0.06 gm^{-3} and a 10 $msec^{-1}$ tunnel velocity. The average mass loading as measured by the FPSSS was 0.055 gm^{-3}, in good agreement with the impactor value of 0.049 gm^{-3}. Run numbers 2 through 6 used a tunnel mass loading setting of 0.58 gm^{-3} and tunnel velocity of 2 and 10 $msec^{-1}$. The FPSSS values range from 0.46 to 0.61; the average value is 0.57. The impactor mass loadings for run numbers 2, 3, 5, and 6 range from 0.42 to 0.5. Run number 4 generated an unexplainable low impactor value of 0.07 (initial weighing is suspect). Run numbers 7 and 8 used set mass loadings of 0.06 gm^{-3} and a tunnel velocity of 10 $msec^{-1}$ (essentially a repeat of run number 1). Again, a very good agreement was found among the FPSSS, impactor, and set mass loading values. The final four runs using the Duke fly ash used a set mass loading of 0.2 mg^{-3} and a tunnel velocity of 5 and 30 $msec^{-1}$. The first of these runs found the FPSSS in good agreement with the set mass

TABLE VI
IERL WIND TUNNEL MASS LOADING COMPARISONS

Run No.	Date	Tunnel Velocity $m\ sec^{-1}$	Time of Day	Time Min.	Set Mass Loading $g\ m^{-3}$	Volume		% Isokinetic	Impactor Mass Loading $g\ m^{-3}$	FPSSS Ave. Mass Loading $g\ m^{-3}$
						ACF	SCF			
1	2-8	10	10:00-11:00 am	57	0.06	25.82	26.5	72.7	0.049	0.055
2	2-8	10	2:40-2:50 pm	10	0.58	4.49	4.61	72.1	0.46	0.61
3	2-8	2	3:33-3:43 pm	10	0.58	4.62	4.74	86	0.50	0.68
4	2-8	2	3:51-4:01 pm	10	0.58	4.62	4.74	86	0.07	0.62
5	2-9	10	10:02-10:17 am	15	0.58	5.66	5.75	63	0.48	0.48
6	2-9	10	10:44-10:59 am	15	0.58	7.35	7.47	82	0.42	0.46
7	2-9	10	11:21 am - 12:21 pm	60	0.06	27.87	28.33.	77.5	0.0575	0.061
8	2-9	10	1:05-2:05 pm	60	0.06	26.7	27.15	74	0.046	0.055
9	2-12	5	9:51-10:06 am	15	0.2	6.2	6.3	85	0.034	0.202
10	2-12	30	11:29-11:49 am	20	0.2	6.5	6.7	72	0.276	0.057
11	2-12	5	3:09-3:39 pm	30	0.2	12.0	12.3	83	0.0632	0.17
12	2-12	30	4:06-4:26 pm	30	0.2	7.5	7.7	83	0.142	0.13
13	2-14	10	10:54 am - 12:54 pm	120	0.06	61.06	62.66	85	0.061	0.085
14	2-14	30	1:52-2:52 pm	60	0.035	38.95	39.7	144	0.028	0.021
15	2-14	30	3:13-4:13 pm	60	0.035	28.4	29.0	105	0.023	0.020

loading while the impactor was more than a factor of 5 lower. In run number 10 the reverse is true, that is, the impactor gave a high value while the FPSSS was more than a factor of 3 lower than the anticipated value of mass loading. The impactor yielded a low value in run number 11, while the FPSSS was quite close with a value of 0.17 gm^{-3}. Run number 12 showed the FPSSS and impactor in good agreement, with values of 0.13 and 0.14, respectively, representing about two-thirds of the anticipated mass loading. The average for the four runs was 0.14 gm^{-3} for the FPSSS and 0.13 for the impactor. These results suggest possible variability in the tunnel (FPSSS and impactor sample locations were as close as possible but still separated by several inches) or errors of unknown origin. It is a bit curious that only in the final run did the FPSSS and impactor show consistency. In each of the prior three runs one or the other measuring device was substantially low, suggesting possible tunnel variations and the need to profile the tunnel, to be discussed later. Inspection of the FPSSS data reveals that the measured number density decreased from 1.2×10^4 to 5.8×10^3 -- thus the discrepancies in mass loading are largely the result of a change in number density and not size.

The final three tests used the iron oxide ash with set mass loadings of 0.06 and 0.035 and a tunnel velocity of 10 and 30 $msec^{-1}$. In the first test the FPSSS produced a slightly higher value than the impactor which was extremely close to the set mass loading of 0.061 gm^{-3}. In the final two runs the FPSSS measured values that were about 40% low, while the impactor values were about 30% lower than the set values of mass loading. After these runs were completed, we found that a lot of the iron oxide ash settled in the contraction section just beyond the injectors. In fact, the material had accumulated to an inch in several places. This would, of course, partially account for the lower readings by both the FPSSS and the impactor; the particles simply never made it through the tunnel. From the noticeable clumping of the iron oxide material one would expect median mass values outside the FPSSS size range. A Coulter analysis of the cyclone sample (on the impactor) gave a median volume diameter of 6.3 microns as compared to the FPSSS value of 5.1 μm (revealed in the accumulative mass distribution ash shown in Figure 55). However, almost all of the material ended up in the cyclone (25 out of 31 mg^{-1} in run number 14 and 17.2 out of 17.7 mg^{-1} in run number 15).

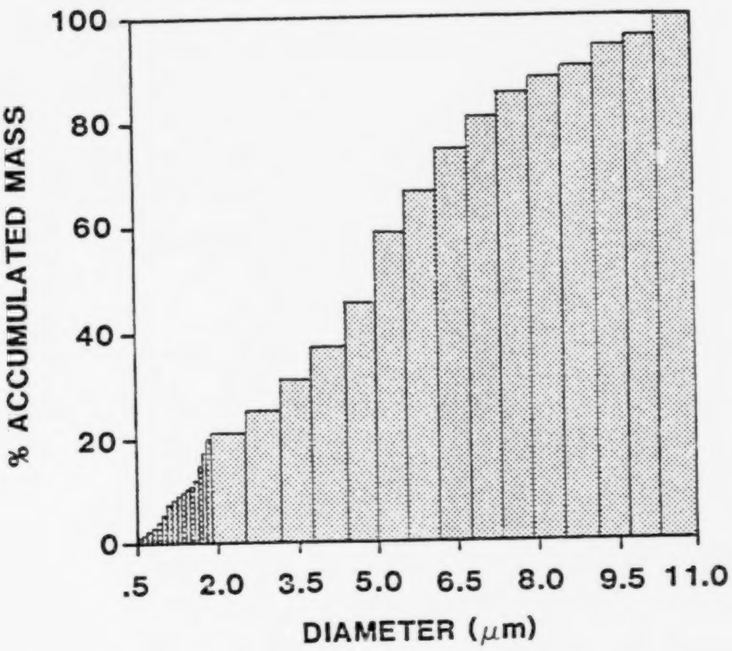

Figure 55. FPSSS accumulative mass distribution for the iron oxide for run #14. A median volume diameter of 5.1 microns is indicated.

In general, what appears to be excellent agreement in most of the above runs is thought to be at least partially fortuitous. As far as the impactor is concerned, errors in weighing, non-isokinetic conditions, and siting errors would restrict overall accuracy to perhaps ± 20% at best. For instance, the samples were weighed twice. The difference between the first and second weighings showed decreases of 50% and 20% for run numbers 1 and 2 but an increase of 40% in run number 3. This, of course, suggests that one must use a statistical approach to impactor sampling and average over many samples. In Table VI, all impactor mass loadings are the final weighing results. With regard to the FPSSS the two sources of greatest error are contamination and errors in assumed density. Laboratory results have already confirmed that the FPSSS should size accurately enough regardless of particle composition. From Figure 52 we can recognize that at least the Duke fly ash is almost entirely composed of particles with spherical morphology; thus shape is of no major concern. Even in the case of the iron oxide, the primary particles are so small (submicron) that shape would not be a strong issue. The large clumps remain an open questions, however.

Contamination of the optics in the FPSSS occurred several times during these tests and, of course, any loss of optical signal results in an undersizing condition generating low mass. In several cases where it was obvious (such as when the probe was misoriented to expose and trap particles rather than shield the optics from particles), results were discarded. The highest levels of contamination observed were during run numbers 5 and 6 which involved the highest mass loadings and 10 $msec^{-1}$ velocities. We also had some difficulty with the oxide ash during cleaning; its more abrasive character permanently damaged the coating on the objective which later required replacement. In any case, contamination was observed to produce up to 50% lower values of mass loading during worst contamination conditions. This corresponds to (approximately) a 20% systematic underestimate of particle diameter. The errors in density can be subtle. The density of the source materials was measured fairly accurately through picnometry; however, it is not known if the density varies as a function of particle size. We have briefly mentioned problems associated with siting of both the impactor and the FPSSS and noted material settling during the final three runs. We must also acknowledge that uncertainties in the set mass loadings are known to exist and, though the magnitude is probably small, must still be regarded as an unknown.

In summary, generally good agreement was obtained between the FPSSS and the mass loading rate fed into the tunnel. Some disagreement between FPSSS and impactor samples was noted, but overall uncertainty averaged less than 20%. Agglomeration and differing constituents are problems with the iron oxide, as evidenced by microscopic examination. Generally poorer and somewhat erratic intercomparisons were noted. The oxide tends to contaminate the FPSSS optics more readily than ash. The FPSSS tended to compare better with the set mass loading input than with the impactor samples.

Turning now to the size and mass distributions, the standard operating procedure was to obtain both for each population measured. For each impactor run, typically 4 or 5 different size and mass spectra were obtained from the FPSSS. There were similarities in all of the spectra for a given material so we will only provide a few representative samples for discussion. The size distribution for run number 1 is shown in Figure 56 and the mass distributions in Figures 57a and 57b. The size distribution shows two statistically significant modes, one at about 0.8 microns and a second at 2.25 microns. The first mode at 0.8 microns is also apparent in the mass distribution while the primary mass mode ranges from 2 to 6 microns, generating a mean mass size of 5.5 microns. The slight tendency for an increase in mass at sizes between 8 and 11 microns is not statistically significant, and, from a number of other distributions, it is estimated that less than 20% of the given mass covered by the FPSSS would lie above its upper 11 micron limit. Figures 58 and 59a show the size and mass distributions characteristic for run number 5. They are strikingly similar to those just discussed for run number 1. The FPSSS's ability to generate the correct (similar) size distribution with an order of magnitude higher mass loading is illustrated. Because of the higher counting statistics the mass distribution is quite smooth out to 11 microns. Extrapolating beyond the 11 microns one would estimate that the mass contributions at 11 microns would be down an order of magnitude from the peak at 6 microns and again would correspond to less than a 10% residual error in unmeasurable mass at sizes larger than 11 microns. Run number 7 had the same mass loading as run number 1 but the greater sample time provided less noisy statistics in the accumulative mass distribution, as revealed in Figure 60. Comparing Figures 60 and 57b differences are noteworthy only in

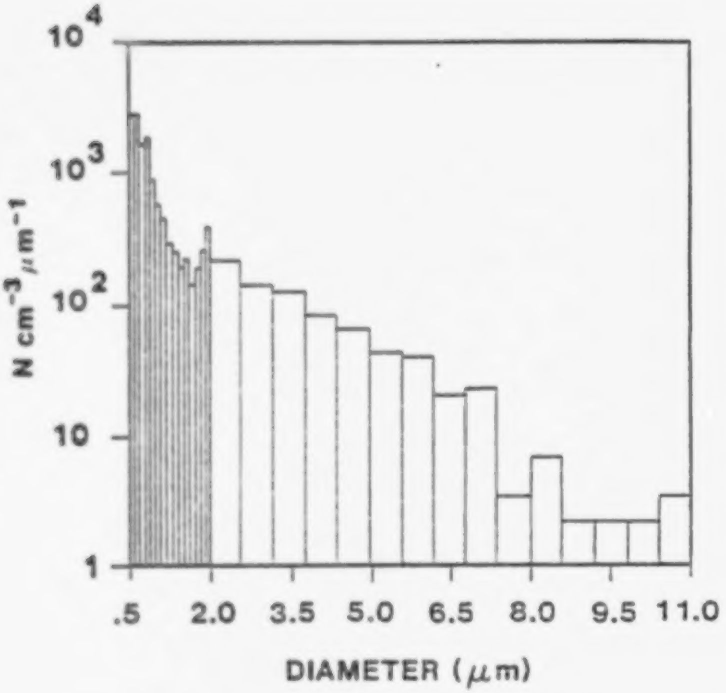

Figure 56. Size distribution for IERL run number 1, ending at 11:20, February 6.

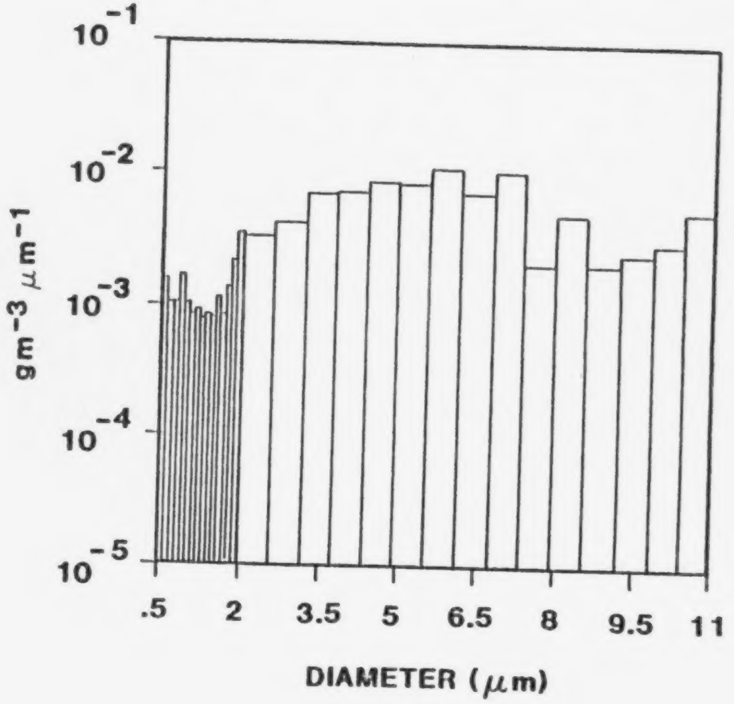

Figure 57a. Mass distribution for IERL run number 1, ending at 11:20, February 6.

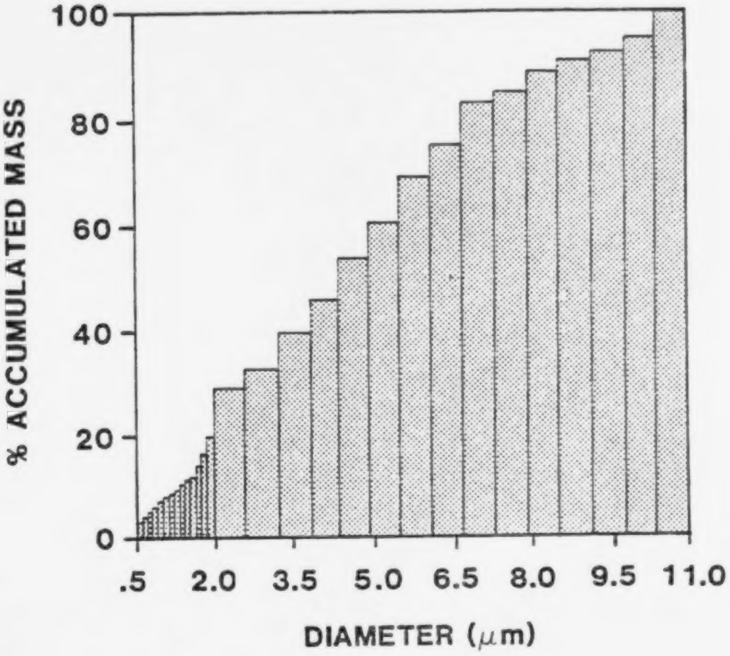

Figure 57b. Accumulative mass distribution for IERL run number 1, ending at 11:20, February 6.

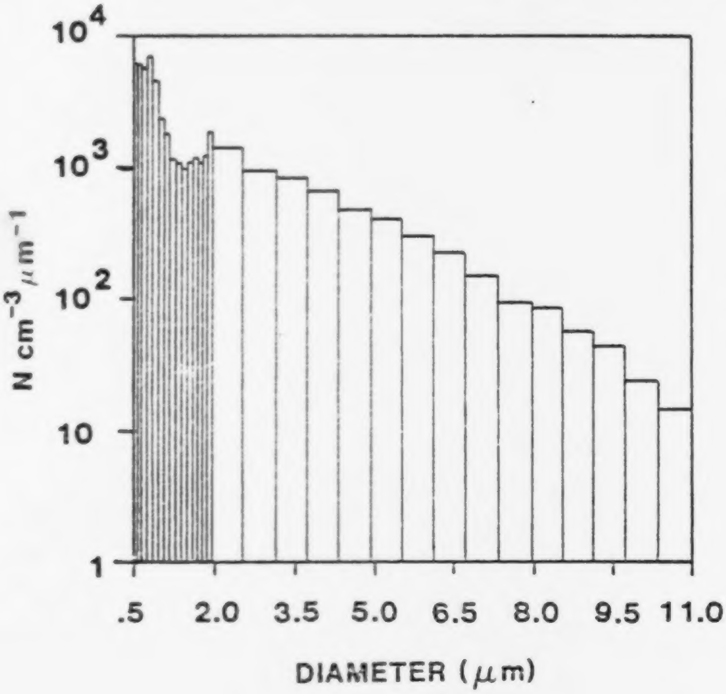

Figure 58. FPSSS size distribution for IERL run number 5, ending at 10:07, February 7.

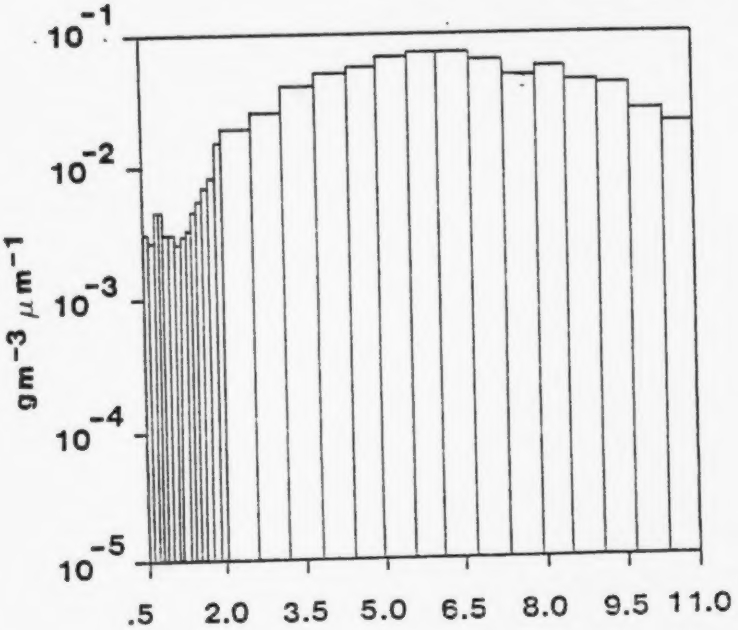

Figure 59a. FPSSS mass distribution for IERL run number 5, ending at 10:07, February 7.

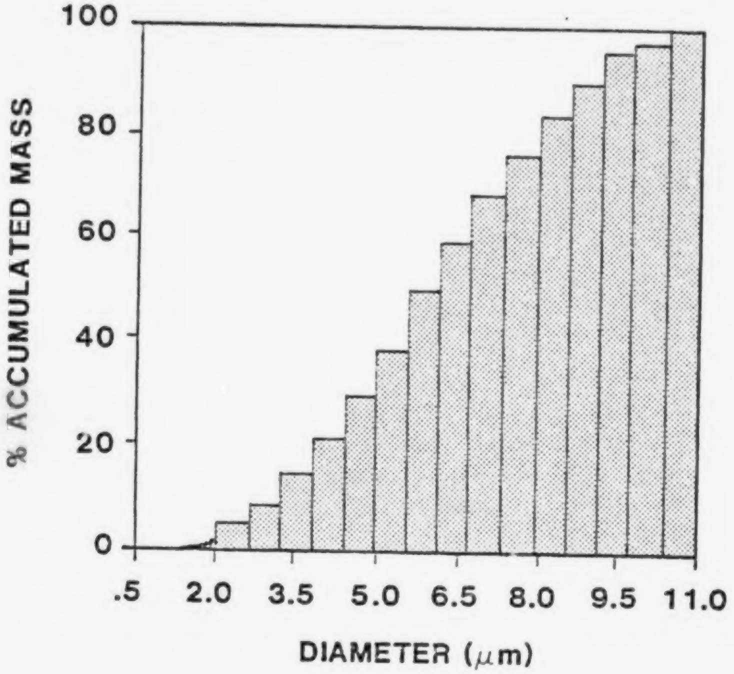

Figure 59b. FPSSS accumulative mass distribution for IERL run number 5, ending at 10:07, February 7.

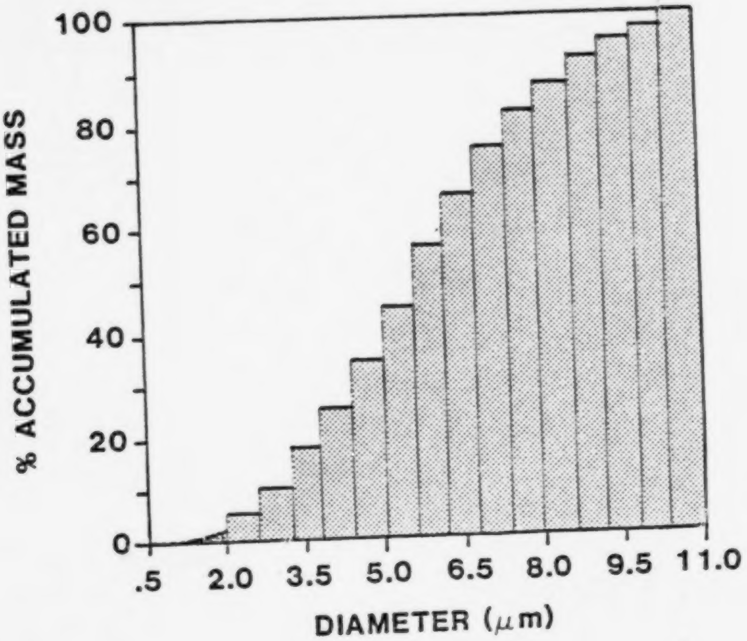

Figure 60. FPSSS accumulative mass distribution for IERL run number 7, ending at 11:45, February 7.

channel-channel comparisons.

The iron oxide in run number 14 was of a lower mass loading and somewhat different size and mass distribution. There is no size or mass mode similar to that previously observed in Figure 59a and 59b at 2 microns and the mass distribution peaks somewhat more strongly. Again, because of the low mass loadings, statistics in the mass distribution at sizes beyond 8 microns were marginal.

Comparison of the actual size distributions derived from the impactors and as measured by the FPSSS were made for all runs. Comparisons show surprisingly good agreement in all cases but particularly good agreement with the first impactor run. This is largely due to the omission of the pre-cutter and cyclone used on all subsequent impactor runs. The pre-cutter and cyclone captured over 90% of the sample, making detailed size resolution a much more difficult task. For completeness we have provided comparisons of the FPSSS and impactor size distribution analysis for the Duke and iron oxide fly ash in Figures 61 and 62. Figure 61 shows the results of impactor run number 1 and the average of runs 5, 6, and 7 compared to appropriate FPSSS samples. Figure 62 provides a similar comparison for run number 14.

The results illustrate the effect of the cyclone on the impactor size analysis. The cyclone used on the impactor during runs 5, 6, and 7 removed a considerable amount of material at smaller sizes when compared to the run 1 results in Figure 61. In spite of the effects of using the cyclone both comparisons in Figures 61 and 62 must be regarded as quite satisfactory.

Alignment Studies and Spatial Profiling between Run Number 1 and Run Number 2. While gravimetric analysis of the impactor samples was being conducted, we were able to run a series of tests of the FPSSS sensitivity to alignment orientations. At this particular period in time the velocity was a constant 10 meters per second with a projected mass loading of 0.06 gm^{-3}. Figure 63 shows a 23 minute run in which the mass loading and number density measured by the FPSSS showed striking stability. Figure 64 shows a succeeding run over a 30 minute period in which the probe orientation was stepped from 0° to 45°. As the figure illustrates, there is surprisingly little sensitivity to changes in alignment until approximately 25° rotation. At rotations beyond 30°, the effects of misalignment are rather dramatic in that 45° shows a drop of about an

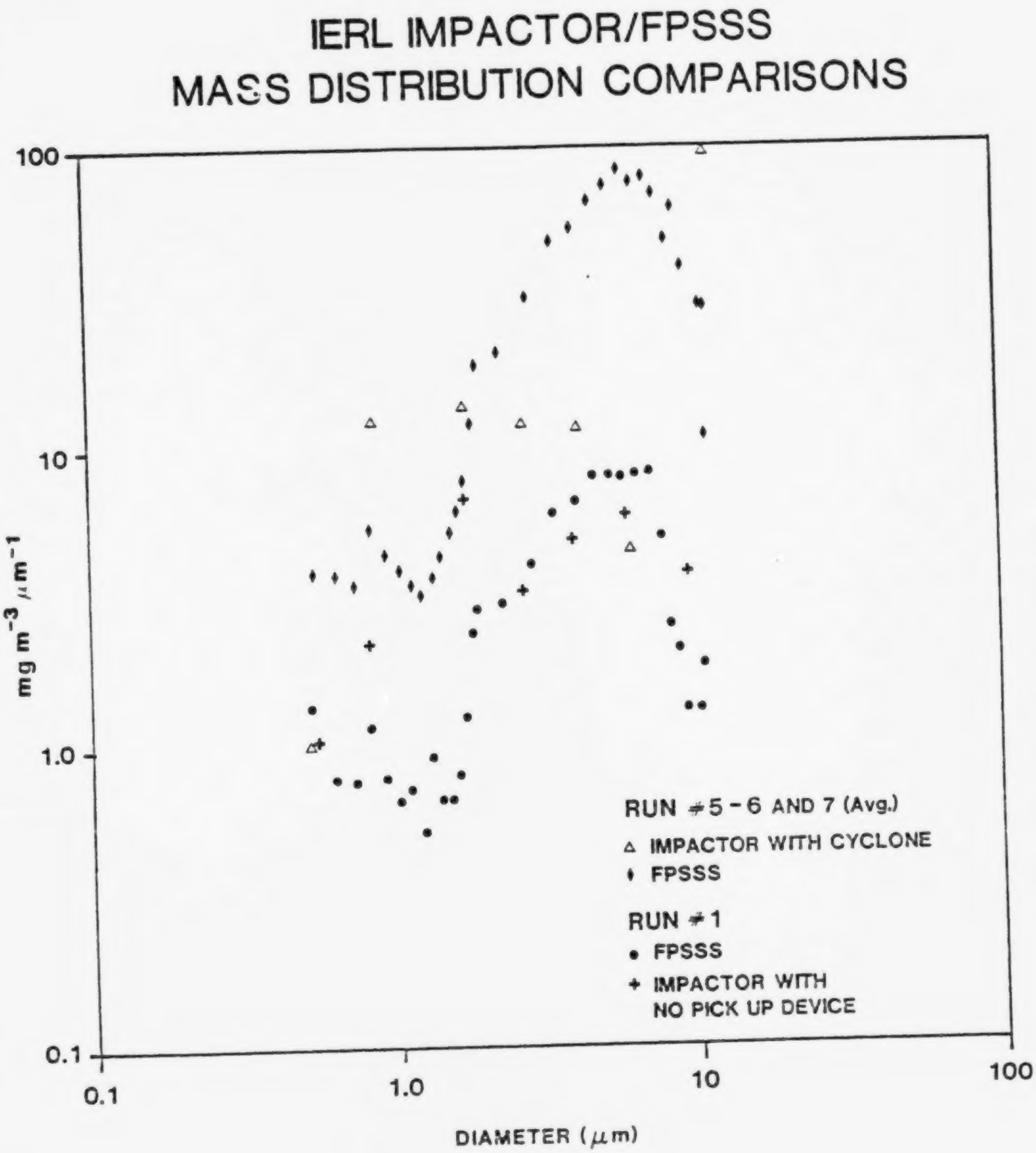
IERL IMPACTOR/FPSSS
MASS DISTRIBUTION COMPARISONS
mg m^{-3} μm^{-1}
100
10
1.0
0.1
0.1
1.0
10
100
DIAMETER (μm)
RUN # 5 - 6 AND 7 (Avg.)
△ IMPACTOR WITH CYCLONE
♦ FPSSS
RUN # 1
● FPSSS
+ IMPACTOR WITH NO PICK UP DEVICE

Figure 61

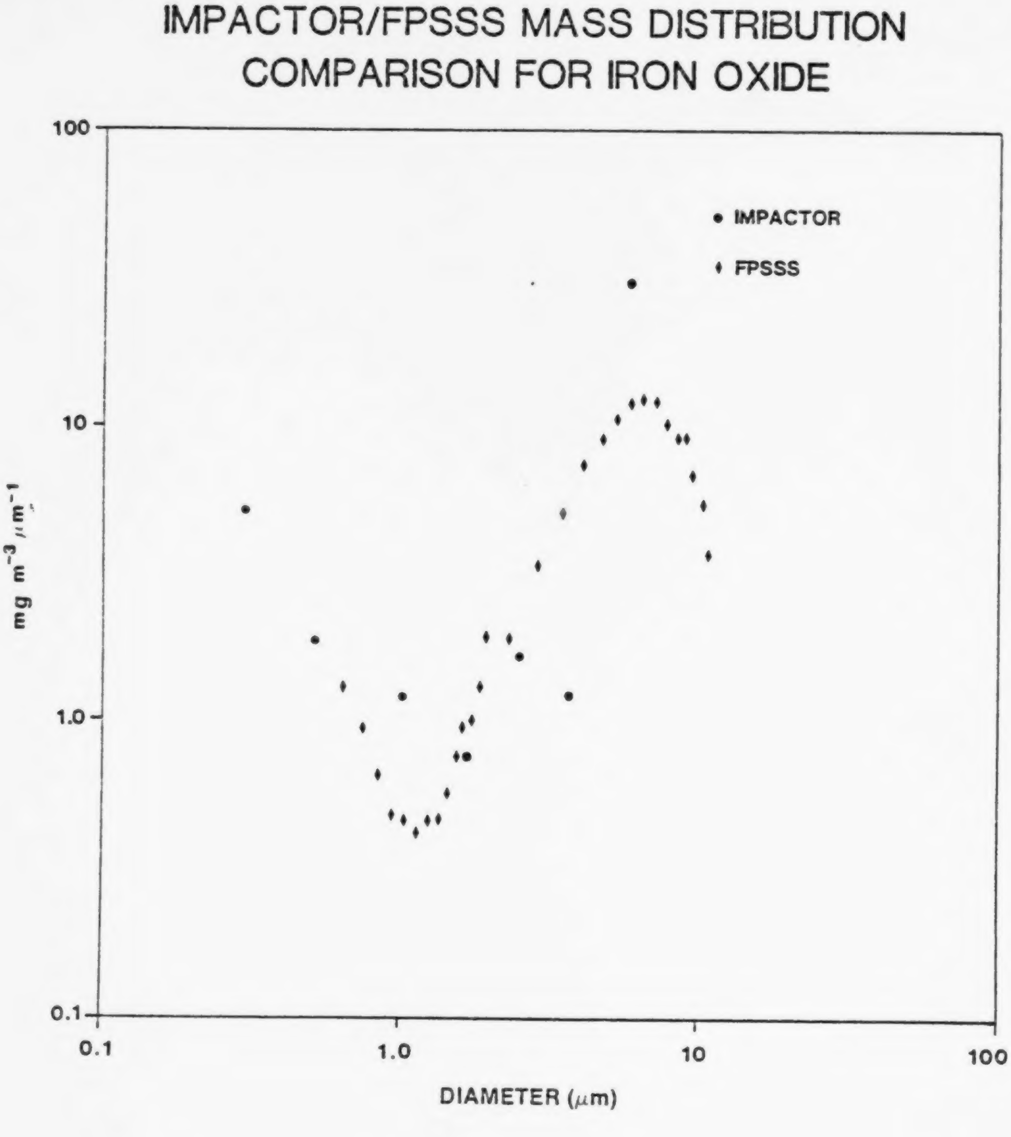
IMPACTOR/FPSSS MASS DISTRIBUTION
COMPARISON FOR IRON OXIDE
● IMPACTOR
♦ FPSSS
mg m^{-3} μm^{-1}
100
10
1.0
0.1
0.1
1.0
10
100
DIAMETER (μm)

Figure 62

TIME SERIES FOR ROTATION OF PROBE HEAD IN WINDSTREAM

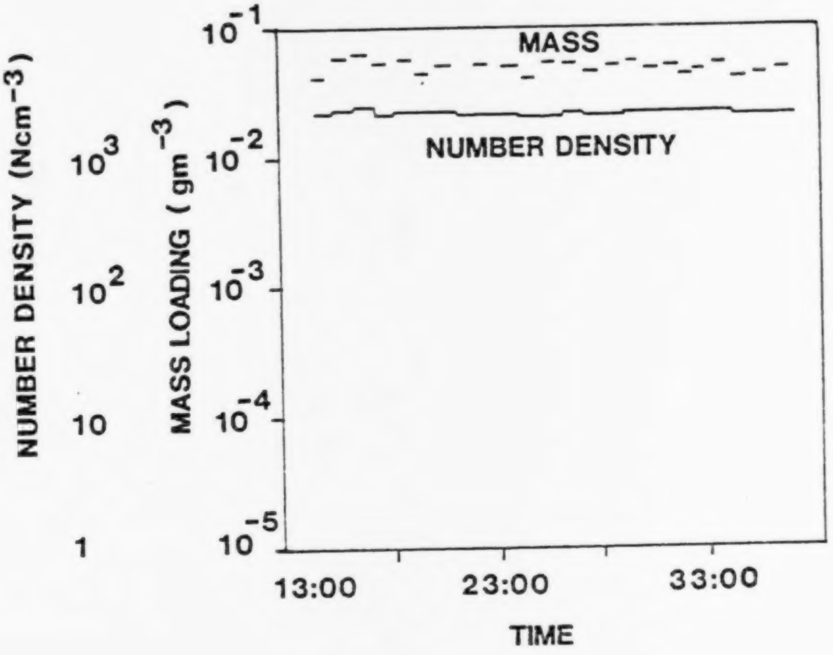

Figure 63. FPSSS time series and number density plot in IERL tunnel. This 23 minute run was performed just prior to the alignment sensitivity study and shows remarkable uniformity in both mass loading and number density.

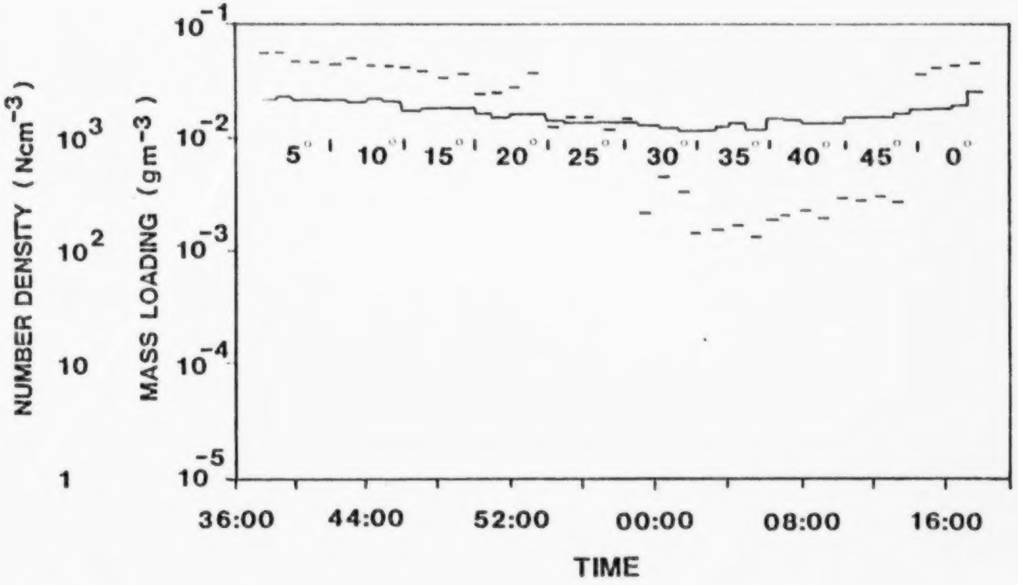

Figure 64. Time series for rotation of probe head in IERL tunnel. During these tests, the FPSSS was rotated through 45° in incremental steps. Note the large change in mass loading and almost negligible change in number density.

order of magnitude in mass loading; the greatest change occurred in the range of 25° to 35°. An examination of Figure 64 shows one rather surprising feature: while the mass distribution changes by an order of magnitude, the number density falls off by about only a factor of 2. This, of course, simply means that the large particles are being rejected more easily than the smaller ones under cases of severe misorientation. Since these results were immediately obvious from the FPSSS printout we elected to look in detail at the size distributions. Figure 65 shows mass distributions measured by alignment errors of 0°, 15°, 30°, and 45°. The 0° and 15° mass distributions are quite similar, the primary effect being slightly less mass at all sizes, with perhaps some further reduction in mass beyond 2 microns. The plot of 30° shows, in general an order of magnitude loss at sizes beyond 2 microns, with a sharp cutoff above 7 microns. At 45° there is a strong effect at sizes larger than 2 microns, showing increasingly greater mass loss with increasing size until cutoff completely at 6 microns.

From this brief treatment it is difficult to say whether the structures produced under the 30° or 45° orientations are entirely reproducible; however, the stronger, general tendency to reject the larger particles is very apparent. The cutoff at some larger size is predictable from imaging considerations and the timing circuitry which establishes the accepted sample volume. Referring to Figure 64 it would seem that misorientations beyond ±20° would produce unreliable data. In Section 8, we discuss field results in which measured asymmetries in the flow were encountered yet acceptable results produced.

Upon completing the alignment sensitivity study, we were able to scan the tunnel diameter to map the variations in number density and mass loading. As shown in Figure 66 the mass loading was maintained at the same 0.6 gm^{-3} values used for the previous studies of probe orientation. The same velocity was also employed. The results show surprisingly uniform distribution in the aerosol across the tunnel. In the actual impactor/FPSSS comparisons, the two sampling points were at most a few inches apart. The results of Figure 66 would only admit to errors of 10% for siting differences between the measurement techniques.

Tests in Heated Tunnel. Tests in the heated wind tunnel at IERL were made on a limited basis but provided one of two opportunities to observe particulates at temperatures nearer to actual stack temperatures. This tunnel is rather small and is designed to study ESP efficiency. The inlet is rectangular (approximately

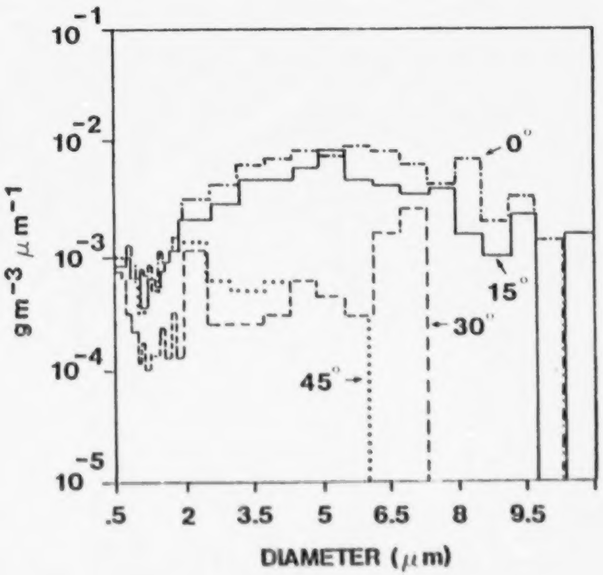

Figure 65. Effects of rotation in windstream on mass-loading. The mass distributions indicate that misalignment results in progressively higher losses the larger the size and alignment error.

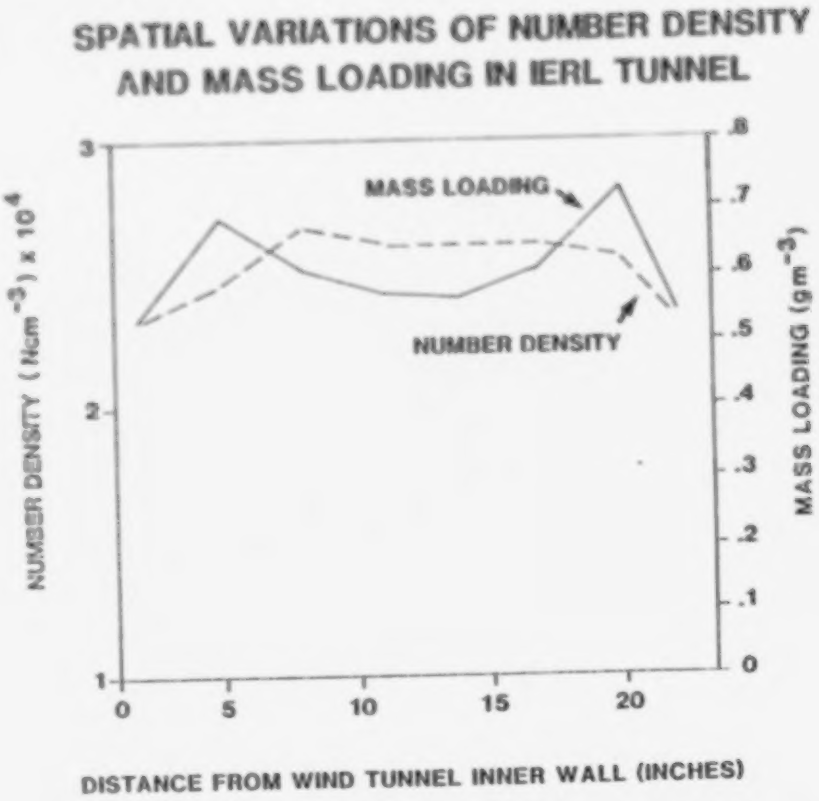

Figure 66. As shown in the figure the tunnel is quite uniform in terms of aerosol dispersal. The higher values near the walls mostly reflect the increase in air speed (measured with the FPSSS) rather than any increased concentration in particulates.

4' x 2') and the flow velocity a relatively slow 1 m sec^{-1}. The same Duke fly ash used in the other tunnel was also dispersed here with a set mass loading of 1 gm^{-3}.

The size and mass distributions characteristic of essentially all of the runs are given in Figures 67 and 68. The integrated mass loading averaged 0.52 gm^{-3}. This lower measured value can be explained in two ways. First, the size distribution revealed that with increasing size there is a faster roll-off in the mass distribution as compared to results given previously (in Figures 57 and 59) for the same fly ash in the other tunnel. This suggests possible loss of the larger particles in the hot tunnel which we attribute to sedimentation. Our measurements were made in the upper part of the inlet cross section. Later, measurements in a lower part of this cross section revealed larger particles and higher mass loadings, a finding that correlates with the second explanation for lower FPSSS mass loadings--uneven distribution in the vertical.

Because of limited access we were not able to profile the tunnel, but we did perform several time series studies. Figure 69 shows a time series of number density and mass loading covering 6 minutes of sampling. Each data point represents either 4 or 12 second averages. The changes in averaging times were made to determine the time scale of the observed fluctuations. As revealed, there is significant structure at both time scales. When we contrast this figure with Figure 63a, we find there is greater variation in the material feed rates, manifesting itself in considerable temporal inhomogeneity. One cannot help but observe what appears to be dropouts in the material flow. For instance, the maximum value of mass loading is invariably close to 1 gm^{-3}; however, values as low as 0.05 gm^{-3} are noted in the 2-second averages. There is a suggestion that there might be times when material is not adequately dispersed but settles to lower levels as clumps. We were able to confirm that a lot of the input fly ash did collect on the floor of the inlet and on the top parts of the FPSSS probe itself with only a short period of exposure. One might suggest further that the truncation of FPSSS measurements at 11 μm could account for the underestimate of mass; but the mass distribution of Figure 68 would not support more than a 15% unaccounted loss unless it were bimodal.

In summary, the FPSSS observed 40-50% lower mass loadings. No other instru-

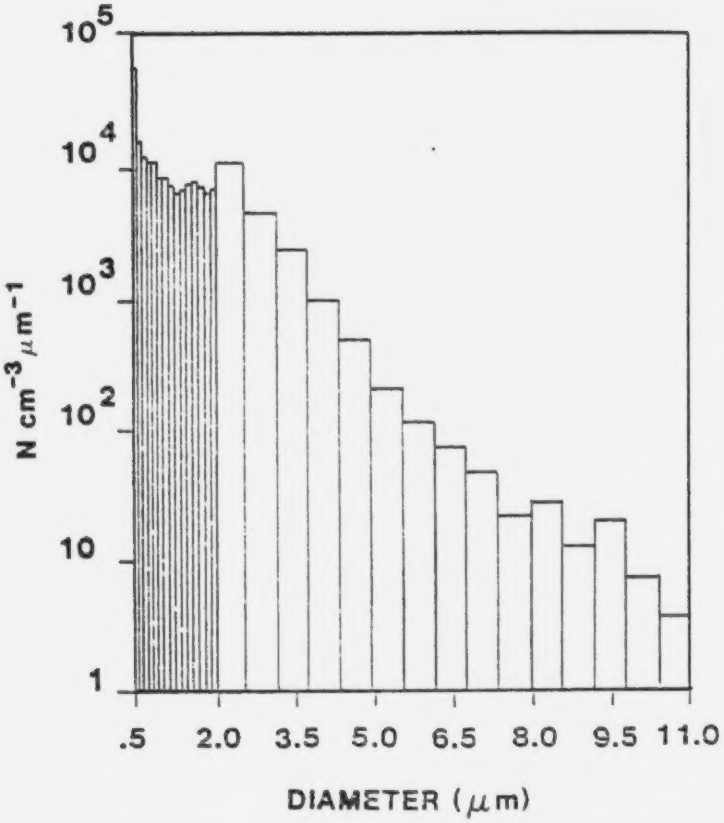

Figure 67. FPSSS size distribution for IERL heated tunnel using Duke fly ash, for run ending at 11:05 on February 8.

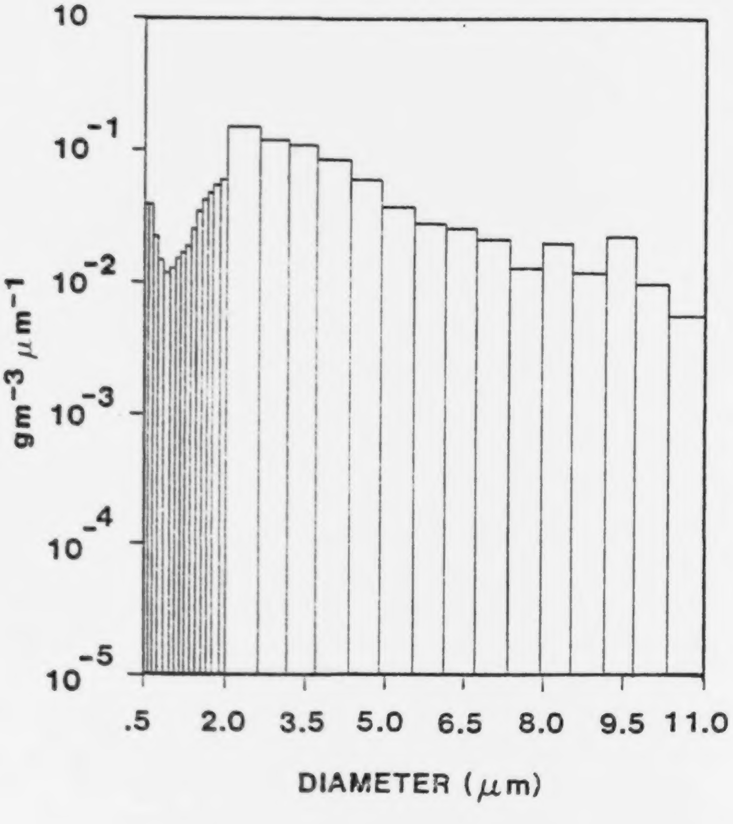

Figure 68. FPSSS mass distribution for IERL heated tunnel using Duke fly ash, for run ending at 11:05 on February 8.

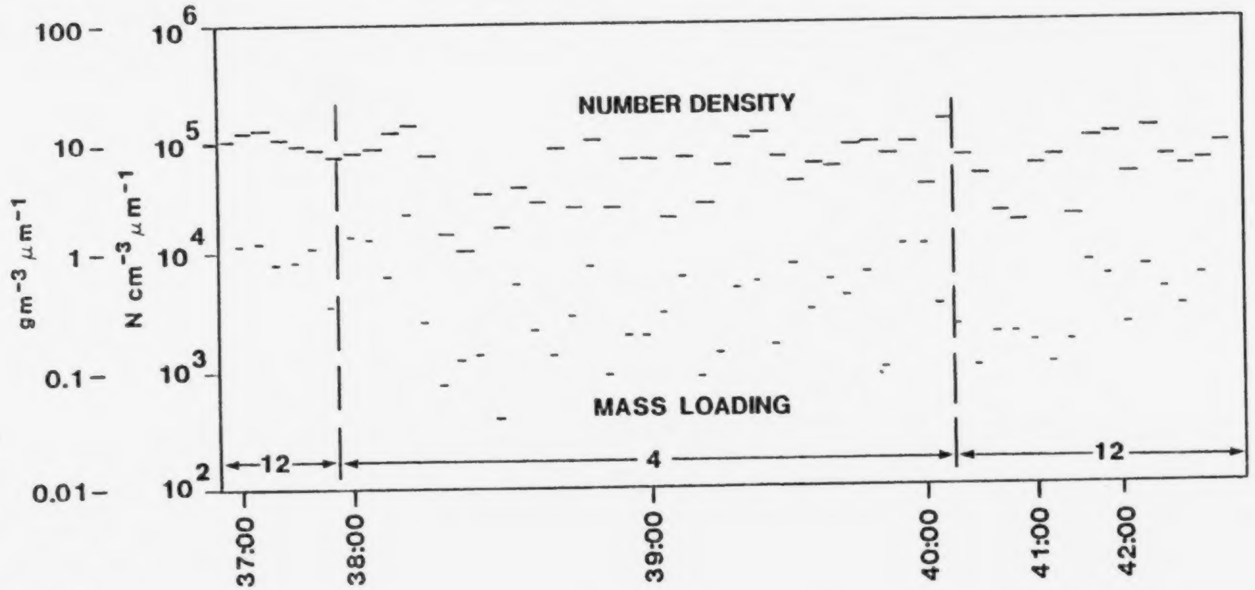

Figure 69. FPSSS time series plot of number density and mass loading for 6 minute run ending at 43:00 on February 8. Note the large fluctuations in number density and mass loading as compared to Figure 63.

ments were intercompared, so conclusions on this phase of the experiment are less definite. The consistent underestimate of mass loading by the FPSSS (compared to input feed rate) may be entirely due to settling losses.

Tests in Fuel Oil Boiler Flue. Tests in the flue of the oil-fired boiler were primarily implemented to provide an entirely different test environment for the FPSSS. The tests were run with #6 fuel oil having ∿ 1% sulfur. The flue velocity varied from 3-4 msec^{-1}. The mass loading was previously determined to vary with the amount of injected water and excess air used in the combustion process; tests were made at 10% and 18% water and with excess air up to 48%.

From prior impactor data, we anticipated the mass loading at 18% water to be 0.06 gm^{-3} and at 10% water, 0.04 gm^{-3}. However, FPSSS measurements gave values at least an order of magnitude smaller--typically only a few mg m^{-3}. Typical size and mass distributions given in Figures 70 and 71 correspond to mass loadings of 0.0065 gm^{-3}. These distributions only cover sizes up to 5.65 μm and perhaps a factor of two increase can be justified extrapolating to larger sizes, but the underestimate will still be quite substantial.

With regard to excess air, the increase in mass loading with decreasing excess air was quite dramatic. Table VII shows that mass loading increases by nearly an order of magnitude for a small reduction in excess air--from 30 to 20%.

TABLE VII

% Excess Air	FPSSS Mass Loading (gm^{-3})
48	0.006
37	0.006
31	0.009
21	0.045

One suspects that the impactor runs were carried out with reduced excess air, but this was not supposed to be the case. The best information available suggested that the predicted mass loadings were more than an order of magnitude higher than that observed by the FPSSS. This might be attributed to a predominance of particulates too small (optically) to be sized or to general undersizing.

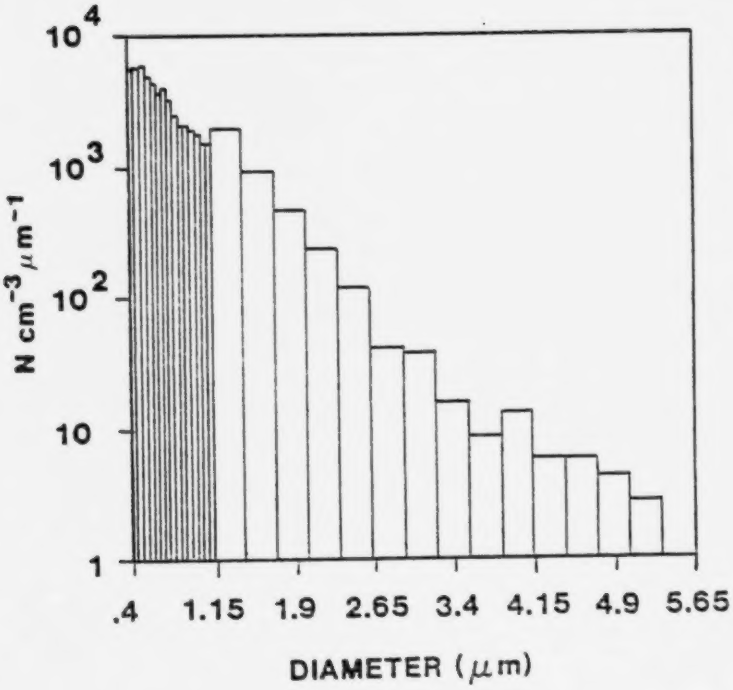

Figure 70. FPSSS size distribution for IERL test in fuel oil boiler flue, ending at 13:00 on February 14.

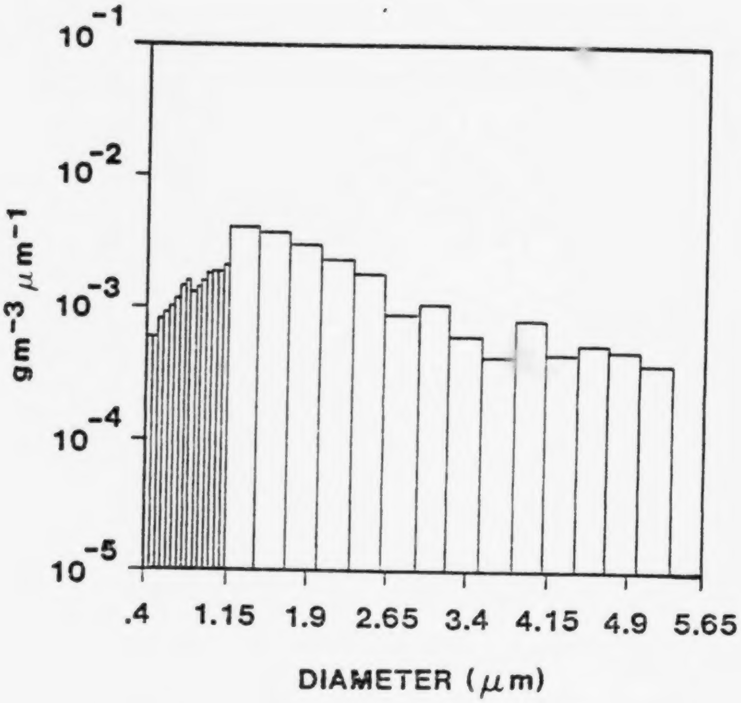

Figure 71. FPSSS mass distribution for IERL test in fuel oil boiler flue, ending at 13:00 on February 14.

While the FPSSS showed poor agreement with the expected result, its relative accuracy seemed reasonable and showed it to be a useful tool for boiler alignment. An error in mass loading of an order of magnitude would require a factor of 2 error in sizing. There is no theoretical basis for such a large undersizing and it cannot be supported by empirical work. We should also point out that the fact that the activity was very low indicated a lower concentration than expected and not simply smaller particles.

8. FIELD TESTING

Field tests of the FPSSS during the course of the contract were conducted at the Colorado Public Service Co. Valmont power plant in Boulder, Colorado, and the Duke Power Riverbend plant at Charlotte, North Carolina. The Valmont power plant served as the primary test site with a variety of short tests during early development as well as final testing with comprehensive impactor intercomparisons. The first full-scale testing at Valmont during April and May 1978 was not with the final electronics and data acquisition system but utilized the same probe head as finally delivered. Size ranges and data processing were different, as will be apparent in the data to be presented. The tests at Charlotte in April 1978 were only partially successful due to a pre-amp failure in the FPSSS which necessitated the more comprehensive final study at Valmont. The final tests at Valmont during September 1979 provide the best overall data set in terms of quality and quantity.

8.1 Initial Testing at Valmont Power Plant

The first field tests of the FPSSS in-stack were conducted at the Valmont power plant on the afternoon of April 24, 1979. The Valmont plant is a 300 MW coal-fired power plant where general operation and control devices are similar to those depicted in Figure 72. Measurements were performed at the 80 foot level on the stack, affording good access. At this level a Lear Siegler Model RM41 Opacity Monitor was also operating. These initial tests were limited to an hour of measurement time and the entire set-up, measurement, and pack-up were completed in less than two hours.

The FPSSS was operated with a set of electronics borrowed from a PMS Model CSAS-100 instrument.* The pulse height analyzer was configured to provide four size ranges of 15 channels each as follows:

	Size Range	Size Interval
Range 1	2.5 - 10 μm	0.5 μm
Range 2	1 - 5.5 μm	0.3 μm
Range 3	0.5 - 2.0 μm	0.1 μm
Range 4	0.4 - 0.85 μm	0.03 μm

---

*Note that these measurements preceded those at IERL discussed in Section 7.

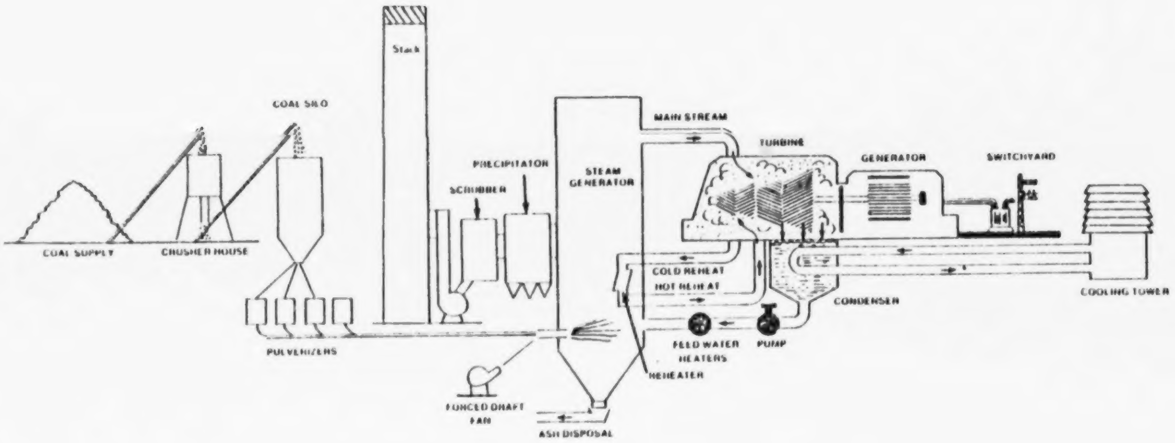

Figure 72. Schematic drawing of a steam electric generating station.

All size intervals were linear, with maximum resolution in range 3 being 0.03 μm. The ability to switch ranges was found to be particularly important in field measurements. Calibrations with particles of known size had been performed previously using latex spheres and glass beads.

The FPSSS performed satisfactorily in these first tests. Samples were taken at two-foot intervals across the diameter of the stack to within 5 feet of the far side. We elected not to extend the FPSSS to its full boom length because of large oscillations induced by gusts inside the stack. We later performed structural tests to determine the maximum loads the boom could withstand fully extended. These tests suggested a heavier wall thickness was needed. After these tests the wall thickness was increased on the final two boom sections.

The stack temperature was 260°F. No difficulty was found in operations at this temperature. For these tests the external 7.5 cm radius mirror was purged but the window was not in order that we could determine its potential exposure problems. The window's accumulated particulates resulted in a 25% loss after an hour's operation. The window had an aerodynamic shield which wind tunnel tests indicated would be quite effective; however, the stack turbulence obviously reduced its effectiveness. A purge-shield fitting similar to that on the 7.5 cm mirror was designed and installed on the FPSSS. We decided to over-pressure the region around the two beam folding plane mirrors as a result of this initial experience. Although no contamination was observed internally, the high humidity in the stack penetrated into this cavity and condensed on the inner side of the window when later extracted and allowed to cool. The above indicated changes were also after completion of these tests.

Measurements were taken at two-foot intervals from 3 to 17 feet in-stack penetration. The stack had an I.D. of 21 feet and we did not have sufficient boom to reach completely across. However, the measurements revealed a symmetric profile of particle flux, and the lack of measurement over the final four feet was not regarded as significant.

Velocity measurements were manually computed from average pulse width measurements. The in-stack velocity profile revealed a greater amount of turbulence than anticipated with gusts of 5 m $\sec^{-1}$ common near the stack center. The mean flow varied from 3 to 12 m $\sec^{-1}$; the highest values were at the center.

No regions of reverse flow could be identified.

The particle size distributions measured at 2 foot intervals were surprisingly uniform as viewed on the CRT spectral display of the CSAS-100 electronics console. In fact, once corrections for variations in flow rate were made, the distributions revealed only minor spatial spectral differences which were of the same order as temporal changes at a fixed location. For this reason, all measurements were integrated together to generate a single average particle size distribution representative of the entire stack (see Figure 73). The particle size distribution is seen to be highest in number at the smallest size (0.4 μm), although the slope is decreasing. The overall slope was quite steep, eliminating the utility of range 1 due to low count statistics. A size distribution with such a steep slope is characteristic of air passed through coarse filters and is steeper than background ambient aerosol size distributions.

The computed average distribution of extinction cross section (2nd moment) as a function of particle size is given in Figure 74. The extinction cross section was computed for a wavelength of 5500 Å in an effort to make comparisons with the opacity monitor operating with a white light source having its spectral maximum at this wavelength. The extinction cross section is seen to peak at sizes of 0.6 μm and has a volumetric integral value of $3.0 \times 10^4 \times \mu m^2\ cm^{-3}$. The integrated cross section over the 6 meter stack diameter provides a computed transmission of 0.83 or an opacity of 27%. The Lear Siegler RM41 had comparable opacity values of 24 to 36% during the period of measurement, as revealed in Figure 75.

The close agreement between the Lear Siegler RM41 and the FPSSS opacities must be regarded as fortuitous at this time. A certain amount of particle cross section also exists below the 0.4 μm lower limit of sensitivity, although probably less than 10% of the total. The exact spectral characteristics of the Lear Siegler RM41 were not available, and in this size range extinction is a strong function of wavelength. Furthermore, an ideal transmissometer still gains contributions from multiple scattering that were neglected in our treatment. Finally, the soiling of the window resulted in a small but obvious underestimate of particle size and opacity.

The average particle volume (mass) distribution (3rd moment) is given in Figure 76a. This is probably the most interesting of all the spectral plots. It

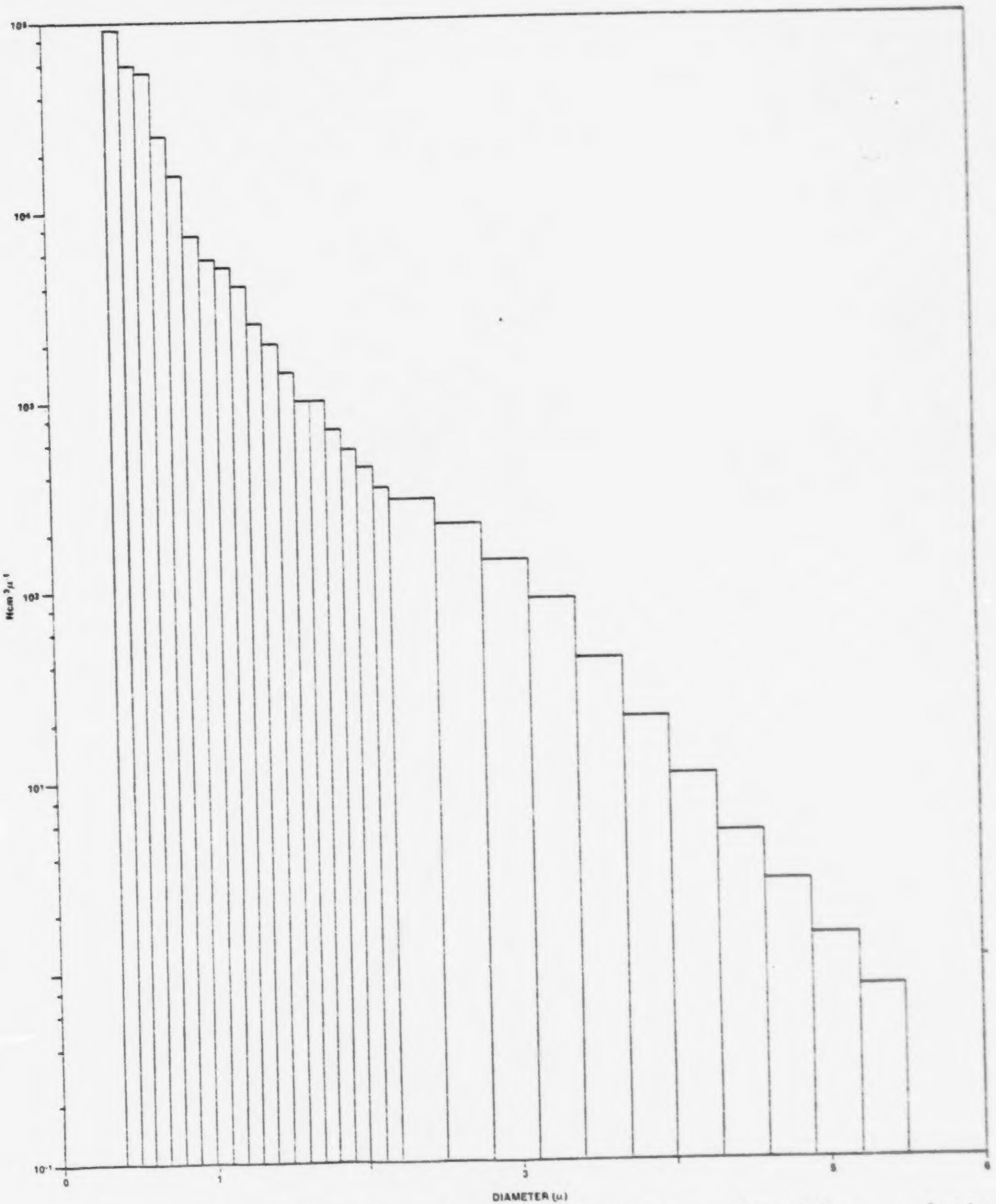

Figure 73. Average in-stack size distribution. The higher resolution data for size range number 3 has been summed into 0.1 μm size classes.

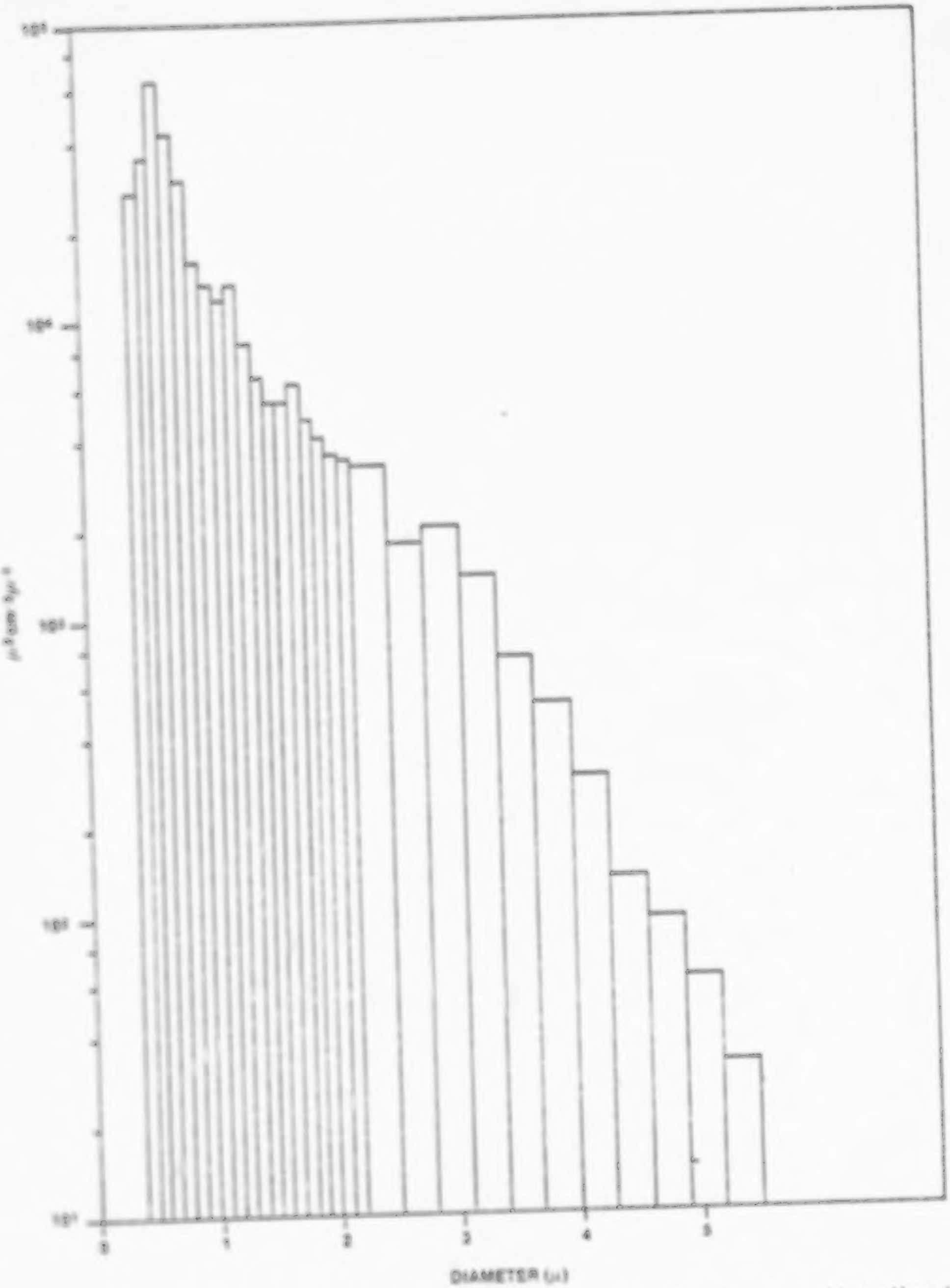

Figure 74. Average in-stack extinction cross section distribution. The higher resolution data for size range number 4 has been summed into 0.1 μm size classes. The mean cross section size is 0.79 μm.

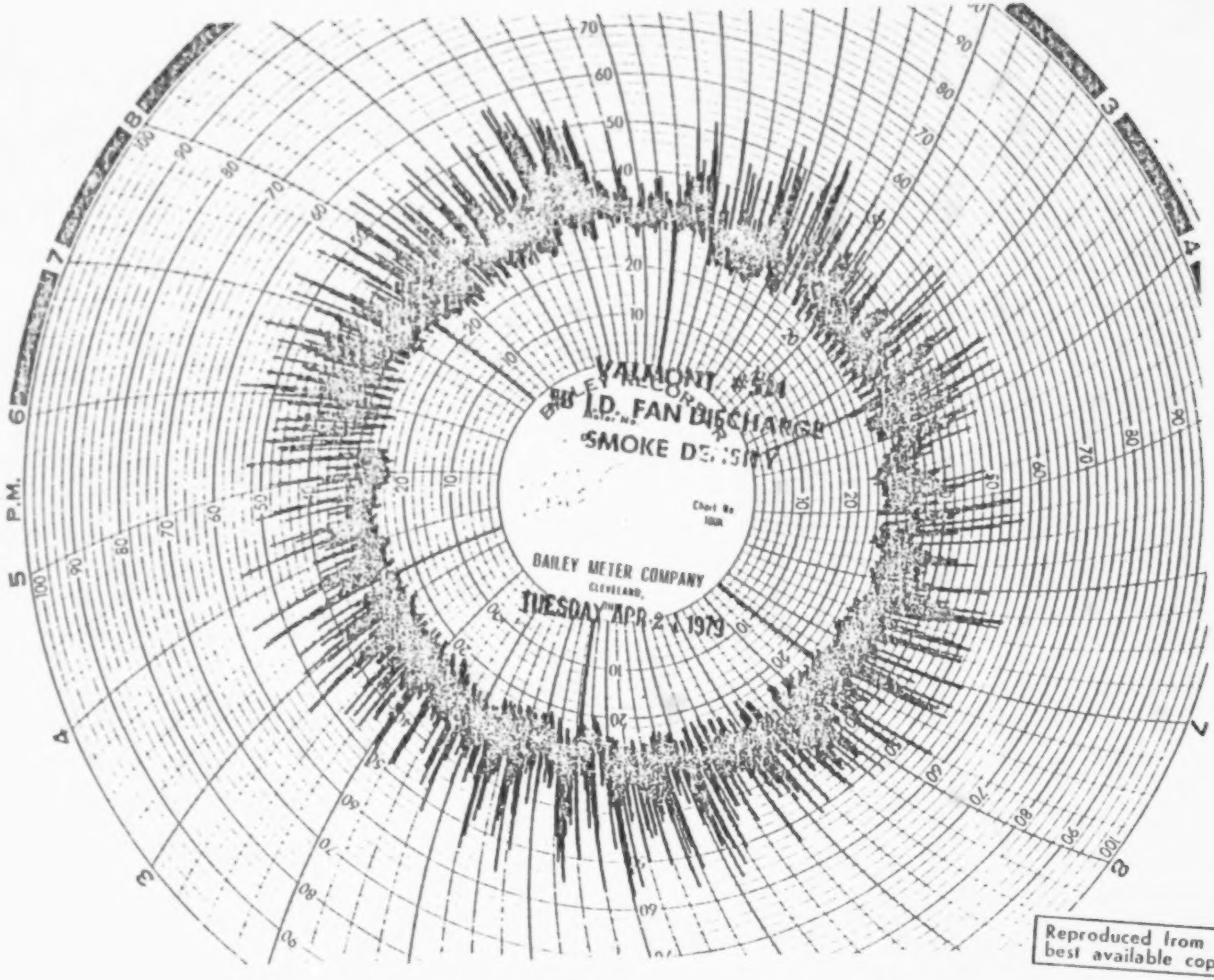

Reproduced from best available copy.

Figure 75. Lear Siegler RM41 opacity record for April 24, 1978 between 14:00 and 15:00, during which the FPSSS performed measurements in the stack. The sharp spikes in the data record are related to the rapping cycle, which is further discussed in Section 8.3.

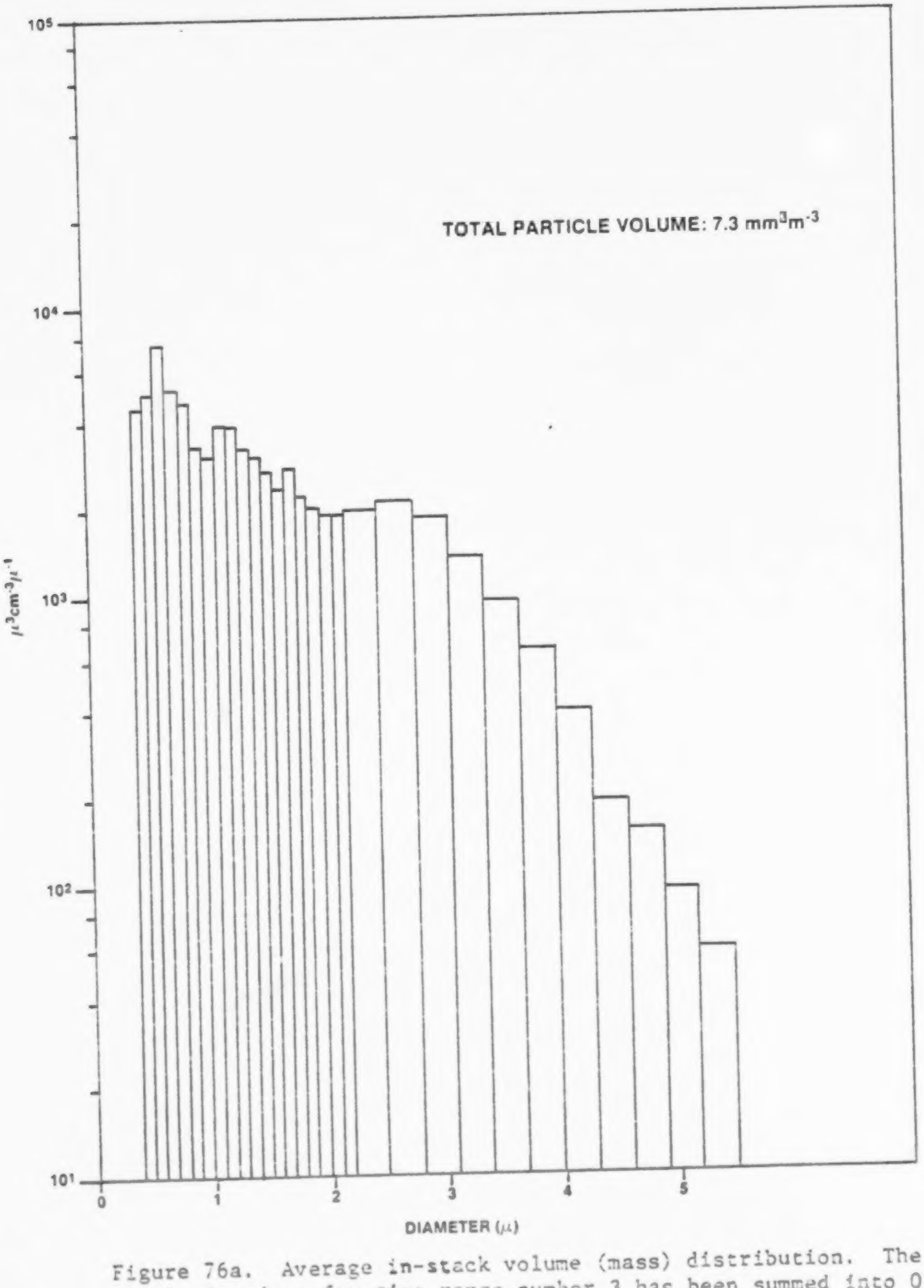

Figure 76a. Average in-stack volume (mass) distribution. The higher resolution data for size range number 3 has been summed into 0.1 μm size classes. The mean volume (mass) size is 1.31 μm.

reveals several dominant mass modes, each being statistically valid. Perhaps most surprising is the dominant mass mode at 0.65 μm. It is more striking when presented with the full resolution of range 4 as shown in Figure 76b. Here there is little doubt that the FPSSS has captured nearly all of the mass. The integrated mass loading was lower than anticipated, being on the order of 0.01 to 0.2 gm m^{-3}, depending on the assumed density. The known undersizing due to the soiled window should have only resulted in underestimates of mass less than 30%.

We expected mass loadings nearer a tenth of a gram; however, the only way in which higher mass loading values would be compatible with opacity values of less than 20% (regulatory compliance value) would be with an increase in size and decrease in number density over that observed. A simple increase in size of a factor of two provides an eight-fold mass increase but also a four-fold increase in cross section and opacity. Since the mass-to-cross-section ratio is proportional to radius, or size, it is necessary to increase size by a factor of 10 and decrease concentration by a factor of 100 to maintain the same opacity by a factor of 10 higher mass loading. Either of the above is totally unreasonable from an instrumental standpoint. We were thus left to conclude that this particular stack did indeed have a lower than expected mass loading, characterized by particles of about 1.3 μm diameter.

These initial measurements were, of course, of great interest. The measurements revealed a fairly uniform concentration across the stack. Within the operating range of 0.4-5.5 microns, the number density averaged 50,000 cm^{-3}. The size distribution indicated the maximum number density at the smallest size whereas the peaks in the extinction cross section and mass distribution were at 0.79 microns and 1.3 microns, respectively. The computed mass loading was only 0.01 to 0.2 gm m^{-3} -- much smaller than expected. However, the integrated extinction cross section produced an integrated opacity of 17%, in close agreement with the opacity monitor reading of 14-16%. These results are fortuitous in that corrections for the reduction in sensitivity due to window contamination were not made and the exact transmission properties of the Lear Siegler opacity monitor were not known; overall, the results were regarded as preliminary, but extremely encouraging.

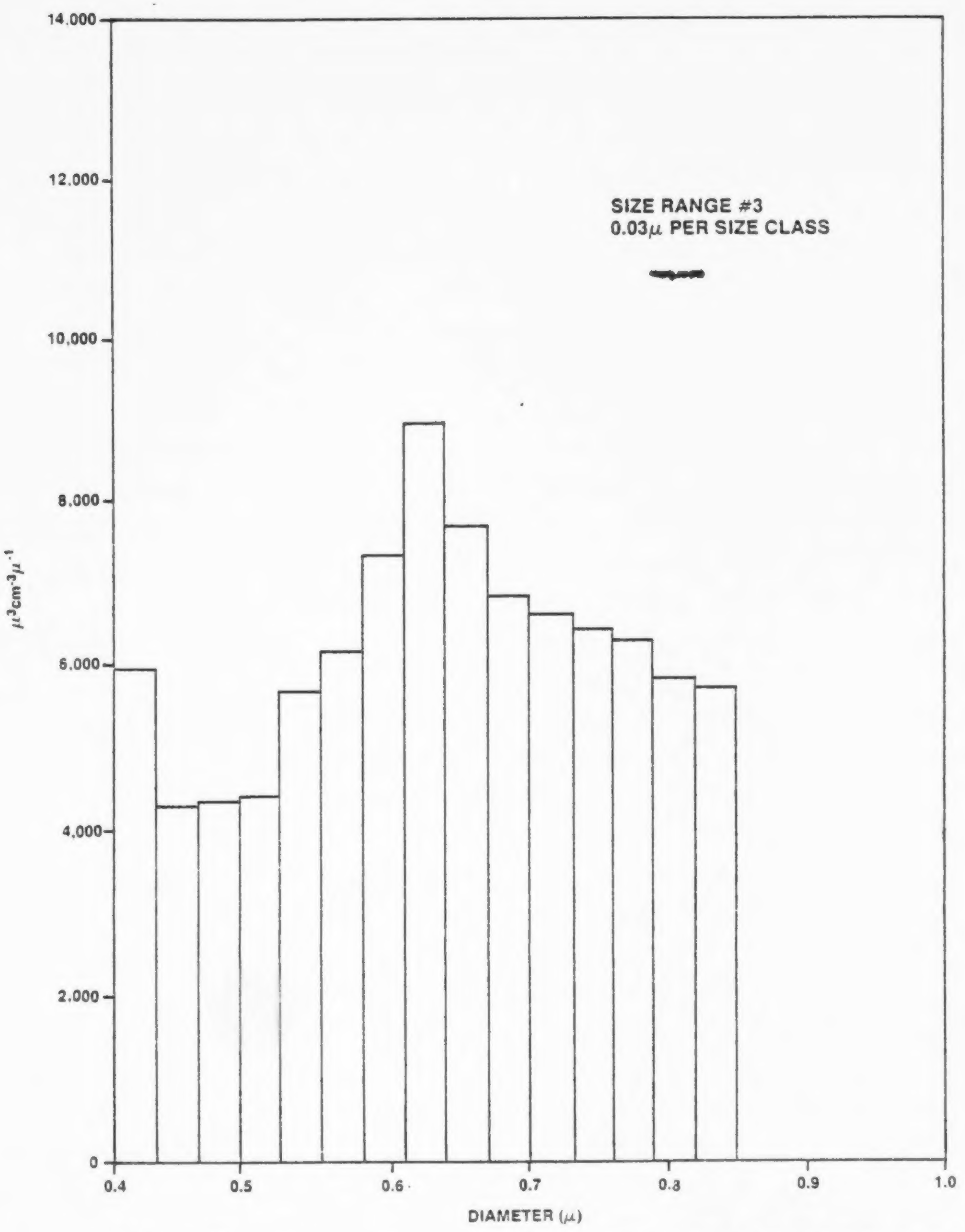

Figure 76b. Average in-stack volume (mass) distribution from 0.4 to 0.85 μm.

On May 11, 1978 a second set of field measurements was performed at the Valmont power plant to obtain data upstream of the control devices. These tests were conducted at two locations on the input to the scrubber and precipitator. When compared to the previous in-stack measurements the results indicated a significant difference in particle size distribution when plotted as a volume (mass distribution). Most noticeable was the abundance of particles larger than 5 microns which were essentially completely absent in the stack. A mean mass size of 4 microns was found as compared to 1.3 microns in the stack. Perhaps most importantly comparing the two mass distributions revealed an efficiency between 95 and 99% in the mass removal above 3 microns but little apparent efficiency at the submicron sizes, shown in Figure 77 as a removal efficiency plot. The data are of course only approximate in that over two weeks elapsed between the pair of measurements. However, the opacity values were nearly identical and no change in coal or operating parameters had taken place; thus, the measurements should be characteristic of conditions at both times.

8.2 Field Tests in Charlotte, North Carolina

An attempt was made on April 17, 1979 to perform comparative measurements with the FPSSS and impactors on a coal fired power plant at Charlotte, North Carolina. This is the Duke Power Riverbend coal fired generating station which has previously been used as a test site for EPA studies. Measurements with the FPSSS were only performed on one day due to the failure of a programmable amplifier in the probe head and the lack of suitable spares. This short period of measurements is discussed here primarily in the interest of being complete. Impactor data analysis was performed by personnel from Northrup Services.

On the 17th, three impactor runs were made, each of 45 minute sample duration, initiated at 10:15, 13:00, and 14:24 LT. The mass loadings measured by the impactor and FPSSS are summarized in Figure 78. A single FPSSS point was obtained around noon and seven samples taken after 14:00. The FPSSS indicated that the mass loading was approximately 2½ times less than the average of the first two impactor runs. In the afternoon period the first FPSSS run at 14:20 was nearly an order of magnitude higher in mass loading than subsequent runs; its value was 13 mg m^{-3}. In this period the FPSSS was set up to

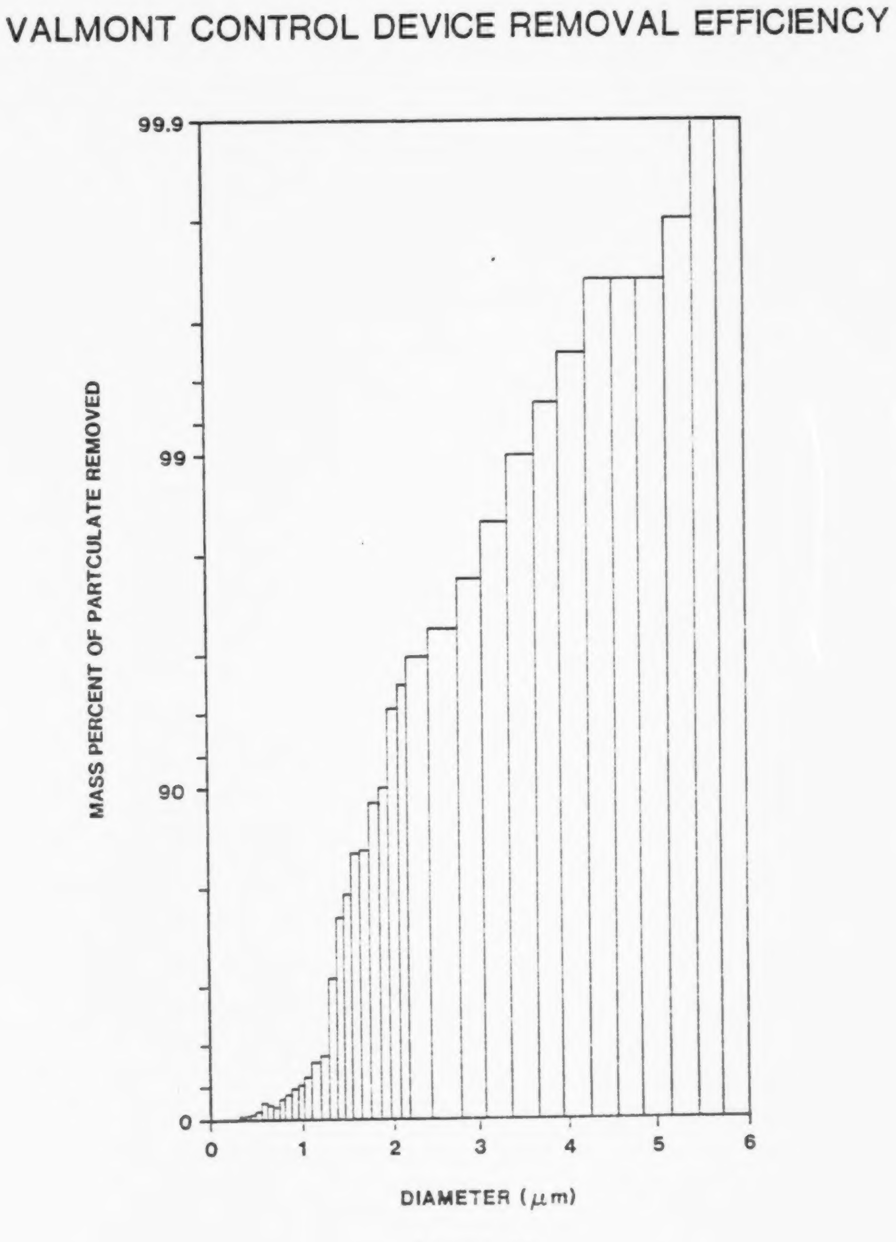
VALMONT CONTROL DEVICE REMOVAL EFFICIENCY
MASS PERCENT OF PARTCULATE REMOVED
99.9
99
90
0
0
1
2
3
4
5
6
DIAMETER (μm)

Figure 77

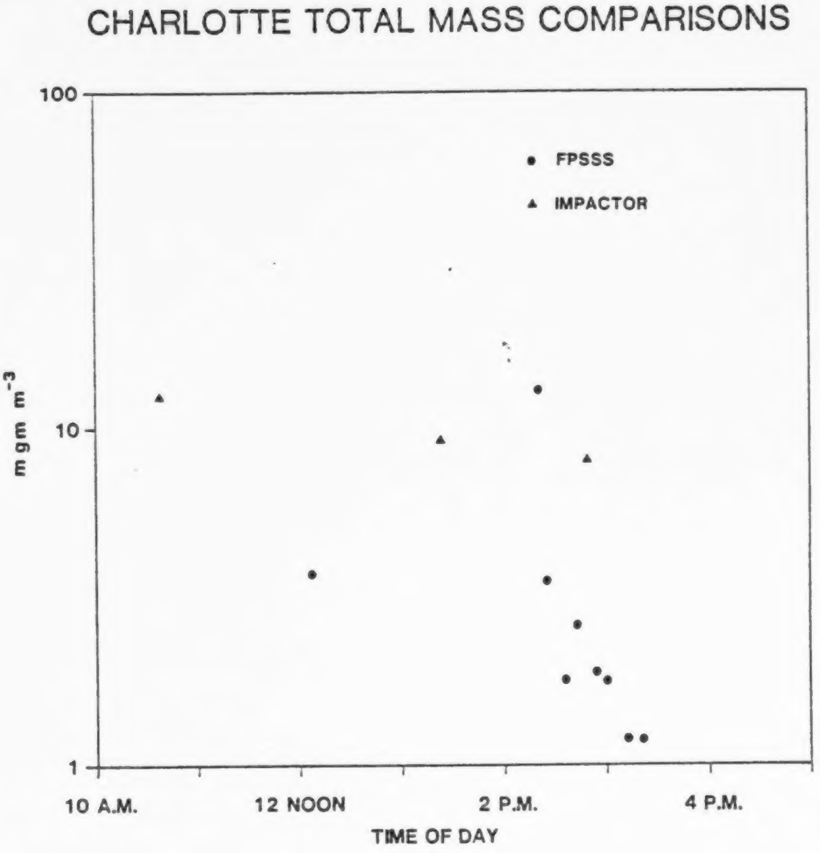
CHARLOTTE TOTAL MASS COMPARISONS
● FPSSS
▲ IMPACTOR
100
10
1
m gm m^{-3}
10 A.M.
12 NOON
2 P.M.
4 P.M.
TIME OF DAY

Figure 78

sample for four minute periods, and considerable variability in measured particle activity was noted. Our analysis of these data has shown that the FPSSS sample intervals were much too short to provide statistical coverage of the stack temporal variability. The size and mass distributions measured by the FPSSS are shown in Figures 79 and 80. Both distributions are extremely steep and, because of the relatively small particle size observed, only the 0.4 to 5.65 micron range was utilized. The only change noted in the size and mass distributions at other times was the reduction in the number of particles. However, the total number density was approximately four times higher for the run at 14:20 LT, which thus largely accounts for its higher number density and mass loading values.

The steepness of the size distribution increases the potential error in mass computations, and in this case the mass distribution rolls off nearly two decades between 1 and 2 microns; thus an undersizing error of only 10% could account for a factor of two in mass. It is also important to examine the impactor data accumulated: 16, 12, and 10 milligrams for each of these three runs. These values are regarded as much lower than desired for gravimetric analysis.

Turning back to the size and mass distributions in Figures 79 and 80, it is interesting to compare these with those measurements at the Valmont power station presented in Figures 73 and 75. The Riverbend data are slightly steeper, with over four decades of roll off in number density between 0.4 and 2 microns. The average number density is less than that found at Valmont, as was the loading, mean mass size, and computed opacity. The range of opacity values computed for the Riverbend plant was from 1% to 3%.

Both Riverbend and Valmont give a significantly steeper distribution than obtained during the IERL wind tunnel test series. Of course, the feed fly ash used at IERL is the material removed between precipitators instead of that which passes through. Comparison of the mass distributions between the FPSSS and the impactors is shown in Figures 81 and 82 for the sum of impactor runs 2 and 3 and the average of the first four afternoon FPSSS samples. The accumulative mass distribution in Figure 82 shows the expected difference due to the 0.4 micron cut-off of the FPSSS. Comparison of sizes larger than 0.4 μm would show reasonably good agreement up to about 1 to 2 microns. Above 1 to 2 microns the impactor data indicate the presence of considerable mass, which is not noted

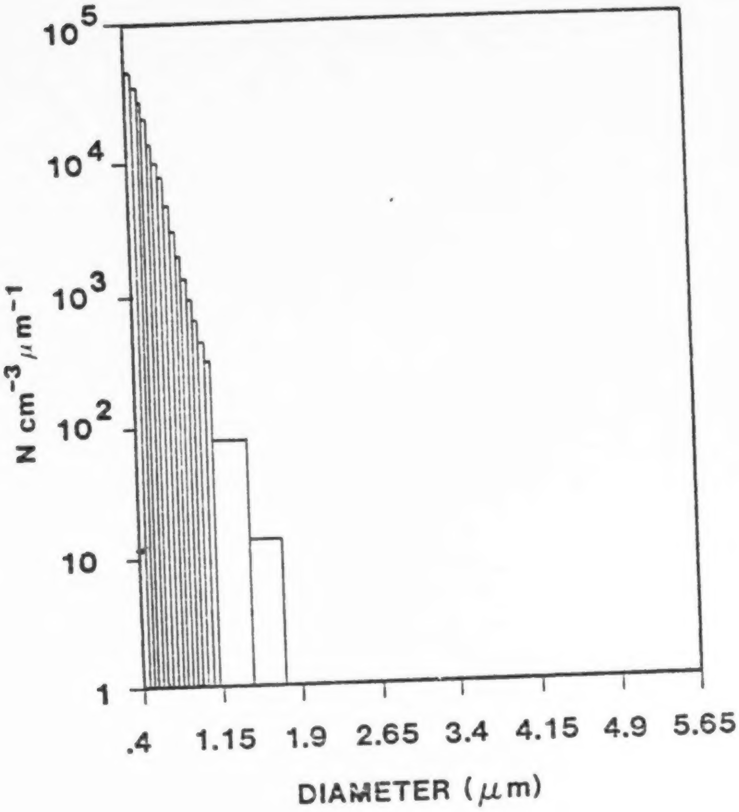

Figure 79. FPSSS number density for sample run ending at 14:55 on April 17.

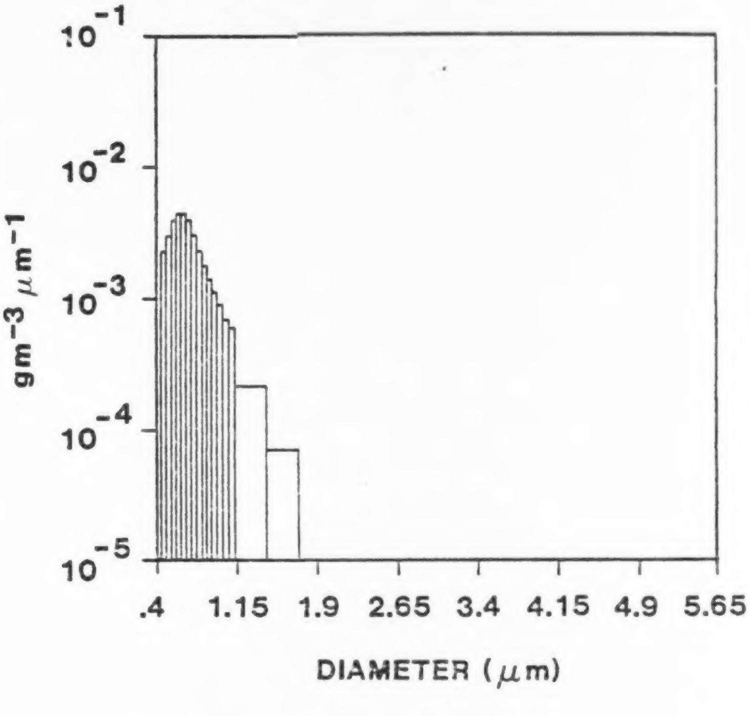

Figure 80. FPSSS mass loading for sample run ending at 14:55 on April 17.

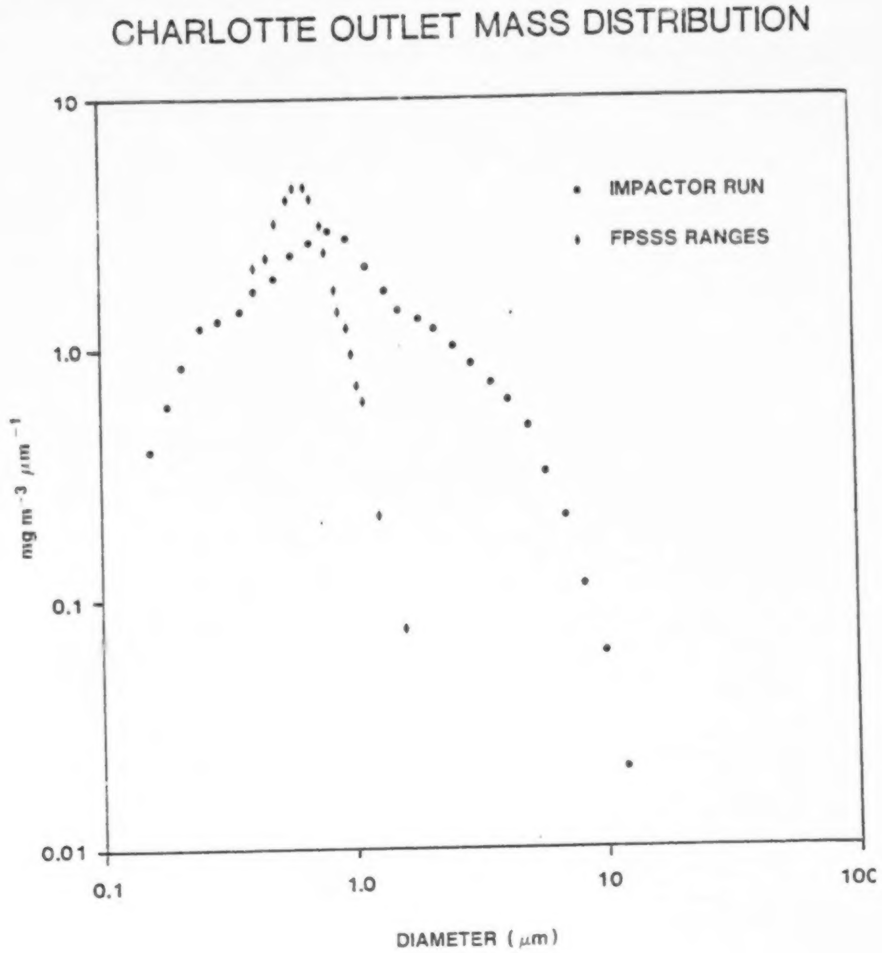

Figure 81. Note the large decrease in mass distributions at sizes larger than 1 micron for the FPSSS relative to the impactor data.

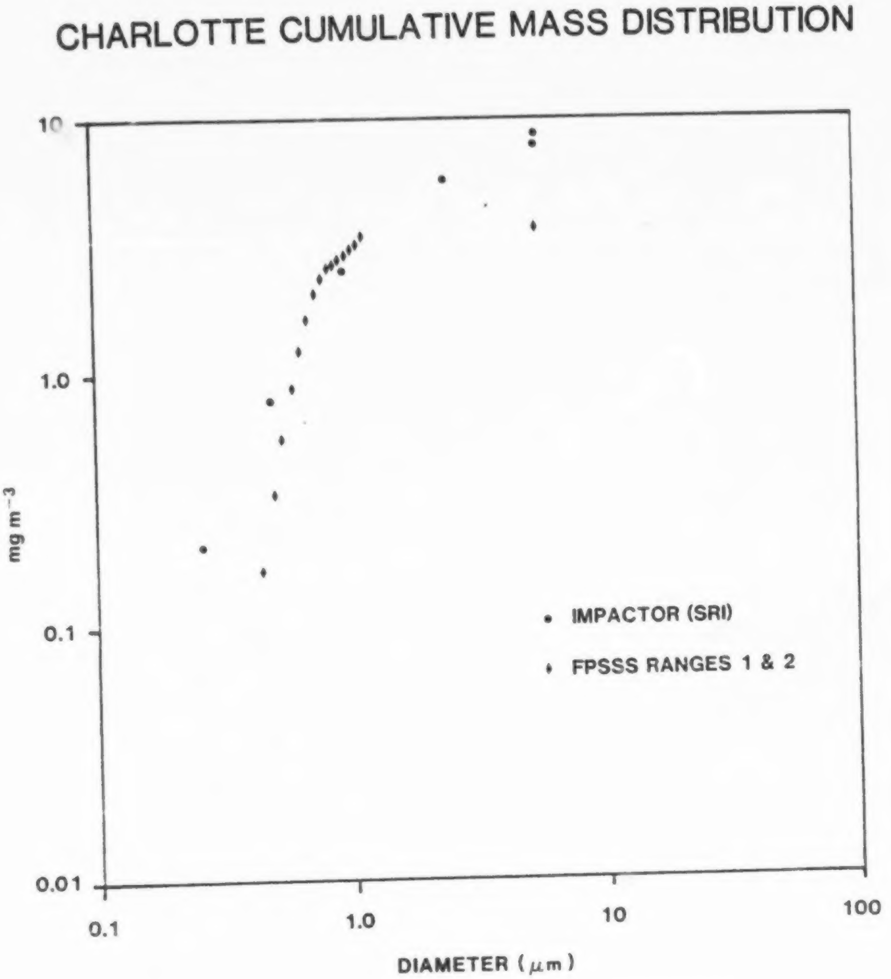

Figure 82. The above comparison illustrates the effects of the 0.4 micron lower limit of the FPSSS and the lack of mass contributions at sizes larger than 1 micron more easily observed in Figure 81.

in the FPSSS data. This is more readily observed in Figure 81 which also shows a much larger contribution of particles of about 0.4 to 1.0 micron diameter than observed by the impactor.

In summary, the data must be considered of a spotty nature due to the limited time of FPSSS operation. The integrated mass and opacity values from the FPSSS are in reasonably good agreement with those derived from the impactor. The size spectral data show, however, considerable mismatch at the larger sizes which is difficult to explain from this data set alone. It is, however, a systematic difference that we see exhibited in other field comparisons between impactors and the FPSSS.

8.3 Final Tests at Valmont

Final field testing of the FPSSS was completed at the Valmont power plant on September 13-15, 1979. Testing was done at both the precipitator inlet and the stack. Primary comparison was with impactor measurements made by Southern Research Institute (SRI). Initial FPSSS comparisons were made in mass loading (with impactors) and opacity (with opacity meter). After analysis of the impactor data by SRI, size distribution comparisons were also made. Transient phenomena were particularly well characterized with the FPSSS during these tests.

The impactors sampled the inlet and the outlet streams of the ESP control device system in parallel with sampling by the FPSSS. University of Washington Mark III Cascade impactors with grease substrates were used exclusively. The flow rate was 0.3 ACFM with a 3/16" nozzle, giving a sampling velocity of 7.5 m sec^{-1}.

During the testing the boiler was stable at 165 MW, burning Rosebud coal with 0.7-0.9% sulfur content. At the inlet ports, the gas stream exited the air heaters at 138°C through two 8.5 x 1.8 meter ducts approximately 3 meters in length. Impactor sampling was performed from above and near the center of one of these ducts with the FPSSS in the adjacent port 1 meter away. The gas velocity at this point was found to vary between 7.6 and 10.1 m sec^{-1}.

The outlet sample ports were in the stack at the same location initially sampled. The temperature was 121°C. The impactors and the FPSSS were inserted to a depth of 3 m at diametrically opposite sides of the stack, leaving about 0.6 m between the two instruments.

These tests were designed to provide coverage for impactor intercomparisons that were lacking or incomplete in prior tests at Valmont and Riverbend. Three impactor runs were conducted on the stack outlet and four at the precipitator inlet at essentially the same sampling points as those conducted in the first test series in April, 1978. Of particular significance to the results obtained during this test series was the fact that the scrubber was off-line during all of these tests and one of the five banks of precipitators was also non-functional. Stack emissions were considerably higher than in prior visits, evidenced by careful scrutiny of the appearance of the plume as well as in the actual measurements. The set-up time on the impactor sample runs as well as data quick checks allowed for other tests using the FPSSS to be conducted between runs. Of particular interest here were time series outputs of mass loading, number density, mass median diameter, and opacity that were correlated with the rapping sequence used on the precipitators.

In addition to the FPSSS and impactor data we were able to compare the Lear Siegler RM41 opacity meter with the FPSSS values on a near real-time basis. Also on September 15 we were able to use a CSAS-100-HTS (CSAS-100 modified for flue gas sampling with a hot test section) to monitor the outlet while we were making inlet runs. The CSAS-100-HTS has greater time resolution than the FPSSS and provided further detail on the precipitator rapping sequence. Finally, the last impactor run from both the precipitator inlet and the stack outlet was analyzed by optical and scanning electron microscope as an aid in interpreting comparative results.

Prior to measurements at either the stack outlet or the precipitator inlet, velocity profiles were taken with a pitot boom arrangement furnished by SRI and with the FPSSS velocimeter. Of particular interest were the velocity measurements in the stack which revealed a rather asymmetric flow and about a factor of two higher velocities on the south port (where the FPSSS was eventually located for all measurements) as compared to the north port (impactor sampling location). Figure B3 shows the measurements taken by the FPSSS and pitot systems. Of course, the two measurement systems could not be co-located during either the velocity measurements or the sampling runs. Because of variations in what appeared to be average stack draft velocities, it was necessary to monitor the FPSSS velocimeter and enter an estimated average velocity for each sample run.

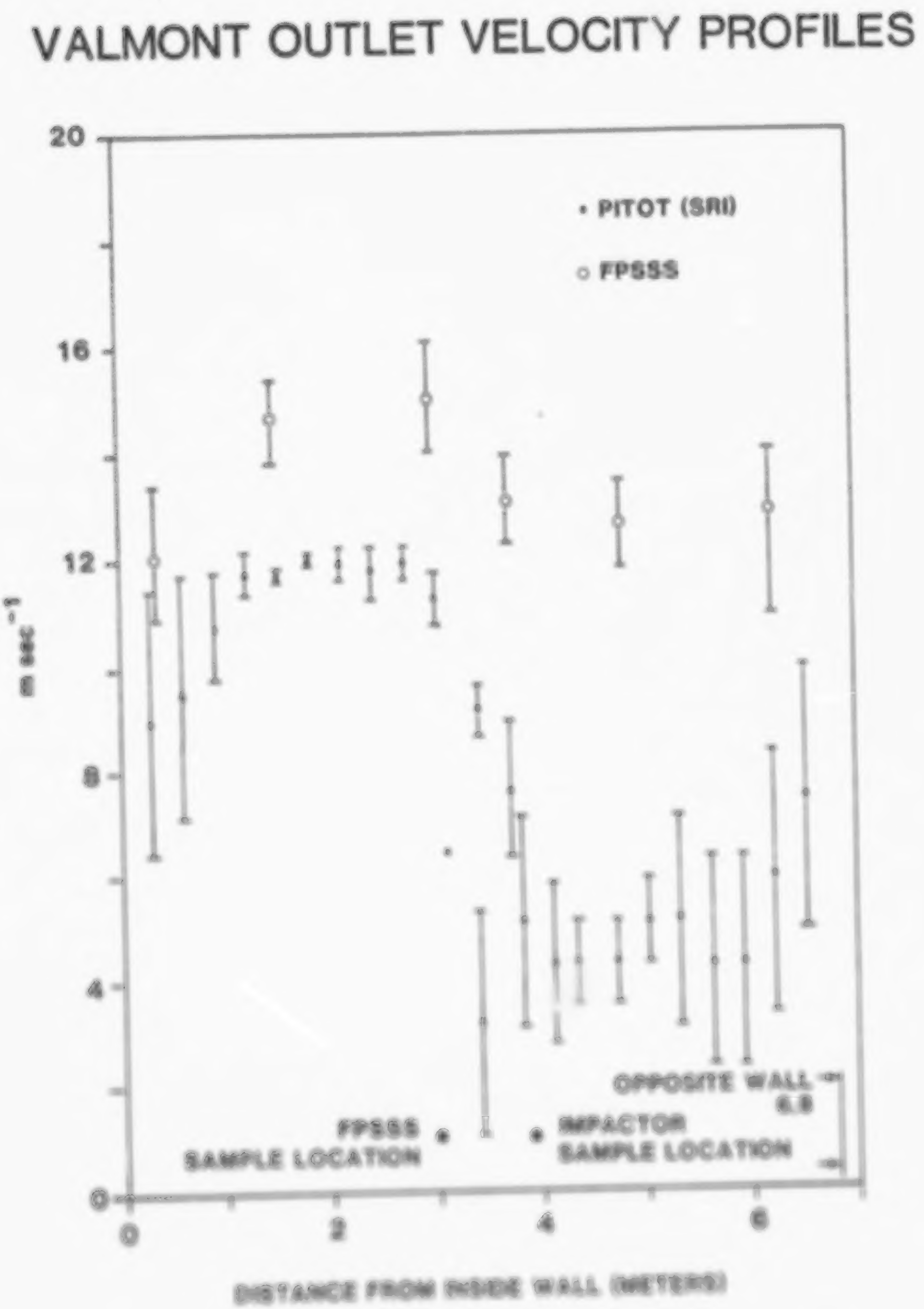
VALMONT OUTLET VELOCITY PROFILES
• PITOT (SRI)
○ FPSSS
20
16
12
8
4
0
m sec^{-1}
FPSSS
SAMPLE LOCATION
IMPACTOR
SAMPLE LOCATION
OPPOSITE WALL
6.8
0
2
4
6
DISTANCE FROM INSIDE WALL (METERS)

Figure 83.

TABLE VIII

SUMMARY OF VALMONT FPSSS, IMPACTOR, & OPACITY DATA

Run	FPSSS (mg/m^3)	FPSSS Opacity %	FPSSS MMD (μm)	(L.S.RM41) Opacity	Impactor (mg/m^3)	Impactor MMD (μm)
Outlet				Outlet		
1	140.0-L 46.5-S	44 -L 33 -S	2.99 -L 1.37 -S	34	53	4.6
2	71.2-L 65.0-S	34 -L 36 -S	2.10 -L 1.27 -S	35	58	4.2
3	79.0-L 62.3-S	27 -L 35 -S	2.89 -L 1.78 -S	34	62	5.0
Inlet						
1	236.0-L		1.88 -L	32	1800	3.4
2	290.0-L		2.20 -L	32	2700	3.6
3	693.0-L 323.0-S		2.0 -L 2.1 -S	35	1300	3.3
4	332.0-L		2.1 -L	35	980	3.3

-S Indicates FPSSS Ranges 1 & 2

-L Indicates FPSSS Ranges 3 & 4

MMD Mass Median Diameter

It is noteworthy that the FPSSS in general gave higher velocities than the pitot system; however, the pitot system is a directional sensor, whereas the FPSSS velocimeter measures the resultant velocity through the laser beam irrespective of direction. Using the pitot we were able to determine that flow components other than axial were generally measurable. Thus, the higher velocity values for the FPSSS are probably more correct for use in its data interpretation than simply using the prior pitot measurements.

Table VIII summarizes the FPSSS and impactor measurements and provides a direct comparison of integrating mass loading and FPSSS and RM41 opacity values. During the first day, two impactor runs were made at the outlet late in the afternoon (#1 and #2). On both of these runs the FPSSS produced four separate reports overlapping each impactor run. For outlet run #1 the 0.5 to 11 micron size range was used on the first report, followed by three reports using the 0.4 to 5.65 micron size range. On outlet run #2, we used the 0.5 to 11.0 micron size range for the first three reports and the 0.4 to 5.65 micron size range for the last report. The size distribution as measured by the FPSSS is given in Figure 84 and the mass distribution in Figure 85. This distribution reveals a much broader size and mass spectrum than previously observed; however, we were not surprised in view of the shut down scrubber and precipitator malfunctioning. We will later see that in fact the mss peak from 8 to 11 microns is an artifact of heavy EMI induced by particle chrge accumulation on the FPSSS and corona discharge through the electronics cosole. It is noteworthy that the distributions observed on the 0.4 to 5.65 miron range at 14:11:01 shown in Figures 86 and 87 reveal a much steeper distibution than the same portion shown in Figures 84 and 85, where the 0.5 to 1 micron range was used. Approximately three times as much mass loading wasobserved on the 0.5 to 11 micron range as compared to the 0.4 to 5.63 micro range. It is also worth noting that the mass median diameter is approximately twice as large on the 0.5 to 11 micron range as compared to the 0.4 to 5.63micron range. The impactor total mass value of 53 milligrams is in good ageement with the three FPSSS reports using the 0.4 to 5.63 micron range. We wil defer discussion of impactor based size and mass distribution with the FSSS until later.

The second impactor run follows completion of the first run by two hours. The size and mass distributions observed by the FPSSS were only slightly dif-

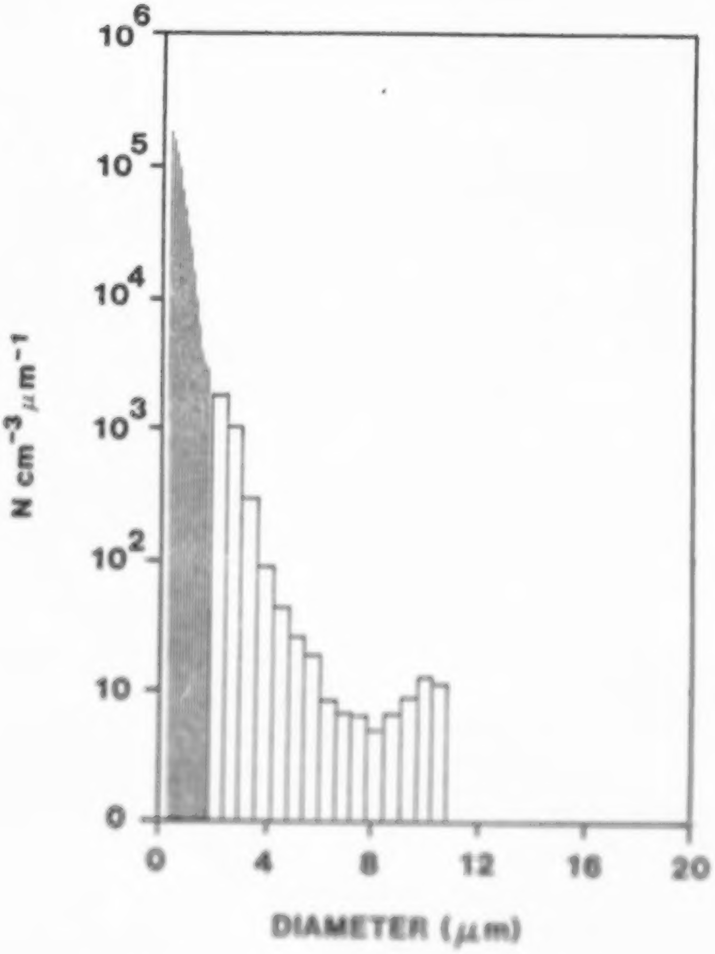

Figure 84. Average FPSSS size distribution observed using ranges 3 and 4 during first impactor run (Valmont outlet).

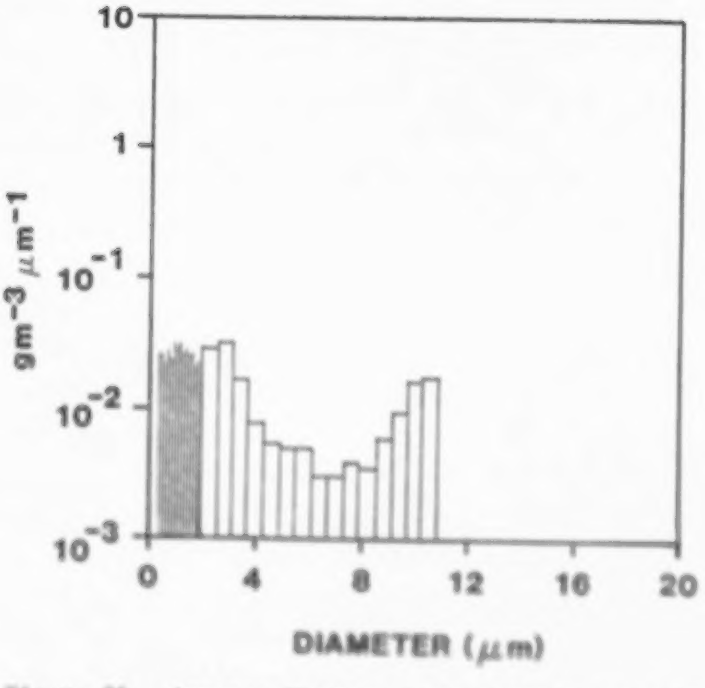

Figure 85. Average FPSSS mass distribution observed using ranges 3 and 4 during first impactor run (Valmont outlet).

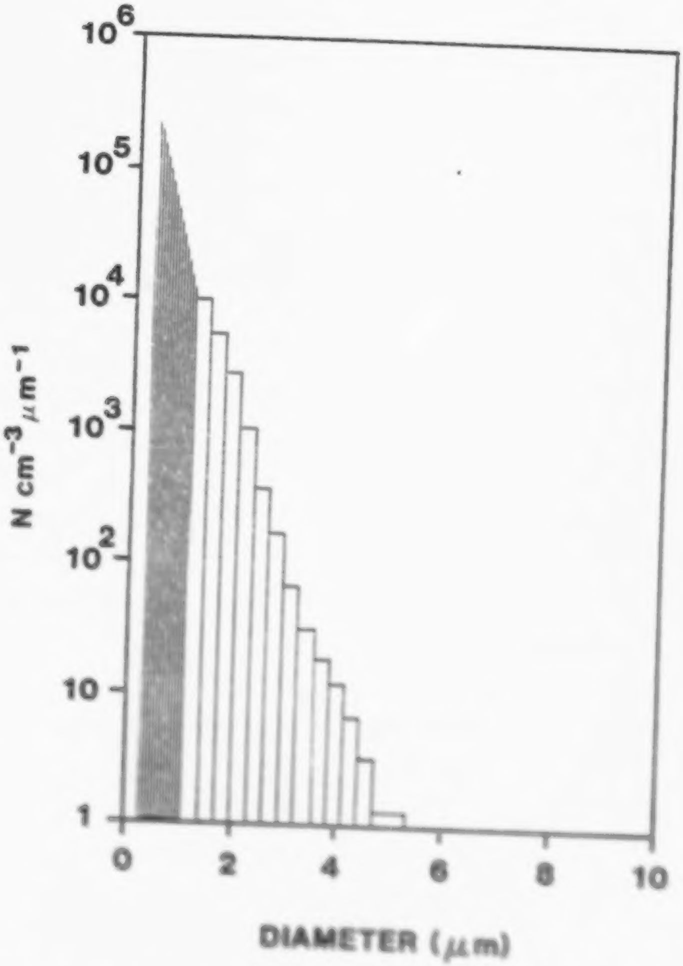

Figure 86. FPSSS size distribution for run ending at 14:11 on September 13 (Valmont outlet).

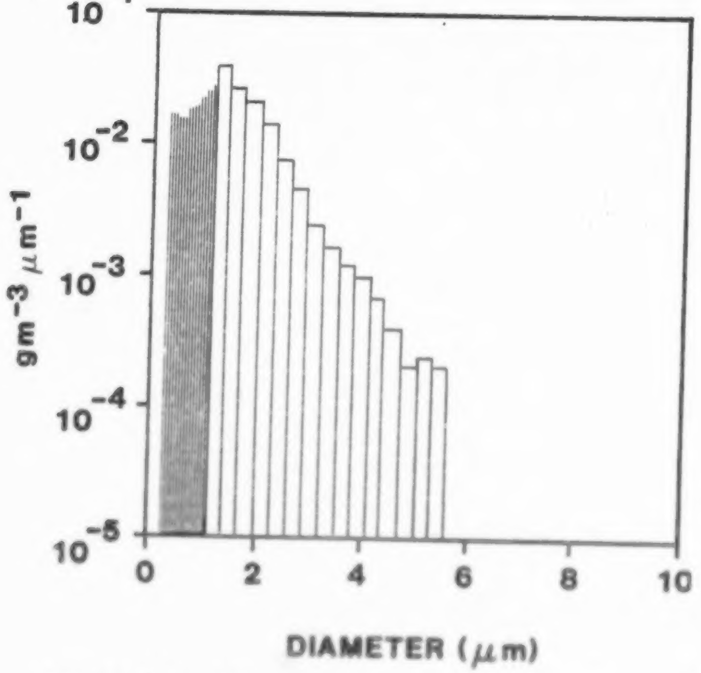

Figure 87. FPSSS mass distribution for run ending at 14:11 on September 13 (Valmont outlet).

ferent from those indicated for the first run when comparing the two sets of ranges. However, the strong second mode observed in Figure 85 was much less pronounced. The observed median mass diameter was 2 microns rather than 3 microns (0.5 to 11.0 micron range) on run 2 versus run 1. The mass loading observed when the 0.4 to 5.65 micron range was used agrees most favorably with the impactor data value of 58 milligrams, although the data from the 0.5 to 11 micron range had fewer of the artifacts at the largest sizes it also showed relatively good agreement.

The third impactor run was on September 14 at 10:00 a.m. Six FPSSS reports were taken averaging over 8 minutes each, four from the 0.4 to 5.65 µm range and two from the 0.5 to 11.0 µm range. The samples from the 0.5 to 11 micron size range suffer from some of the large particle artifacts, as is evident in the higher masses and mass median diameters. The size and mass distributions at 10:14 and 10:23 exhibit some differences from those observed the previous day (See Figures 88-91). Perhaps of greatest relevance is the appearance of a mass mode around 3 microns which was not observed the previous day. It occurs on both the 0.4 to 5.65 micron and 0.5 to 11 micron size ranges. The start of a mass mode (third) between 4 and 6 microns must be regarded with some suspicion due to low statistics, although it may well be real. It is also noteworthy that during this period of operations we observed a number of interesting transient phenomena with opacity values exceeding 60% at several points in time.

After completion of the third impactor run the impactor sampling apparatus was moved to the inlet and the FPSSS left to explore the outlet transient phenomena. We will discuss these in greater detail later; however, it was also during this time period that we noticed fluctuations in the laser reference voltage of sufficient magnitude to make the data suspect. These fluctuations only occurred with the probe in the stack and did not appear to be related to operating temperature. We attributed them to static discharging from collected particle charges. The temporary fix in the form of a large filter capacitor was added to the reference output, eliminating the problem (but not the source). The size distribution also lost its large particle tail in the 8 to 11 micron range, making the 0.4 to 5.65 micron range sufficiently wide to cover the largest particles observed. Note the difference in the size and mass distributions shown

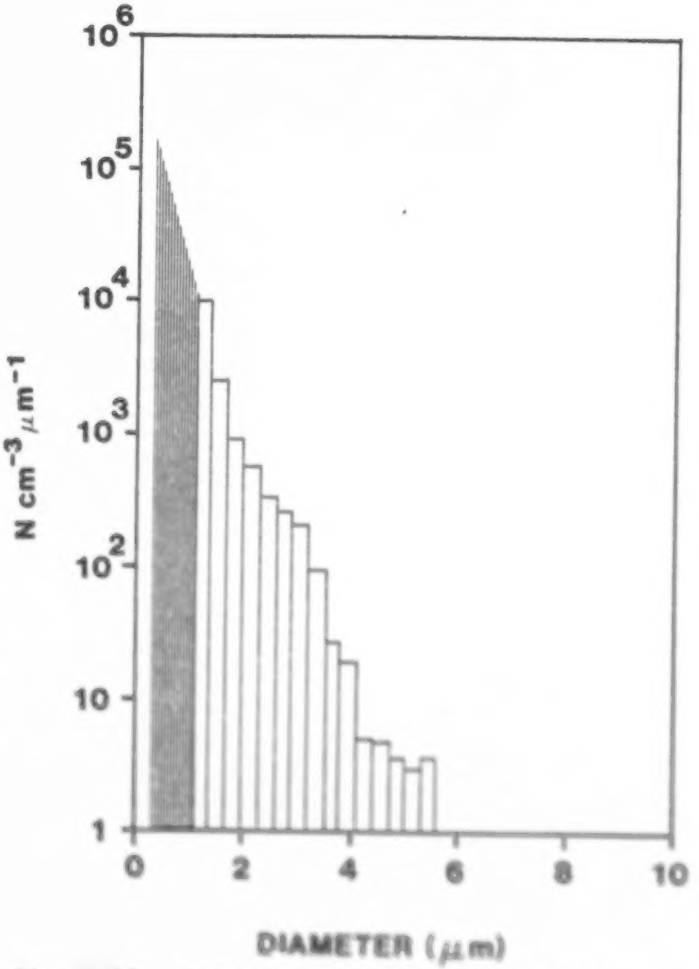

Figure 37. FPSSS size distribution covering third impactor run, ending at 10:14 on September 14 (Valmont outlet).

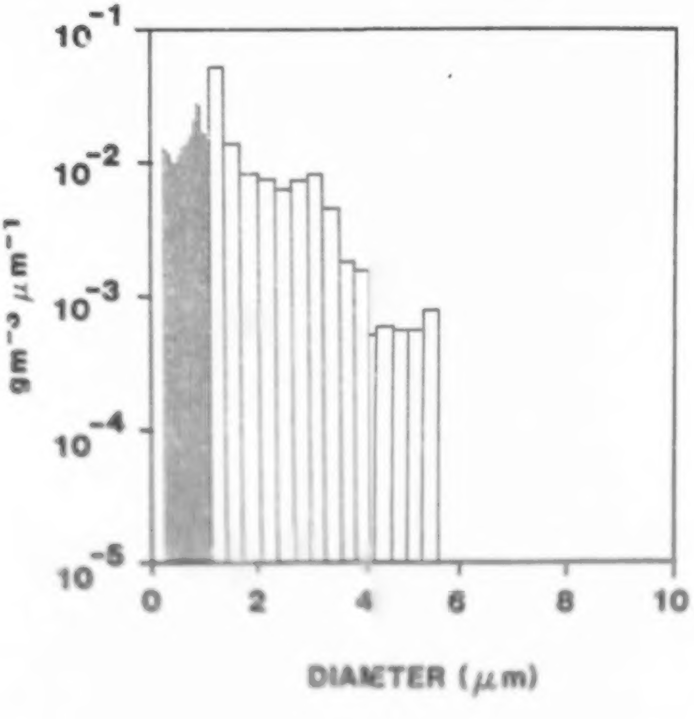

Figure 89. FPSSS mass distribution covering third impactor run and ending at 10:14 on September 14 (Valmont outlet).

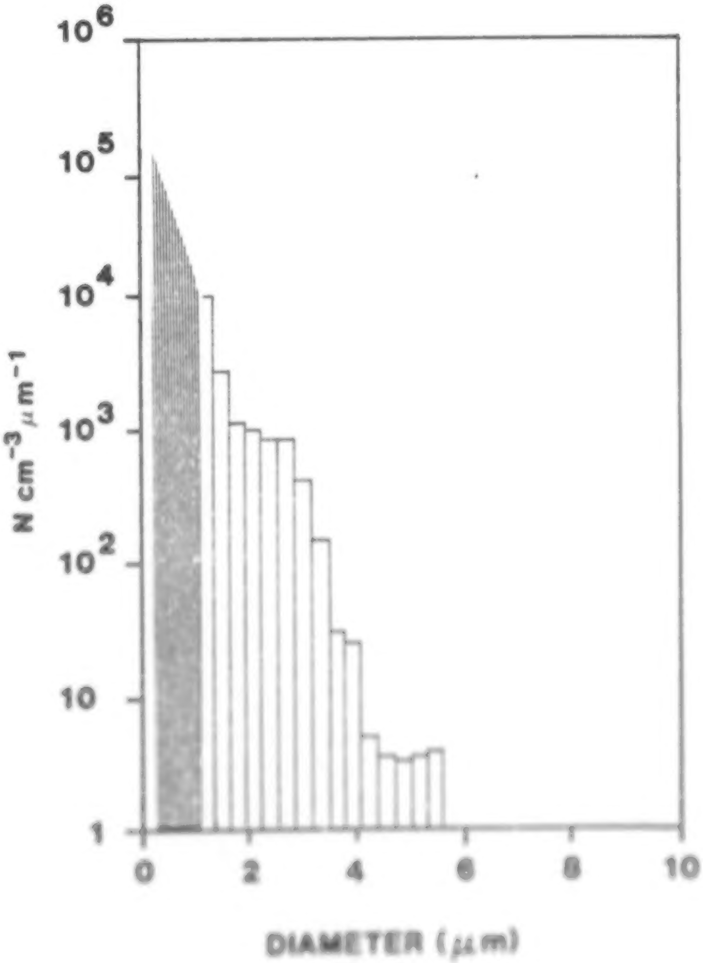

Figure 90. [illegible] size distribution for time period ending at 10:23 on September 14 (Valmont outlet).

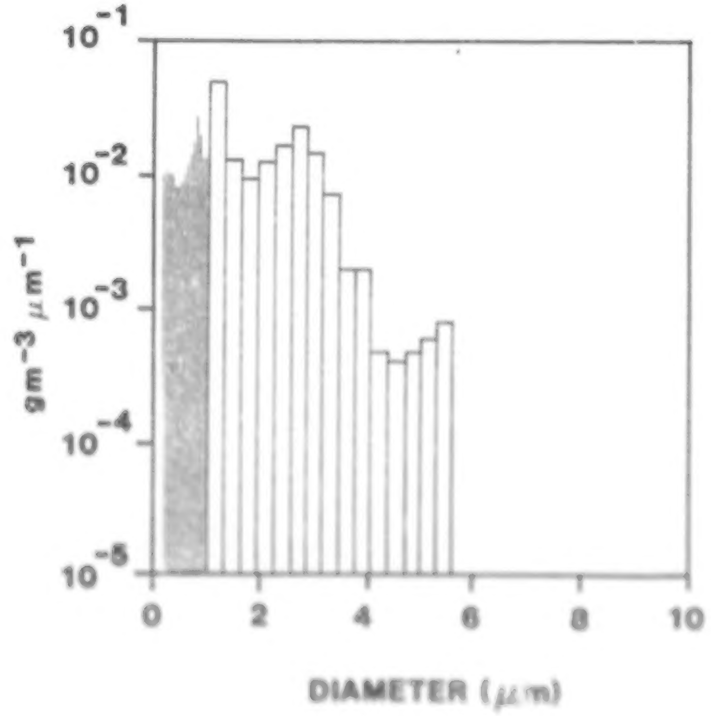

Figure 91. FPSSS mass distribution for time period ending at 10:23 on September 14 (Valmont outlet).

in Figures 92 and 93 for this period of time as compared to Figures 84 and 85 during impactor run number 1. The mass loadings observed after the EMI fix are somewhat lower than previously observed; however, the stack was also producing lower opacity values; thus, it is not possible to say that the 0.4 to 5.65 micron range did or did not have some contamination from EMI artifacts that were noticeable on the 0.5 to 11 micron range. However, in our judgment the effect is smaller than the other known sources of error.

On the afternoon of the 14th, two impactor runs were taken at the precipitator inlet. These sample runs were each 5 minutes in length and, because of the higher mass loading, collected about 2 grams of fly ash during each run. The FPSSS coverage included two reports during the first run and a single report during the second run, with a fourth report in between. The total mass loading average from the two FPSSS runs is seen to be approximately one-third of that reported by the impactor. The size and mass distributions for a 4 minute FPSSS sample completed at 16:49:14 are given in Figures 94 and 95. These data indicate much larger particles present than found at the outlet. For the FPSSS mass loadings the activity correction was nearly a factor of two (see Section 6.2 for collection relationship). Because of the high number density, activities of 70-80% were observed on the most sensitive size range.

The velocity used for all FPSSS computations was 9 ms^{-1} in this section of inlet. Because the flow is unrestricted here we did not expect or find the large fluctuations in the flow found in the stack. We thus felt the pitot measurements might be more accurate than those reported by the FPSSS. The FPSSS measured systematically higher values, more typically 12 ms^{-1}, which we knew to be somewhat high; however, the FPSSS mass loadings computed would be underestimated by up to 30% if the FPSSS velocities measured were to be accepted. Because considerable mass lies well beyond the range of the FPSSS, this discrepancy is in reality of minor concern.

During the final day of tests (September 15) two additional impactor runs were conducted. The third precipitator inlet impactor run was from 10:08 to 10:13, with the fourth from 10:26 to 10:31. Bracketing these runs were 8 FPSSS reports, each of 4 minutes duration. The mass loading values from the

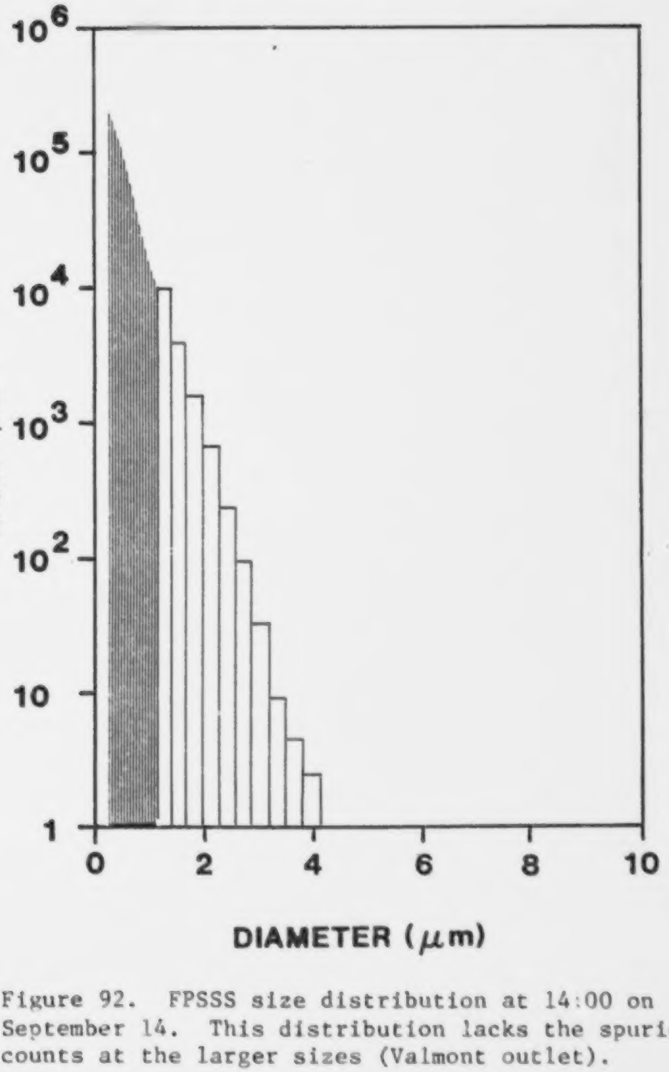

Figure 92. FPSSS size distribution at 14:00 on September 14. This distribution lacks the spurious counts at the larger sizes (Valmont outlet).

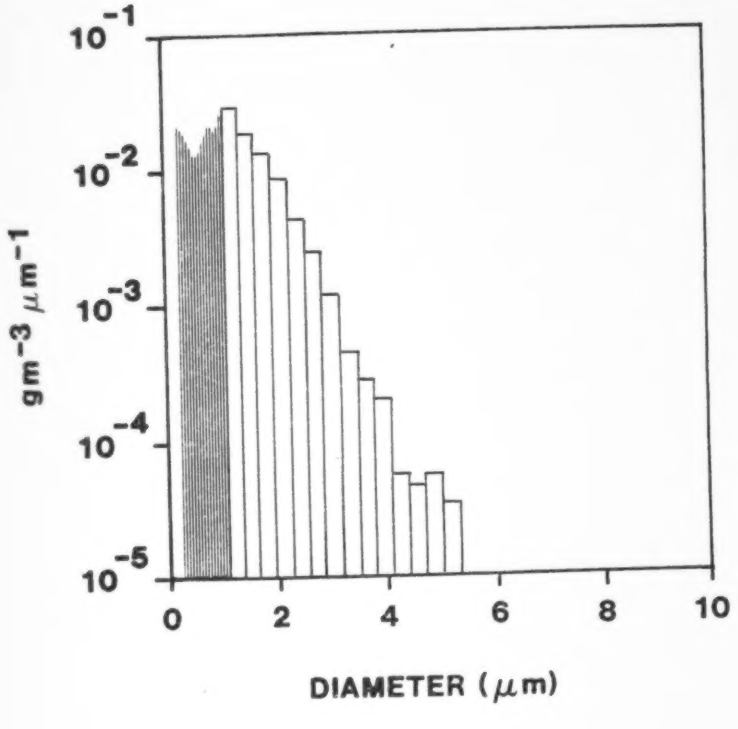

Figure 93. FPSSS mass distribution at 14:00 on September 14. This distribution lacks the spurious counts at the larger sizes (Valmont outlet).

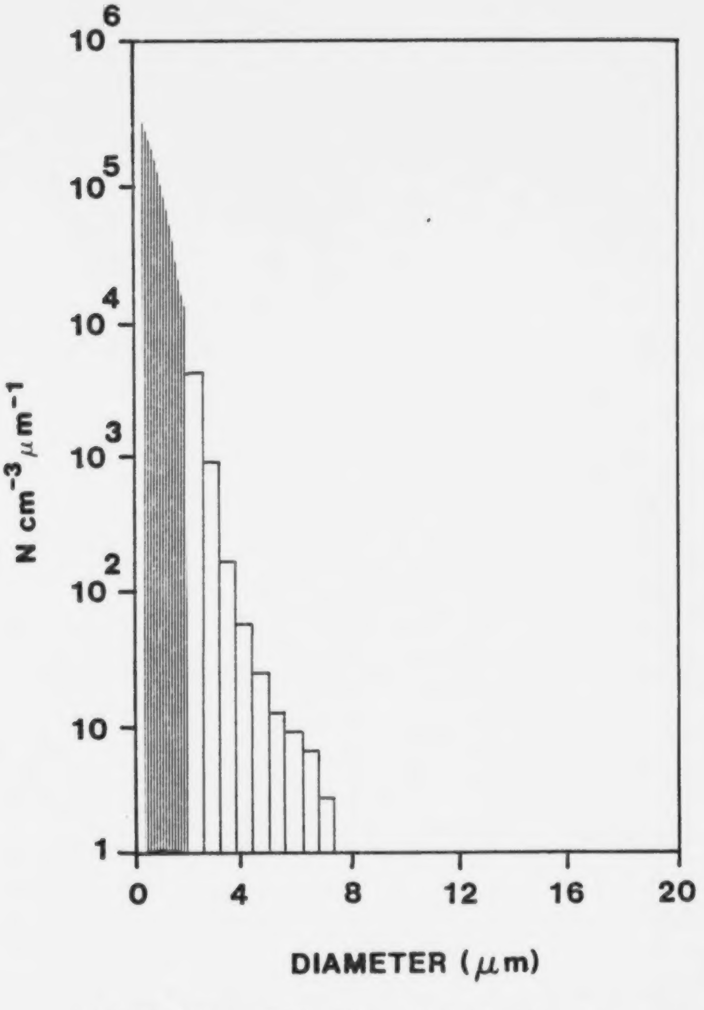

Figure 94. FPSSS size distribution for run ending at 16:49 on September 14 (Valmont inlet).

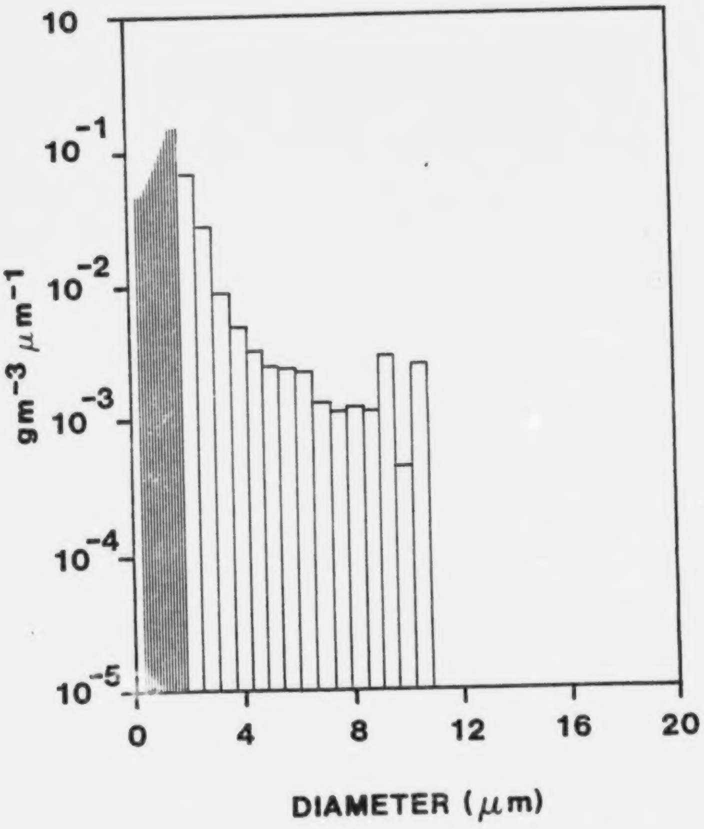

Figure 95. FPSSS mass distribution for run ending at 16:49 on September 14 (Valmont inlet).

FPSSS are somewhat higher than those on the previous day while the impactor shows a reduction in mass values. A typical set of size and mass distributions is shown in Figures 96 and 97 for the FPSSS report ending at 10:13:24. The primary difference between the data for the final two runs and the data on the 14th is found to be that the number density is systematically higher. The size and mass distributions show remarkable similarities. The mass median diameter at the inlet averages 2.2 microns for all the FPSSS runs, but, of course, its bias to the low side is due to the cut-off at 11 microns. A closer examination of Figures 96 and 97 also indicates a potential flattening in the mass distribution at sizes above 8 microns. We were somewhat suspicious that, in fact, a second mass mode beyond the instrument range might well be indicated. Of course, with FPSSS mass values running one-third to one-fourth those of the impactor, one would suspect either a second mass mode or at least a fairly flat mass distribution out to some tens of microns.

The difference between the FPSSS/impactor values on the 15th and the 14th is difficult to explain. However, it may be due to actual velocity differences and the fact that the FPSSS computations used a constant 9 m sec^{-1} velocity. Support for this argument comes from the observation of measured (uncorrected for activity) number densities above 10^5 cm^{-3} on the 15th. Laboratory computations and testing indicate that the FPSSS cannot measure this high. If the velocity was, in fact, higher (supported by FPSSS velocimetry), the actual number density would decrease and the observed mass loadings on the 15th would be similar to those on the 14th.

There were several opportunities during this test series to utilize the FPSSS to observe transient phenomena. Perhaps most illustrative of the observed changes in stack emissions is the opacity. Figure 98 is a plot of opacity and mass median diameter for an 8 minute period on the afternoon of the 14th, while we were waiting for SRI to move the impactor sampling equipment to the inlet. The results clearly show a 2 minute precipitator rapping cycle. Notice that the maximum values of opacity are 60-80% while the quiescent values are 15-20%. This sharp maximum is about a half minute in duration. It corresponds to the period when the final row of precipitation plates are rapped. The precipitator is configured with three rows of plates, each having 12 individual subsets all rapped at 2½ second intervals. Thus, it takes 30 seconds to rap

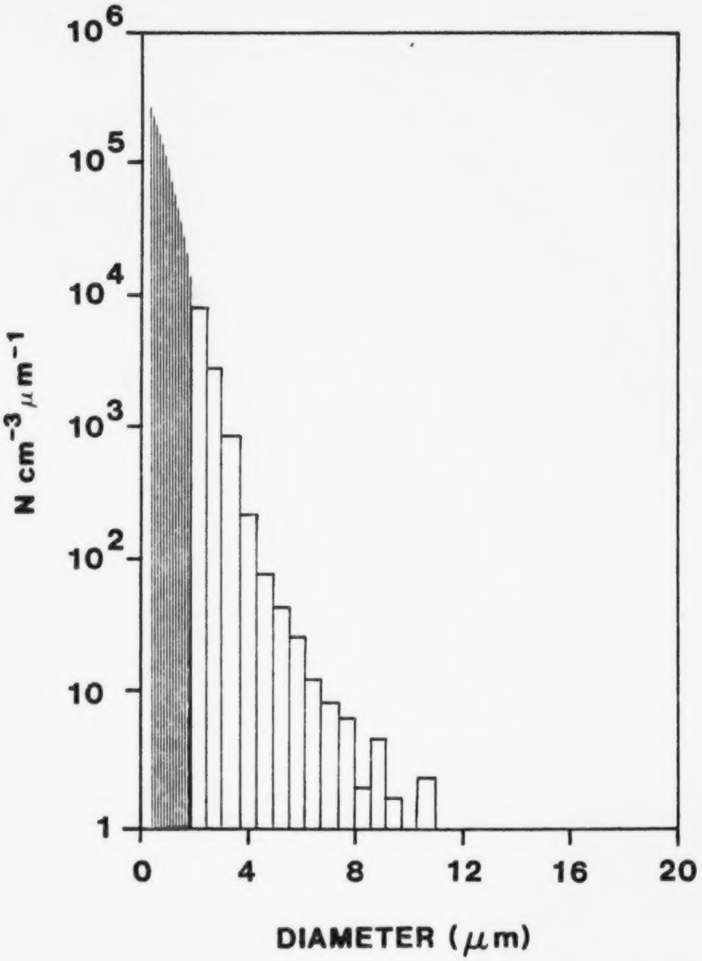

Figure 96. FPSSS size distribution for run ending at 10:13:24 on September 15 (Valmont inlet).

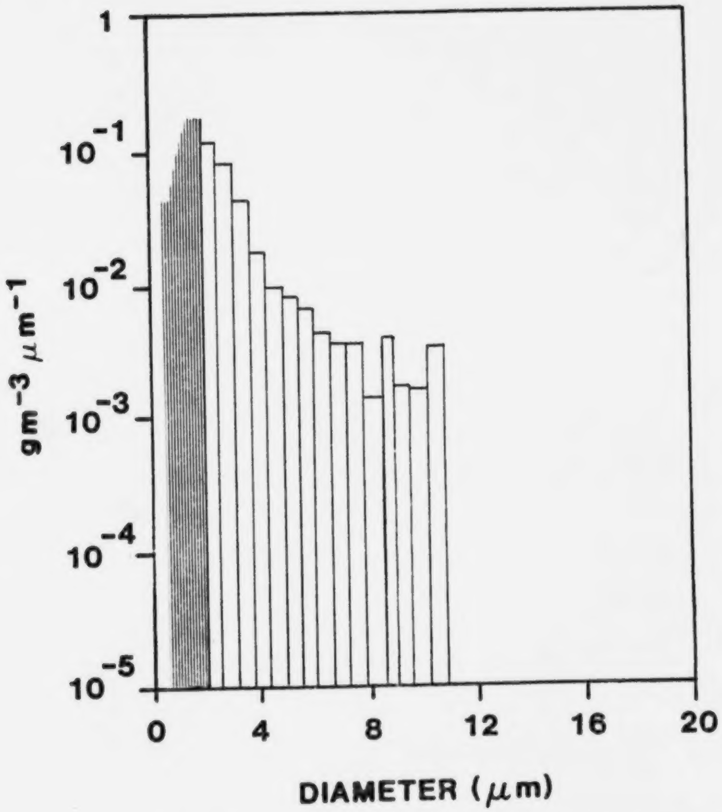

Figure 97. FPSSS mass distribution for run ending at 10:13:24 on September 15 (Valmont inlet).

VALMONT RAPPING SEQUENCE AS OBSERVED IN OPACITY AND MASS MEDIAN DIAMETER

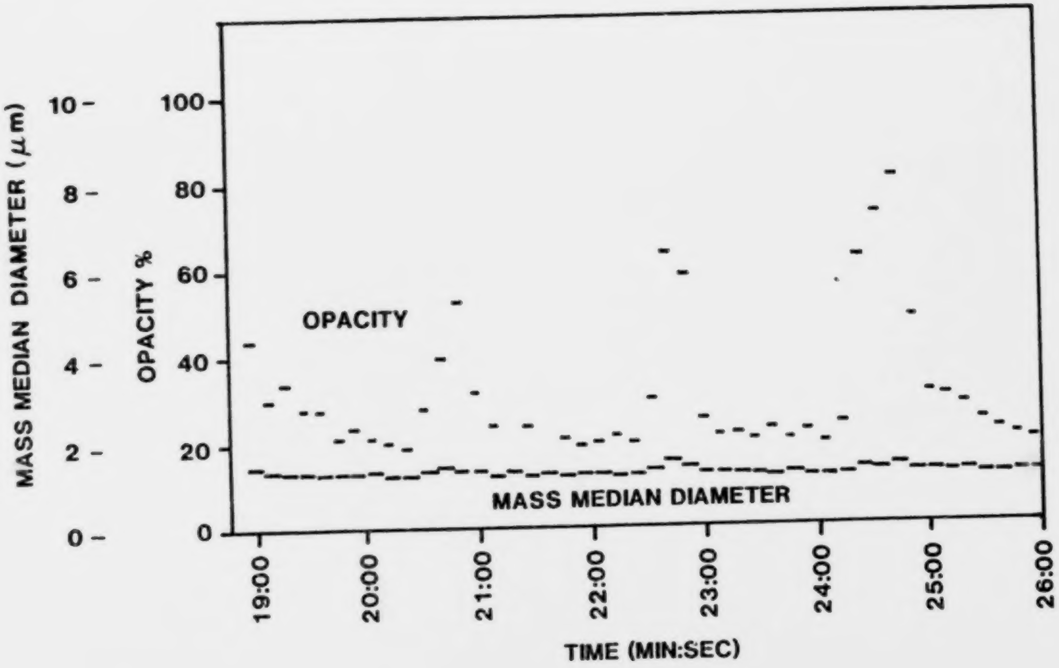

Figure 98

all plates in each row. The first row (closest to the inlet) is rapped twice as often as rows 2 and 3, thus generating a 1-2-1-3 sequence. What is revealed in the data peak is the rapping of row number 3 plates which clearly recollect most of the material exhausted when rows 1 and 2 are rapped.

We observed the same phenomenon with a PMS model CSAS-HTS instrument on September 15th (when the FPSSS was making measurements at the inlet). Figures 99a and 99b show two sets of data taken at 2-second intervals. Here we see a factor of 5 increase in the 2 μm sizes, but essentially no change in the submicron sizes (the observed count decrease on the graph is cancelled when the activity correction is applied). These compare well with the changes in the size distribution measured by the FPSSS during a rapping sequence. Both the FPSSS and CSAS-HTS essentially show zero or little change at sizes of 0.5 μm but a factor of 2 to 5 increase at sizes of 1-3 μm.

The opacity values seen in Figures 98 and 99 correspond rather well to the RM41 data seen in Figure 100. Although the RM41 records are noisy, it is not difficult to verify that the opacity seldom goes below 10%, in correspondence with the FPSSS, and the peaks have similar amplitudes. In fact, during one 1-hour time period, which included times from Figure 98, we were able to match the 2-minute rapping peaks with nearly one-to-one correspondence, as indicated in the scattergram of Figure 101. Figure 101 reveals excellent correlation between the minima and maxima for the FPSSS/RM41 instruments. The maximum opacity and number density variations are typically a factor of 3, while the mass median diameter increases approximately 30%. This may be due to agglomeration, which occurs in the electrostatic precipitator. The rapping cycle is not so apparent in the number density, but is again easily observed in mass loading. Figure 102 shows a time series of mass loading and number density values taken just after the sample in Figure 98. A three-fold increase in mass loading is evident, while the total number density changes slightly. This is consistent with the particle sizes that are responsible for the observed changes in opacity and mass loading being close to the mean mass size or perhaps the mean cross section size, but certainly not much smaller. Otherwise, there would be a larger change in number density than opacity or mass loading. This is, of course, consistent with the rapping process that literally shakes collected material off the ESP plates into hoppers. Some of this material is unavoidably re-entrained

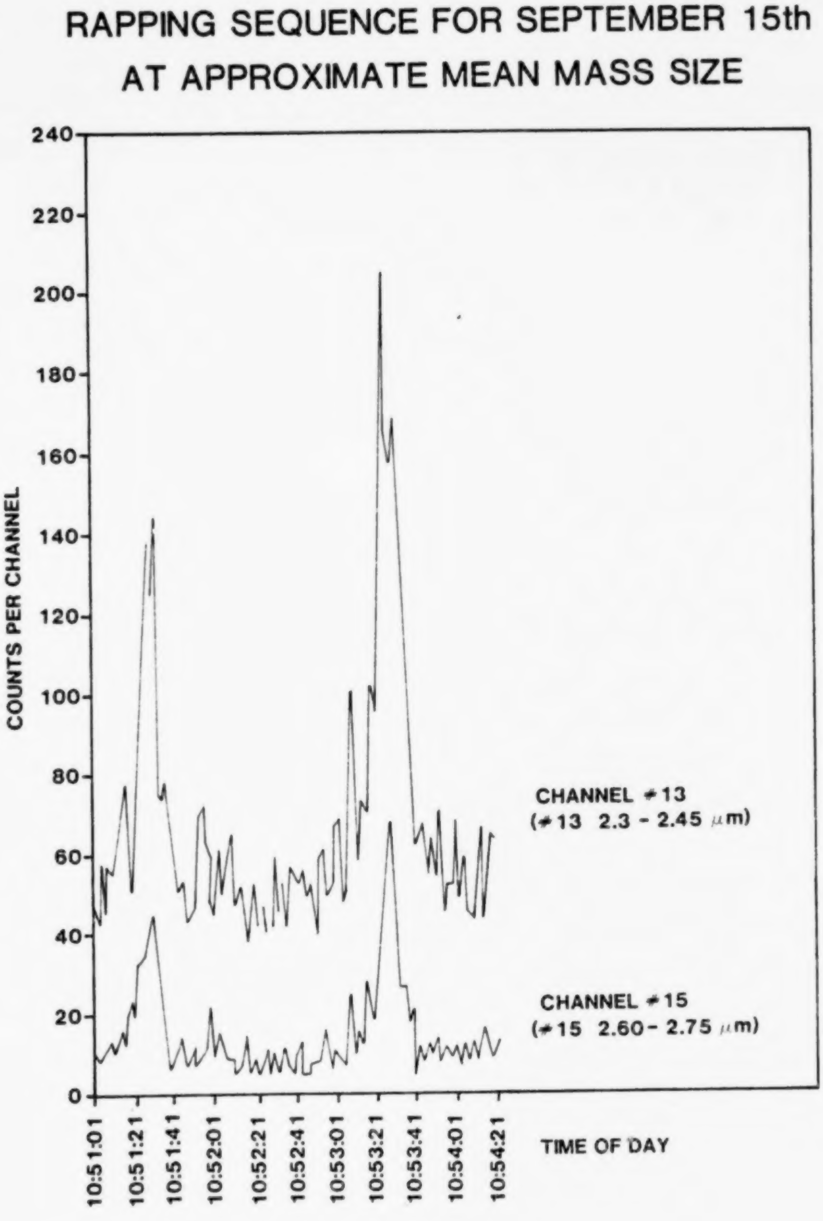

RAPPING SEQUENCE FOR SEPTEMBER 15th AT APPROXIMATE MEAN MASS SIZE

Figure 99a

RAPPING SEQUENCE FOR SEPTEMBER 15th AT SUBMICRON SIZES
(CSAS-HTS)

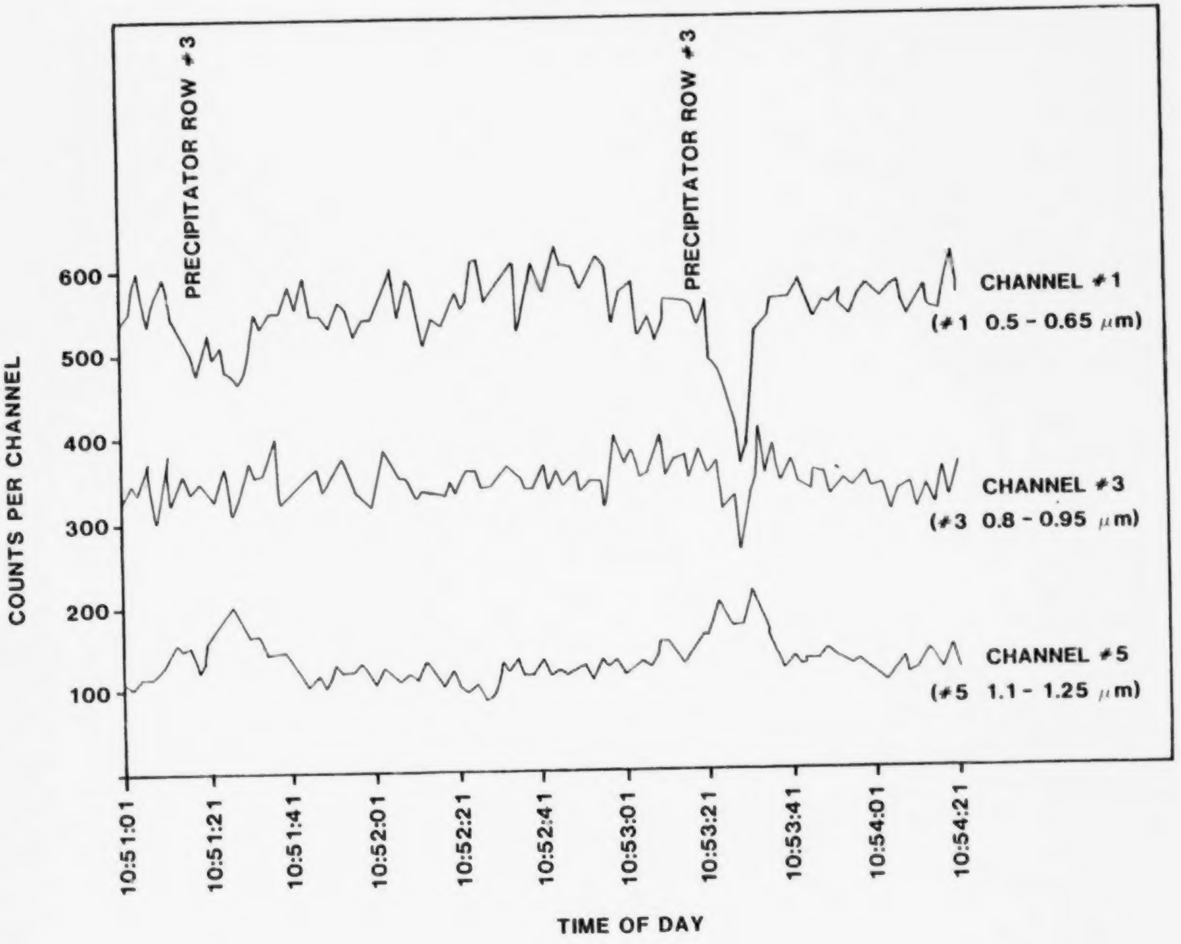

Figure 99b

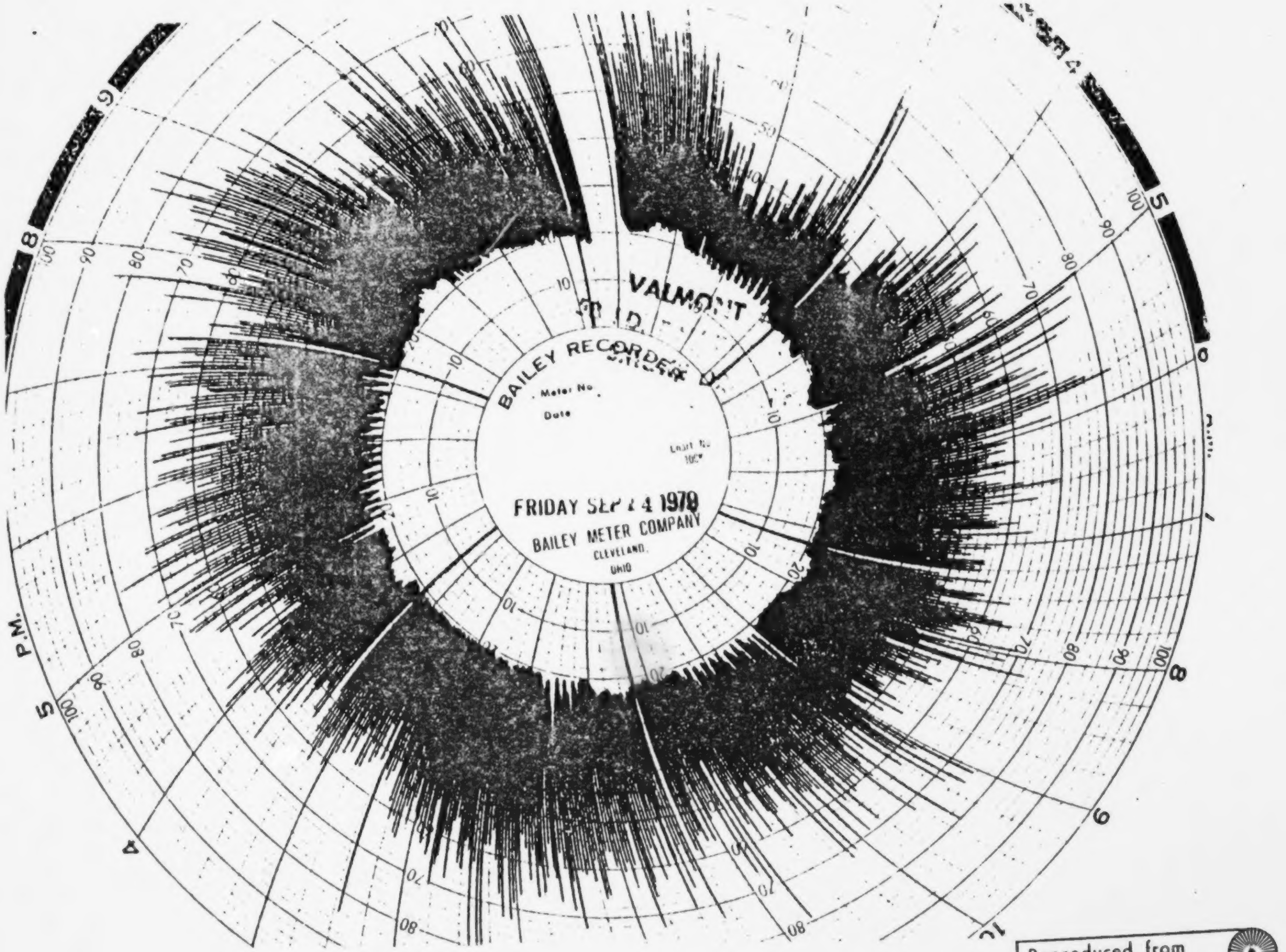

Figure 100. Lear Siegler RM41 opacity record for September 14. Note the much greater amplitude in the opacity data spikes as compared to Figure 75.

Reproduced from best available copy.

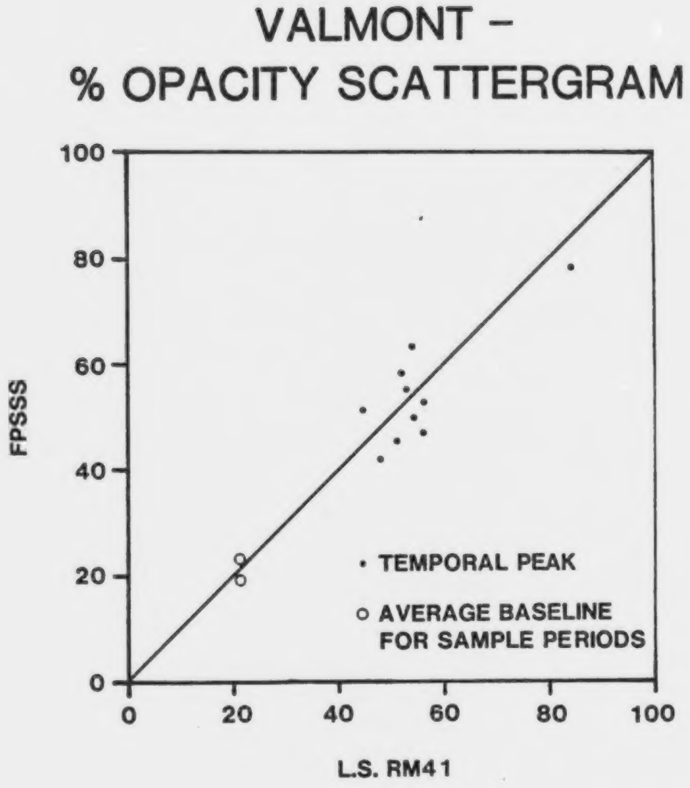
VALMONT -
% OPACITY SCATTERGRAM
FPSSS
100
80
60
40
20
0
0
20
40
60
80
100
L.S. RM41
• TEMPORAL PEAK
○ AVERAGE BASELINE FOR SAMPLE PERIODS

Figure 101

VALMONT RAPPING SEQUENCE AS OBSERVED IN MASS LOADING AND NUMBER DENSITY

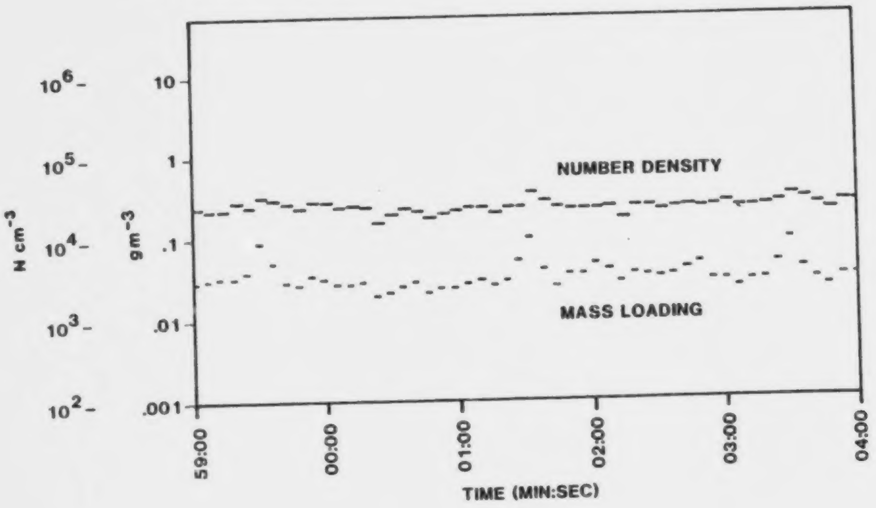

Figure 102

into the outlet flow. One would expect it to consist of larger sizes, as is observed.

After extensive analysis of the impactor data by SRI, the size distributions measured at the ESP inlet and outlet were compared with the FPSSS measurements. Essentially all four of the impactor samples from the outlet were indistinguishable from each other, as were all three inlet samples. It is thus sufficient to select one of the impactor runs from both the inlet and the outlet for comparison purposes. These results are presented in Figures 103-106. In addition to the impactor and FPSSS data at the outlet we have included data from the CSAS-HTS operating on September 15th.

The mass distribution comparison on an accumulative basis (Figure 104) looks quite good at the outlet; however, noticeable differences arise when examining the differential mass distributions of Figure 103. The FPSSS and CSAS-HTS instruments are in close agreement, while the impactor only reveals equal contributions around 2-3 μm, with reduced particles of smaller size yet increasingly larger numbers of larger sized particles. This is essentially the same result observed at Charlotte and leads us to conclude that the differences are systematic and that it's necessary to account for them.

The mass distributions shown in Figures 105 and 106 at the inlet are both in poorer agreement primarily due to one additional factor. This is that there exists a considerable amount of mass beyond the 11 μm limit of FPSSS and no attempt has been made to account for it. Activity on the FPSSS was also much higher at the inlet than at the outlet and certainly the smaller sizes could be easily off by 10-20% in corrected number density -- and possibly by much more if the potential velocity change previously discussed is real. However, a quick comparison of Figures 104 and 106 reveals the same discrepancy at sizes larger than a few microns. It is this discrepancy that we were most concerned with because the lower impactor values at submicron sizes are not so large and easily explained. We will address this problem in the remainder of this section.

First, we must recognize that the differences between the FPSSS and the impactor data at sizes larger than 3 microns appear to be systematic. If we had found the difference to be of a random nature we would probably not be terribly concerned, since considering all of the possible errors involved, vari-

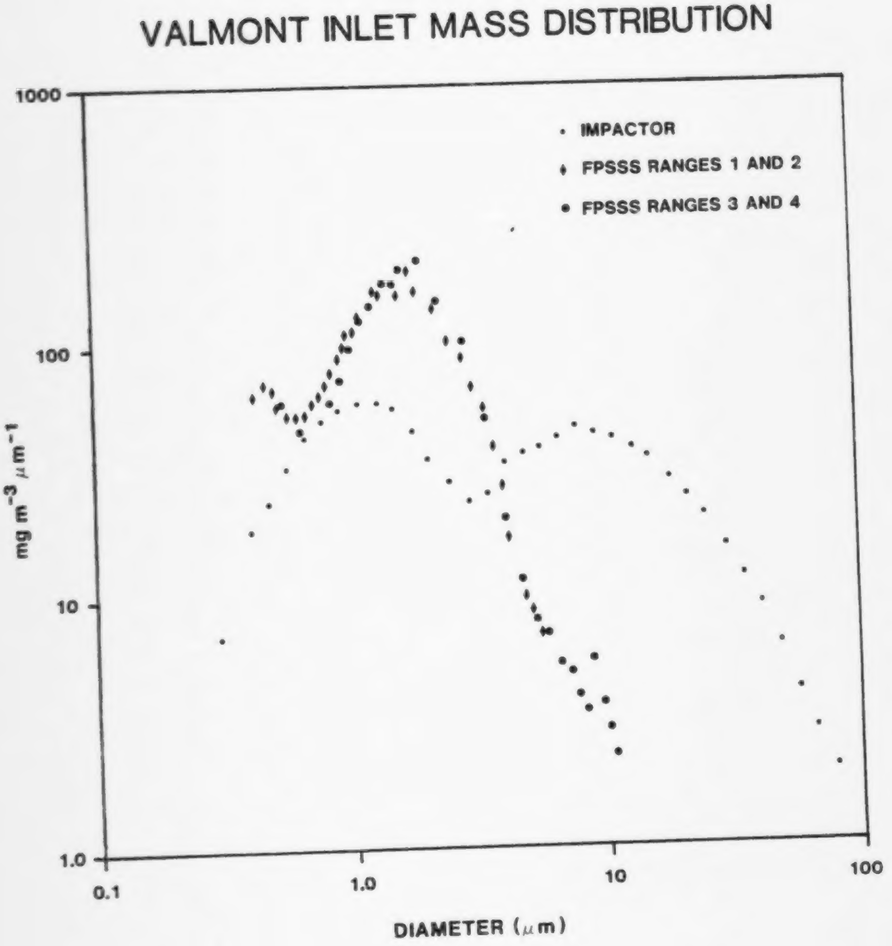
VALMONT INLET MASS DISTRIBUTION
• IMPACTOR
♦ FPSSS RANGES 1 AND 2
● FPSSS RANGES 3 AND 4
1000
100
10
1.0
mg m^{-3} μm^{-1}
0.1
1.0
10
100
DIAMETER (μm)

Figure 103

VALMONT INLET IMPACTOR RUN #6
CUMULATIVE MASS LOADING

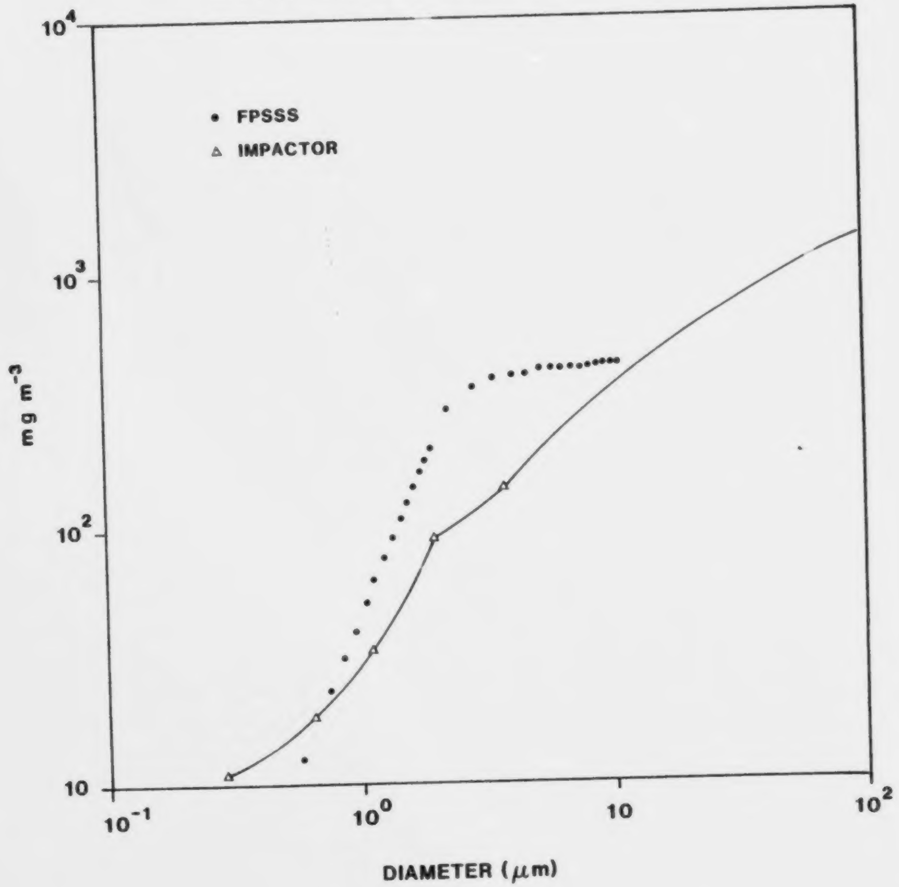

Figure 104

VALMONT OUTLET MASS DISTRIBUTION

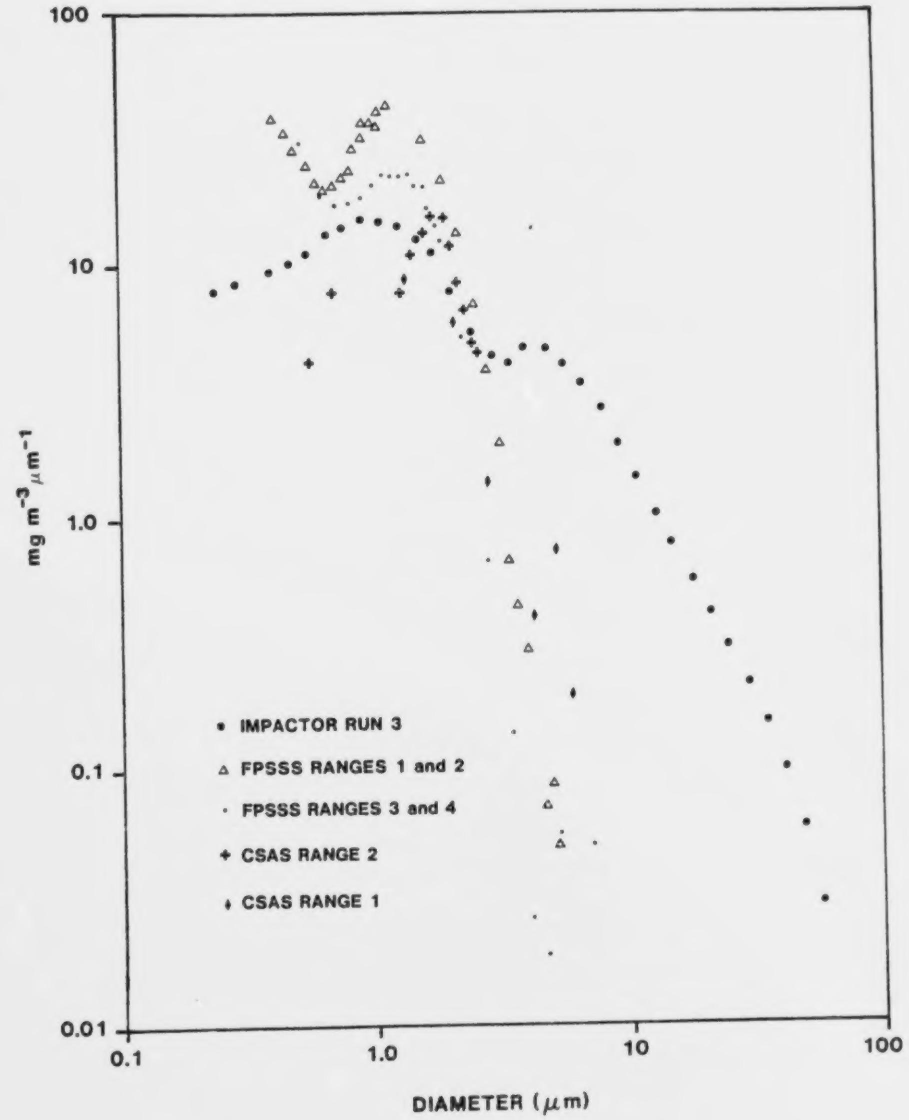

Figure 105

VALMONT OUTLET CUMULATIVE MASS LOADING FPSSS/IMPACTOR COMPARISON

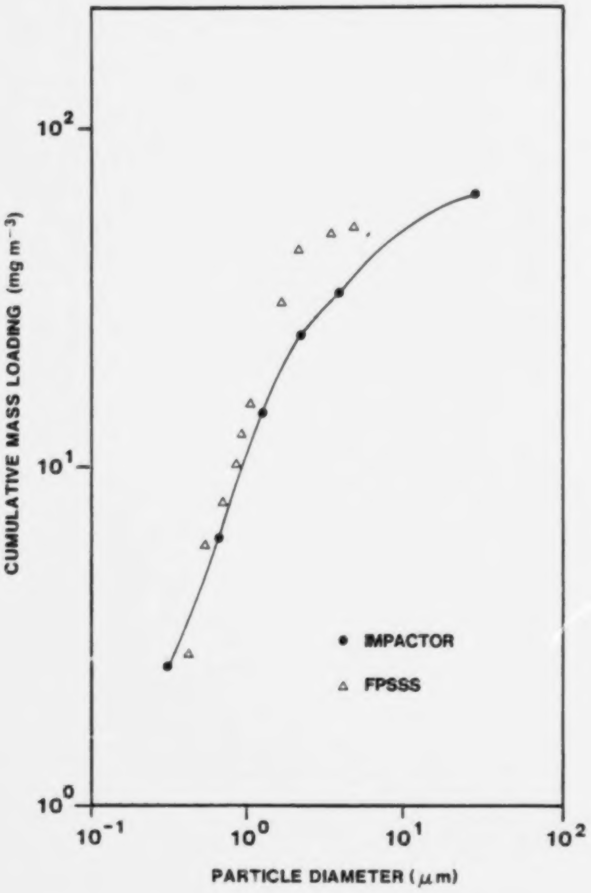

Figure 106

ations of this magnitude are to be accepted. But the fact that the comparisons show systematic differences incites one to believe that with proper resolution either or both techniques might eventually be substantially improved.

We must bear in mind that there are uncertainties with both the FPSSS and the impactor methodologies. The FPSSS is a high resolution instrument measuring physical (optical) diameters of particles. By comparison, the impactor is a lower resolution device that measures aerodynamic diameters. We, of course, do not in reality know that the density does not vary with particle size; however we were able to obtain samples of the Valmont fly ash at both the outlet and the inlet and have carefully examined and photographed them with optical and scanning electron microscopes (SEM), examples of which are shown in Figure 107. The samples shown were obtained from the actual impactor stages for run 3 at the inlet and run 4 at the outlet. One can, of course, attempt to extract size distributions from the SEM data; however, that task is extremely difficult in view of the large depth-of-field produced by the SEM and the difficulty in establishing the actual volume in any size analysis performed.

The resolution of the impactor is not limited simply to the fact that only 7 discrete size bins are afforded, but also by the mixing in sizes collected between stages. In other words, the bin edges are "soft" and a given size has a finite, and perhaps significant, probability of being sampled on more than one stage. It is a known fact that limited resolution will produce a decrease in the slope of a distribution parameter; thus, one would expect the FPSSS to produce a slightly steeper distribution than the impactor from resolution considerations alone. The SEM samples in Figure 107 show that sizes ranging over factors of 3 to 4 are common within any one stage; however, a detailed examination has revealed that quantitatively, the predominant effect is one of small particles trapped on the upper stages as opposed to larger particles trapped on the final stages. This, of course, has the interpretation that some of the mass of smaller particles is being assigned to stages reserved for larger particles. It again has the effect of flattening the distribution shown. But can it produce the magnitude of the discrepancy indicated? We must finally keep in mind that at sizes larger than a few microns the impactor analysis is admittedly less certain and the second mode in the bimodal mass distribution of Figure 103 should not be

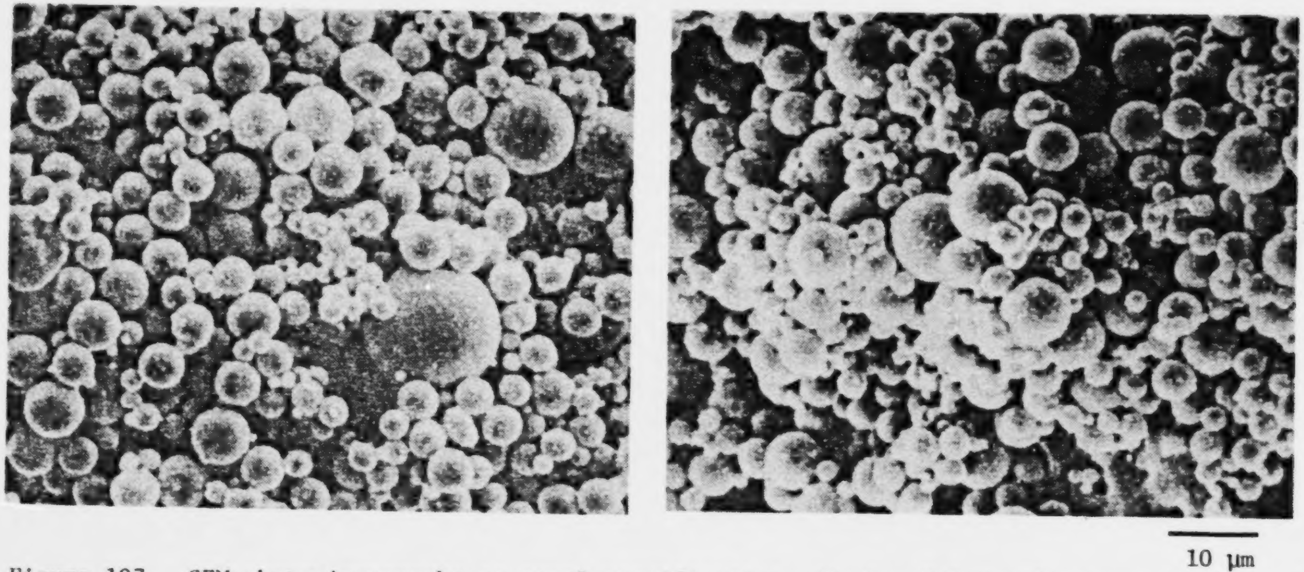

Figure 107. SEM photomicrographs at equal magnifications display Valmont Impactor samples. The outlet samples (below) demonstrate the effect of the E.S.P. when compared with inlet samples (above). Stage 1 photos are on the left, with Stage 2 on the right.

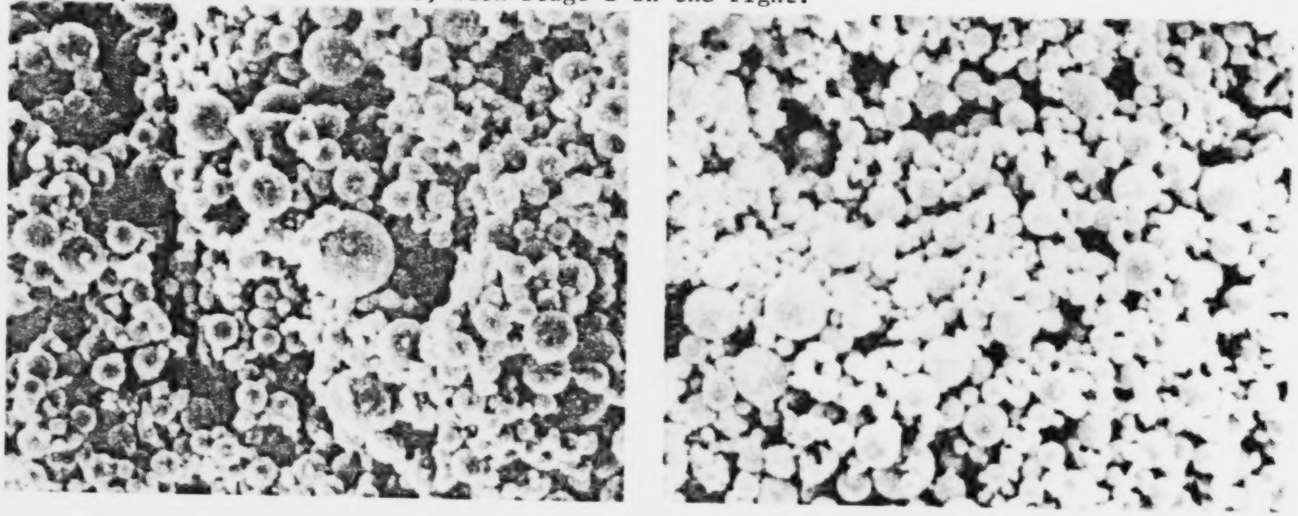

assigned much significance.

It is also worthy to note that the outlet FPSSS size distributions provided cross sections and opacities in excellent agreement with the opacity monitors. Impactor size distributions tend to underestimate opacity supporting the idea that the small particle fraction is underestimated.

With regard to the FPSSS, it is intrinsically more accurate in sizing smaller particles than larger ones. This arises from two sources: (1) the calibration curve becomes steeper at sub-micron sizes, and (2) the rejection process is less subject to error when the actual image size is infinitesimal. With the above in mind we performed two kinds of analyses to shed further light on the problem. First, all indications are that the impactor underestimates the number of particles less than 3 microns relative to particles larger than 3 microns. If we accept the FPSSS values as being correct below 3 μm, we can artificially adjust the impactor data upwards to match in this region and then reduce the mass sizes larger than 3 microns by an equivalent amount (conservation of mass). One might, of course, ask what justification we have in moving the impactor data upwards at sizes less than 3 microns in view of the fact that the CSAS-HTS data are still less. We know the opacity arises from sizes in this region and thus believe the CSAS-HTS should read less in this region. Furthermore, the CSAS-HTS has associated plumbing losses that cannot be accounted for. In any case, requiring the impactor data to match the FPSSS at sizes less than 3 microns results in significant lowering of the curve at sizes larger than 3 microns. This results in substantial improvement in the comparison but there remains some residual disagreement as one proceeds to larger sizes. The discrepancies increase in magnitude owing to the difference in distribution slope generated by the two classes of devices. Of course, we should be aware that any fair comparison must end at about 11 microns, the upper size limit of the FPSSS.

From past experience with the FPSSS we know that it can reject large particles if it is misoriented. If the flow is turbulent, a certain percentage of particles would invariably be misoriented. Recall the observed cutoff of larger sizes observed in Figure 64; could we be losing large particles because of misorientation produced by turbulence? Upon examining Figure 105, we find that the FPSSS and the CSAS-HTS are in excellent agreement at sizes larger than 3 microns and conclude that misorientation cannot be effecting the FPSSS; however, a closer look at the data indicates some support for higher counts by the CSAS-HTS relative to the FPSSS and we have previously mentioned that the CSAS-HTS has some unmeasurable line losses. One would thus conclude that indeed the FPSSS may be rejecting higher numbers of larger particles than in fact it should. Of course, the CSAS-HTS was not even operating on the same day as the FPSSS but from the opacity records in Figure 100 one would suspect that the stack was overall significantly cleaner on the 15th day than on the 14th and, if anything, the CSAS-HTS should have seen fewer large particles by comparison. At the present time, we probably are not warranted in adjusting the FPSSS data upward at the larger sizes since we do not in fact have proof that it is an error. Suffice to say that with suitable randomization of particle trajectories, some loss of larger particles due to unfavorable rejection is likely. Further study of this effect is warranted. It is, however, abundantly clear that it is not in error by the amount indicated by the impactor data. Correction of the impactor data for the small particle contributions previously indicated would bring about excellent agreement. We do not believe the rejection of large particles by the FPSSS to be unduly large. On the other hand, in laboratory comparisons at IERL, where the flow was sufficiently laminar to preclude any rejection bias by the FPSSS, no systematic discrepancies were observed. Differences between IERL and SRI impactors and analyses must be recognized, however. We are thus left to conclude that the "best guess" as to the size distribution from 3 to 11 microns lies somewhere between the impactor and the FPSSS but most likely closer to the FPSSS than to the impactor.

Finally, we should mention that it is not logical for the FPSSS to be correct below 3 microns and at the same time significantly undersample at larger sizes. For such to be true, the opacities would be in error by as much as a factor of 2 and we would be computing much higher masses with poorer agreement than indicated. We must, therefore, conclude that the FPSSS, being in agreement with indicated opacity and measured mass loading using two other independent techniques, must be providing a pretty fair representation of the size distribution, and furthermore, that the optical and mass properties of the particles are probably adequately covered by its finite size range at the stack outlet. At the inlet the FPSSS covers only a fraction of the size range contributing to the observed impactor mass loading. It, however, again provides sufficient size range coverage to adequately characterize particle optical properties.

9. CONCLUSIONS

From the results presented in the theoretical analysis and laboratory and field testing we are encouraged to believe that the FPSSS will be a satisfactory instrument for *in situ* size distribution measurements in a hot stack environment. The theoretical response computations discussed in Section 5 indicate that systematic errors typically associated with light scattering devices have been precluded in the selected 2-11° collecting solid angles. The FPSSS has been tested with monodispersed latex and polydispersed glass spheres and intercomparisons made with several other non-optical, as well as optical, particle size spectrometers. In field comparisons with impactors and opacity meters, the agreements in derived mass loading and opacity are probably within the known expected errors in measurement. There is little doubt that the FPSSS has the required accuracy and flexibility, at least potentially, to greatly aid in the evaluation of control devices and stack stationary emission sources.

The above mentioned positive results do not fully indicate the real value of the FPSSS. The FPSSS was not really intended to be a replacement for impactors; it is simply much too expensive a device to compete with impactor techniques, although it gives higher resolution in the measurement of the size distribution. Clearly, its advantage lies in its much greater resolution in size and time, the latter being a much more subtle parameter. Although the FPSSS does not sample but a minute fraction of the air measured by impactors (the ratio of their equivalent sample areas being about a factor of 200), it is capable of measuring a mass increment as small as 10^{-13} g. Probably the minimum weighable mass difference on an impactor stage is 10^{-4} g. This difference in intrinsic mass resolution of 10^{9} gives the FPSSS the capacity to measure relatively low outlet mass loadings (with minimal statistical sampling error) in less than a second, compared to an hour of actual sampling by an impactor followed by an even larger analysis time, particularly if size analysis is desired. This much higher temporal resolution gives the FPSSS the ability to reveal temporal phenomena that clearly cannot be addressed by impactors and to make that information available immediately.

The size distribution in our analysis is not sharply resolved by impactors due to the lack of sharp limits to the size bin associated with a given stage. The problem is accentuated when the size distribution is particularly steep.

This effect may be only of academic importance, since, for all practical purposes, the sizing differences are small and the resulting spectra from either an FPSSS or an impactor would probably not surprise anyone. Nor would anyone be able to decide easily which spectrum represents a more desirable emissive product.

We have found it of great benefit in our field evaluation to be able to compare opacity values computed by the FPSSS with those generated by in-place opacity meters. The good opacity correlation, simultaneous with reasonable impactor mass comparisons, leaves little possibility of sizable FPSSS size distribution errors. It may also not be apparent, but the FPSSS, like all near forward scattering particle sizing devices, is capable of generating essentially correct opacity values irrespective of the particle response oscillations associated with Mie computations (as described in Section 5). This is because the full extinction cross section (from which opacity is computed) follows the scattering response (or partial scattering cross section) computed in Section 5 in magnitude as well as in qualitative signature. In other words, a particle size that corresponds to a resonant peak and generates a larger scattering signal than some larger size also generates a correspondingly larger extinction loss. You may not be able to measure its true size exactly, but its scattering and extinction cross sections are essentially error free at wavelengths close to those of the He-Ne laser line. The passband of the opacity meters is sufficiently close to the He-Ne line that the errors are negligible. Of course, over a large, smooth size spectrum such effects would largely average out anyway. We would thus encourage future users of the FPSSS to utilize opacity measurements as a valuable method of cross checking.

It is helpful when analyzing the performance of a new instrument to bear in mind the tradeoffs made in its design. With regard to the FPSSS two come to mind immediately. One has resulted in the current lower size limit of 0.4 μm and the other limits the maximum measurable number density to a lower level than desirable. These two factors are synergistic.

The EPA initially asked for a size range of 0.5 to 5.0 μm. We felt that a 0.3 μm sensitivity could be obtained since standard PMS instruments currently size that small. Our current instrument has a 0.4 to 11.0 μm range. The difference between 0.3 and 0.4 μm is about a factor of 3 in signal. An expansion of the collecting angles from 11 to 20° could pick up this difference. However, this would require moving the sample region closer to the prime objective since its size cannot be increased by the rough factor of 2 required and still allow the FPSSS head to fit in standard 4 in-stack ports. Our wind tunnel results do not preclude moving the sample region closer but it obviously will not be as aerodynamically clean as it currently is. In view of the turbulent conditions observed in the Valmont stack, clean aerodynamics may not be a profitable design feature and movement of the sample volume closer could indeed be a better choice.

The current instrument design can handle number densities up to several tens of thousand per cubic centimeter although coincidence losses must be corrected for. An increase in magnification from 20 to 30X should provide measurements approaching 10^5 cm^{-3}. An increase in the inner collecting angle from 2 to 4° also doubles the maximum number density where measurements can be made. Halving the laser beam diameter has a four-fold effect.

We previously mentioned that achieving a higher maximum number density limit and greater sensitivity were strongly related. First, it should be obvious that increasing the sensitivity automatically increases the number of particles viewed and thus coincidence losses. Conversely, doubling the inner collecting angle reduces the light collected. The overall sensitivity is obviously reduced as well, but there is a more subtle effect. The 2° inner angle allows for very accurate measurements out to 10 μm by collecting the diffracted light at small forward scattering angles. A deterioration in sizing performance would result if the inner angle were increased above 3° for 10 μm particles or about 5° for 5 μm particles. The latter choice would further require enlarging the outer collecting angle to achieve adequate sensitivity. Halving the laser beam diameter aids sensitivity as well as maximum number density limits. However, here one must be absolutely sure that alignment will be extremely stable. To decrease the beam diameter by a factor of 2 requires either using a condensing mirror of half the radius of the current one or doubling the laser beam diameter input to the mirror.

Probably the easiest means would be to increase the magnification to 30X. The only penalties paid are in increasing the detector bandwidth (admitting more noise) to see the relatively shorter pulses that would result and possibly increasing the probability of unfavorable trajectory of large particles. An increase in bandwidth is required because the photodiode is sized to view the full transit of a particle and any increase in magnification will truncate the time a particle is viewed.

There remain a number of unanswered questions that further use of the FPSSS in the field should clarify. For instance, we indicated the possibility that large particles might be rejected more easily if turbulence indicates significant trajectory deviations from normal flow. Though we were not convinced that any problem existed during our field measurements, it is something that deserves further study. Users of the FPSSS in situations where large particles are dominant would be wise to rotate the probe head and ascertain whether any position other than normal to the flow maximizes count rate at large sizes and leave it in that position if it does. Further use of the FPSSS in the near future should clarify this open issue. There are ways to reduce the sensitivity to orientation. One requires a reduction in the gain ratio used to establish the rejection criteria and thus sample volume. The mask on the beam splitter can also be modified so it is wider at the edges than at the center (like an hourglass), permitting a wider spread in trajectory alignment. We currently cannot say whether either is warranted.

We are also somewhat unsure of the stability of the internal velocimeter. We indicated that its accuracy is probably 10-15%. It may well be the limiting factor in the overall accuracy of the basic measurement system. Unlike impactors, which only measure velocity to attempt to provide isokinetic matching but then accurately meter the actual sample flow, the FPSSS is an *in situ* device requiring *in situ* flow measurements as accurate as the final desired result. Again, possible improvements in the circuitry could alleviate instrumental sources of error, but there is little one can do if the laser beam width is not stable. The laser beam width is, of course, directly related to the transit time and thus velocity computation. Multimode lasers can undergo temporal fluctuations in output beam diameter amounting to at least 10%. Thus, it is probably impossible to achieve better accuracy without additional optical hardware. For instance, one could provide a separate detector (photodiode and beam splitter) that measures transit time across a mask. As long as the mask is always smaller than the laser beam, fluctuations in the laser beam diameter would not be a factor. One other attractive possibility is to use a laser operating in TEM_{oo} mode. This is a doughnut-shaped beam profile where size is invariant. It is also a smaller beam that could allow for measurements at still higher number densities without changes to the optical system.

We should finally recognize that the FPSSS is a new and highly sophisticated device. There are more opportunities for failure than with conventional techniques. It becomes contaminated with time, requiring cleaning. It is thus viewed primarily as a research or investigative tool and not a routine monitoring device. As is the case for all measurement processes, an experienced operator is the best guarantee of successful use. Anyone who has tried to make measurements around stacks knows of the difficulties that can occur. In designing the FPSSS, we have tried to remain fully cognizant of the user's environment and attempted to maximize the usefulness of the instrument. The real utility of a device like the FPSSS is not in extending sensitivity to the smallest particles or in having the ability to handle the highest number densities. Rather, it is that it provides measurements of sufficient spectral quality to gain insight into processes that produce changes in particle size and number density and it retains reasonable verisimilitude in integrated properties such as mass loading and opacity.

REFERENCES

Knollenberg, R. G., 1977: Light Scattering and Imaging Array Particle Sizing Methods for Stack Measurements, presented at Air Pollution Control Assn., Ontario Section Symposium, April 27, 1977

___________, and Hunten, D. M. 1979a: Clouds of Venus: Particle Size Distribution Measurements, Science Volume 203, 23 February 1979, pp 792-795

___________, and Hunten, D. M., 1979b: Clouds of Venus: A Preliminary Assessment of Microstructure, Science Volume 205, 6 July, 1979, pp 70-74

___________, and Hunten, D. M., 1980: The Microphysics of the Clouds of Venus: Results of the Pioneer-Venus Particle Size Spectrometer Experiment, Journal of Geophysical Research Volume 85, No. A13, pp 8039-8058, December 1980

___________, and Gilland, J. R., 1980: Sounder Probe Particle Size Spectrometer, IEEE Volume GE-18, No. 1, January 1980, pp 100-104

___________, and Luehr, R., 1975: Open Cavity Laser 'Active' Scattering Particle Spectrometry from 0.05 to 5 Microns, Fine Particles, Aerosol, Generation, Measurement, Sampling, and Analysis, Benjamin Y. H. Lui, Editor, pp 669-696

___________, 1976a: Three New Instruments for Cloud Physics Measurements: The 2-D Spectrometer, The Forward Scattering Spectrometer Probe, and The Active Scattering Aerosol Spectrometer, presented at the International Cloud Physics Conference, July 25-August 6, 1976. A. Meteor. Society Preprint Volume, pp 554-561

___________, 1976b: The Use of Low Power Lasers in Particle Size Spectrometry, presented at the Optical, Electro-Optical, Laser and Photographic Technology Symposium, August 23-27, 1976. SPIE, Volume 92

Borne & Wolfe, 1972: Principles of Optics, 3rd Edition, Pergamon Press Ltd, England

Cooke, D. D. and Kerker, M., 1975: Response Calculations for Light-Scattering Aerosol Particle Counters, Appl. Optics, Volume 14, No. 3, March 1975

APPENDIX I. THE PMS CALIBRATION WIND TUNNEL FACILITY

The PMS wind tunnel is designed as a complete calibration facility for particle environments encountered in flight and other high flow rate conditions. The tunnel is an open circuit tunnel with an energy ratio of 6:5. It is aerodynamically clean and has a completely variable velocity control using an axivane variable pitch fan, (see Figures A1 and A2). The tunnel is capable of velocities in excess of 200 knots in a 30" test section. A calibrated water injection system duplicates flight conditions in cloud and precipitation environments. Complete monitoring of actual particulate size spectra with PMS spectrometers enables thorough calibration of various instruments as well as providing test conditions for research studies. A dedicated data acquisition/recording system provides high resolution detailed data samples. During winter months the tunnel can operate as an icing facility during below freezing weather. Precipitation in the form of snow (or rain) is drawn into the tunnel for certain test work. When combined with water injection mixed phase studies are possible.

The wind tunnel is fully instrumented with standard PMS spectrometers, full state parameter sensors and data acquisition systems. Computer software exists to assist the experimenter in handling all of these data. The following instrumentation is dedicated to tunnel operations.

Spectrometers:

1. Forward Scattering Spectrometer Probe (FSSP)
   Size Range: 0.4 - 45 μm
2. 2-D Cloud Droplet Optical Array Spectrometer (OAP-2D-C)
   Size Range: 25 - 800 μm
3. Experimental Airborne 2-D Grey-Scale Optical Array Spectrometer Probe

State Parameter Measurements:

1. Total Air Temperature (2)
2. True Air Speed
3. Volumetric Airflow
4. Pitot Pressure
5. Static Pressure
6. Dew Point Hygrometer

Data Systems:

1. PMS Data Acquisition System - DAS-64
2. PMS Dual 2-D Data Acquisition System
3. Particle Data Processing System - PDPS-11C
4. Pertec Tape Recorder and Formatter
5. Versatec Printer/Plotter

Of particular importance to many programs is the existence of aerosol sourcing apparatus which can be used to study and characterize *in situ* measurement capabilities by the proposed FPSSS. A large 4 m^3 vessel is normally used to generate controlled populations of aerosol particles (see Figure A3). Populations of monodispersed latex, glass beads, salt nuclei or polydispersed smokes are generated in the vessel and exhausted into the tunnel to provide calibration points during tunnel calibration runs. As an example this set-up has been used to calibrate the sample-inlet tube for NCAR's Electra/Sabreliner Air-Sampling program. An inlet of this type is shown installed in the tunnel in Figure A4. Note the paired FSSP's which provide *in situ* characterization of the aerosol populations in free-stream. Besides the obvious sampling efficiencies that can be determined for such inlets, problems with regard to sample lag and acoustical resonance (standing waves) are being studied.

The PMS Calibration Wind Tunnel Facility was of considerable benefit to this program. It was the primary test-tool in validating how well the FPSSS design maintained its *in situ* characteristics.

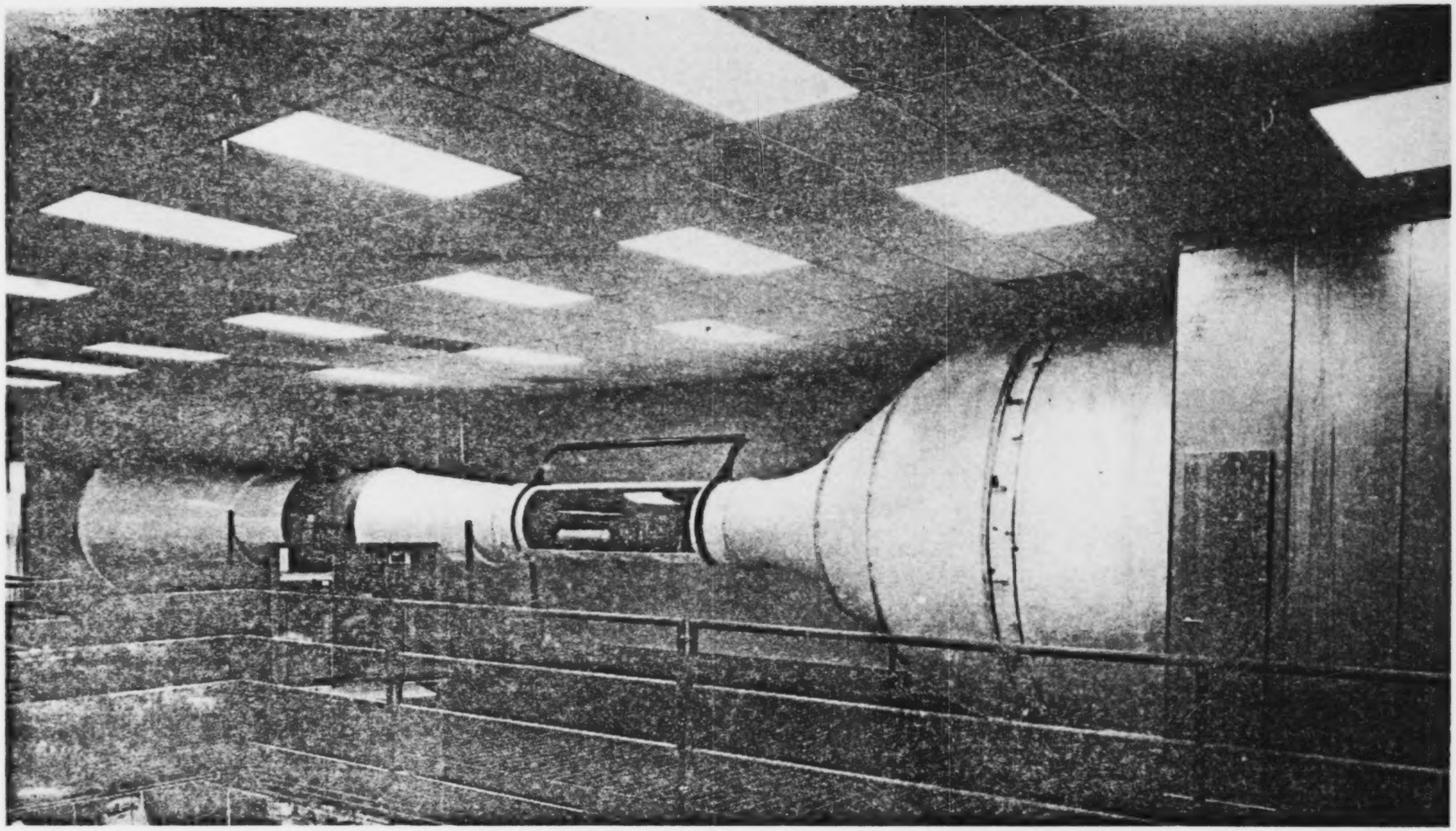

Reproduced from
best available copy.

Figure A1. Photograph of PMS Calibration Wind Tunnel Facility

PMS CALIBRATION WIND TUNNEL FACILITY

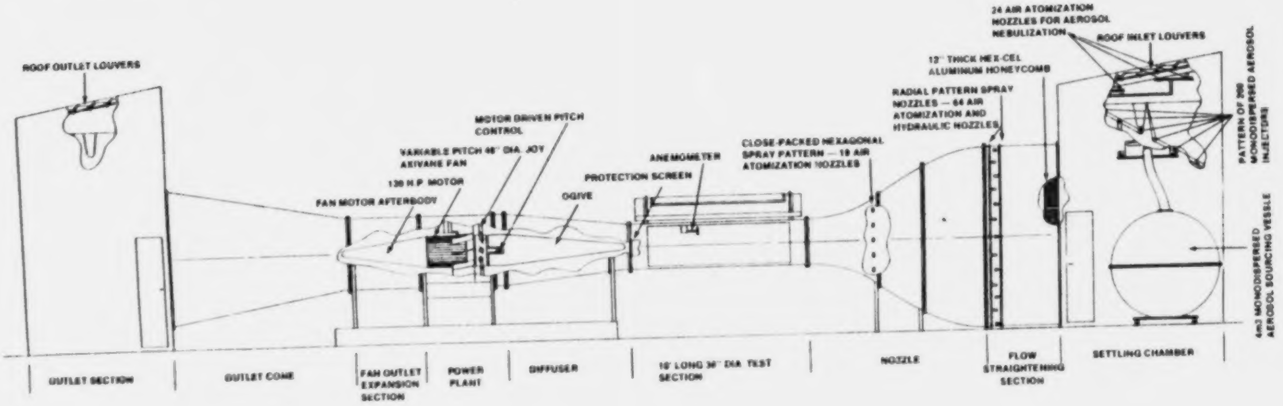
ROOF OUTLET LOUVERS
FAN MOTOR AFTERBODY
130 H.P MOTOR
VARIABLE PITCH 46" DIA. JOY AXIVANE FAN
MOTOR DRIVEN PITCH CONTROL
OGIVE
PROTECTION SCREEN
ANEMOMETER
CLOSE-PACKED HEXAGONAL SPRAY PATTERN — 19 AIR ATOMIZATION NOZZLES
RADIAL PATTERN SPRAY NOZZLES — 64 AIR ATOMIZATION AND HYDRAULIC NOZZLES
12" THICK HEX-CEL ALUMINUM HONEYCOMB
24 AIR ATOMIZATION NOZZLES FOR AEROSOL NEBULIZATION
ROOF INLET LOUVERS
PATTERN OF 200 MONODISPERSED AEROSOL INJECTORS
4m3 MONODISPERSED AEROSOL SOURCING VESSLE
OUTLET SECTION
OUTLET CONE
FAN OUTLET EXPANSION SECTION
POWER PLANT
DIFFUSER
10' LONG 36" DIA TEST SECTION
NOZZLE
FLOW STRAIGHTENING SECTION
SETTLING CHAMBER

Figure A2

Reproduced from
best available copy.

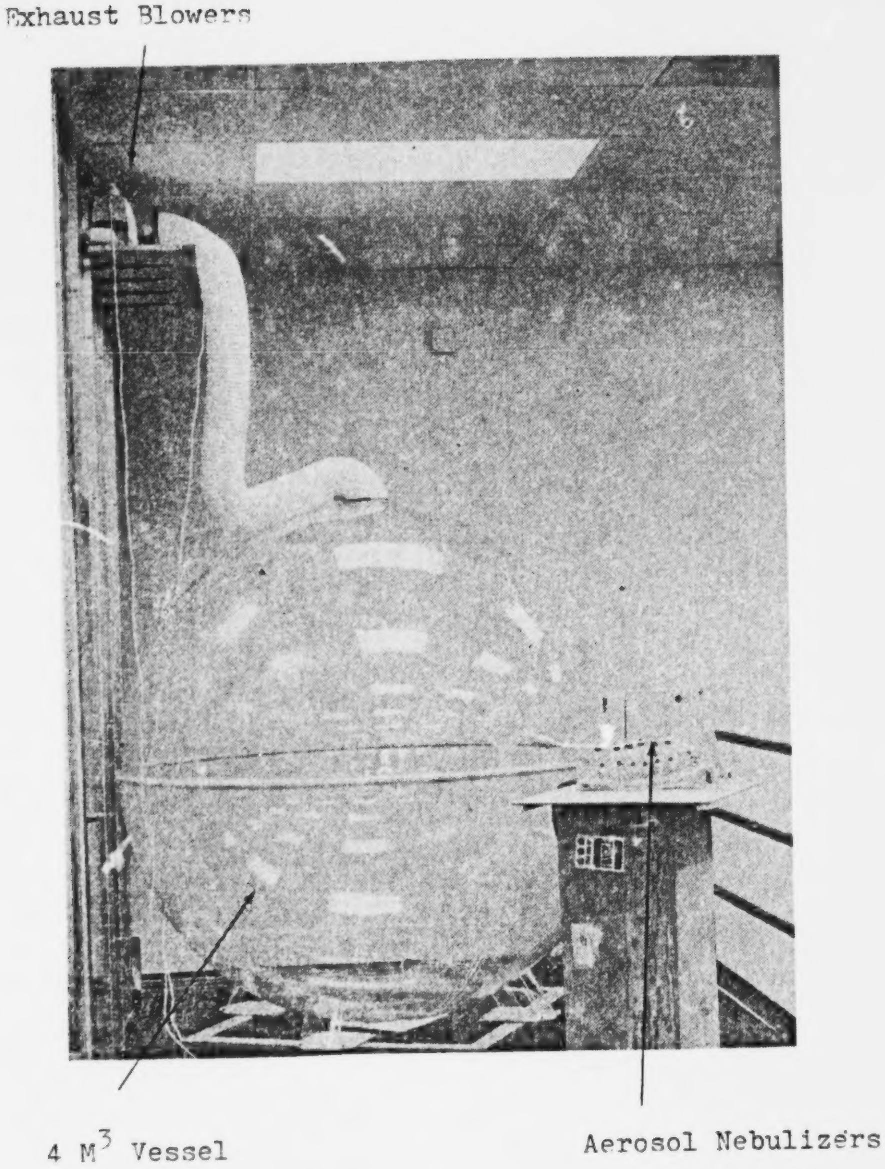

Figure A3. Wind Tunnel Monodispersed Sourcing Subsystem

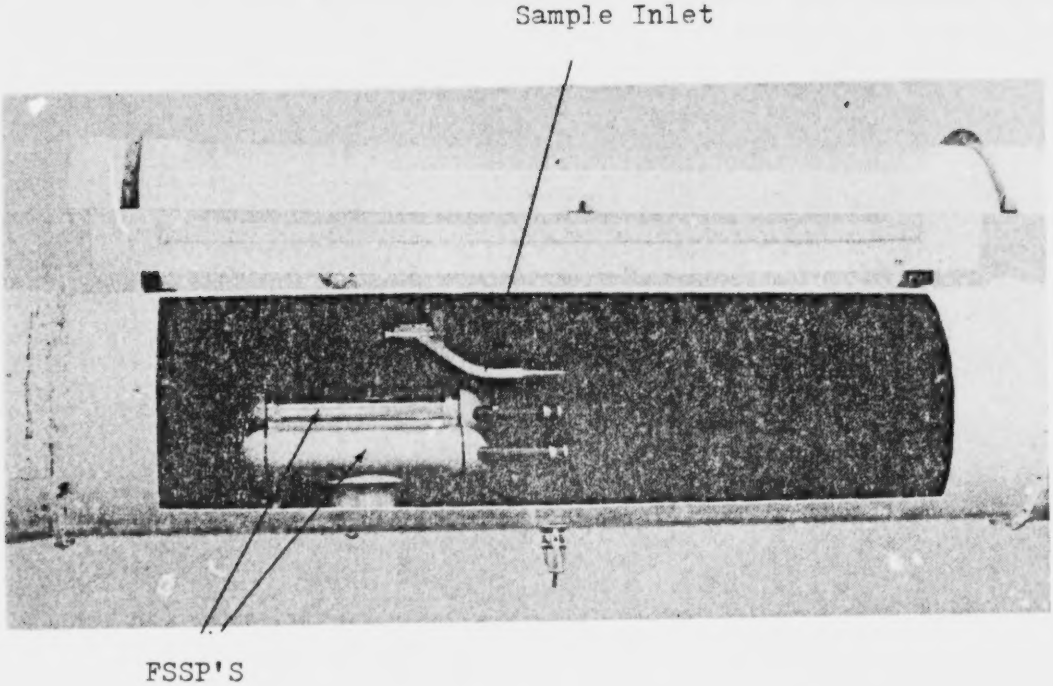

Figure A4. Sample Inlet Tube Installed in Tunnel Test Section with FSSP'S. Pumping System and other Samplers are Behind Tunnel.

ADDENDUM

Since the completion of the prototype FPSSS, four more Systems have been fabricated. Two of these were purchased by Southern Research Institute (SRI), Montgomery, Alabama. The third unit was purchased by Shell Development Laboratory of Houston, Texas. The fourth unit will be retained by PMS for contract services work. The units purchased by SRI are being used in field studies while Shell's unit is being applied in a research combustion facility. Feedback from these initial users has brought about certain modifications which we believe have increased the utility of the FPSSS.

From work with the prototype unit the one area of greatest concern was with the velocimeter. These additional four units had velocimeters of an improved design. Improvement primarily resulted from increasing the bandwidth of the signal amplifier train and by providing separate pulse amplifiers for processing pulse widths (velocity information) tailored to the particular size range selected. These changes brought the velocimeter to within ±10% over the 2-30 $msec^{-1}$ velocity range. This improved velocimeter was the only noteworthy change in these four units as compared to the prototype.

With regard to early feedback through customer use of the three shipped units, no problems were encountered in stack measurements; however, contamination problems were encountered when performing measurements prior to control devices. The particulate matter was found to be contaminating the inside surface of the window and the primary objective. Since this region is supposed to be in an overpressure area, sealing of the stainless steel jacket had to be faulty.* However, since some additional contamination was noticed on the outside surface of the window, we elected to correct the problem by modifying the window purge-air shrouds and increasing the purge-air supply as well as improving the sealing of the stainless steel jacket. The single diaphram air pump housed within the heat exchanger has been replaced with the double diaphram unit with twice the airflow capacity. The air lines have also been increased in size. We are considering the installation of an airflow meter to enable the operator to adjust the purge-air according to particle flow velocity. This will preclude possible purge-air disturbance of sample volume at low flow velocities.

---

*In one case corrosive vapors condensed upon the surface of the objective's first element and etched into the glass sufficiently to require that the element be replaced.

After completion of these modifications, contamination of optical elements essentially ceased. There still are, however, when measuring before control devices, instances where number densities exceeded the instrument's capacity at the smaller sizes. There remains a number of additional possible modifications that could benefit the user. We have recently found a superior insulation material (to the fiberglass) in the form of a moldable insulation material. The fiberglass wrap blankets are difficult to handle and deteriorate with each disassembly/reassembly of the probe head. In certain cases it would be desirable to provide a single shorter section of boom for use in small work areas. We have found the lateral bearing to be awkward and unable to withstand the constant exposure to corrosive gases. A new support clamp has been designed to replace the bearing for stationary installations. An air seal on the lateral support bearing has also been devised.

With regard to data treatment and presentation it would appear that the FPSSS will cover the needs of most users. In fact, it appears desirable to reduce the number of size classes, providing one single size range of 32 size classes, in the interest of instrument simplicity. We plan to build such a unit in the near future. We would also like to increase the maximum particle number density the FPSSS can handle although here only small gains are possible. The laser beam diameter at the sample plane can be further reduced by upwards of a factor of 2 which will allow measurements at 4X higher number densities. This will require the addition of a negative lens assembly in the condensing path and necessitate an x-y adjustment on the secondary objective for final alignment, the latter a possible worthwhile improvement in any case. Thus it would appear that 100,000 particles per cm^3 is a practical upper limit for the FPSSS in the future. It is clear that number densities can be encountered well in excess of this limit. Accommodation to higher numbers will require fundamental changes in head design to allow scattering measurements at 90°. Using 90° scattering number densities in excess of $10^6 cm^{-3}$ are accessible.